To Study the Effect of Morphology on the Optical, Magnetic and Electrical properties of Some Nanostructured Transition Metal Oxides

Thesis Submitted by

Swarupananda Bhattacharjee

Doctor of Philosophy (Engineering)

Department of Metallurgical and Material Engineering,

Faculty Council of Engineering & Technology

Jadavpur University

Kolkata, India

2018

INDEX NO. 285/16/E

1.   Title of the thesis:

To Study the Effect of Morphology on the Optical, Magnetic and Electrical properties of Some Nanostructured Transition Metal Oxides

2.   Name, Designation & Institution of the Supervisors:

I. Prof. Gopes Chandra Das

Department of Metallurgical and Material Engineering

Jadavpur University

Kolkata, India

II. Dr. Chandan Kumar Ghosh

School of Materials Science and Nanotechnology

Jadavpur University

Kolkata, India

3.   List of publication:

I.   International peer-reviewed journal papers:

This thesis is based on the following publications:

1. *Non-inversion anisotropy energy in NiO coral structure: Asymmetric hysteresis loop at room temperature*; S. Bhattacharjee, G. C. Das, A. Roychowdhury, D. Das, C. K. Ghosh, D. Bhattacharya, and P. Sen; Applied Surface Science, 449 (2018) 389-398.

2. *Electron–Phonon interaction to tune metal–Semiconductor junction characteristics: Ultralow potential barrier and less non-thermionic emission*; S. Bhattacharjee, A. Dey, S. Dey, A. Roychowdhury, P. P. Ray, D. Das, G. C. Das and C. K. Ghosh; Physica B: Condensed Matter, 547 (2018) 101-110.

3. *Fractional-dimension approach to tune non-adiabatic interfacial charge transfer and pseudocapacitive properties of NiO*, S. Bhattacharjee, A. Ray, S. Podder, A. Samanta, G. C. Das, S. N. Das, A. K. Mukhopadhyay and C. K. Ghosh, *(Communicated)*

4. *The effect of particle size on the dielectric behaviour of nanocrystalline nickel(III) oxide;* S. Bhattacharjee, A. Ray, P. Maji, G. C. Das, S. Das and C. K. Ghosh, *(Communicated).*

5. *Non-stoichiometric Ni₂O₃ nanoparticles as a fast and efficient photocatalyst for dye degradation in industrial waste water;* S. Bhattacharjee, S. day, G. C. Das and C. K. Ghosh, (Co*mmunicated*).

II. **Other publication:**

1. *Room temperature synthesis of hydrated nickel (III) oxide and study of its effect on Cr (VI) ions removal and bacterial culture*; S. Dey, S. Bhattacharjee, R. S. Bose and C. K. Ghosh; Applied Physics A, 119 (2015) 1343-1354.

2. *Correlation between the dielectric and electrochemical properties of TiO₂-V₂O₅ nanocomposite for energy storage application*. A. Ray, A. Roy, S. Bhattacharjee, S. Jana, C. K. Ghosh, C. Sinha, and S. Das; Electrochimica Acta, 266 (2018) 404-413.

3. *NiO/Ag heterostructure: enhanced UV emission intensity, exchange interaction and photocatalytic activity*; S. Majumder, S. Bhattacharjee, and C. K. Ghosh; RSC Advances, 6 (2016) 56503-56510.

4. *Synthesis of pure nickel (III) oxide nanoparticles at room temperature for Cr (VI) ion removal*; S. Dey, S. Bhattacharjee, M. G. Chaudhuri, R. S. Bose, S. Halder, and C. K. Ghosh; RSC Advances, 5 (2015) 54717-54726.

5. *NiFe$_2$O$_4$ nanorod: porosity effect on spin canting, quadrupole splitting and hyperfine magnetic properties*. T. S. Mondal, <u>S. Bhattacharjee</u>, A. Roychowdhury, S. Majumder, D. Das,M. K. Mitra, and C. K. Ghosh; Materials Research Express, 2 (2015) 046102.

6. *Cold white light emission from environmental friendly hedge-hog Zno/Ag heterostructure: enhanced quantum yield and different re organizational energy for recombination centres*; P. Bhattacharyya, <u>S. Bhattacharjee</u>, M. Bar, U. K. Ghorai, S. Baitalik and C. K. Ghosh; (Communicated).

7. *Au Nanoparticle-Decorated Aragonite Microdumbbells for Enhanced Antibacterial and Anticancer Activities*; A. Samanta, S. Podder, M. Kumarasamy, C. K. Ghosh, D. Lahiri, P. Roy, <u>S. Bhattacharjee</u>, J. Ghosh and A. Mukhopadhyay; (Communicated).
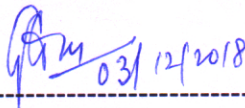
4.   List of Patents: Nil

5.   List of presentations in National/International/Conferences/Workshops:

1. *Study on photocatalytic activity of nanosized Co$_{0.3}$Zn$_{0.7}$Fe$_2$O$_4$ synthesized by hydrothermal method*. R. Mondal, K. Sarkar, S. Dey, <u>S. Bhattacharjee</u>, C. K. Ghosh and S. Kumar; AIP Conference Proceedings, 1942 (2018) 050072.

2. *Synthesis of nanorods assembly NiO and the adsorption for Congo red in water*; <u>S. Bhattacharjee</u>, G. C. Das and C. K. Ghosh; Fourth International Symposium on Semiconductor Materials and Devices (ISSMD-4, 8th -10th March, 2017, Jadavpur University, Kolkata, India).

3. *Non-inversion anisotropy energy in NiO coral structure: asymmetric hysteresis loop at room temperature*; <u>S. Bhattacharjee</u>, G. C. Das, A. Roychowdhury, D. Das and C. K. Ghosh; 4th International Conference on Nanoscience and Nanotechnology (ICONN 2017, 09th -11th August, 2017, SRM University, Kattankulathur, India).
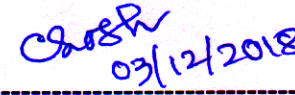
CERTIFICATE FROM THE SUPERVISORS

This is to certify that the thesis entitled "**To Study the Effect of Morphology on the Optical, Magnetic and Electrical properties of Some Nanostructured Transition Metal Oxides**" submitted by **Shri Swarupananda Bhattacharjee**, who got his name registered on 27/06/2016 for the award of **Ph.D. (Engineering)** degree of **Jadavpur University** is absolutely based upon his own work under the supervision of **Prof. Gopes Chandra Das** and **Dr. Chandan Kumar Ghosh** and that neither his thesis nor any part of the thesis has been submitted for any degree/diploma or any other academic award anywhere before.

1. ———————————————
03/12/2018

Prof. Gopes Chandra Das

Signature of the Supervisor
and date with Office seal
Retd. Professor
Metallurgical & Material Engg. Deptt.
Jadavpur University
Kolkata   700 032

2. ———————————————
03/12/2018

Dr. Chandan Kumar Ghosh

Signature of the Supervisor
and date with Office seal

DR. Chandan Kumar Ghosh
Assistant Professor
School of Materials Science
& Nanotechnology,
Jadavpur University
Kolkata - 700 032

DECLARATION OF THE SCHOLAR

I, **SWARUPANANDA BHATTACHARJEE**, hereby declare that the work encompassed in this present thesis has been carried out by me in the Nanoscience Laboratory, Metallurgical and Material Engineering Department, Jadavpur University under the supervision of **Prof. Gopes Chandra Das**, Metallurgical and Material Engineering Department and **Dr. Chandan Kumar Ghosh**, School of Materials Science and Nanotechnology, Jadavpur University, Kolkata – 700032. Neither this thesis nor any part of this thesis has been submitted for any degree/ diploma or other academic award anywhere before.

Date.. 03/12/18

SWARUPANANDA BHATTACHARJEE
Index No. 285/16/E

To my beloved parents, brother and wife…

"Somewhere, something incredible is waiting to be known."

- Carl Sagan

Preface

Nanoparticles, which are smaller in size, are essential in a characteristic framework in view of their high surface region and surface reactivity, and their related properties of adsorption or binding to the organic contaminants and trace metals. This is most likely due, in partially, to the differences in the surface and atomic structure near the surface, also with crystal form and surface topography, as a function of the smallest size. Besides the particle size and shape, the morphology of nanoparticles strongly influences their properties. For example, the catalytic materials effects on the surface of a particle. A few process can be utilized to produce different morphology either by mixing require materials previously before the nucleation or by adding new materials after nucleation in the synthesis procedure. But in same procedure, the morphology can be tuned to some degree by the procedure parameters, such as, relative measures of the materials, temperatures, and living arrangement times. Although, the material properties like surface energies, and chemical properties, decide the morphology of the final materials. Morphology variation is a remarkable method for adjusting functionality of nanomaterials, because it is involving surface transforming without the change of the main material. Morphological variation has principal significance particularly for nanomaterials, while these materials as a rule contain an extensive number of surface atoms that decide their physical and chemical properties. However, most of the nanomaterials are thermodynamically unstable, and their nonequilibrium morphologies comprise to low free energy of the system.

A remarkable aspect of nanomaterials is that various factors can impact their physical, electronic chemical, magnetic and optical properties. These factors can strongly influence their properties as well as their size, shape, surface area, dielectric condition and inter-particle interactions

I

The work presented in this doctoral thesis describes the synthesis of nickel oxide and different oxidation state of nickel oxide via some novel synthesis strategies. Particularly, the facile hydrothermal processes and wet chemical processes are found to be appropriate to prepare various morphology of nickel oxide. The thesis starts with a general introduction (chapter 1) of nanotechnology, defects, magnetism, electrochemistry, interface of metal-semiconductor, dielectric properties and photocatalytic properties are given in this chapter. In chapter 2, literature review on above properties of nickel oxide as well as presented some of the breakthrough reports.

Coral – like microstructure of NiO has been synthesized via a facile template free hydrothermal technique followed by calcination which are described in chapter 3. Magnetic study illustrates spin-glass like behaviour and asymmetric hysteresis loop at room temperature. Non-inversion symmetry of the anisotropic energy barrier, introduces by defect induced ferromagnetic domain within antiferromagnetic matrix of NiO. Numerical values of the anisotropy parameters have also been evaluated using law of approach method. Interparticle interaction, inherent of this particular microstructure via surface defects, is strong enough to give asymmetric hysteresis at room temperature.

The effect of morphology on electrochemical and catalytic properties of different nanostructure NiO prepared via hydrothermal methods are described in chapter 4. Applying Marcus theory, it has been demonstrated that the charge transfer process in catalytic as well as in electrochemical process within the synthesized nanostructures are non-adiabatic in nature, guided by electron – phonon interaction. And finally, it is concluded that lattice polarization, caused by electron – phonon interaction, imparts the crucial role specific pseudocapacitance while charge transfer resistance and charging or discharging time are determined by activation energy of process where the same electron – phonon interaction also plays significant role.

In chapter 5, the characteristic of nanostructured Ni_2O_3/Al heterojunctions are investigated under the dark and illumination conditions and the device parameters have been measured. The effect of these parameters has been identified that the charge-transport across the junction follows non-adiabatic mechanism. Our results suggest a new insight into current transport mechanism that may be generalized to understand microstructural, defect dependence MS junctions.

A low temperature chemical route has been adapted to synthesize nickel (III) oxide (Ni_2O_3) nanoparticles whose particle size can be varied by tuning the reaction temperature which are presented in chapter 6. Study the dielectric properties of the Ni_2O_3 nano particles and delineate the role of grain and grain boundary on to the dielectric properties and investigated the degradation if congo red and methylene blue by the nanostructured Ni_2O_3 are presented in chapter 7.

Finally, in chapter 8, summary of the major findings of this thesis are discussed.

December, 2018

Swarupananda Bhattacharjee
Department of Metallurgical and Material Engineering
Jadavpur University
Kolkata – 700 032
India

Acknowledgement

At the edge of submission of my doctoral thesis titled "**To Study the Effect of Morphology on the Optical, Magnetic and Electrical properties of Some Nanostructured Transition Metal Oxides**", the research work behind which commenced from December, 2012 under the supervision of Prof. Gopes Chandra Das, Department of Metallurgical and Material Engineering, Jadavpur University, and Dr. Chandan Kumar Ghosh, School of Materials Science and Nanotechnology, Jadavpur University, I find myself immensely fortunate to utilize this opportunity to thank a lot of people who have helped me in several stages of my research work.

First of all I would like to extend my cordial gratitude to my respected teachers and supervisors, **Prof. Gopes Chandra Das and Dr. Chandan Kumar Ghosh**, without whose spirited help, generous support and pertinent direction, it wouldn't have been possible for me to accomplish this work. They were greatly responsive to me in every situation. I feel gratified to have them for productive and precious suggestions, active teamwork and persistent inspiration all the way through the exploration.

I am also gratified to Prof. M. K. Mitra, ex-dean, Faculty of Engineering & Technology, Jadavpur University, Prof. K. K. Chattopadhyay, Director, School of Materials Science and Nanotechnology, Prof. S. Mukherjee, Dr. M. G. Chowdhury, faculty members of the School of Materials Science and Nanotechnology, Jadavpur University, for allowing me to utilize the valuable resources, instruments, laboratory and library facilities of the school. It is a great pleasure to acknowledge my respected teacher **Prof. P. K. Chakraborty** and **Prof. R. Dey**, Department of

I must mention the name of **Mr. Anirban Bagchi** for his precious friendship. I really cannot value his support. I would like to thank Dr. Sourav Sarkar for his valuable support all the way. He has always helped me just like my elder brother.

I must appreciate the hearty support of all my family members, especially my brother Mr. Vivekananda Bhattacharyya whose endless support and inspiration in all my success and failures makes me even stronger in life. This effort would not have been a success without the enduring support, encouragement and love of my wife who helped me all the way to stay focused in my research work.

Finally, my thanks must go to all my well-wishers, friends and teachers, whom I shall always keep in mind to remember throughout my life.

To conclude, I must convey the affection of my adored parents that has sustained me amidst many difficulties throughout the voyage of my life. Their silent efforts behind my every success in life is invaluable. This work would not have been possible without their unconditional support, patience and love.

December 2018

(Swarupananda Bhattacharjee)
Department of Metallurgical and Material Engineering
Jadavpur University, Kolkata-700032
India

Contents

List of Figures

XIII

XV

List of Tables

Chapter 1 — Introduction

1.1.   Nanotechnology and morphological effect

Historically, human dreams and imaginations have resulted in new breakthroughs in science and paved the way for new disciplines. Nanotechnology, a 21st-century wilderness, was resulting from such dreams. Nanotechnology is related to the control of issues at measurements in the vicinity of 1 and 100 nm where modification in properties drive the novel applications. Advancement of nanotechnology has happened continuously with time, however, progressive advancement has been enrolled in the midst of the modern world. The idea of a "*nanometer*" was first proposed by Richard Adolf Zsigmondy, the 1925 Nobel Prize honoree in chemistry. He introduced the term nanometer clearly to characterizing particle size and he was the first to quantify the particles size using microscope. One of the example of his measurement was gold colloids utilizing a microscope. In present day nanotechnology was the brain child of Richard Feynman, the 1965 Nobel Prize honoree in physics. He demonstrated a lecture titled, "*There's Plenty of Room at the Bottom*", during the 1959 American Physical Society meeting at Caltech, in which he presented the idea of controlling issue at the atomic level. Prof. Feynman said, "*The principles of physics, as far as I can see, do not speak against the possibility of maneuvering things atom by atom". It is not an attempt to violate any laws; it is something, in principle, that can be done; but in practice, it has not been done because we are too big*" [1, 2]. His thoughts have paved a new scientific direction and Feynman's hypotheses have since been demonstrated right. It is thus that he is viewed as the father of modern nanotechnology. However, in 1974, Almost 15 years later, a Japanese scientist, Norio Taniguchi, was the first to utilize "*nanotechnology*" to describe semiconductor with nanometer order [3]. The word 'nano' has taken from the Greek word 'nanos' which signifies '*dwarf*'. The General Conference on Weights and Measures (CGPM) officially permitted the utilization of nano as a standard prefix in the year 1960. This unit prefix which

signifies 'one billionth' indicated by the letter 'n' and is utilized frequently modern days in science and technology, nano as a prefix to the units of time, length and mass specifies to a scale of magnitude 10^{-9} unit. Particles with a size between nanometer (nm) range is defined as "nanomaterial", Nanomaterials can be extensively classified as nanostructured minerals, crystal, microscopic organisms etc. and man-made viz. metal, earthenware and polymer nanoparticles. Nanotechnology, from that point onward, has been a blast of understanding, planning and manufacturing new nanomaterials for application of interest, in any field. With the advance technology that helped make dives forward in the field of microscopy, which influenced the prospering to field achievable, researchers saw the beginning of another period. TEM, SPM, STM and AFM are those apparatuses with which the investigation at a size of nanometers is done and each field on earth is impacted [4-6]. During the most recent couple of years, massive undertakings have been made by specialists to understand these materials whose attributes between the plainly visible and make them profitable for a few applications [7-9].

1.1.1. Morphology effect

Specifically, nanoparticles, which are smaller in size, are essential in a characteristic framework in view of their high surface region and surface reactivity, and their related properties of adsorption or binding to the organic contaminants and trace metals. This is most likely due, in partially, to the differences in the surface and atomic structure near the surface, also with crystal form and surface topography, as a function of the smallest size [10]. Besides the particle size and shape, the morphology of nanoparticles strongly influences their properties. For example, the catalytic materials effects on the surface of a particle. A few process can be utilized to produce different morphology either by mixing require materials previously before the nucleation or by adding new materials after nucleation in the synthesis procedure. But in same procedure, the

morphology can be tuned to some degree by the procedure parameters, such as, relative measures of the materials, temperatures, and living arrangement times. Although, the material properties like surface energies, and chemical properties, decide the morphology of the final materials. Morphology variation is a remarkable method for adjusting functionality of nanomaterials, because it is involving surface transforming without the change of the main material. Morphological variation has principal significance particularly for nanomaterials, while these materials as a rule contain an extensive number of surface atoms that decide their physical and chemical properties. However, most of the nanomaterials are thermodynamically unstable, and their nonequilibrium morphologies comprise to low free energy of the system.

Bottom up fabrication resembles building a brick house. Rather than setting one by one to create a house, bottom up fabrication systems put molecules or atoms each one in turn to assemble the desired nanostructure. Such procedures are taking. Morphology of various nanostructures may vary significantly on the basis of their material composition, crystal structure and synthesis process. Existing synthesis techniques permit the fabrication of nanoparticles of different shapes (flower, rods, spheres, tubes etc.) and sizes [11-14]. Assembling different morphology by self-assembly process was attempted by hydrothermal technique. Only the variation of parameters of such hydrothermal technique as temperature, reagent concentration, pressure, and time produced different morphologies. In this thesis we have used the bottom up approach. The bottom up approach assumes have become essential in the creation and handling of nanostructures. There are a few purposes behind this. The bottom up approach has potential superior opportunity to get nanostructures with not so much imperfections but rather more homogeneous chemical arrangement. Self-assembly of organic architectures involve the following type of interactions within the involved components: electrostatic interaction, hydrogen bonding, van de Waals or

donor-acceptor effects. The self-assembly particles incorporate specific electrical, magnetic, chemical, catalytic properties and so on and their assembling architecture on a nanometer scale actuates a scope of novel properties.

Self-assembly by hydrogen bonding prompts two or three-dimensional architectures which frequently have a normal length size of a couple of nanometers. The self-assembling of structures requires the presence of hydrogen-bonding subunits which decide the topology of the morphology. Surfactant plays an important part in the development of morphology constructed by nanoparticles. The last includes the outlined control of atomic associations (e.g. hydrogen bonding, and so on.) and recognition processes to create main chain or side-chain of surfactant by self-assembly of require components.

Bonding effects are required to play a crucial part in the get together and self-assembling process. The controlled and required morphology opens the route to the using surfactant building of nanostructured morphology.

A remarkable aspect of nanomaterials is that various factors can impact their physical, electronic chemical, magnetic and optical properties. These factors can strongly influence their properties as well as their size, shape, surface area, dielectric condition and inter-particle interactions [15-17]. Such noticeable varieties in properties of nanomaterials are because of their architecture being comparable to the de Broglie wavelength of the charge carriers, which adjust their properties significantly [18]. As a consequence, the development of morphology led to realization that nanoscale morphology would be of future interest.

1.2. Defects of the crystals

Perfect crystals are not thermodynamically stable. In fact, for a given temperature, the presence of point defects, makes this crystal thermodynamically stable. Apart from stability the defects in solids play an important part, to understand the electrical, optical and many diffusion induced properties to name a few. On approach to find the defect concentration is to make use of statistical thermodynamic. Another approach is to use the defect chemistry where defects are treated as chemical entities and this formation of defects, is represented by a defect equation. Then one can use equilibrium thermodynamics to calculate the defect concentration at a given temperature. However, to use this approach, one has to use a proper notation to represent the defects. In this thesis, we shall briefly discuss the defects in solids using the very commonly used Kroger-Vink notation. For further details, one can refer to the classical text, Introduction to ceramics, edited by Knigery *et. al.* [19]

1.2.1. Representation of defects

Let MX represents a binary compound. Following are the different types of defects that occur in MX.

1. *Vacancy*: It is defined as the missing of an atom/ion from its site. V_M and V_X represent the M and X vacancy respectively. In this notation V stands for vacancy and subscript stands for the site, where vacancy occurs.

2. *Interstitial*: These are represented by M_i and X_i where M and X stand for atom/ion, and subscript 'i' stands for interstitial.

3. *Misplaced atom/ion*: Represented by M_X and X_M. In this notation the symbol represents atom/ion and subscript represents the site. Thus, M_X means atom/ion M

occurs at the site X, hence M atom is misplaced. In normal condition, M atom should be at its site M, i.e. M_M.

4. *Solid solution*:

   (i) Substitutional: Solute atom S, appearing at either site M or X would be represented by S_M or S_X respectively.

   (ii) Intestinal: Solute atom appearing at interstitial site 'i' of the host lattice and this is represented by S_i.

For ionic solid, the effective positive and negative charges associated with ions, are designated by dot (•) and dash ('). Clearly, this is different from + (positive) and − (negative) changes which are actually associated with a cation and anion.

5. *Subatomic defect*: Electron in conduction band and holes in the valance band are considered as subatomic defects and they are represented by e' and h• respectively.

1.2.2. Rules of defect reaction equations

In order to explain these rules, let us consider a binary metallic oxide MO, where M stands for metal and O stands for oxygen.

Over and above the mass balance, required for ordinary chemical equation, two more rules are to be absorbed for defect equation as stated below:

1. *Charge balance*: Since changes cannot be created or annihilated during defect equations, charge on either side of the equal to '=' has to be same.

2. *Site ratio rule*: For a binary solid M_aO_b. The ratio of number of M atoms to the number of O atoms is given by a/b ratio.

The ratio has to be mentioned even after the formation of defect. For example, let N_M and V_M represent the number of M atoms and number of vacancy at M site. Similarly N_0 and V_0 represent the number of oxygen atoms and number of oxygen vacancies Thus,

$$\frac{N_M + V_M}{N_0 + V_0} = \frac{a}{b} \quad , \text{ must be preserved.}$$

To discuss the generations of defect through the defect equation, let us consider a binary metallic oxide MO.

1. *Formation of Oxygen vacancy (V_0)*: The formation of oxygen vacancy can be represented by the following equation :

$$O_0 = V_0 + \tfrac{1}{2} O_2 \qquad\qquad 1.1$$
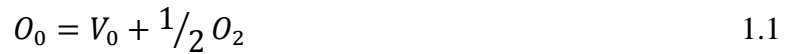
The equilibrium constant K_{red} is given by

$$K_{red} = [V_0] \cdot PO_2^{1\backslash 2} \qquad\qquad 1.2$$

$$[V_0] = \frac{K_{red}}{PO_2^{1\backslash 2}} \qquad\qquad 1.2a$$

Thus for a given temperature the lower the partial pressure PO_2, the more is the concentration of oxygen vacancy $[V_0]$.

In MO, metal M^{2+} and oxygen O^{2-} are ions and, with these changes the solid MO is electroneutral. Thus when, oxygen vacancy is created it can be visualize as follows: The O^{2-} leaves two electrons (2e') at the oxygen vacant site, V_0 and escapes in the atmosphere as neutral oxygen molecule. Now if one e' associate at the V_0 site is excited to the conduction band, then $V_0^{\bullet}$ site becomes effectively positively charged. This is called ionization of defect. This ionization of V_0 can be represented by follows:

$$V_0 = V_0^\bullet + e' \qquad\qquad 1.3$$

Assuming $[V_0] = [e']$, the equilibrium constant K_{rad1} is given by,

$$K_{rad1} = \frac{[V_0^\bullet]^2}{[V_0]}$$

$$[V_0] = \frac{[V_0^\bullet]^2}{K_{rad1}} \qquad\qquad 1.4$$

Pulling $[V_0]$ in equation (1.2a) and rearranging,

$$[V_0^\bullet] = \frac{\sqrt{K_{rad} \cdot K_{rad1}}}{pO_2^{1\backslash 4}} \qquad\qquad 1.5$$

Equations (1.2a) and (1.5) give the partial pressure dependent variation of $[V_0]$ and $[V_0^\bullet]$ respectively.

2. *Formation of metal vacancy*: The generation of metal vacancy in the MO can be represented by the following defect equation:

$$\tfrac{1}{2}O_2 = O_0 + V_M \qquad\qquad 1.6$$

When oxygen diffuses into MO and occupies an oxygen site, O_0, and an extra site in metal has to be created in the form of vacancy, V_M, to maintained site ratio rule. At a given temperature equilibrium constant K_{oxi}, can be given by,

$$K_{oxi} = \frac{[V_M]}{pO_2^{1\backslash 2}} \qquad\qquad 1.7$$

This implies the more the prevailing oxygen pressure the more will be the metal vacancy and this we expect intuitively. As discussed in connection with oxygen vacancy neutral metal vacancy V_M is associated with two holes ($2h^\bullet$). Therefore, when holes sink to the valance band the metal vacancy V_M becomes ionized as per the following equation:

$$V_M = V_M' + h^\bullet \qquad\qquad 1.8$$

Equilibrium constant K_{oxi1}, can be given by,

$$K_{oxi1} = \frac{[V_M']^2}{[V_M]} \qquad\qquad 1.9$$

Assuming, $[V_M'] = [h^\bullet]$. From equations (1.7) and (1.8)

$$[V_M'] = \sqrt{K_{oxi} \bullet K_{oxi1}} \bullet pO_2^{1\backslash 4} \qquad\qquad 1.10$$

Equation (1.7) and (1.8) give the oxygen partial pressure dependent concentration of $[V_M]$ and $[V_M']$. This means by controlling the external partial pressure one can control the concentration of metal vacancies.

3. *Variable valency metal oxide:* Let us assume that the metal M can have valency 2 and 3. Then the generation of M^{3+} in MO host oxide, can be represented by the following defect equation,

$$M_M = M_M^\bullet + V_M' \qquad\qquad 1.11$$

The equilibrium constant K_{vari}

$$K_{vari} = [M_M^\bullet][V_M'] \qquad\qquad 1.12$$

In principle formation and analysis of any defect within the frame work Kroger and Vink can be carried out as delineated above [20].

So far the discussion is on the variation of the defect as a function of partial pressure under isothermal condition. The temperature dependent variation of defect concentration could be taken into consideration by using Vant Hoff equation, which represents the variation of equilibrium constant as a function of temperature and this is given by,

$$\frac{\partial lnK}{\partial T} = \frac{\Delta H^0}{RT^2} \qquad\qquad 1.13$$

where K, R, ΔH^0 and T are respectively equilibrium constant, universal gas constant, standard enthalpy change and absolute temperature.

1.3. Origin of magnetism

Over the past decades, extensive research work has been carried out on nanomaterials due to their importance in fundamental research from both the application and theory perspective. Magnetism is one of the new field of interest due to its vast applications. All materials in nature are organized by atoms while atoms are made of positively charged nuclei surrounded by negatively charge electrons. The magnetism in material arises due to the orbital motion and spin motion of the electrons in atoms. Orbital motion of electrons and electron spin are respectively associated with orbital angular momentum and spin angular momentum. Fig. 1.1 shows the orbital motion of electron around the nucleus and the spin motion of the electron around own axis. These give rise to permanent orbital and spin magnetic dipole moments. Each unpaired electron give rise to a magnetic dipole moment of Bohr magneton (μ_B). Out of these two contributions, major contribution comes from this spin particularly for the first transition series of elements. An applied magnetic field (H) induces magnetization (M) (magnetic dipole moment per unit volume) of a material and magnetization is given by M= χH, where the proportionality constant χ is called susceptibility.
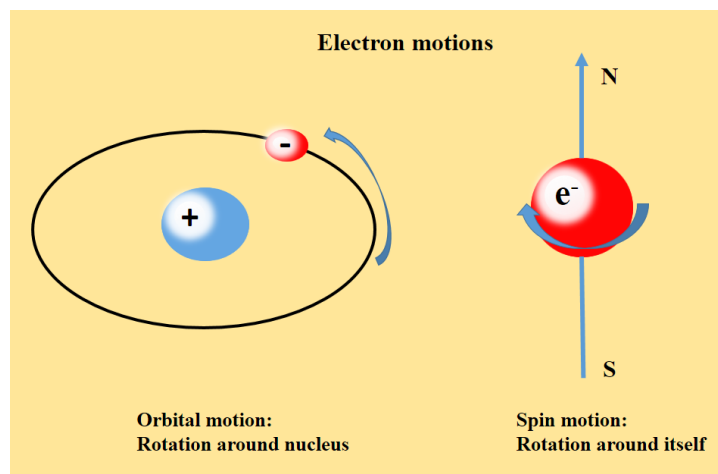
Fig. 1.1 The orbital motion of electron around the nucleus and spin motion of electron around own axis.

1.3.1. Classification of magnetic materials

The basic classification of magnetic materials depends on whether permanent magnetic dipole is present or not. The material which does not possess the permanent magnetic dipole moment is classified as diamagnetic materials. The other magnetic materials which process the permanent magnetic dipole moment, are further classified into paramagnetic, ferromagnetic, anti-ferromagnetic and ferrimagnetic depending on the interaction among the permanent magnetic dipoles.
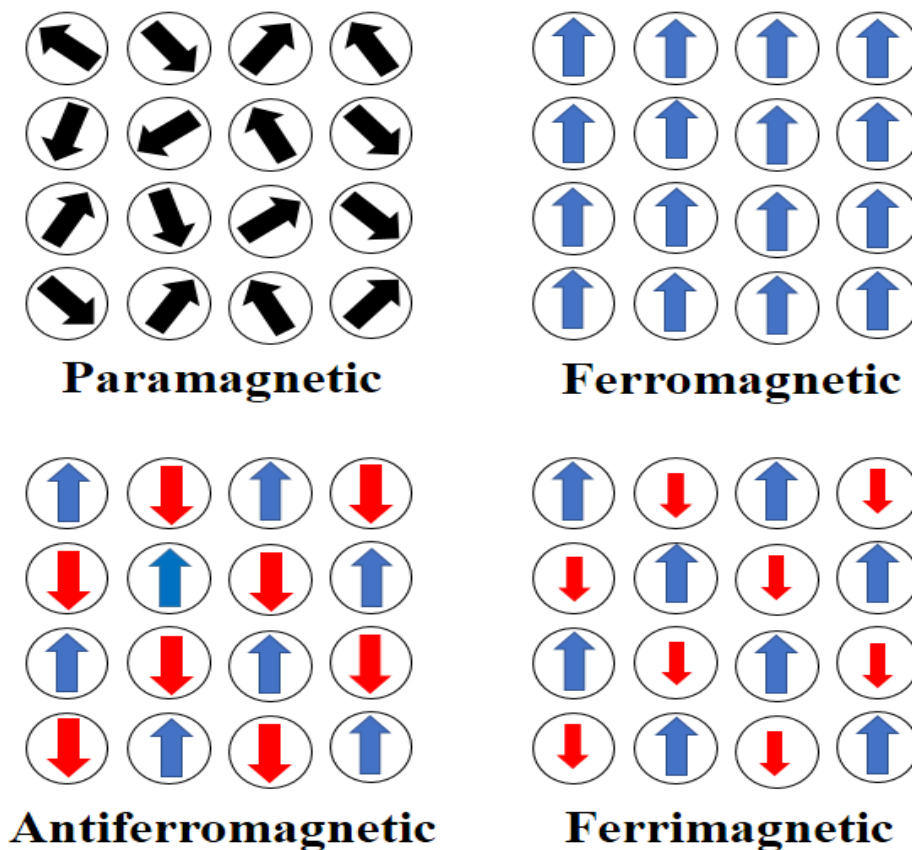
Fig. 1.2 Different class of magnetic ordering in materials.

Diamagnetism is the basic properties of all materials and it contributes weak magnetism. Non-cooperative behaviour of orbital electrons in presence of external magnetic field is the basic concept of diamagnetism. In the presence of an applied magnetic field, diamagnetism materials oppose the applied magnetic field due to the atomic current loops produced by the orbital motion of electrons. In terms of electronic configuration of diamagnetic substances, all the electronic sub shells are filled and no unpaired electron exists in the shells. Thus, the overall magnetic moment cancel each other and net magnetic moment of the diamagnetic material is zero (e.g., hydrogen, nitrogen, boron, sulfur etc.). In this case, when an external magnetic field is applied, orbital motion of electrons opposes the magnetic field and thus the magnetic susceptibility of these diamagnetic material is negative and temperature independent ($\chi < 0$).

In the *paramagnetic* materials, the interaction among the permanent dipole moments is negligible and hence at a temperature, the magnetic dipole moments are randomly oriented giving rise to net zero magnetization (Fig. 1.2). If the external magnetic field is applied, there will be a partial alignment of the atomic magnetic moments along the direction of applied field which causes a low magnetization in the same direction. Thus, these paramagnetic materials (e.g., chromium, sodium, oxygen etc.) processes positive susceptibility and it is usually much smaller ($\chi \approx 0$). The magnetic susceptibility is inversely temperature dependent. That means when the temperature increases the alignment of the atomic magnetic moment will be randomize and decreases the magnetization. The temperature dependent variation of magnetic susceptibility follows the Curie law of paramagnetism.

In *ferromagnetic* materials (e.g., iron, cobalt, nickel etc.) there is a strong interaction among the permanent dipoles, as a results the magnetic dipoles are arranged parallely in absence of external magnetic field (Fig. 1.2). This spontaneous magnetization is a characteristic feature of

ferromagnetic materials. The strong interaction among the magnetic dipoles is attributed to quantum mechanical spin exchange interaction which occurs below a certain temperature called Curie temperature. In this spontaneous magnetization region, the hysteresis in M-H loop is being observed and above Curie temperature due to thermal randomization, ferromagnetic materials behaves like a paramagnetic material and the temperature dependent susceptibility fellows the Curie-Weiss law.

Ferrimagnetism behaviour found in materials (mostly ceramic oxide compounds) is due to the antiparallel orientation of magnetic dipole moments of unequal magnitude (Fig. 1.2). These type of materials are easily magnetized and demagnetized compared to ferromagnetic materials thus also known as soft magnets. The macroscopic behaviour is usually similar to ferromagnetism. Above T_c, the long-range spin ordering becomes randomized and the material behaves like paramagnetism.

Materials (e.g., nickel oxide, iron manganese, hematite etc.), having antiparallel alignment of magnetic dipole moments with equal magnitude, are known as *antiferromagnetic* materials (Fig. 1.2). The spins in these materials are aligned via exchange interaction to the opposite direction and therefore produce no net magnetization. Beyond a critical temperature thermal energy randomizes the alignment of magnetic moment producing paramagnetism. This particular temperature is defined as Néel temperature (T_N).

1.3.2. Hysteresis

In presence of applied external magnetic field, spins within the magnetic material are fully aligned along the field direction and achieved the maximum value of magnetization, known as saturation magnetization. Once the external field is removed, magnetic materials can retain a memory. Upon applying of magnetic field, in the opposite direction the subsequent alignment and

again reorientation take place. The variation of magnetization (M) as a function of magnetic field (H) as depicted in Fig. 1.3 is known as hysteresis loop. The saturation magnetization (M_s) observed when a sufficient strength of external magnetic field is applied. On reversing when the field is reduced to zero, even then the magnetization does not become zero. The remaining non zero magnetization is called remanence magnetization (M_r). Increasing the external field toward negative direction, at a point where the induced magnetization becomes zero, that point is known as coercivity (H_c).
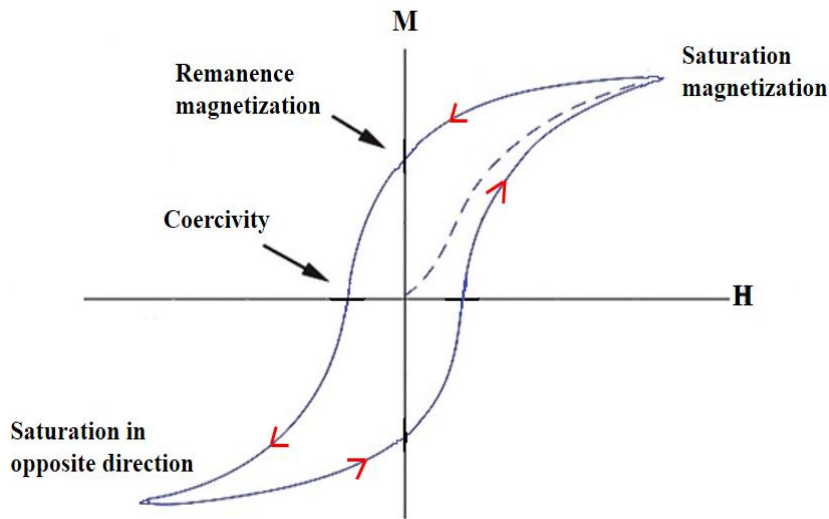
Fig. 1.3 Schematic hysteresis loop for ferromagnetic and ferrimagnetic material.

The characteristic of hysteresis loop governs the suitability of magnetic materials for particular applications. For example, more square-shaped hysteresis loop, with two stable magnetization states, is suitable for magnetic data storage, while a sifted hysteresis loop indicates saturated nature of spin-glass like magnetization or exchange bias effect. Thus, the various hysteresis parameters or various nature of hysteresis loop are not the intrinsic properties of magnetic materials but it is dependent on the nature of the materials.

1.3.3. Exchange interaction

Exchange interaction between magnetic ions is the most essential phenomenon in molecular magnetism. Depending on metallic or non-metallic and different type of delocalization of the magnetic moments of solid many exchange couplings were established. We shall discuss here mainly the superexchange and double exchange phenomena.

A superexchange interaction was first proposed by Kramer [21] and developed by Anderson and Van Vleck [22, 23]. For such cases let us consider two identical transition metal ions each having one unpaired electron in non-degenerate orbital. Heisenberg Hamiltonian expression can describe the magnetic exchange interaction among these two electrons, such as $\hat{H}$ = $-J\hat{S}_1\hat{S}_2$, where J denotes the exchange interaction parameter, and the two spins of the electrons are coupled. Developed Anderson's theory showed that on the metal orbitals these two electrons are not fully localized. Due to covalencey effect, some spin density found on orbitals of the surrounding ligands. In transition metal oxides 3d- orbitals are coupled with the oxygen 2p-orbitals. Distance between the ions and arrangement of anion and cation orbitals affect exchange interaction. When two same valency cations and an intermediate anion points towards each other having large overlap form 180° metal-oxygen-metal bonds then the exchange interaction is strong and antiferromagnetic in nature. The superexchange mechanism is schematically represented in the following Fig. 1.4.
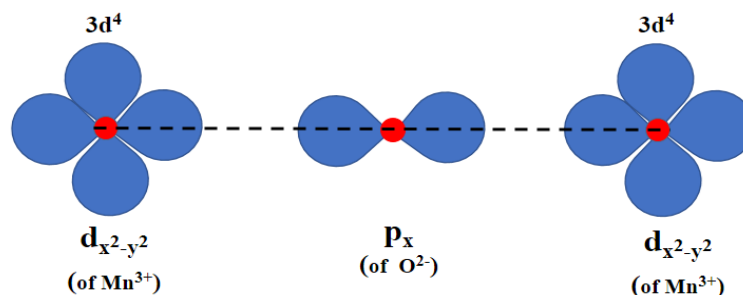
Fig. 1.4 Schematic of Superexchange interaction in metal-oxygen-metal.

This double exchange interaction arises between $3d$-orbitals which have both localized and delocalized d-orbital. A double-exchange material, such as calcium doped $LaMnO_3$, has both valency state of Mn^{4+} and Mn^{3+} ions (d^3 and d^4) to maintain the charge neutrality. Both cations Mn^{4+} and Mn^{3+} are separated by anion O^{2-} ions. For d^3 core electrons are localized in a narrow $t^{\uparrow}_{2g}$ band where fourth d electron at $e^{\uparrow}_{g}$ band hybridized with oxygen and hops to the vacant e_g level in the neighboring Mn^{4+} ion. However, the electron hopping occurs between Mn^{3+} and Mn^{4+} ion due to Hund's coupling between two band (t_{2g} and e_g) electrons if their spins position are parallel but if they are antiparallel hopping does not occur. Fig. 1.5 shows the schematic representation of double exchange interaction.
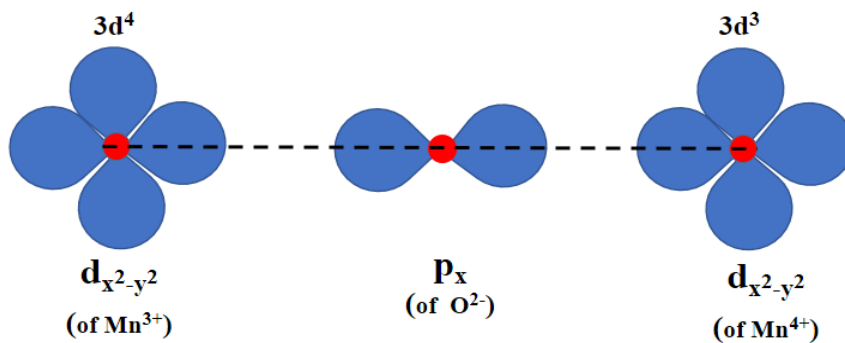
Fig. 1.5 Schematic of double exchange interaction in metal-oxygen-metal.

1.4. Electrochemical energy storage system

The concern of the consumption of fossil energy brings about tremendous enthusiasm for advanced technologies in renewable energy, for example, wind farms, solar cells, tidal electricity generation etc. [24]. In recent days, reliable and constant energy storage system are needed because of uneven usage of electricity and discontinuous production of electricity. In this context, different energy storage devices like fuel cell, batteries, and electrochemical capacitors have been developed by researchers having their own advantage and disadvantages. For the high speed and high mileage

of the advance vehicles such as electric and hybrid vehicles, high capacity energy storage systems are needed. Batteries and electrochemical capacitors of electrochemical energy storage systems are the mostly used in recent time. Lithium ion batteries (Li-ion) and nickel-metal hydride batteries (Ni-MH) are used in many fields such as telecommunication devices, computers, vehicles etc. for their high energy density and moderate power density. Electrochemical capacitors have also show strong potentiality of delivering high power within a short period of time and are generally divided into two categories: double-layer capacitance and pseudocapacitance. The charge storage process of Electric double layer capacitor is mainly based on adsorption of the ions at electrode / electrolyte interfaces by non-Faradic electrostatic process. Carbonaceous material such as carbon nanotube, graphene, activated carbon etc. are generally used as electric double layer supercapacitor electrode materials [25]. Advantages of electric double layer capacitors includes high power density, long life cycle and stability, but they don't possess high value of specific capacitance (C_m) [26]. In this contest, pseudocapacitor stores charges at electrode / electrolyte interface on the basis of reversible redox reaction utilizing multi-oxidation states of the electrode materials in a Faradaic process. It has been investigated by several researchers that pseudocapacitors exhibit higher energy density and C_m compared to double layer capacitors. Generally, transitional metal oxides / hydroxides or electrically conducting polymer are used for pseudocapacitors. In this regard, it has been investigated that transitional metal oxides / hydroxides are better alternative for electrode materials. Earlier, ruthenium oxide (RuO_2) has been used as electrode materials for pseudocapacitors due to its high specific capacitance (760 F/g) in aqueous electrolyte [27]. But, its utility gets limited due to toxicity and high cost [27]. After RuO_2, different cost effective transitional metal oxides like MnO_2, NiO, V_2O_5, Co_3O_4 etc. have been examined as replacements of RuO_2.

In general, the electrochemical process occurs at the electrode-electrolyte interface. Charge transfer processes at the electrode- electrolyte interface is usually studied by the controlled-potential technique which is based on dynamic (non-zero current) situations. In this technique, electrode potential is used to drive an electron transfer reaction and the resulting current is measured. Mainly, this electron pressure drives the chemical species to either gain or lose an electron during reduction or oxidation reaction. The main advantage of this controlled potential technique is that the high sensitivity to electroactive species where detection is extremely low limits (nm range), can be achieved with small amount of samples (5-20 µL).

1.4.1. Faradaic processes

1.4.1.1. Equilibrium electrochemistry

Electrochemically reversible redox reaction is shown below:

$$O(aq) + ne^-(m) \rightleftharpoons R^{n-}(aq) \qquad 1.14$$
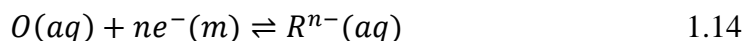
where O is the oxidized and R is reduced forms of a redox process. The above equation express the charge transfer mechanism between the metallic electrode (m) and electrolyte (aq). When a suitable electrode, as a source of electrons, is placed into the electrolyte then the reaction occurred. This is an interfacial process where reaction involves electron as charge transfer species within electrode surface. Therefore, a net charge separation is developed because the electron transfer moves towards the equilibrium. So it creates potential difference between electrode (ϕ_m) and solution (ϕ_s) interface. Thus the potential drop across the interface is represented by,

$$\Delta\phi = \phi_m - \phi_s \qquad 1.15$$

For the complete conducting circuit, a reference electrode is used to maintain the fixed potential difference between the electrode-electrolyte interfaces. Therefore, this potential difference is given by,

$$E = (\phi_m - \phi_s) + X \qquad 1.16$$

where *E* is the potential difference and *X* is constant which refers to role of reference electrode.

1.4.1.2. Dynamic electrochemistry

In dynamic electrochemistry, thermodynamic parameters (reaction free energies, equilibrium constants, entropies and pH) are not extensively used and that is the advantage of these processes. Thus commercially these processes are used for electroanalytical applications.

In this process, controlled-potential electroanalytical measurement is carried out to get a current response during redox process by observing the electron transfer of the target analyte. Electrochemically redox reaction is shown below:

$$O(aq) + ne^-(m) \rightarrow R^{n-}(aq) \qquad 1.17$$
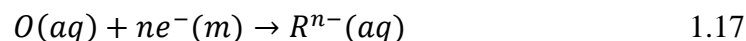
The above redox reaction occurs under the application of an applied potential and the consequent current developed is given by,

$$i = nAFj \qquad 1.18$$

where *i* is the magnitude of the current, *j* is the flux ($cm^{-2}s^{-1}$) of the species in solution, F is the Faraday constant, n is the number of electrons involved in electrochemical process and A is the electrode area. The electron transfer process occurs via quantum mechanical tunneling between the electrode and reactant close to the electrode.

1.4.2. Cyclic voltammetry (CV)

For the cyclic voltammetric measurement, three electrodes setup which consists of working electrode, counter electrode and reference electrode is being used. All the electrodes are connected to a potentiostat which prevents the ohmic drop and controlled minimal interface within working and reference electrode. The current through reference electrode is kept minimum to avoid the polarization of the reference electrode, resulting the stable potential between working and reference electrode. Fig. 1.6 shows the three electrode experimental setup where reference electrode can be Ag/AgCl, counter electrode should be non-reactive high surface area like platinum and working electrode should have deposited material which we want to measure. In electrochemical process, observed electrode current is dependent on mass transport which occurs in series with chemical reactions, adsorption/desorption and heterogeneous rate constant. The working electrode dips into an electrolyte which contains electroactive species and supporting electrolyte salt, to achieve the required connectivity and minimize the ohmic (IR) drop. Fig. 1.7 shows a schematic representation of electrochemical reactions.
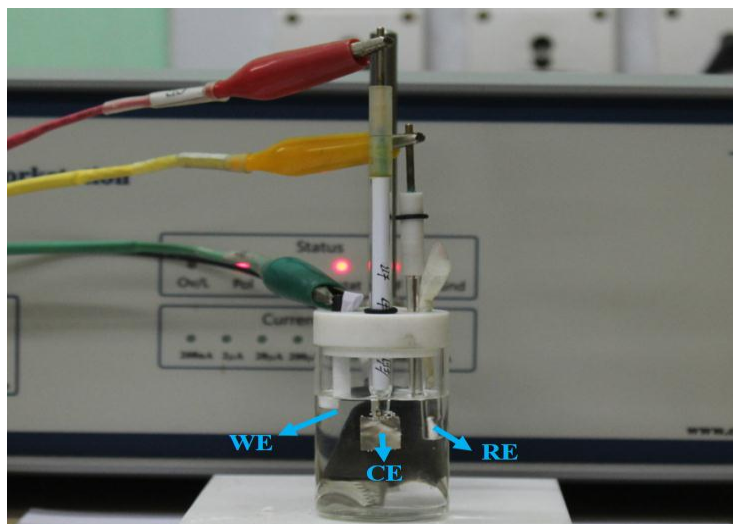
Fig. 1.6 A typical experimental three electrode set-up showing reference electrode (RE), counter electrode (CE) and the working electrode (WE) deeps into an electrolyte solution.
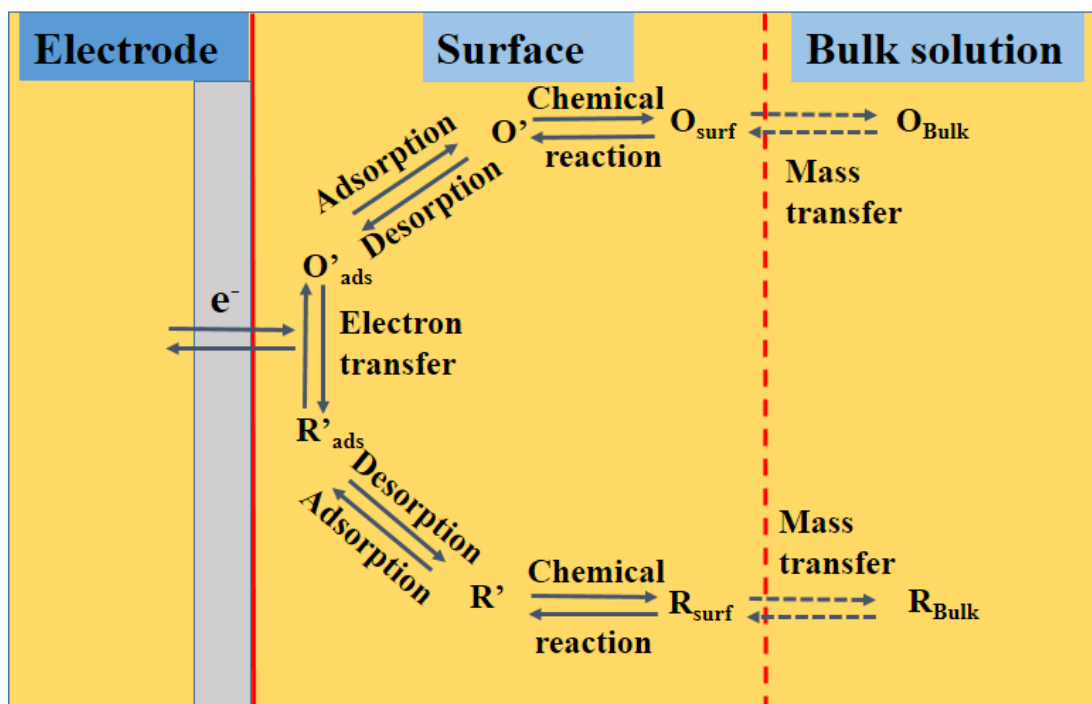
Fig. 1.7 A schematic representation of electrochemical reaction.

Hence, the applied voltage is the key factor for occurrence of electrochemical reactions. Since, V= Joule /Coulomb, such that energy is required to move charge. Such voltage, defined as the energy per coulomb acts as electrochemical pressure. The current at the working electrode is plotted versus the applied voltage to give the CV trace and the specific capacitance has been calculated from the CV curves according to the equation:

$$C_m = \frac{\int i \, dv}{2 \times m \times s \times \Delta V}$$

1.19

where, $\int idv$ is the area under the CV curve, 'm', 's' and $\Delta V = (V_1 - V_2)$ represent working electrode material mass (in g), scan rate and applied potential window (V) respectively.

1.4.3. Galvanostatic charge discharge (GCD)

GCD is the standard technique used to investigate the charge storage ability of the electrodes. Mostly, charge and discharge are conducted at constant current until a set voltage is reached and the charge of each cycle is measured. The capacitance is calculated by,

$$C = \frac{Q}{V} \qquad\qquad 1.20$$

where C is the capacitance, in farads (F), V is the voltage window and Q is the charge in coulombs. The each number of cycles indicates the cycle-life of the capacitor. The current at the working electrode is plotted versus the time to give the GCD trace and the specific capacitance has been calculated from the GCD curves according to the equation:

$$C_m = \frac{i \times t}{V \times m} \qquad\qquad 1.21$$

where 'i', 't', 'V' and 'm' represent discharge current (in A), discharge time (in sec), voltage range for full cycle (V) and mass of the electrode material (in g).

1.4.4. Electrochemical Impedance Spectroscopy (EIS)

ESI is a most used technique to investigate electrode properties. This method for measuring the equivalent series resistance models to describe underlying reaction mechanisms. AC excitation signal is applied to the investigated during this measurement, and AC response is measured. The impedance Z of the electrode is calculated, expressed in terms of magnitude of Z in ohm and phase-shift in degrees.

1.5. Interface of metal-semiconductor

The most essential part in the structure of the semiconductor devices is the metal-semiconductor (MS) contact which helps to connect outdoor world. The barrier potential

developed between the metal Fermi level and the majority carrier bands plays an important role in this MS junction device. Depending on the fabrication of solid-state devices, MS junction can be categorized in two different types. The non-rectifying contact termed as Ohmic contact and the Schottky contact is the one which is rectifiable. In Ohmic contact, heavily doped semiconductor and junction processes low resistance that helps to flow the current equally to the both biasing directions. For each semiconductor device this kind of junction is fundamental because the final conductor is metal. For Schottky contact allows the current flow to the one biasing direction and blocks the current flow to the opposite direction which means the resistance of the blocking current direction is very high. This kind of contact also known as Schottky-boundary diode (SBD) or surface-barrier diode. The fundamental concept behind it is due to the energy band discontinuity at the interface. The reason of band discontinuity is injected carriers which imply excess energy and is also known as a hot-carrier diode or hot-electron diode. In modern semiconductor devices technology SBDs is an essential component for its rectifying properties. Comparatively fabrication method is easy and very important part of this kind of junction is that they do not exhibit minority carrier effects (e.g., diffusion capacitance, long reverse recovery time, etc.) as like p-n junction devices [28]. The SBDs are used in many devices, for example, photodetectors, solar cells, High-electron-mobility transistors (HEMTs), metal–semiconductor field-effect transistors (MESFETs), RF attenuators, rectifiers, microwave mixers, Zener diodes and few integrated circuits [29]. Therefore, the improvement of the Schottky junctions will increase the performance of previously mentioned devices. Metal like aluminum, gold and platinum are often used in metal-semiconductor junctions.

1.5.1. Basic concept of Schottky Barrier Junctions

Ohmic junction or Schottky (rectifying) junction formed because of the work function of semiconductor and metal when a metal and a semiconductor come in the state of physical contact. In a material the energy difference between the Fermi level and vacuum level is known as work function (ϕ). For the ohmic junction, the work function of metal (ϕ_m) is less than n-type semiconductor (ϕ_s) i.e. $\phi_s > \phi_m$ and if the work function of an n-type semiconductor (ϕ_s) is less than that of metal (ϕ_m) i.e. if $\phi_s < \phi_m$, then the junction forms Schottky (rectifying) junction. But for the junctions between a p-type semiconductor and a metal the above conditions are reversed i.e. $\phi_s < \phi_m$ for ohmic junction and $\phi_s > \phi_m$ for Schottky (rectifying) junction.

Schottky and Mott first developed the band bending concept and established the rectifying effect of metal−semiconductor contacts [30, 31]. Fig. 1.8 shows the ideal energy band diagrams of the *n*-type semiconductor and metal for their work function ϕ_s and ϕ_m respectively. E_{vac} represent the vacuum energy, E_c denotes the energy of conduction band minimum, E_v known as the energy of valence band maximum and χ_s is the electron affinity of the semiconductor. $E_{F,s}$ and $E_{F,m}$ represent the Fermi levels of semiconductor and metal respectively. The work function of a metal (ϕ_m) has a surface contribution. The work function of semiconductor (ϕ_s) varies with the doping. Though, the electron affinity χ_s of a semiconductor does not depend on doping concentration.
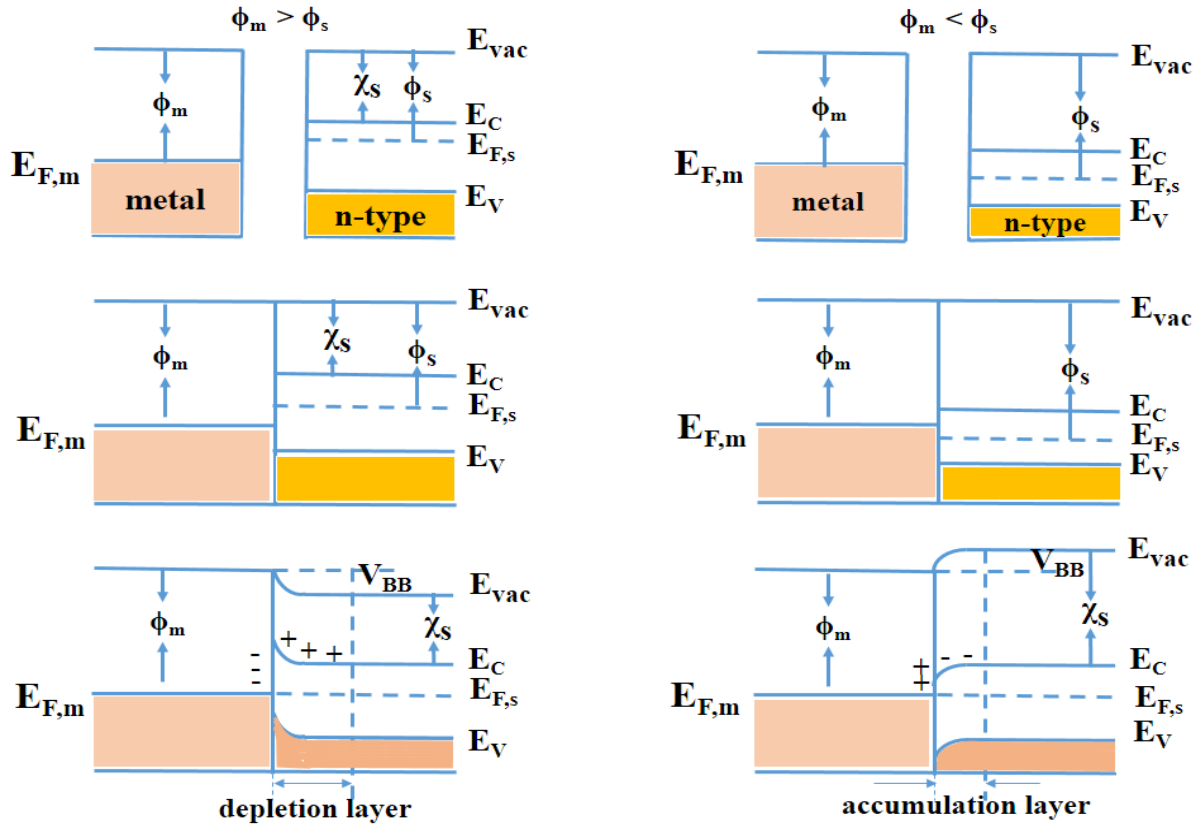
Fig. 1.8 Energy band diagrams of metal and n-type semiconductor. Three different contact position represented, non-contact, contact and contact under equilibrium condition.

In the absence of an external electric field, when both metal and semiconductor come in contact, the bands bend in the vicinity of the junction of the semiconductor equalize the potentials and the electrical charge flow from one material to the other. Due to the work function difference of metal and semiconductor the free electrons will transfer when the metal and semiconductor are in contact. When the work function of metal (ϕ_m) is higher than the semiconductor (ϕ_s), ($\phi_m > \phi_s$) the electrons will flow continuously from the semiconductor to the metal until the Fermi levels of metal ($E_{F,m}$) and semiconductor ($E_{F,s}$) become identical. The metal surface is negatively charged and semiconductor is positively charged due to electrostatic induction and established a Helmholtz double layer at the metal/semiconductor interface under equilibrium condition. For the low

concentration of free charge carriers in the semiconductor, electric field between metal and semiconductor interfaces cannot be effectively screened. At the semiconductor surface, the free charge carrier concentration gathers compared to the bulk, and this region is known as space charge region. Depletion layer is formed when the electrons are depleted in the space charge region for the n-type semiconductor (electrons as majority charge carriers) when $\phi_m > \phi_s$. On the other hand when $\phi_m < \phi_s$, the electrons are accumulated at the space charge regained forms the accumulation layer.

The charge separation at the junction due to the internal electrical field causes the band bending. When $\phi_m > \phi_s$, upward the energy bands bend toward the interface and when $\phi_m < \phi_s$, downward the energy bands.

At the semiconductor interface the degree of bending of the energy band is equal to the work function difference between metal and semiconductor. This energy difference is given by,

$$qV_i = (\emptyset_m - \emptyset_s) \qquad 1.22$$

where q is the electronic charge and V_i is expressed in volts and is known as contact potential difference or the built-in potential of the junction. For the *n-type* semiconductor, when $\phi_m > \phi_s$, a barrier formed at the metal−semiconductor interface, which is known as the Schottky barrier (ϕ_{SB}),

$$\emptyset_{SB} = (\emptyset_m - \chi_s) \qquad 1.23$$

Since,

$$\emptyset_S = (\chi_s + \emptyset_n) \qquad 1.24$$

$$\emptyset_{SB} = (qV_i + \emptyset_n) \qquad 1.25$$

where $\emptyset_n$ is the separation between the conduction band edge (E_c) and the Fermi level (E_F). For *n-type* semiconductor, When $\phi_m < \phi_s$, no Schottky barrier is formed but the ohmic metal−semiconductor contact is formed.

The accurate shape of the potential barrier can be calculated from the charge distribution inside the space charge layer. In general, the barrier height $\emptyset_{SB}$ is orders of magnitude larger than the thermal voltage *kT/q*, and a high-resistivity is developed in the space charge region of the semiconductor. The shape of the barrier is determined from the donor distribution in the semiconductor. As per the assumption of Schottky, The semiconductor gives rise to a uniform charge density in the depletion region as it was uniformly doped up to the metal interface.

1.6. Brief introduction to dielectric properties

The nanosize materials have received widespread attention among the scientific community due to its unusual electrical properties different from single crystals, polycrystals (bulk), thin films and glasses even though they are identical in chemical composition [32-34]. Besides, nanosize materials have shown great potential to device applications including sensors, electrodes, switching devices, microelectronic devices and solar cells [14, 35]. Furthermore, the electrical properties of nanosize materials are different from their bulk because of the high surface to volume ratio of the grains, high defect density, quantum confinement of charge carriers and disordered grain boundary [36]. Disordered grain boundary in nanosize materials without short or long order arrangement have been shown by many researchers. In nanosize materials, the nature of the defect, grain and grain boundaries play a very significant role for the electrical properties. In this context, nanosize oxide materials have drawn attention of researchers.

Dielectric (basically nonconducting) characteristics of the materials are improved continuously as the applications of dielectric materials are ever increasing. Among the many applications, dielectric material is used as capacitive component in electronic circuits as electrical insulator and it is also used to describe electrical energy storage, dissipation and energy transfer. For these applications most important factors of dielectric materials are dielectric constant, dielectric loss etc. These type of materials are electrical insulators that can be polarized by an applied electric field [19].

1.6.1. Electrical phenomena

1.6.1.1. Capacitance

That electrical charge Q can be stored is the principle characteristic of a capacitor. Consider a simple system containing two parallel metal plates separated by a distance d and of area A. DC voltage the same magnitude of positive and negative charge on the plates. The voltage is directly proportional to the charge storage. The charge on the capacitor is defined as:

$$Q = CV \qquad\qquad 1.26$$

where V is the applied voltage and C is the capacitance. If the surface charge density (σ_s) on the can be represented by

$$Q = C(Ed) = \sigma_s A \qquad\qquad 1.27$$

where E is the electric field strength, which is equal to V/d. Thus,

$$C_0 = \frac{Q}{V} = \frac{\sigma_s A}{Ed} = \varepsilon_0 \frac{A}{d} \qquad\qquad 1.28$$

where ε_0 is the permittivity or dielectric constant of vacuum. If a material of permittivity ε' is placed between the capacitor plates

$$C = C_0 \frac{\varepsilon'}{\varepsilon} = C_0 k' \qquad\qquad 1.29$$

where k' is the relative permittivity or relative dielectric constant. This is the material property determines the capacitance of a circuit element.

1.6.1.2. Dielectric loss

When an electric field is applied between the parallel plate capacitor then the total current (J_T) is given by

$$J_T = J + \frac{dD}{dt} = J + \varepsilon^* \frac{dE}{dt} \qquad\qquad 1.30$$

where J is the current density and ε^* is the complex dielectric permittivity, which is introduced to take into account dielectric losses due to application of an alternating electric field. The ε^* is defined by

$$\varepsilon^* = \varepsilon' - j\varepsilon'' \text{ , where } j = \sqrt{-1} \qquad\qquad 1.31$$

where ε' and ε'' are respectively the real and imaginary part of the dielectric constant.

When an alternating field given by $E = E_0 e^{i\omega t}$ is applied to a dielectric material, it induces phase lag δ is the flux density, given by the following equation

$$D = D_0 e^{i(\omega t - \delta)} \qquad\qquad 1.32$$

Further D is given by,

So, $$D = k^* E \qquad\qquad 1.33$$

Where k^* is given by,

$$k^* = k_s e^{-i\delta} = k_s(cos\delta - isin\delta) \qquad\qquad 1.34a$$

In the above expression k_s is defined as $k_s = D_0/E_0$ and the complex relative dielectric permittivity is defined as follow,

$$k^* = k' - ik'' = \frac{\varepsilon^*}{\varepsilon_0} = \frac{1}{\varepsilon_0}(\varepsilon' - i\varepsilon'') \qquad 1.34b$$

from equation (1.34a) and (1.34b)

$$k' = k_s cos\delta \qquad 1.35$$

$$k'' = k_s sin\delta \qquad 1.36$$

So the loss tangent is

$$tan\delta = k''/k' = \varepsilon''/\varepsilon' \qquad 1.37$$

1.6.1.3. Electric Polarization

Electric polarization (P) refers to a phenomenon of the relative displacement of the positive charge and negative charge of atoms or molecules change the dipole orientation to the direction of the field, or separation of mobile charge carriers at the interfaces of impurities, or other defect boundaries, resulting from an applied external electric field. Compared to a free space, charge carriers of dielectric material react to an electric field differently and get displaced. The charge displacement can neutralize a part of the applied field. Hence, $V = Q/C$ and $C = k'C_0$, then

$$V = \frac{Q/k'}{C_0} \qquad 1.38$$

where Q/k' is the free charge. The remainder, the bound charge, is neutralized by polarization of the dielectric. Assume the total electric flux density D as the sum of the electric field E and the dipole charge P. then,

$$D = \varepsilon_0 E + P = \varepsilon' E \qquad 1.39$$

where the polarization is the surface charge density of the bound charge, equal to the dipole moment per unit volume of material.

$$P = N\mu \qquad\qquad 1.40$$

where N is the number of dipoles per unit volume and μ is the average dipole moment. The electric dipole moment corresponds to two electric charges of opposite polarity $\pm Q$ separated by the distance d and is given by,

$$\mu = Qd \qquad\qquad 1.41$$

Thus polarization can equivalently be designated either the bound-charge density or the dipole moment per unit volume

$$P = \varepsilon'E - \varepsilon_0 E = \varepsilon_0(k' - 1)E \qquad\qquad 1.42$$

1.6.1.4. Various types of polarization

The various types of polarization in a dielectric material are electronic polarization, atomic or ionic polarization, orientation polarization, and interface or space charge polarization. The displacement of electron cloud of atoms and molecules resulting the polarization and it requires very small time but while polarization causes by the orientation of permanent dipoles of migration of electrons or ions, it will take longer time to execute.

When the electron cloud of atoms or molecules is displaced from the originally symmetrical distribution by the electric field then arises *electronic polarization*. This kind of displacement occurs at outer electron cloud compared to the inner positive nucleus. This polarization occurs at the very high frequency region (above 10^{14}-10^{16} Hz) because of the low mass of electrons.

If the atom or ions of a polyatomic molecule are displaced with respect to each other by the electric field then *atomic or ionic polarization* arises. This is basically the distortion of the normal lattice vibration, and thus it also known as vibrational polarization. This type of polarization occurs below the optical frequencies in the infrared range, around 10^{13} Hz.

Orientation polarization occurs when dipoles reoriented towards the direction of the field. These polarization arises only in materials containing permanent dipole moments. The materials which composed of molecules with an asymmetrical structure and contain positive and negative charge, possess permanent dipole moments in the absence of electric field. The permanent dipole moments reorient by the external field. But if the electrical field is removed the net polarization will become zero. This occurs at the microwave region.

Space charge polarization: The above three polarization are bound within the atom or molecule itself and linked with positive and negative charge. But the space charge polarization is migration of charge carriers from space charge at interfaces or grain boundaries and accumulation of free charges at interface.

1.6.2. AC conductivity

If the AC voltage is applied to a dielectric material then due to ohmic resistance or impedance there will have some loss current. If the potential difference between the two plates is *V* volts, *Q* is the charge in coulombs, *A* is the area and *d* is the distance between the plates then ac conductivity (σ_{ac}) is,

$$\sigma_{ac} = \frac{J}{E} \qquad\qquad 1.43$$

where *J* is the current density and *E* is the electric field strength vector.

The electric field vector $E = \frac{D}{\varepsilon}$. Displacement vector of the dipole charges is D. and ε is the complex permittivity of the material. From the known equation electric field intensity (E) is the ratio of the potential difference and distance between the plates.

$$E = \frac{V}{d} \qquad\qquad 1.44$$

Since the current density $J = \frac{dq}{dt}$ but q is given by $\frac{Q}{A} = \frac{V\varepsilon}{d}$

So,
$$J = \frac{dq}{dt} = \frac{d}{dt}\left(\frac{V\varepsilon}{d}\right) = \frac{\varepsilon}{d}\frac{dV}{dt} \qquad\qquad 1.45$$

So,
$$J = \frac{\varepsilon}{d}Vj\omega \qquad\qquad 1.46$$

Substitution for E and J

$$\sigma_{ac} = \frac{J}{E} = \varepsilon^* j\omega = (\varepsilon' - j\varepsilon'')j\omega = \varepsilon' j\omega + \varepsilon''\omega \quad 1.47$$

Hence, ac conductivity is the real quantity so complex term has to be neglected

$$\sigma_{ac} = \varepsilon''\omega \qquad\qquad 1.48$$

In the dielectric material some power loss occurs when the dipole rotates. When an ac field is applied then the charging current I_C will be 90° phase with the voltage.

Now, in dielectric materials, some loss current (I_L) will produce a charge in phase with voltage due to the absorption of electrical energy. The I_L and charging current (I_C) will make angle θ and δ respectively with the total current I passing through capacitor.

$$\varepsilon'(\omega) = D_0 cos\delta / E_0 \qquad\qquad 1.49$$

$$\varepsilon''(\omega) = D_0 sin\delta / E_0 \qquad\qquad 1.50$$

So,
$$tan\delta = \frac{\varepsilon''(\omega)}{\varepsilon'(\omega)} \qquad\qquad 1.51$$

Substituting the value of $\varepsilon''(\omega)$ from the above equation (1.50) then it can be written as

$$\sigma_{ac} = \omega tan\delta\varepsilon'(\omega) \qquad\qquad 1.52$$

where $\omega = 2\pi f$ and $\varepsilon' = \varepsilon_0\varepsilon_r$, here ε_r is the relative permittivity of the material and ε_0 is the permittivity of the free space.

So, $$\sigma_{ac} = 2\pi f tan\delta\varepsilon_0\varepsilon_r \qquad\qquad 1.53$$

where $tan\delta$ is the dielectric loss.

1.7. Photocatalysis and its basic principle

Photocatalysis is an advance oxidation process (AOP). This process, usually in presence of solar, chemicals and other source of energy, relies on the in-situ generation of highly reactive radical species basically hydroxyl radicals ($HO^\bullet$) and superoxides ($O_2^{-\bullet}$). This process has the ability to oxidize and mineralize the organic material from hazardous to non-hazardous like carbon dioxide, ammonia, nitrates, phosphates and water. The advantages of this process compared to other conventional methods are the generation of end-products which are harmless. This process can be performed in various media such as aqueous, gaseous and to some degree in solid medium and also it has ability to destroy industrial toxic and waste organic compounds present in the wastewater. These process requires less chemical to perform reaction and to control the reaction time by changing the parameters. Due to the above advantage, these process are adopted worldwide.

Photocatalytic reactions occur when illuminated by light (photon) energy on semiconductor such that the energy of the photons is equal to or greater than the semiconductor bangap energy ($h\upsilon \geq \Delta E_g$). In photocatalytic degradation, usually the following reaction occur

due to the presence of photo assisted electron hole pairs. The reaction procedure are given bellow stepwise:

$hv + photocatalyst \rightarrow e^- + h^+$ (Excited by photon generating electron hole pair)

$e^- + O_{2ads} \rightarrow O_2^{-\bullet}$ (Formation of super oxide radical)

$O_2^{-\bullet} + H^+ \rightarrow HOO^\bullet$ (Hydroperoxyl radical and hydrogen peroxide formation)

$HOO^\bullet + e^- \rightarrow HOO^-$

$HOO^- + H^+ \rightarrow H_2O_2$

$e^- + H_2O_2 \rightarrow HO^\bullet + OH^-$ (Hydroxyl radicals formation)

$h^+ + H_2O_{ads} \rightarrow H^+ + HO^\bullet_{ads}$

$h^+ + OH^-_{ads} \rightarrow OH^\bullet_{ads}$

$h^+ + Organics \rightarrow CO_2 + H_2O$ (Mineralization or degradation of organic compound)

$HO^\bullet + Organics \rightarrow CO_2 + H_2O$

$HO^\bullet + Organics_{ads} \rightarrow CO_2 + H_2O$

1.8. Nickel oxide crystal structure and applications

The first-series of Transition-Metal Oxides (TMOs) are among the most interesting materials which exhibit wide variations in physical properties related to electronic structure. Among them optical and magnetic behaviour, in particular, form the basis for the enormous range of applications including microelectronic circuits, gas and bio-sensors, batteries, solar and fuel cells, super capacitors, paints and pigments, magnetic data storage etc. As a result of which these have been the subject of extensive experimental and theoretical investigations in the recent past.

The unusual properties of transition-metal oxides can partly be attributed to the unique electronic structure of metal-oxygen bond that gives rise to a strong correlation between structural, electronic and magnetic properties. Several of these phenomena occurring in TMOs can be explained on the basis of the valence d electrons of the transition metal (TM). In a free (ground state) TM atom or ion, the d-orbitals are degenerate. When surrounded by the crystal field of oxygen ions (or other ligands), the degenerate d orbital split energetically in the oxide to give d electrons that differ in their energies. If the d electrons are localized, as is the case with stoichiometric Nickel Oxide (NiO), the TMO is insulating. However, their nonstoichiometric (metal deficient) compounds are p-type semiconductors. As a result, TMOs exhibit a variety of interesting properties. They for example, can be metallic (RuO_2, TiO, ReO_3), semiconducting (TiO_2, ZnO), insulating (CoO, MnO, NiO, $BaTiO_3$) or superconducting (CuO perovskites). The magnetic ordering in several closely related oxides also varies: CrO_2 used in magnetic recording, for example, is ferromagnetic; whereas Cr_2O_3 is antiferromagnetic. NiO used in giant magnetoresistance and spin valve devices is antiferromagnetic with a Neel temperature of around 523K, while the structurally very similar MnO is paramagnetic at room temperature with a Neel temperature of -151°C.

NiO was discovered in 1858 by R. Bunsen that is why NiO also known as bunsenite and only found pure in nature in a few places around the world. The pure bulk mineral is green while nanoparticle of NiO is black in colour. Bulk NiO has a face centered cubic NaCl structure with space group *Fm3m*, and a lattice parameter of $a = 4.177$Å. Cubic structure of NiO is illustrated in Fig. 1.9. Due to, non-stoichiometric NiO or formation of defect, created Ni^{2+} vacancies and gives p-type conduction.
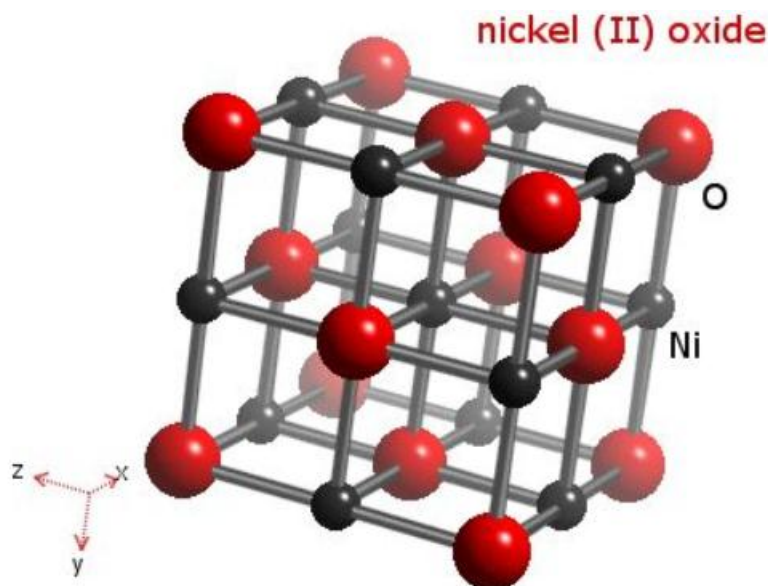
Fig. 1.9 The structure of NiO. Ni is shown as black and oxygen as red.

In this particular material, there are two components of spin configurations due to the non-local exchange interaction. The first of which is the direct exchange interaction between the nearest neighbour of Ni ions that favors paring of spins to lower energy. For second one, a very strong interaction comes from the superexchange between the next-nearest neighbour of Ni ions. Thus these two interactions make the antiferromagnetic spin structure for the ground state of NiO. NiO, a semiconducting metal oxide with a wide band gap of ~ 3.6 eV, is an important material for use in many important applications such as catalysis, electrochromic smart windows, gas sensors, supercapacitors, lithium-ion batteries and also it has high chemical and thermal stability, and it is environmental friendly.

Nickel, being a transition metal, exists variable valencies. However, apart from most stable NiO, higher oxides like Ni_2O_3, NiO_2, Ni_3O_4 etc. are not common due to their unstable nature. However, Cairns and Ott [37] successfully prepared $Ni_2O_3.2H_2O$ and studied its structure and composition using X-ray diffraction technique. It was established from the chemical bonding

analysis that the higher oxide of nickel was a pseudo hydrate and hence on heating, it decomposes to form NiO instead of anhydrous Ni_2O_3. Richardson [38] studied electronic and magnetic properties of $Ni_2O_3.H_2O$ and found it to be an n-type semiconducting material with ferromagnetic coupling between the nickel atoms.

Now we have successfully prepared pure Ni_2O_3 nanoparticles at four different temperatures and showed the Cr(VI) ion adsorption capacity of the prepared particles and its dependence on the particle size and surface charge.

In order to enhance the applicability of the material, it could be assumed that surface area modifications can be a viable way forward. It could achieve, if we increase the surface area of the nanomaterials through morphology variations, the desired results. From this possibility, we aim at optimizing a synthesis procedure that would enable us to have a controlled growth mechanism of the desired morphologies and thus giving us the ability to control the surface area of the synthesized materials. It is perhaps appropriate to mention here that previous researches have shown that enhanced surface area can lead to improved absorption characteristics dyes, improved magnetic properties, improved Lithium Storage battery Performances etc.

1.9.   References

1.   J. Gribbin and M. Gribbin, *Richard Feynman: A life in science*, Icon Books, 2018.

2.   R. P. Feynman, in *Handbook of Nanoscience, Engineering, and Technology, Third Edition*, CRC Press, 2012, pp. 26-35.

3.   N. Taniguchi, C. Arakawa and T. Kobayashi, *Proceedings of the International Conference on Production Engineering,* 1974, 8.

4. G. Binnig and H. Rohrer, *Scientific American*, 1985, **253**, 50-58.

5. J. H. Hoh, J. P. Cleveland, C. B. Prater, J. P. Revel and P. K. Hansma, *Journal of the American Chemical Society*, 1992, **114**, 4917-4918.

6. G. G. Leppard, *Current Nanoscience*, *Current Nanoscience,* 2008, **4**, 278-301.

7. S. K. Kulkarni, *Nanotechnology: principles and practices*, Springer, 2015.

8. C. P. Poole Jr and F. J. Owens, *Introduction to nanotechnology*, John Wiley & Sons, 2003.

9. C. Rao and A. Cheetham, *Journal of Materials Chemistry*, 2001, **11**, 2887-2894.

10. S. N. Souto Filho, M. C. Alves, C. M. Monreal and C. d. S. Bonini, *Revista Brasileira de Engenharia Agrícola e Ambiental*, 2017, **21**, 530-536.

11. M. A. El-Sayed, *Accounts of chemical research*, 2001, **34**, 257-264.

12. S. Link and M. A. El-Sayed, *Journal, ACS Publications*, 1999.

13. C. Burda, X. Chen, R. Narayanan and M. A. El-Sayed, *Chemical reviews*, 2005, **105**, 1025-1102.

14. J. H. Pan, Q. Huang, Z. Y. Koh, D. Neo, X. Z. Wang and Q. Wang, *ACS applied materials & interfaces*, 2013, **5**, 6292-6299.

15. P. Buffat and J. P. Borel, *Physical review A*, 1976, **13**, 2287.

16. M.-C. Daniel and D. Astruc, *Chemical reviews*, 2004, **104**, 293-346.

17. S. Link and M. A. El-Sayed, *The Journal of Physical Chemistry B*, 1999, **103**, 4212-4217.

18. U. Kreibig and M. Vollmer, in *Optical properties of metal clusters*, Springer, 1995, pp. 13-201.

19. W. D. Kingery, H. K. Bowen and D. R. Uhlmann, *Introduction to ceramics*, Wiley New York, 1976.

20. F. Kröger and H. Vink, in *Solid state physics*, Elsevier, 1956, vol. 3, pp. 307-435.

21. H. Kramers, *Physica*, 1934, **1**, 182-192.

22. P. W. Anderson, *Physical Review*, 1959, **115**, 2.

23. J. Van Vleck, *Journal de Physique et le Radium*, 1951, **12**, 262-274.

24. P. Pisu and G. Rizzoni, *Vehicle Power and Propulsion, IEEE Conference,* 2005, 8.

25. U. Singh, A. Banerjee, D. Mhamane, A. Suryawanshi, K. K. Upadhyay and S. Ogale, *RSC Advances*, 2014, **4**, 39875-39883.

26. X. Ren, C. Guo, L. Xu, T. Li, L. Hou and Y. Wei, *ACS applied materials & interfaces*, 2015, **7**, 19930-19940.

27. P. Ragupathy, D. H. Park, G. Campet, H. Vasan, S.-J. Hwang, J.-H. Choy and N. Munichandraiah, *The Journal of Physical Chemistry C*, 2009, **113**, 6303-6309.

28. S. Sze, *Selected Solutions for Semiconductors Devices: Physics and Technology*, John Wiley and sons, 1985.

29. A. Di Bartolomeo, *Physics Reports*, 2016, **606**, 1-58.

30. N. F. Mott, *Proceeding of the Royal Society of London A*, 1939, **171**, 27-38.

31. W. Schottky, *Z. Physik*, 1939, **113**, 367.

32. N. Sivakumar, A. Narayanasamy, N. Ponpandian and G. Govindaraj, *Journal of applied physics*, 2007, **101**, 084116.

33. S. A. Makhlouf, M. A. Kassem and M. Abdel-Rahim, *Journal of materials science*, 2009, **44**, 3438.

34. H. Gleiter, *Advanced Materials*, 1992, **4**, 474-481.

35. H. Steinebach, S. Kannan, L. Rieth and F. Solzbacher, *Sensors and Actuators B: Chemical*, 2010, **151**, 162-168.

36. R. Birringer, *Materials Science and Engineering: A*, 1989, **117**, 33-43.

37. R. Cairns and E. Ott, *Journal of the American Chemical Society*, 1933, **55**, 527-533.

38. J. T. Richardson, *The Journal of Physical Chemistry*, 1963, **67**, 1377-1378.

Chapter 2   Review of past works

2.1. Brief history of nickel oxide

Over the last decade, extensive research work has been carried out on transition metal oxide nanoparticles due to their importance in fundamental research as well as in application in different fields [1]. Among various oxides nanoparticles investigated so far, nanocrystalline NiO has particularly drawn much attention of scientists and researchers due to its potential applications in battery cathodes, catalysis, smart windows, gas sensor, p-type transparent conducting oxide films, electrochromic films, active optical fibers, photovoltaics, supercapacitors etc. [2-4]. NiO nanostructure has also proven its candidature as an upcoming material for next generation resistive switching memory devices [5]. Till date, the synthesis of NiO nanomaterials with controllable hierarchical structures like hollow spheres [6], nanorods, nanowires [7], polyhedrons [8], plates [9], have gained interest because these hierarchical nanostructures often exhibit a number of unique properties completely different from bulk. Some past research has already been carried out on optical, catalytic, electrical properties, magnetic property of NiO with different hierarchical structures.

2.2. Review of past work on nickel oxide magnetic properties

Although bulk NiO possesses antiferromagnetic characteristic, it is being widely used in magnetic multilayer devices, magnetic spin valves, magnetic tunnel junctions due to its high Neel temperature ($T_N = 523$ K) [10]. In contrast to antiferromagnetic bulk NiO, its nanostructure shows a variety of new magnetic phenomenon such as weak ferromagnetic response, enhanced coercivity and hysteresis loop etc.

Kodama *et al.* [10] reported large coercivity and loop shifts at low temperatures which could be explained by multi-sublattice configuration whereas earlier developed two-sublattice

model was not able to explain it. It is generally attributed to the reduced coordination of surface spins. Briefly weak coupling between sublattices, generated reversal paths resulting high coercivities and loop shifts in the presence of applied field.

Winkler *et al.* [11] identified that spin glass response due to freezing of the surface spins where their response strongly depends on the crystal structure, morphology of the nanoparticles. Here, it is generally accepted that these nanoparticles are consisting of antiferromagnetically ordered core and magnetically disordered surface shell. At low temperature, magnetically ordered core gets blocked by anisotropy energy barriers, while surface spins shows spin-glass like behaviour and causes a strong enhancement of magnetic anisotropy with higher coercivity.

Makhlouf *et al.* [12] shows shifted hysteresis loop at low temperature due to exchange coupling between the uncompensated spins and antiferromagnetic core and also shows that due to the uncompensated spins above the blocking temperature of the particles, the reversible magnetization does not follow the Langevin function. They also show from the temperature dependent magnetization curve that magnetic behaviour depends on the particle size and lower particle size exhibits irreversibility and large coercive forces.

Duan *et al.* [13] reported the effect of the size of nanoparticle on magnetic properties and they showed that the bifurcation temperature and blocking temperature shift to lower temperature for lower size particles, while saturation magnetization, remanent magnetization and coercivity increase with decrease of particle size. At temperature lower than the surface spin freezing temperature, re-magnetization curve surpasses the initial magnetization curve due to coupling between surface and core spins.

Gao *et al.* [14] reported magnetic behaviour of NiO nanotubes. Hysteresis and non-zero coercive fields at room temperature illustrate the ferromagnetism behaviour of NiO nanotubes

though NiO is antiferromagnetic in bulk phase. Ferromagnetic behaviour had been assigned due to surface spins. Therefore the surface effect is the cause of ferromagnetic behaviour at room temperature.

Cui *et al.* [15] investigated magnetic properties of flower-like microspheres NiO and found that the blocking temperature and bifurcation temperature shift towards higher temperature due to interparticle interaction. They assigned the shift in hysteresis loop to uncompensated surface spins at Ni sites.

Tadic *et al.* [16] observed that NiO nanoparticles are antiferromagnetic and low Néel temperature (T_N=56 K), is attributed to weak inter-particle interactions, which significantly depends on particle size and defects. Seehra *et al.* [17] also have shown interparticle interaction is present in case of NiO nanorods.

Proenca *et al*. [18] examined the effect of size on the magnetic behaviour of nanocrystalline spherical NiO. They found that as particle size decreases, the effective magnetic anisotropy increases. At the low temperature, hysteresis loop displayed shifts from the origin and enhancement of coercive field have been identified due to uncompensated spins. Here, an existence of ferromagnetism at the surface and antiferromagnetism at core of the nanoparticles exhibits an exchange bias effect.

Tiwari *et al.* [19] prepared NiO nanoparticles through sol-gel process and studied the magnetic behaviour of different sizes. They proposed that Ni-O broken bond at the surface reduces superexchenge interaction energy. The average coordination number of cation and bond angles, bond length at the surface are likely to be different compared to bulk that gives rise to surface spin disorder that results spin-glass behaviour.

Cooper *et al.* [20] synthesize the core/shell NiO nanoparticles and investigate the magnetic properties. They have shown that core of particles is antiferromagnetic and the shell displays unexpectedly large permanent moment due to surface defect/vacancies. They also have shown two magnetic transitions at higher temperature paramagnetic to superpara-magnetism and at low temperature to a state of large magnetic anisotropy. However they did not shown any exchange bias effect in hysteresis loops.

Ge *et al.* [21] prepared NiO nanoflowers and observed anomalous magnetic properties at low temperature. They have shown cusp in temperature dependent curves and also investigated that the hysteresis loop were shifted due to the exchange bias between the surface layer and the inner core. They conclude that the each NiO nanoflower exhibits porous crystals with holes and Ni atoms surrounding the holes contribute to the net magnetic moment which means uncompensated spins surrounding the holes trigger the anomalous magnetic behaviours.

Ichiyanagi *et al.* [22] investigated the magnetic properties of NiO nanoparticles. They have found less transition temperature due to uncompensated surface spins and quantum confinement. It has also observed that above blocking temperature, magnetization exhibits superparamagnetic behaviour attributed to larger thermal energy in comparison to the anisotropy energy of Ni^{2+} moments. They also found hysteresis loop with coercivity.

Madhu *et al.* [23] synthesized nanostructured NiO and investigated the defect induced ferromagnetic interaction with core-shell magnetic structure. An antiferromagnetic core and ferromagnetic/spin-glass like ordering shell was revealed from temperature dependent magnetization measurement. They found that uncompensated moments of total spins vary directly with concentration of O^{2-} vacancy. The bifurcation temperature gets decreased with increasing particles size, suggesting significant uncompensated surface spins effect. The hysteresis studies

revealed the interaction between antiferromagnetic core and the ferromagnetic shell, where O^{2-} vacancies act as donor impurities and facilitate the alignment of magnetic moments related with Ni^{2+} vacancies. Hence, ferromagnetic contribution decreases with increase of the particles size. The reduction of O^{2-} vacancies decrease the magnetic polarons and effective magnetization.

So from above discussion, it is clear that the different magnetic behaviour of the NiO nanoparticles with different hierarchical structure is still under debate and needs further investigation.

In this thesis, magnetic property of NiO coral structure has been investigated after synthesizing them using hydrothermal method. Here, shift in the hysteresis loop and transition state of magnetic ordering have been identified and examined briefly.

2.3. Review of past work on nickel oxide electrochemical behaviour

Due to rapid consumption of the natural energy resource, demand of advanced, cost – effective and environment friendly energy storage devices are growing rapidly to meet society's requirement in the field of various energy sectors like hybrid electric vehicles, space gadjets, memory back-up, mobile etc. [24-26]. In this context, pseudocapacitors exhibit higher energy density and C_m compared to electric double layer capacitors. Ruthenium oxide (RuO_2) was found to be a potential electrode material for pseudocapacitor due to its high C_m (~ 760 F/g) in aqueous electrolyte. But, its usage is limited due to toxicity and high cost [27]. NiO particularly has gained interest of researchers for potential electrode material due to its high theoretical value of C_m ~ 2573 F/g within 0.5V [28]. The charge storing capacity of NiO fundamentally includes reduction and oxidation of NiO at an applied potential which in consequence significantly depends on the morphology of NiO nanostructures [29].

Wang *et al.* [30] investigated the wave like NiO via immersion method and performed charge-discharge process and cyclic voltammetry at different scan rates. They found that capacitance of NiO enhances with lower current and the specific capacitance are 525, 455 and 380 F/g were calculated from discharge current of 5, 10 and 20 mA respectively. At lower and slow scan rate of cyclic voltammetry the nickel oxide exhibited high value of capacitance. They showed capacitance of 628 and 586 at scan rate of 1mV/s and 2 mV/s respectively.

Meher *et al.* [29] prepared flakelike morphology via conventional reflux method whereas hierarchical porous ball like surface morphology was prepared via microwave method. The specific capacitance of flakelike and ball like morphology were found to be 388, 313, 247 F/g and 598, 576, 541 F/g respectively at the same scan rate at 5, 10 and 20 mV/s. They found the loss of specific capacitance value 36.3% for flakelike and 9.5% for ball like respectively and this shows the higher current response for ball like NiO morphology due to maximum contact with OH⁻ ions for redox reaction. They also reported that during OH⁻ ion propagation effectively utilized both outer and inner pore surface of the electrode materials at lower scan rates but at higher scan rates, ions utilized only outer regions of the pores. They demonstrated that the NiO ball like morphology, showed the electro-active rippled- shaped porous surface and so it becomes a batter material for higher frequency pseudocapacitance application.

Wang *et al.* [31] obtained NiO microspheres via hydrothermal synthesis. They identified that the due to hollow sphere composed of nanoparticles and coarse surface, enhanced the electrochemical performance. They also inferred from the nature of charge-discharge curve that it is ideal for energy storage devices.

Nathan *et al.* [32] investigated single phase nanostructure NiO via solvothermal method. They identified that the presence of small particles in the nanometer scale exhibits high surface

area, high surface energy which help to increase the contact area and improve the electron tunneling length and it therefore increases the rate of electrochemical kinetics. The cyclic voltammetry curves gave 200 F/g specific capacitance.

Xing *et al.* [33] prepared mesoporous NiO via template method where anionic sulfate was used as a template and calcined the precursor at 250, 300, and 350 °C to investigate the effect on specific capacitance. The specific capacitances of those samples were calculated to be 124, 106, and 68 F/g respectively. Form the cyclic voltammetry curves they conclude that the capacitance of the mesoporous NiO samples increases with increase in calcination temperature which varies the surface area and surface reactivity.

Zhang *et al.* [34] synthesized nanocrystalline NiO via liquid-phase process and evaluated the electrochemical properties by cyclic voltammetry. They reported specific capacitance was 300 F/g at a sweep rate of 5 mV/s.

Zheng *et al.* [35] adopted hydrothermal methods to fabricate NiO flake-like morphology and investigated the electrochemical capacitive behavior. They reported that these materials retained 91.6% of initial capacity over 1000 charge-discharge cycles. These electrodes have attained specific capacitance of 137.7 F/g.

Zhang *et al.* [36] synthesized nanocrystalline NiO by solid-state method and microwave method. They obtained good capacitive behaviour from cyclic voltammetry and the specific capacitance of both samples were 186 F/g and 97 F/g for solid-state and microwave prepared samples respectively. They concluded that these behaviour are due to high surface redox reactivity of nanostructures.

Xu *et al.* [37] prepared NiO nanosheets and nanotubes through a template based mild solution route. They reported specific capacitance was 960 F/g at the end of 1000 cycles. Moreover, the open surface ends of these nanosheets and nanotubes provide additional paths for electrolyte ions and hence it gives rise to the improved electrochemical performance.

Ding *et al.* [38] prepared hierarchical NiO nanosheet hollow spheres and investigated supercapacitive performance. They obtained capacitance of 415 F/g with the retention of 91% of the initial value after 1000 cycles and these results are attributed to the hollow nanosheets.

Zhang *et al.* [39] synthesized NiO hierarchical hollow nanofibers and investigated the performance of supercapacitor electrodes. The specific capacitance of 700 F/g was obtained from the electrochemical measurements with retention of 96% over 5000 cycles.

Cao *et al.* [40] prepared hierarchical porous NiO nanotube arrays and investigated the supercapacitor behaviour by cyclic voltammetry and galvanostatic charge/discharge measurements. They obtained the specific capacitance of 675 F/g and good cyclic stability.

Liu *et al.* [41] synthesized porous NiO and investigated the effect of their specific capacitance as supercapacitor electrodes. They found the specific capacitance of 1396 F/g after 1000 cycle.

Xiong *et al.* [42] prepared different morphology of NiO samples via hydrothermal method. They reported that different specific capacitance is generally attributed to different redox reaction rate, surface area, diffusion path length of ions and it also significantly depends on the morphology of the electrode material. It is generally accepted that electrode material with higher surface area exhibits higher specific capacitance.

Ma *et al.* [43] fabricated various metal hydroxides/oxides on nickel foam and studied as the supercapacitor electrode materials. They proposed that electrical conductivity of the electrode material is also found to play a crucial role on specific capacitance, since the kinetics of the Faradic reaction determining redox reaction gets slowed down by poor conductivity of the electrode material.

Xu *et al.* [44] prepared 1D composites of CQDs coated NiO nanorods. They reported that 1D nanostructured NiO possesses high surface area and superior electrical conductivity and those are beneficial for pseudocapacitive property of NiO.

Pang *et al.* [45] synthesized NiO nanowires and investigated the length effect on their electrochemical properties. They showed that the specific capacitance depends on the length of the NiO nanowires and have obtained the highest specific capacitance for the longest length of NiO nanowire.

Though vast research has already been carried out on preudocapacitive activity of NiO, but specific capacitance is found to be far below from what is theoretically calculated. Thus technical challenges still remain open to researchers for commercial usage of NiO based electrochemical cell and vast researches are still being carried out by scientists. The generally accepted mechanism for pseudocapacititive activity suggests that electrons travel towards electrode / electrolyte interface (in case of charging) or away from interface (in case of discharging) to drive Faradic redox reaction at electrode surface followed by electron transfer across the interface. Materials having weak electron – phonon coupling exhibits adiabatic electron transport and transfer across the interface solely depend on the effective mass of the electron. But in nanostructured materials where electrons are strongly coupled with phonon, possesses non-adiabatic electron transport process where the electron – phonon interaction plays significant role in the electronic conduction.

Though significant researches have already been carried out on pseudocapacitive activity of NiO, but the effect of electron – phonon interaction on this activity has not been carried out. In this thesis, the effect of electron – phonon interaction on pseudocapacitive property of NiO nanostructured electrodes has been investigated. Here, we have also emphasized the dependence of electron – phonon interaction on the morphology of the synthesized nanostructures. In this context, we have found that the fractional dimension of the nanostructures is crucial for electron – phonon interaction. Hence the pseudocapacititive activity of NiO nanostructures could be tuned by this interaction.

2.4. Review of past work on nickel oxide based metal-semiconductor Schottky diode and barrier height effect

Oxide nanostructures exhibit multifunctional activity in different fields including medicine, food technology, electronic devices, photovoltaics, sensors etc. [46, 47]. Among them, photosensitive oxide nanostructures that convert light into electrical signal has attracted researchers owing to their potentiality in few emerging fields such as imaging, light-wave communication, memory storage, optoelectronic circuits, smart windows, photodetector etc. [48]. Searching of high-performance photosensitive materials with high speed and low-power consumption is one of the interesting research trend in these fields. Recent researches demonstrate that heterostructure consisting of photosensitive material and metal often shows better performance in optoelectronic devices compared to bare photosensitive materials.

Tung *et al.* [49] proposed electron transport at metal-semiconductor interface by dipole-layer approach. They showed that many anomalies in the experimental results due to presence of inhomogeneities in the Schottky-barrier height. The effect of fluctuation of the barrier height on

the current has been investigated by employing the ballistic electron emission spectroscopy. They concluded that Schottky barrier at polycrystalline metal-semiconductor interface is locally nonuniform.

Biber *et al.* [50] investigated the effect of Schottky metal thickness on inhomogeneity of the barrier height. The effect of lateral barrier inhomogeneity on ideality factor is a measure of non-ideal I–V characteristic. They also showed ideality factor differed from diode to diode.

Endo *et al.* [51] prepared Schottky ultraviolet photodiode by hydrothermal method. They observed that metal-semiconductor junction characteristic gets also influenced by the dipole moment, formed at MS interface. They reported dipole moments perpendicular to either Zn-polar or O-polar surfaces at Pt/ZnO metal-semiconductor junction lead different interfacial structure, barrier height.

Coppa *et al.* [52] performed Au contacts deposited on ex situ and in situ cleaned surface and they observed the electron accumulation layer and the increase of surface conductivity and this is due to the presence of hydroxide monolayer for ex situ condition. But for in situ condition, upward band bending is observed and due to the formation of depletion layer and as a results the surface conductivity is reduced. But they didn't observe any polarity effect in Au/ZnO metal-semiconductor junction.

Seyidov *et al.* [53] observed temperature-dependent polarity reversal in Au/TGaSe$_2$ Schottky junction by I-V characteristics. Temperature dependent behaviour classified by the tunneling current and related with barrier width.

Berg *et al.* [54] prepared NiO/Crystalline n-Si Heterojunction. They found that NiO film blocks electrons to a heterojunction compared to other diodes without NiO. They found that

$1/C^2$curve shifts towards right due to NiO, signifying a large voltage build-in. They also showed that the electrons overcome the build-in potential of the Schottky barrier, travel through the NiO defect states and recombined with the holes at the Si/NiO interface.

Kokubun *et al.* [55] fabricated p-type NiO and n-type β-Ga_2O_3 p-n heterojunction diodes. They found that this diode showed good rectifying properties with 1.4V turn-on voltage and obtained exponentially increased forward current. The recombination current has been obtained from ideality factor.

Reddy *et al.* [56] fabricated Au/NiO/n-GaN heterojunction Schottky diodes to investigate the effect of NiO on electrical properties. They also fabricated Au/n-GaN Schottky junction. The NiO heterojunction showed excellent rectifying behaviour, low-reverse leakage current and achieved higher barrier height which indicated that the NiO insulating layer has modified the barrier height.

Ryger *et al*. [57] investigated pt/NiO ring based Schottky diode and investigated the hydrogen sensory performance. They showed that the parameter of gate interface (ideality factor, barrier height) and sensory performance of hydrogen were controlled by the thickness of NiO interfacial layer.

Stamataki *et al*. [58] fabricated Al/NiO Schottky diode to investigate the hydrogen gas sensory performance. They obtained the ideality factor around 14 from the forward bias curve. Fermi level of the semiconductor is higher than metal, and builds a potential barrier at the depletion region and under zero bias condition the transport of carriers occurs from semiconductor to metal. For the forward bias current decreases due to increase of effective barrier height.

Saha *et al*. [59] prepared heterojunction of P-type NiO and n-type FTO to investigated the response of photoresponse through metal oxide hole transport layer. They showed p-type conductivity occurred in the NiO film due to formation of delocalization of defect carriers which originated from crystal defects. The holes created in NiO due to Ni^{2+} vacancies which act as hole transport at the heterojunction interface. They studied forward and reverse current density vs. applied voltage in presence of both illumination and dark. Under illumination condition the photo generated electron hole pair move in the opposite direction under the reverse biased condition and as a result remarkably high reverse current is obtained

Mrovec *et al.* [60] performed first-principles DFT calculation and revealed atomic and electronic arrangement at transitional metal/$SrTiO_3$ heterojunction for correct description of junction barrier height.

Tamura *et al.* [61] illustrated tunability of Pt / TiO_2 (001) junction between MS and Ohmic typed interface. They showed metal-induced gap states makes oxygen deficiency energy small at the interface. They also demonstrated that the Schottky barrier height was strongly affected by oxygen vacancy.

Ma *et al*. [62] investigated the interface Schottky barrier height effect on the performance of metal-semiconductor heterostructures in various applications. They studied the first-principle calculations and the tight-binding method. Thus, they reported strain due to lattice mismatch also has effect on the heterojunction barrier height and photosensitivity. Mainly, the interfacial Schottky barrier height of Au/TiO_2 (001) interface decreases by strain.

Bao *et al*. [63] illustrates that AgBr crystals showed high electron-hole separation rate. They conclude on the basis of light absorption spectra, Mott-Schottky tests, DFT calculation and photo-oxidation deposition that nanostructure based heterojunction exhibits higher efficiency than

traditional thin-film or bulk material based heterojunction due to unique electrical, light absorption properties, attributed to higher surface to volume ratio.

It has been investigated by many researchers including us that electron – phonon interaction has a significant role in electron's response in any nanostructures. Though a few experimental evidences exist on morphological dependence of current – voltage ($I – V$) characteristics of MS heterojunction and associated photosensitivity, but no investigation on the effect of electron – phonon interaction on $I – V$ characteristic of MS heterojunction and its photosensitivity has been attempted. In this thesis, we have studied the influence of this interaction on charge transport through MS heterojunction using Ni_2O_3 as a model semiconducting materials.

In this thesis, Al (metal) / Ni_2O_3 MS heterojunction has been fabricated and we have analysed $I – V$ characteristics under dark and photo-irradiation followed by explanation on the basis of electron – phonon interaction. The present study illustrating the strong effect of electron – phonon interaction on $I – V$ characteristic may also be generalized to other MS nanostructure heterojunction.

2.5. Review of past work on nickel oxide dielectric behaviour

The nanosize materials have received widespread attention among the scientific community due to its unusual electrical properties different from single crystals, polycrystals (bulk), thin films and glasses even though they are identical in chemical composition [64-68]. Besides, nanosized materials have shown great potential to device applications including sensors, electrodes, switching devices, microelectronic devices and solar cells [2, 69-71]. Furthermore, the electrical properties of nanosize materials are different from their bulk because of the high surface

to volume ratio of the grains, high defect density, quantum confinement of charge carriers and disordered grain boundary [72-74].

Maheswari *et al*. [75] investigated the effect of defect structure on dielectric properties of NiO. They showed that the microstrain of nanocrystals, affects the dielectric properties. The bulk resistance and relaxation time of charge carriers are higher for nanocrystalline samples having high microstrain and defects.

Biju *et al*. [68] prepared nanocrystalline NiO with particle size 2-3 nm through chemical route. They prepared pellets of the nanoparticles for investigating the electrical properties as a function of applied AC signal and temperature. The presence of two relaxation processes is related with the grain boundary and grain interior of the nanoparticles. They concluded the high value of dielectric constant and loss at low frequencies associated with grain boundaries of the insulating grains.

Chen *et al*. [76] perform low-temperature impedance and dielectric properties of nanocrystals NiO of different particle sizes. They found that as the particle size decreases first the conductivity increases to a maximum value followed by decrease in the conductivity with the further decrease in particle size. They also showed that the activation energy for the dielectric relaxation process does not significantly change from bulk conduction which administered by the hopping of holes.

Biju *et al*. [77] investigated the DC conductivity of consolidated NiO nanoparticles. They showed the conductivity increases by six to eight orders of magnitude arising out of high density of Ni^{2+} vacancy in this sample compared to the single crystals NiO. They observed that the large polaron conduction is related with holes in the 2p band of O^{2-} and also observed the decrease in

activation energy compared to bulk is associated with the presence of high defects in nanoparticles. They discussed the electrical conductivity in terms of grain, grain boundaries and triple junctions.

Fuschillo *et al*. [78] prepared undoped and Li doped NiO to investigate the dielectric properties as a function of frequency and temperature. They showed dielectric constant of Li doped NiO increased at low frequency region. The behavior of the AC conductivity at lower frequencies can be explained due to the non-adiabatic hopping of charge carriers but at the high frequency region, it could be explained by the adiabatic hopping of charge carriers.

Tharayil *et al*. [79] prepared different particle sizes of nickel-cobalt oxide nanostructured by chemical co-precipitation method to investigate the dielectric behavior and AC conductivity as a function of frequency and temperature. In nanostructured material there are large number of atom/ions near the grain boundaries and as a results of which large number of defects is generated. Thus each interface acts as a capacitor of the material. They also showed dielectric permittivity and activation energy were high.

Lin *et al*. [80] synthesized Li and Al co-doped NiO-based ceramic materials and investigated high permittivity. They showed that the remarkable change in dielectric properties is due to Al ions distributed in grain boundaries and dielectric constant at low frequency remains constant around four to five order at 1 kHz but at high frequency decrease steplike. They conclude that this type of dielectric constant is attributed to Maxwell-Wagner polarization.

Gokul *et al*. [81] investigated dielectric properties and AC conductivity as a function of frequency and temperature of non-stoichiometric NiO nanoparticles prepared by wet chemical preparation. They showed that at low frequency dielectric constant increased but with increasing temperature below 10^4 Hz dielectric constant decreases and above this frequency dielectric constant increases with temperature and this phenomenon has been explained by Debye relaxation

theory. Loss peak shifted towards higher frequency and this is attributed to long range hopping of charge carriers. Grain and grain boundary resistance decreases are shown in Nyquist plot, as a function of temperature. AC conductivity is found to increase with increase in temperature. The high activation energy is correlated with the grain boundary effect due to requirement of more energy for hopping of charge carriers.

There is no report on the electrical properties of single phase Ni_2O_3 samples. In this thesis, we have prepared different particle sizes of Ni_2O_3 using low temperature chemical precipitation method with varying temperature and investigated the electrical properties. The impedance spectroscopic analysis and ac conductivity of different Ni_2O_3 nanoparticles have been measured at room temperature. The separate contribution of grain and grain boundaries on the conductivity of nano crystalline Ni_2O_3 is obtained from impedance spectroscopy analysis.

2.6. Review of past work on nickel oxide catalytic activity

Congo red (CR), a benzidine-based anionic diazo dye and methylene blue (MB), a phenothiazine derivative cationic dye are among the commonly used dyes that are found mostly in the industrial discharge water. Both CR and MB have vast range of side effects starting from cardiovascular to haematologic [82]. In catalytic degradation, toxic dyes are converted into their non-toxic oxidized products. Most metal oxides e.g. ZnO [83], TiO_2 [84], NiO [85], CuO [86] and their composites are used as [87-90] catalyst.

Ameta *et al*. [91] studied photocatalytic activity of semiconducting NiO. They investigated that the presence of solar energy, in the visible region increases the rate of photocatalytic bleaching of the dye. They also observed the effect of concentration of dye, amount of semiconductor, pH, and light intensity on the rate of photocatalytic activity. The photocatalytic activity followed the

pseudo-first order kinetics. The bleaching activity increases with increasing pH up to 6.5, and with further increases on pH the reaction rate decreases. The increase in reaction rate with increase in pH is due to the generation of •OH radicles. They also showed photocatalytic bleaching increases with increasing concentration of the catalyst but it decreases with increases concentration of the dye.

Motahari *et al*. [92] synthesized the nanostructured NiO and investigated the photocatalyst application for dye pollution wastewater treatment. They showed 2.83eV band gap which confirms the semiconductive nature of NiO nanostructures indicating the potential application for photocatalyst. Degradation of Rodamine B dye investigated with UV irradiation times, pH, quantity of catalyst and concentration of dye. In presence of UV irradiation, degradation of dye is around 80%. Degradation rate increases with pH 3 to 8 and with catalyst dosage but with increases dye concentration, deep colored solution protects the UV light and as a result radical •OH formation is reduced and hence it decreases the degradation of dye. Reaction kinetic revealed that photodegradation reaction kinetic followed the improved Langmuir-Hinshelwood model.

Song *et al*. [6] prepared NiO hierarchical architectures with controlled morphology and sizes and investigated the dependence of morphology with photocatalytic activity. They showed NiO hollow microsphere degraded 93%. The high surface area increases the active surface sites and therefore increases the surface charge carrier transfer rate in photocatalytic activity.

Duan *et al*. [93] synthesized different particle sizes of single crystalline NiO. They showed small particles exhibit blue shift in UV-vis spectrum due to quantum confinement effect. Investigated the photocatalytic activity in degradation of dye under UV irradiation. The small particles showed larger activity due to very small size, fine dispersion and high surface area.

Christy *et al*. [94] prepared NiO nanoparticle using solution combustion method. They evaluated the photocatalytic activity of NiO nanoparticles. They employed pseudo-first order reaction to obtain rate constant of dye degradation in presence of UV irradiation. They conclude crystalline nature and shape factor of the particles enhance the photocatalytic activity.

Wan *et al*. [95] synthesized nano scale NiO with different morphology and size by hydrothermal method and investigated the photocatalytic activity. They showed perfect crystal structure, and smaller particle size increase the surface area and so the degradation rate increases compared to poor crystallinity material. They concluded that more number of deep level defect sample showed poor photocatalytic activity. The shallow trapped holes in less defect sample, interact with chemisorbed OH^- or H_2O to produce •OH radicals which induce high photocatalytic activity.

Ahmed [96] prepared mesoporous NiO/TiO_2 nanoparticles by sol-gel method to study the performance of photodegradation of methylene blue dye. The author observed that doped NiO samples exhibited higher rate of mineralization of hazardous dye compared to pure TiO_2. The degradation reaction of methylene blue dye follows the pseudo first-order reaction kinetics and the observed rate constant increases with increasing doping concentration up to 5% NiO.

Rakshit *et al*. [97] investigated the effect of morphology of NiO for the photodegradation of phenol. They observed the characteristic fluorescence emission of phenol that NiO sample showed good photocatalytic activity in the decomposition of phenol up to 82%. They concluded that the phenol molecules in presence of UV light react with •OH radicals at the excited NiO surface, and get decomposed.

Zhang *et al*. [98] synthesized hierarchical NiO hollow microspheres by refluxing method to investigate the performance of Congo red adsorption from aqueous solution. They observed that

for different sizes of NiO hollow microspheres showed different adsorption capacities for CR. Hierarchical structures and high specific surface areas increase the effective adsorbents for the CR pollutant. They showed that the adsorption nature followed the Langmuir isotherm model which indicated homogeneous surface nature of the sample and formation of monolayer coverage of CR molecule on the outer surface of adsorbent. Maximum adsorption capacity achieved is 526.3 mg/g at room temperature.

Rong *et al*. [99] prepared NiO/graphene nanosheets by hydrothermal method to investigate the performance of adsorption performance of Congo red adsorption from wastewater solution to find adsorption kinetic model and isotherm of adsorbent. They showed adsorption follows pseudo second-order kinetic model and equilibrium experimental data followed Redlich-Peterson model. The identified adsorption process of CR on adsorbent was found to be multilayer adsorption process.

Among different transition metal oxides (TMOs) used as photo catalysts, porous nickel oxide nanostructures and their composites having non-stoichiometric defects have shown excellent photo degradation properties over the entire solar spectrum [100-104]. However, the synthesis methods of these materials involve rigorous steps, high temperature operation, sophisticated instrumentation and specific reagents which are not very user and environmentally friendly. Thus, an environmentally friendly synthesis technique involving lesser complex reagents and lower synthesis temperature can be suggested for preparing non-stoichiometric nickel oxide which can serve as excellent photocatalyst by creating a chemically oxidizing environment at room temperature or even below. As a proof of concept, the authors have already prepared nickel (III) oxide (Ni_2O_3) nanostructures within 0°C to 70°C for excellent adsorption mediated Cr(VI) ion removal/monitoring in their previous works [105-108]. In this thesis, we present non-

stoichiometric Ni_2O_3 nanoparticles synthesized by a mild environmentally friendly room temperature oxidative co-precipitation approach and these are excellent wide band photocatalyst capable of degrading CR and MB under solar irradiation. The degradation efficiency, reusability and stability of the catalyst have been studied under different reaction conditions (exposure time and pH). A dye degradation mechanism was proposed considering the effect of induced surface defects and non-stoichiometric band tailoring on the photo catalytic activity of Ni_2O_3 catalysts.

2.7. Objectives and scope of the work

Under the backdrop of the above literature survey following are the main objectives of this thesis:

1. Synthesis of different nanostructures (coral, flake, flower etc.) of NiO and Ni_2O_3 of by hydrothermal method, followed calcination and chemical oxidation respectively.

2. Detailed characterization of the synthesized nanostructured materials by XRD, FTIR, FESEM, TEM and Raman.

3. To study the effect of morphology of nanostructure NiO on the hysteresis behaviour at room temperature and its detailed interpretation.

4. To study the electrochemical properties of the above mentioned nanostructure NiO by cyclic voltammetry, galvanostatic charging-discharging and electrochemical impedance techniques and the effect has been explained for the first time by involving the electron-phonon interaction.

5. To prepare the nanostructured Ni_2O_3/Al heterojunction and to study the junction parameters have been measured under the dark and illumination conditions. The effect of these parameters have been explained by electron-phonon interaction.

6.   To study the dielectric properties of the Ni$_2$O$_3$ nano particles and delineate the role of grain and grain boundary on to the dielectric properties.

7.   To study the catalytic property of degradation of congo-red and methylene blue by the nanostructured Ni$_2$O$_3$.

2.8. References

1.   C. N. R. Rao, *Annual Review of Physical Chemistry*, 1989, **40**, 291-326.

2.   H. Steinebach, S. Kannan, L. Rieth and F. Solzbacher, *Sensors and Actuators B: Chemical*, 2010, **151**, 162-168.

3.   J. H. Pan, Q. Huang, Z. Y. Koh, D. Neo, X. Z. Wang and Q. Wang, *ACS Appl Mater Interfaces*, 2013, **5**, 6292-6299.

4.   J. M. Tarascon and M. Armand, *Nature*, 2001, **414**, 359-367.

5.   H. D. Lee, B. Magyari-Kope and Y. Nishi, *Physical Review B*, 2010, **81**, 193202.

6.   X. Song and L. Gao, *The Journal of Physical Chemistry C*, 2008, **112**, 15299-15305.

7.   Z. P. Wei, M. Arredondo, H. Y. Peng, Z. Zhang, D. L. Guo, G. Z. Xing, Y. F. Li, L. M. Wong, S. J. Wang, N. Valanoor and T. Wu, *ACS Nano*, 2010, **4**, 4785-4791.

8.   W. Zhou, M. Yao, L. Guo, Y. Li, J. Li and S. Yang, *J Am Chem Soc*, 2009, **131**, 2959-2964.

9.   J. Hu, K. Zhu, L. Chen, H. Yang, Z. Li, A. Suchopar and R. Richards, *Advanced Materials*, 2008, **20**, 267-271.

10.   R. Kodama, S. Makhlouf and A. Berkowitz, *Physical Review Letters*, 1997, **79**, 1393-1396.

11. E. Winkler, R. D. Zysler, M. Vasquez Mansilla, D. Fiorani, D. Rinaldi, M. Vasilakaki and K. N. Trohidou, *Nanotechnology*, 2008, **19**, 185702.

12. S. A. Makhlouf, F. T. Parker, F. E. Spada and A. E. Berkowitz, *Journal of Applied Physics*, 1997, **81**, 5561.

13. W. Duan, S. Lu, Z. Wu and Y. Wang, *The Journal of Physical Chemistry C*, 2012, **116**, 26043-26051.

14. H. Gao, D. Gao, J. Zhang, Z. Zhang, G. Yang, Z. Shi, J. Zhang, Z. Zhu and D. Xue, *Micro & Nano Letters*, 2012, **7**, 5-8.

15. Y. Cui, C. Wang, S. Wu, G. Liu, F. Zhang and T. Wang, *CrystEngComm*, 2011, **13**, 4930-4934.

16. M. Tadic, D. Nikolic, M. Panjan and G. R. Blake, *Journal of Alloys and Compounds*, 2015, **647**, 1061-1068.

17. M. Seehra, H. Shim, P. Dutta, A. Manivannan and J. Bonevich, *Journal of Applied Physics*, 2005, **97**, 10J509.

18. M. P. Proenca, C. T. Sousa, A. M. Pereira, P. B. Tavares, J. Ventura, M. Vazquez and J. P. Araujo, *Phys Chem Chem Phys*, 2011, **13**, 9561-9567.

19. S. Tiwari and K. Rajeev, *Physical Review B*, 2005, **72**, 104433.

20. J. Cooper, A. Ionescu, R. Langford, K. Ziebeck, C. Barnes, R. Gruar, C. Tighe, J. Darr, N. Thanh and B. Ouladdiaf, *Journal of Applied Physics*, 2013, **114**, 083906.

21. M. Ge, L. Han, U. Wiedwald, X. Xu, C. Wang, K. Kuepper, P. Ziemann and J. Jiang, *Nanotechnology*, 2010, **21**, 425702.

22. Y. Ichiyanagi, N. Wakabayashi, J. Yamazaki, S. Yamada, Y. Kimishima, E. Komatsu and H. Tajima, *Physica B: Condensed Matter*, 2003, **329**, 862-863.

23. G. Madhu, K. Maniammal and V. Biju, *Physical Chemistry Chemical Physics*, 2016, **18**, 12135-12148.

24. T. Smith, J. Mars and G. Turner, *Power Electronics Specialists Conference,2002 IEEE 33rd Annual, IEEE,* 2002, 124-128.

25. P. Pisu and G. Rizzoni, *Vehicle Power and Propulsion, 2005 IEEE Conference, IEEE,* 2005, 8.

26. M. Meinert, *Power Electronics and Applications, 13th European Conference, IEEE* 2009, 1-10.

27. P. Ragupathy, D. H. Park, G. Campet, H. Vasan, S.-J. Hwang, J.-H. Choy and N. Munichandraiah, *The Journal of Physical Chemistry C*, 2009, **113**, 6303-6309.

28. C. Wei, H. Pang, C. Cheng, J. Zhao, P. Li and Y. Zhang, *CrystEngComm*, 2014, **16**, 4169-4175.

29. S. K. Meher, P. Justin and G. R. Rao, *Nanoscale*, 2011, **3**, 683-692.

30. K. Wang, L. Li and H. Zhang, *Int. J. Electrochem. Sci*, 2013, **8**, 4785-4791.

31. L. Wang, Y. Hao, Y. Zhao, Q. Lai and X. Xu, *Journal of Solid State Chemistry*, 2010, **183**, 2576-2581.

32. T. Nathan, A. Aziz, A. Noor and S. Prabaharan, *Journal of Solid State Electrochemistry*, 2008, **12**, 1003-1009.

33. W. Xing, F. Li, Z.-f. Yan and G. Lu, *Journal of Power Sources*, 2004, **134**, 324-330.

34. F.-b. Zhang, Y.-k. Zhou and H.-l. Li, *Materials Chemistry and Physics*, 2004, **83**, 260-264.

35. Y.-z. Zheng, H.-y. Ding and M.-l. Zhang, *Materials Research Bulletin*, 2009, **44**, 403-407.

36. Y. Zhang, Y. Gui, X. Wu, H. Feng, A. Zhang, L. Wang and T. Xia, *International journal of hydrogen energy*, 2009, **34**, 2467-2470.

37. X. Xu, J. Liang, H. Zhou, S. Ding and D. Yu, *Rsc Advances*, 2014, **4**, 3181-3187.

38. S. Ding, T. Zhu, J. S. Chen, Z. Wang, C. Yuan and X. W. D. Lou, *Journal of Materials Chemistry*, 2011, **21**, 6602-6606.

39. M. Zhang, Q. Li, D. Fang, I. A. Ayhan, Y. Zhou, L. Dong, C. Xiong and Q. Wang, *Rsc Advances*, 2015, **5**, 96205-96212.

40. F. Cao, G. Pan, X. Xia, P. Tang and H. Chen, *Journal of Power Sources*, 2014, **264**, 161-167.

41. M. Liu, J. Chang, J. Sun and L. Gao, *Electrochimica Acta*, 2013, **107**, 9-15.

42. S. Xiong, C. Yuan, X. Zhang and Y. Qian, *CrystEngComm*, 2011, **13**, 626-632.

43. X. Ma, Y. Li, Z. Wen, F. Gao, C. Liang and R. Che, *ACS Appl Mater Interfaces*, 2014, **7**, 974-979.

44. J. Xu, Y. Xue, J. Cao, G. Wang, Y. Li, W. Wang and Z. Chen, *Rsc Advances*, 2016, **6**, 5541-5546.

45. H. Pang, Q. Lu, Y. Zhang, Y. Li and F. Gao, *Nanoscale*, 2010, **2**, 920-922.

46. Q. Tan, C. Du, Y. Sun, G. Yin and Y. Gao, *Journal of Materials Chemistry A*, 2014, **2**, 1429-1435.

47. J. Tian, Z. Zhao, A. Kumar, R. I. Boughton and H. Liu, *Chemical Society Reviews*, 2014, **43**, 6920-6937.

48.   D. Wu, Y. Jiang, Y. Zhang, Y. Yu, Z. Zhu, X. Lan, F. Li, C. Wu, L. Wang and L. Luo, *Journal of Materials Chemistry*, 2012, **22**, 23272-23276.

49.   R. Tung, *Physical Review B*, 1992, **45**, 13509.

50.   M. Biber, Ö. Güllü, S. Forment, R. Van Meirhaeghe and A. Türüt, *Semiconductor science and technology*, 2005, **21**, 1.

51.   H. Endo, M. Sugibuchi, K. Takahashi, S. Goto, S. Sugimura, K. Hane and Y. Kashiwaba, *Applied physics letters*, 2007, **90**, 121906.

52.   B. Coppa, C. Fulton, S. Kiesel, R. Davis, C. Pandarinath, J. Burnette, R. Nemanich and D. Smith, *Journal of Applied Physics*, 2005, **97**, 103517.

53.   M. Y. Seyidov, R. A. Suleymanov and Y. Bakış, *Journal of Applied Physics*, 2009, **105**, 043710.

54.   A. H. Berg, G. S. Sahasrabudhe, R. A. Kerner, B. P. Rand, J. Schwartz and J. C. Sturm, *Device Research Conference (DRC), 74th Annual, IEEE,* 2016, 1-2.

55.   Y. Kokubun, S. Kubo and S. Nakagomi, *Applied Physics Express*, 2016, **9**, 091101.

56.   V. R. Reddy, P. S. Reddy, I. N. Reddy and C.-J. Choi, *Rsc Advances*, 2016, **6**, 105761-105770.

57.   I. Rýger, G. Vanko, T. Lalinský, P. Kunzo, M. Vallo, I. Vavra and T. Plecenik, *Sensors and Actuators B: Chemical*, 2014, **202**, 1-8.

58.   M. Stamataki, C. Sargentis, D. Tsamakis, I. Fasaki and M. Kompitsas, *Sensors, IEEE,* 2008, 843-846.

59.   B. Saha, K. Sarkar, A. Bera, K. Deb and R. Thapa, *Applied Surface Science*, 2017, **418**, 328-334.

60. M. Mrovec, J.-M. Albina, B. Meyer and C. Elsässer, *Physical Review B*, 2009, **79**, 245121.

61. T. Tamura, S. Ishibashi, K. Terakura and H. Weng, *Physical Review B*, 2009, **80**, 195302.

62. X. Ma, Y. Dai, L. Yu and B. Huang, *Nanoscale*, 2016, **8**, 1352-1359.

63. S. Bao, Z. Wang, X. Gong, C. Zeng, Q. Wu, B. Tian and J. Zhang, *Journal of Materials Chemistry A*, 2016, **4**, 18570-18577.

64. N. Sivakumar, A. Narayanasamy, N. Ponpandian and G. Govindaraj, *Journal of applied physics*, 2007, **101**, 084116.

65. S. A. Makhlouf, M. A. Kassem and M. Abdel-Rahim, *Journal of materials science*, 2009, **44**, 3438.

66. P. Marquardt, G. Nimtz and B. Mühlschlegel, *Solid state communications*, 1988, **65**, 539-542.

67. H. Gleiter, *Advanced Materials*, 1992, **4**, 474-481.

68. V. Biju and M. A. Khadar, *Materials Science and Engineering: A*, 2001, **304**, 814-817.

69. S. Shrestha, C. Yeung, C. Nunnerley and S. Tsang, *Sensors and Actuators A: Physical*, 2007, **136**, 191-198.

70. J. H. Pan, Q. Huang, Z. Y. Koh, D. Neo, X. Z. Wang and Q. Wang, *ACS applied materials & interfaces*, 2013, **5**, 6292-6299.

71. X. Wang, G. Sun, N. Li and P. Chen, *Chemical Society Reviews*, 2016, **45**, 2239-2262.

72. R. Birringer, *Materials Science and Engineering: A*, 1989, **117**, 33-43.

73. M. Abdulkhadar and B. Thomas, *Nanostructured materials*, 1998, **10**, 593-600.

74.   C.-W. Nan, A. Tschöpe, S. Holten, H. Kliem and R. Birringer, *Journal of applied physics*, 1999, **85**, 7735-7740.

75.   A. Uma Maheswari, S. R. Mohan, M. Sivakumar and S. Saravana Kumar, *Journal of nanoscience and nanotechnology*, 2015, **15**, 9423-9430.

76.   L. Chen, L. Li and G. Li, *Journal of Solid State Chemistry*, 2008, **181**, 2073-2077.

77.   V. Biju and M. A. Khadar, *Materials Research Bulletin*, 2001, **36**, 21-33.

78.   N. Fuschillo, B. Lalevic and B. Leung, *Thin Solid Films*, 1974, **24**, 181-192.

79.   N. J. Tharayil, S. Sagar, R. Raveendran and A. Vaidyan, *Physica B: Condensed Matter*, 2007, **399**, 1-8.

80.   Y. Lin, J. Wang, L. Jiang, Y. Chen and C.-W. Nan, *Applied physics letters*, 2004, **85**, 5664-5666.

81.   B. Gokul, P. Matheswaran, K. Abhirami and R. Sathyamoorthy, *Journal of Non-Crystalline Solids*, 2013, **363**, 161-166.

82.   E. Brillas and C. A. Martínez-Huitle, *Applied Catalysis B: Environmental*, 2015, **166**, 603-643.

83.   M. Pirhashemi and A. Habibi-Yangjeh, *Journal of colloid and interface science*, 2017, **491**, 216-229.

84.   K. Alamelu, V. Raja, L. Shiamala and B. M. J. Ali, *Applied Surface Science*, 2018, **430**, 145-154.

85.   S. V. Sancheti, C. Saini, R. Ambati and P. R. Gogate, *Catalysis Today*, 2018, **300**, 50-57.

86.   S. Mosleh, M. R. Rahimi, M. Ghaedi, K. Dashtian and S. Hajati, *Ultrasonics sonochemistry*, 2018, **40**, 601-610.

87.   E. Abroshan, S. Farhadi and A. Zabardasti, *Solar Energy Materials and Solar Cells*, 2018, **178**, 154-163.

88.   T. A. Kurniawan, L. Yanyan, T. Ouyang, A. B. Albadarin and G. Walker, *Materials Science in Semiconductor Processing*, 2018, **73**, 42-50.

89.   M. Nasirian, C. F. Bustillo-Lecompte and M. Mehrvar, *Journal of environmental management*, 2017, **196**, 487-498.

90.   F. Siadatnasab, S. Farhadi and A. Khataee, *Ultrasonics sonochemistry*, 2018, **44**, 359-367.

91.   P. Ameta, A. Kumar, R. Ameta and R. Malkani, *Iranian Journal of Chemistry and Chemical Engineering (IJCCE)*, 2010, **29**, 43-48.

92.   F. Motahari, M. R. Mozdianfard, F. Soofivand and M. Salavati-Niasari, *Rsc Advances*, 2014, **4**, 27654-27660.

93.   H. Duan, X. Zheng, S. Yuan, Y. Li, Z. Tian, Z. Deng and B. Su, *Materials Letters*, 2012, **81**, 245-247.

94.   A. J. Christy and M. Umadevi, *Materials Research Bulletin*, 2013, **48**, 4248-4254.

95.   X. Wan, M. Yuan, S.-l. Tie and S. Lan, *Applied Surface Science*, 2013, **277**, 40-46.

96.   M. Ahmed, *Journal of photochemistry and Photobiology A: Chemistry*, 2012, **238**, 63-70.

97.   S. Rakshit, S. Chall, S. S. Mati, A. Roychowdhury, S. Moulik and S. C. Bhattacharya, *Rsc Advances*, 2013, **3**, 6106-6116.

98.   P. Zhang, X. Ma, Y. Guo, Q. Cheng and L. Yang, *Chemical engineering journal*, 2012, **189**, 188-195.

99.   X. Rong, F. Qiu, J. Qin, H. Zhao, J. Yan and D. Yang, *Journal of Industrial and Engineering Chemistry*, 2015, **26**, 354-363.

100. M. A. Ahmed, *Journal of Photochemistry and Photobiology A: Chemistry*, 2012, **238**, 63-70.

101. H. Derikvandi and A. Nezamzadeh-Ejhieh, *Journal of Hazardous Materials*, 2017, **321**, 629-638.

102. F. Hashemzadeh, A. Gaffarinejad and R. Rahimi, *Journal of Hazardous Materials*, 2015, **286**, 64-74.

103. A. Pourtaheri and A. Nezamzadeh-Ejhieh, *Chemical Engineering Research and Design*, 2015, **104**, 835-843.

104. F. Torki and H. Faghihian, *RSC Advances*, 2017, **7**, 54651-54661.

105. S. Dey, S. Bhattacharjee, R. S. Bose and C. K. Ghosh, *Applied Physics A*, 2015, **119**, 1343-1354.

106. S. Dey, S. Bhattacharjee, M. G. Chaudhuri, R. S. Bose, S. Halder and C. K. Ghosh, *RSC Advances*, 2015, **5**, 54717-54726.

107. S. Dey, S. Podder, A. Roychowdhury, D. Das and C. K. Ghosh, *Journal of environmental management*, 2018, **211**, 356-366.

108. S. Dey, S. Santra, A. Midya, P. K. Guha and S. K. Ray, *Environmental Science: Nano*, 2017, **4**, 191-202.

Chapter 3

Non-inversion anisotropy energy in NiO coral structure: asymmetric hysteresis loop at room temperature

Abstract

-

Abstract

Coral – like microstructure of NiO has been synthesized via a facile template free hydrothermal technique followed by calcination. Structure and morphology of the synthesized samples have been examined by x-ray diffractometer, field emission scanning electron microscope and transmission electron microscope. Positron annihilation spectroscopy reveals high porosity (37%) and cationic vacancies within the microstructures. Magnetic study illustrates spin-glass like behaviour and asymmetric hysteresis loop at room temperature. Later one is attributed to non-inversion symmetry of the anisotropic energy barrier, introduces by defect induced ferromagnetic domain within antiferromagnetic matrix of NiO. Numerical values of the anisotropy parameters have also been evaluated using law of approach method. The present study evidences that the microstructure could be helpful for developing magnetization based memory devices due to its high barrier height ~ 2.50×10^6 erg/cm^3.

3.1. Introduction

Over the last decade, extensive research work has been carried out on transition metal oxide nanostructures due to their importance in fundamental researches as well as in applications in many fields [1]. Among different transitional metal oxide based nanostructure, investigated so far, NiO nanostructures have particularly drawn attention due to their potentiality in different application fields e.g. battery cathodes, catalysis, smart windows, sensing, p-type transparent conducting oxide films, electrochromic films, active optical fibers, photovoltaics, supercapacitors etc. [2-4]. NiO nanostructures have proven its candidature as an upcoming material for next generation resistive switching memory devices, spin valves, tunnel junction etc. [5]. Till date, various hierarchical nanostructures of NiO such as hollow spheres [6], nanorods nanowires [7], polyhedrons [8], plates [9], has been synthesized and it has been observed that they often exhibit exotic properties

completely different from bulk, thus applicational opportunity in additional fields gets opened up. Comparatively less attention has been given to investigate magnetic properties of different NiO hierarchical structures. But, few studies that have already been carried out demonstrates that they often exhibit unique magnetic properties that has not been observed in bulk NiO [10]. For example, in contrast to antiferromagnetic bulk NiO, hierarchical structures show weak ferromagnetism, enhanced coercivity, enhanced hysteresis loop, well-described by Kodama *et al*. on the basis of multi-sublattice spin configuration [10], while earlier two-sublattice model, proposed by L. Neel in the year 1961, was not able to explain these newly observed magnetic properties [10]. Recently, spin glass response due to freezing of the surface spins has been observed in NiO structure by Winkler *et al.* [11]. In general, uncompensated surface spins and their interaction with local environment that significantly depends on morphology determine their magnetic properties where interparticle interaction plays crucial role [11-13]. In this context, magnetic properties of lotus-root and flower-like micro-spherical NiO were investigated by Cui *et al*. [14]. Proenca *et al*. examined the effect of size on the magnetic behaviour of nanocrystalline spherical NiO [15]. Here, it is to state that for better understanding the dependence of magnetic properties of hierarchical structure of NiO upon morphology and underlined magnetic interaction, intense research has to be carried out on various hierarchical structure of NiO. In this chapter, magnetic property of NiO coral-like hierarchical structure has been studied first time and role of defects within the synthesized structure is discussed.

3.2. Experimental

3.2.1. Synthesis of NiO hierarchical nanostructure

The synthesis protocol of highly crystalline NiO coral-like structure was derived from Pan *et al*. [4]. $Ni(NO_3)_2$, urea and poly ethylene glycol - 600 (PEG) of analytical grade

(Merck, India) were used as the precursor materials without further purification. In this typical synthesis process, 1.570 g of $Ni(NO_3)_2$, $6H_2O$ and 1.622 g of urea were dissolved into 90 mL of distilled water followed by addition of PEG mixture of different amount (0.72, 1.44, 2.87 ml). Then the whole mixture solution was transferred into a 100 ml Schott Duran glass bottle, sealed, and heated at 90°C for 12 h. The greenish intermediate product thus formed was collected after centrifugation, washed repeatedly with water and ethanol, and dried at 60°C for 10 h. Finally the coral-like NiO was obtained by heating the intermediate product at 400°C for 2 hours in open atmosphere. In order to optimize the synthesis condition, we prepared the sample at various PEG concentration (0.72, 1.44, 2.87 ml, named as S1, S2 and S3 respectively) and different time (24 and 8 h, named as S4 and S5 respectively).

3.2.2. Characterization

As-prepared products were characterized by Ultima-III x-ray diffractometer (XRD, Rigaku, Cu K_α radiation, $\lambda = 1.5404$ Å), field emission scanning electron microscope (FESEM, S – 4800, Hitachi) and transmission electron microscope (TEM, JEOL). Thermal analysis was carried out by thermogravimetry (TG; Perkin). Fourier transform infrared (FTIR) spectra were recorded by IR – Prestige (Shimadzu, Japan). Raman spectra were obtained by alpha 300, Witec (excitation wavelength 530 nm, power 3 mW and spot size: 2 μm). We adopted Rietveld's powder structure refinement analysis using the JAVA based software program MAUD [16-20] to obtain the structural and microstructural refinement parameters through a least-square method. Experimental profiles were fitted with the most suitable pseudo-Voigt [19] analytical function with asymmetry and the background of each pattern is fitted with a fourth order polynomial function. Positron annihilation lifetime spectroscopy giving information about porosity and ions vacancy on the surface of the

synthesized nanostructure was utilized using fast-fast coincidence system consisting of two 1 inch tapered off BaF_2 scintillators coupled to XP 2020Q photo multiplier tubes. The lifetime data was analysed by the PATFIT program [21]. The time resolution of PALS, used here, is about 290 pico-seconds and employs ^{60}Co source. In order to gain insight into the oxidation states of the elements present in the sample, it was characterized by x-ray photoelectron spectroscopy (XPS, PHI5000, Versa Probe II, Ulvac-Phi, Inc., USA) using Al Kα (hν = 1486.6 eV) as a source of x-ray. Its binding energy position was calibrated on the basis of C 1s. Magnetic properties were investigated by physical property measurement system (PPMS, Cryogenic, UK).

3.3. Results and discussion

3.3.1. Characterization of the 3D hierarchical α-Ni(OH)₂ nanostructure, formed at intermediate step

XRD pattern of intermediate, un-calcined greenish product (shown in Fig. 3.1 (a)) consists of five peaks at 2θ = 11.94, 24.01, 33.62, 37.36 and 60.26° those can readily be indexed by reflection from (003), (006), (101), (015) and (110) planes of the hexagonal α-Ni(OH)₂ with lattice parameters a = 3.08, c = 22.2 Å and space group $R\overline{3}m$ [22, 23]. High asymmetric nature of the peak, observed between 2θ = 33.62 and 37.36, is attributed to two-dimensional reflection from various chemical species intercalated turbostratically stacked layers of α-Ni(OH)₂ [22, 24]. In order to gain insight about intercalated specie, intermediate products were characterized by FTIR spectroscopy and one typical spectrum is presented in Fig. 3.1 (b). As observed, broad band, appeared between 3200 - 3600 cm⁻¹, is attributed to O − H stretching vibrational mode of the H-bonded water molecules present in interlamellar space between layers [22, 25], while other intense band at 2228 cm⁻¹ is assigned to the C ≡ N stretching vibration of OCN⁻ ions, produced in the intermediate step

[26]. The band at 1480 cm^{-1} representing N-O stretching vibration mode of NO$_3^-$ with C$_{2v}$ symmetry, appears due to grafting of the ions towards α-Ni(OH)$_2$, whereas the band at 1396 cm^{-1} is assigned to N-O stretching mode of NO$_3^-$ with D$_{3h}$ symmetry within the interlayers [27].
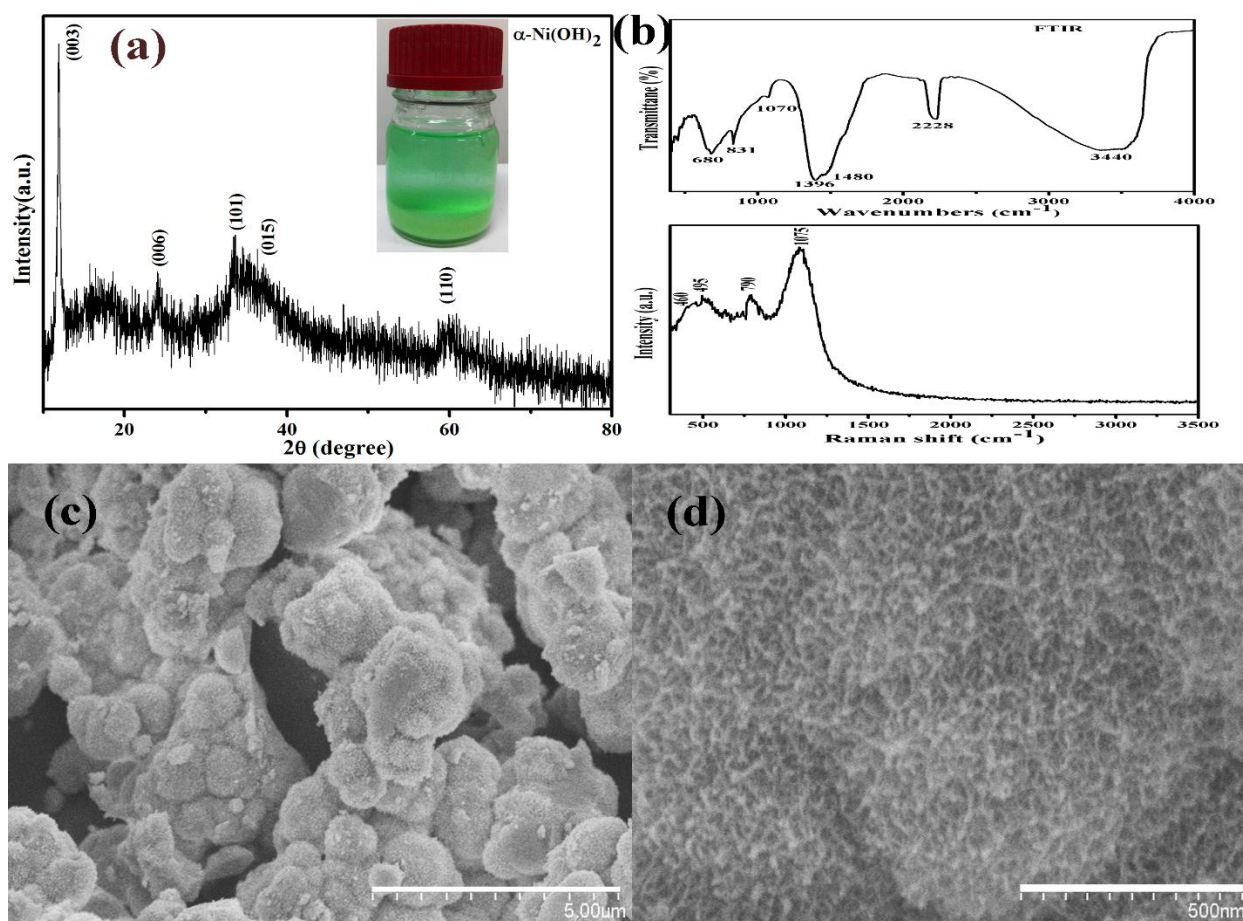
Fig. 3.1 (a) XRD pattern, (b) FTIR and Raman spectrum, (c), (d) FESEM images of α-Ni(OH)$_2$.

Bands appearing at 1070, 831 and 680 cm^{-1} represent the stretching vibrations of C − O bond, bending vibration of C − H bond of poly ethylene glycol and characteristic bending vibration of Ni − OH of α-Ni(OH)$_2$ respectively [25, 28]. Based on the above analysis, it may be stated that turbostatic character gets formed due to intercalation of OCN$^-$ and NO$_3^-$ ions. All four peaks at 460, 495, 790 and 1075 cm^{-1} (shown in Fig.3.1 (b)), appeared in

Raman spectra of the as prepared intermediate product, are ascribed to α-Ni(OH)$_2$ [29]. Appearance of these peaks confirms proper phase formation of α-Ni(OH)$_2$. FESEM images (shown in Fig. 3.1 (c and d)) evidence that structure of the intermediates product consists of large number of α-Ni(OH)$_2$ nanoparticles.

Formation of the structure can be explained as follows: urea decomposes into NH$_3$ that reacts with Ni^{+2} ions to form [Ni(NH$_3$)$_6$]$^{2+}$ complex. Water-soluble PEG, having long flexural chain, acts as 'in-situ' chain for absorbing [Ni(NH$_3$)$_6$]$^{2+}$ ions on its coalescent sites via Coulomb interaction between [Ni(NH$_3$)$_6$]$^{2+}$ and O in the periodic –CH$_2$CH$_2$O– group of PEG. Ordered accumulation of [Ni(NH$_3$)$_6$]$^{2+}$ at various coalescent sites generates one-dimensional colloidal structures of [Ni(NH$_3$)$_6$]$^{2+}$ - PEG complex as given below,

$$(O\text{-}CH_2\text{-}CH_2\text{-}O)_n \ + \ [Ni(NH_3)_6]^{2+} \ \rightarrow \ \text{-}O\text{ –}CH_2\text{- }CH_2\text{-}O\text{-}Ni\text{-}O\text{-}CH_2\text{-}CH_2\text{-}$$
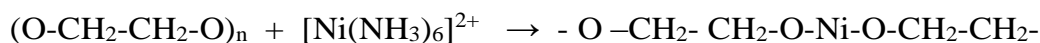
When the complex attains supersaturation limit within the solution, it reacts with OH$^-$ ions and leads to the formation of α-Ni(OH)$_2$. Due to instantaneous accumulation of the α-Ni(OH)$_2$ to share the same 3D crystallographic orientation and subsequent coalescence, loose rod-like structures are formed those act as building block of coral structure and finally aggregate to form desired structure [30].

3.3.2. Transformation of α-Ni(OH)$_2$ to NiO and its activation energy

In order to assess the calcination process of α-Ni(OH)$_2$ into NiO, TG analyses was carried out in N$_2$ atmosphere in the temperature range between 30^{0}C and 600^{0}C at a heating rate of 5^{0}C/min (shown in Fig. 3.2 (a)). Derivative of the percentage of the weight loss is also represented in the inset of Fig. 3.2 (a). Two sharp deeps, found at 100^{0}C and 280^{0}C, in the derivative curve correspond to the multi-step weight losses originating from

dehydration and decomposition of α-Ni(OH)$_2$. Approximately 25% weight loss around 100^{0}C corresponding to endothermic reaction is assigned to the removal of the intercalated and physically adsorbed water. Such high percentage of the weight loss, observed here, imparts high porosity of synthesized samples [28, 31]. Weight loss above 250^{0}C, though derivative maxima occurs at 280^{0}C, is ascribed to the complete catalytic oxidation of reactants including poly ethylene glycol and simultaneous formation of NiO from α-Ni(OH)$_2$ [28]. No significant weight loss at higher temperature (> 400^{0}C) rules out any additional phase formation or structural change of NiO. Therefore we kept our calcination temperature fixed at 400^{0}C. Activation energy (E$_a$), associated with decomposition of α-Ni(OH)$_2$, has been evaluated on the basis of Kissinger's model, [32-34] using TG curves, taken at two other heating rates 10^0 C/min and 20^0 C/min. (shown in Fig. 3.2 (b and c). TG curves and its derivative shift (inset of Fig. 3.2 (b and c)) towards higher temperature within increasing heating rate which is ascribed to the lagging of temperature at the centre compare to temperature at surface due to poor thermal conductivity of α-Ni(OH)$_2$.
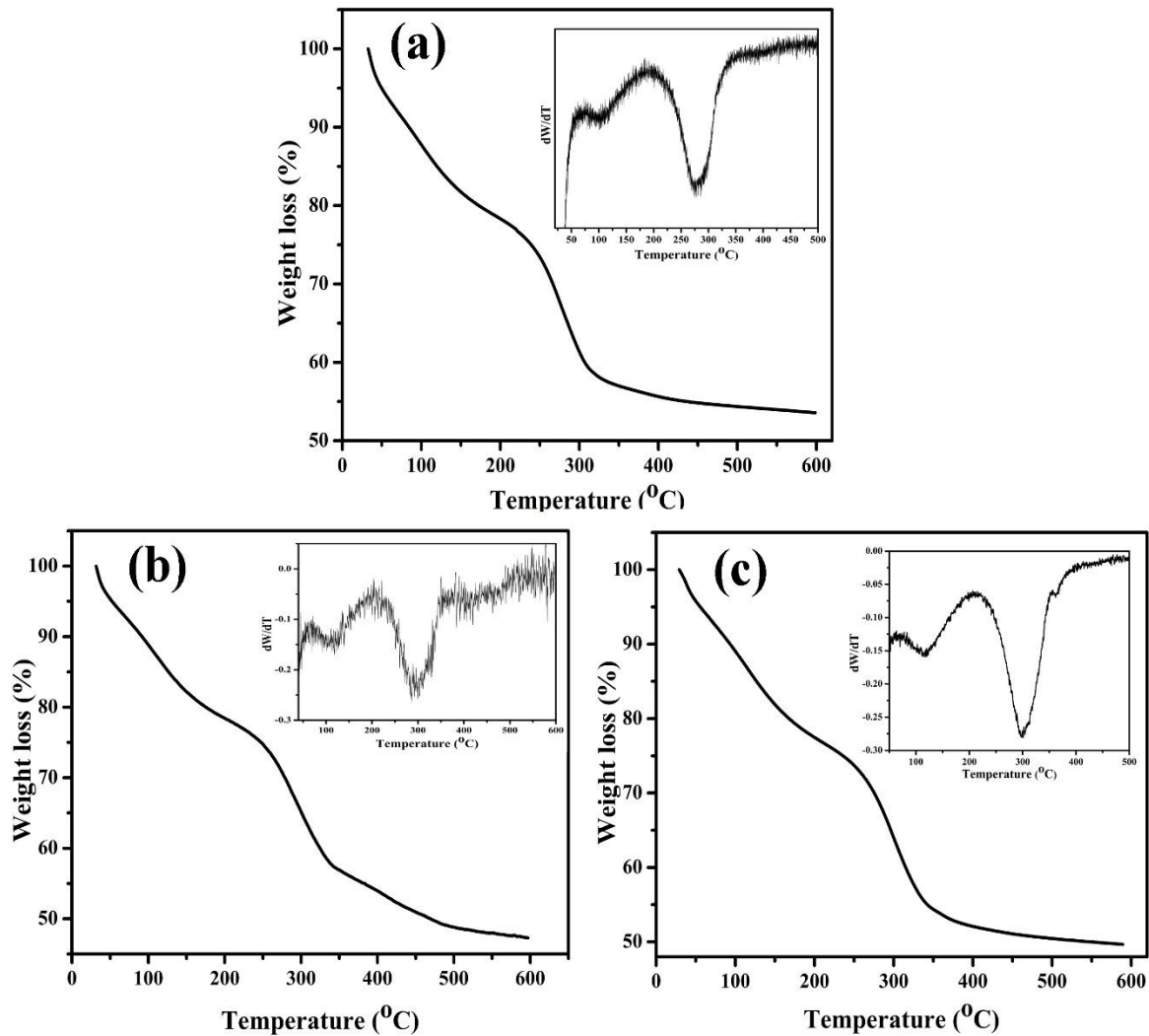
Fig. 3.2 TG and weight loss curves of intermediate product at different heating rate (a) 5, (b) 10 and (c) 20⁰C/min. Inset shows derivative of the weight loss with respect to temperature.

According to Kissinger model, the temperature (T_M) at which maximum weight loss occurs, heating rate (β) and activation energy (E_a) are related by the following relation [33]:

$$\ln \frac{\beta}{T_M^2} = -\frac{E_a}{k_B T_M} + C \qquad\qquad 3.1$$

After determining T_M from the derivative of the TG curve, E_a has been evaluated from slope of the linear plot of $ln\frac{\beta}{T_M^2}$ vs $\frac{1}{T_M}$ and is found to be 1.71 eV.

3.3.3. Investigation of the structure and morphology of NiO nanostructure

To identify proper phase formation and secondary phases (if any), present within the samples, calcined samples were investigated by XRD.
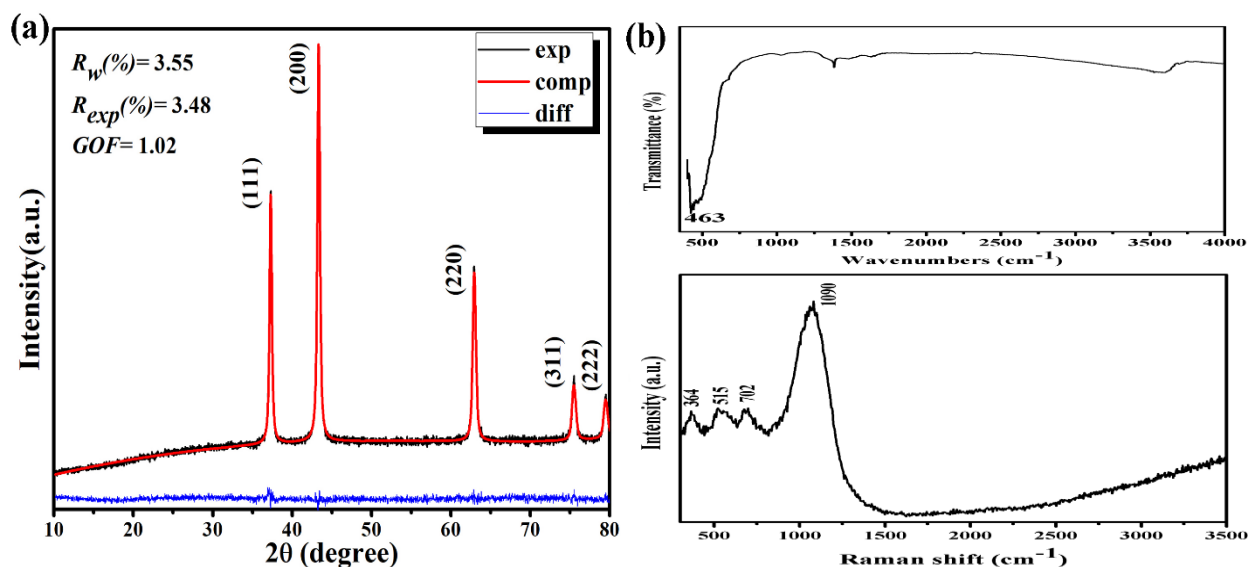
Fig. 3.3 (a) X-ray diffraction pattern and (b) FTIR and Raman spectra of sample S2.

One typical diffraction pattern of the sample S2, represented in Fig. 3.3 (a), is consisting of five diffraction peaks at $2\theta = 37.14°$, $43.18°$, $62.79°$, $75.33°$, $79.34°$, indexed as reflection from (111), (200), (220), (311) and (222) planes corresponding to face centered cubic phase (FCC) of NiO (JCPDS card no. 47-1049). It would be interesting to mention that all diffraction peaks match very well with respective peak positions as well as relative peak intensities. Lattice parameter, obtained by Rietveld refinement (shown in Fig. 3.3 (a)), is found to be a = 4.18Å. Good structure refinement parameters e.g. $R_{wp} = 3.55\%$, $R_{exp} = 3.48\%$ and goodness of fit (GOF) = 1.02 support reliability of the refinement process. Room temperature Raman spectra of NiO (shown in Fig. 3.3 (b)) is consisting of four peaks at 364, 515, 702 and 1090 cm^{-1} that can be assigned to first-order transverse optical (1TO)

and longitudinal optical (1LO) and their second harmonics respectively [35]. Single deep in the FTIR transmittance spectra (shown in Fig. 3 (b)) of NiO, measured at 463 cm^{-1}, is attributed to Ni – O bond [36] and corroborates pure NiO.
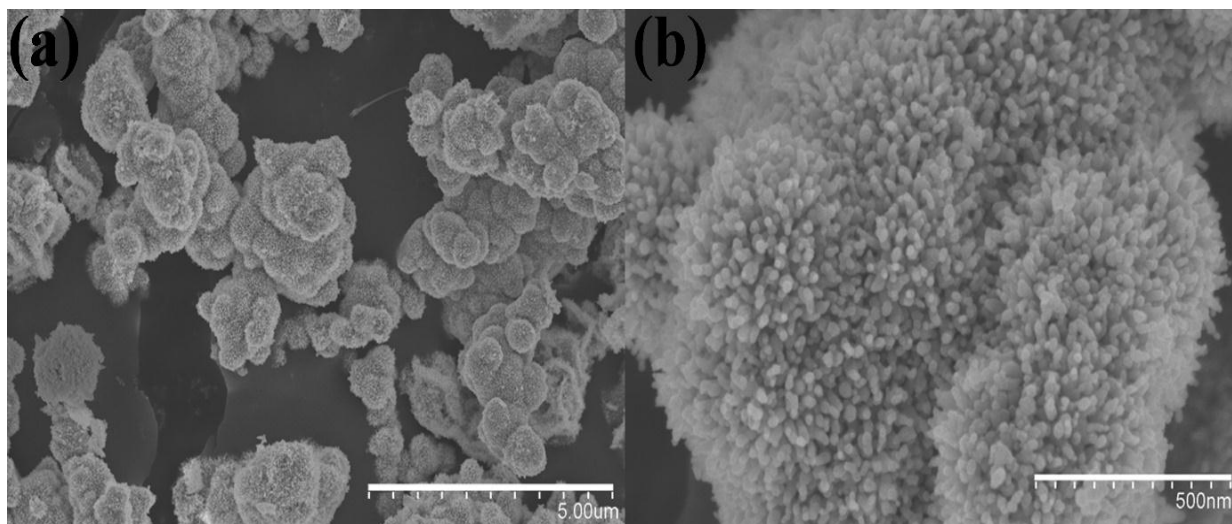
Fig. 3.4 (a) and (b): FESEM images of S2 with low and high magnification images respectively.

Formation of coral – like hierarchical structure (~ 2 – 4 micrometre) is evident from FESEM images of S2 (shown in Fig. 3.4 (a)). High magnification images show that this microstructure gets formed by large number of NiO nanorods with diameter ~ 20 nm and length ~ 50 nm, radiated outwards in all directions (shown in Fig. 3.4 (b)). It has also been noticed that each nanorod is made of nanoparticles having mean diameter ~ 20 nm. It has been examined that NiO, synthesized at lower PEG ratio (sample S1), consists of spherical nanoparticles (shown in Fig. 3.5 (a)), whereas at higher PEG ratio (sample S3), no definite structure gets formed (shown in Fig. 3.5 (b)).
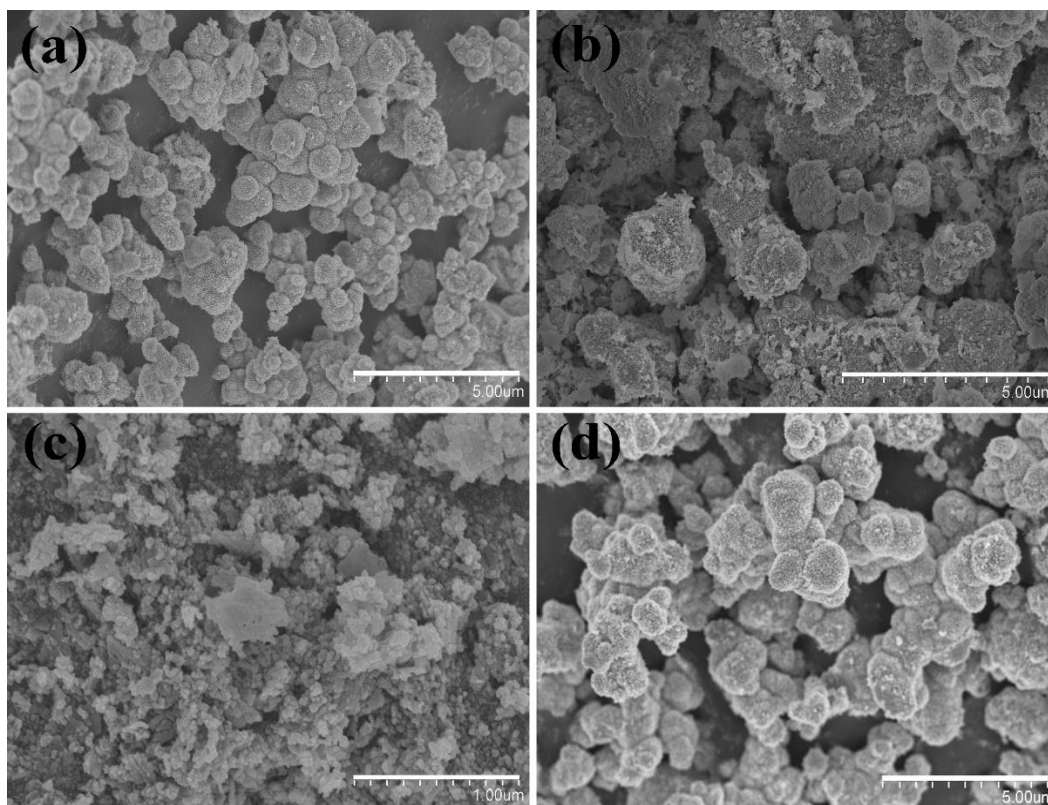
Fig. 3.5 FESEM images of (a) sample S1, (b) sample S3, (c) sample S4 and (d) sample S5.

In addition, it is observed that hydrothermal treatment time also has crucial role on the formation of structure e.g. at higher treatment time nanoparticles (S4) gets formed (shown in Fig. 3.5 (c)), while lower treatment time leads agglomeration (S5, shown in Fig. 3.5 (d)).

Microstructure of S2 has been further clarified by TEM analysis.
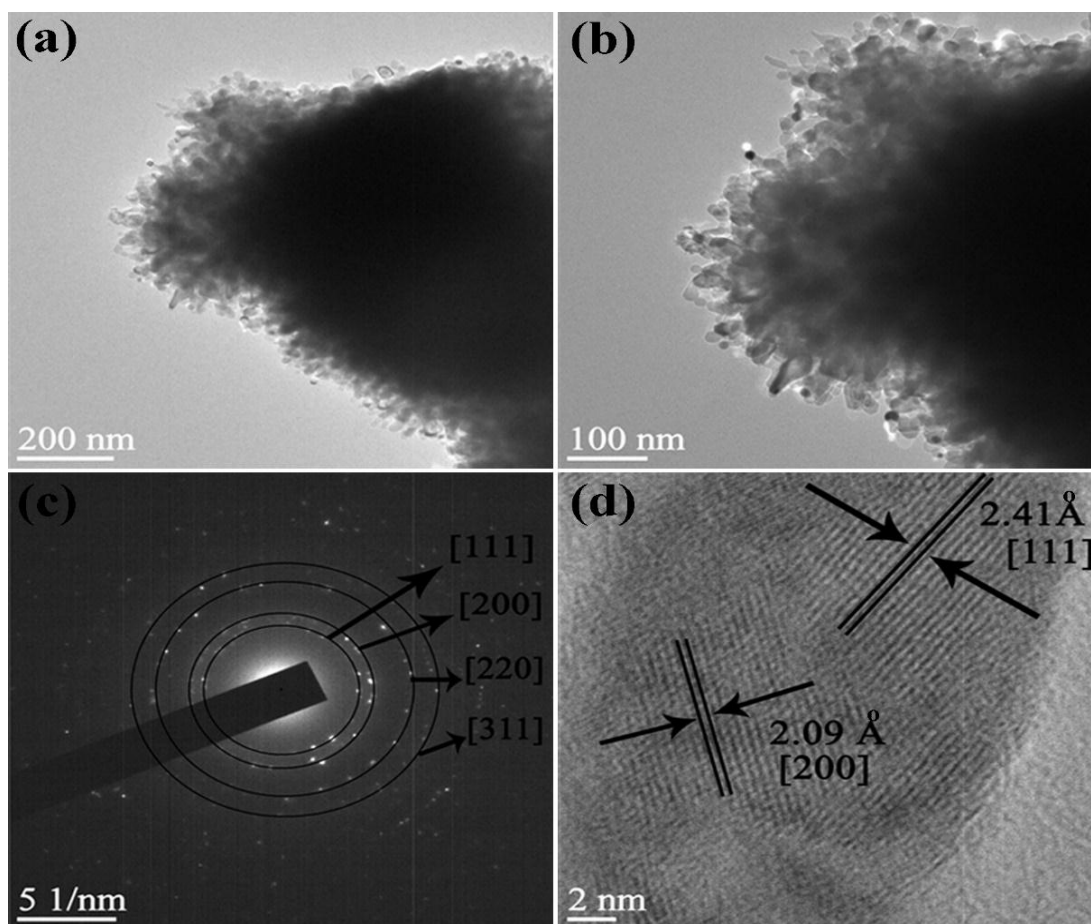
Fig. 3.6 (a) and (b) TEM image, (c): SAED pattern and (d): HRTEM lattice image of S2.

Typical TEM images (shown in Fig. 3.6 (a & b)) manifest abundantly the formation of coral – like microstructure and reveal that the microstructure is indeed made up of distinguishable NiO nanorods with diameter ~ 20 nm and protrude out from the centre. Sharp contrast among dark edges of the nanorods and their faded area illustrates the difference in compactness of the nanorods in central part rather than exterior region of the structure, assigned to difference in electron density (discussed later). TEM images, collected after ultrasonication, are in well agreement with FESEM images, so is may be concluded that the nanorods are very stable against ultrasonication e.g. integrating force between rods is chemical in nature rather than weak van der Waals. Selected area electron

diffraction (SAED) pattern (shown in Fig. 3.6 (c)) is indexed as the diffraction from (111), (200), (220) and (311) planes of cubic phase of NiO, in well agreement with XRD results [37]. High resolution transmission electron microscopic (HRTEM) images (shown in Fig. 3.6 (d)) illustrate lattice spacing ~ 2.09 Å and 2.41 Å corresponding to (200) and (111) planes of NiO nanorods. Therefore, XRD and TEM studies reveal the formation of well-crystalline, phase pure NiO coral – like microstructures.

3.3.4. Determination of electronic structures and defects at the surfaces of NiO nanostructures by x-ray photoelectron and positron annihilation spectroscopy respectively

XPS has been employed to elucidate oxidation states of our synthesized coral-like NiO nanostructures (sample S2). XPS survey scan of the synthesized NiO nanostructures, shown in Fig. 3.7 (a), consists of peaks corresponding to Ni, O and confirms absence of any impurity. Careful analyses of the high resolution XPS spectra of Ni 2p (represented in Fig. 3.7 (b)) reveal that the spectra is consisting of four peaks, measured at 855.6, 861.1, 872.4 and 879.3 eV, and two weak peaks, measured at 853.8 and 865.6 eV. Peaks at 855.6 and 872.4 are attributed to Ni $2p_{3/2}$ and Ni $2P_{1/2}$ respectively of Ni^{2+} while peaks at 861.1 and 879.3 eV represent their satellite peak. In this context, it may be stated that the result is in well agreement with our previous XPS results [38, 39]. Two peaks of relatively low intensity are assigned to Ni $2p_{3/2}$ and Ni $2P_{1/2}$ states of Ni^{3+} [40]. Origin of Ni^{3+} is ascribed to the Ni^{2+} vacancy, described by the following Kröger – Vink equation:

$$Ni_{Ni}^{\times} \rightarrow Ni_{Ni}^{\cdot} + V_{Ni}' \qquad\qquad 3.2$$

High resolution scan of O 1s peak, represented in Fig. 3.7 (c), exhibits one main peak at 529.4 eV, attributed to O bound to Ni^{2+} and a shoulder peak at 531.1 eV which may be assigned to O bound to cations of higher oxidation states *viz.* Ni^{3+} here [41].
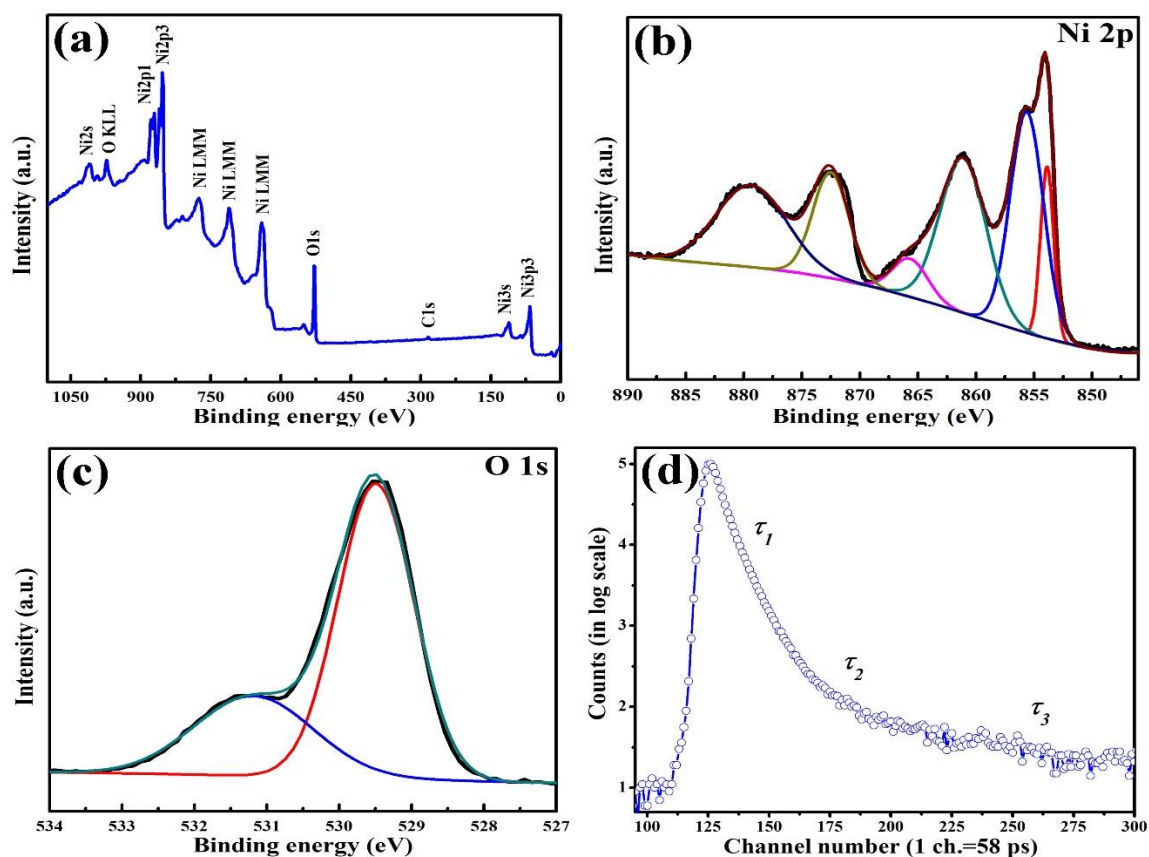
Fig. 3.7 (a) Survey XPS spectra, (b) high resolution XPS spectra of Ni 2p states, (c) high resolution XPS spectra of O 1s and (d) positron lifetime spectrum of S2.

Positron annihilation lifetime spectroscopy (PALS), used widely to investigate cationic vacancies induced defects in bulk as well as nanostructured materials, is adopted here [42, 43]. Qualitative determination of positron annihilation parameters illustrate defect-related processes [44]. The positron lifetime spectrum of the sample S2 is shown in Fig. 3.7 (d). Careful analysis reveals that the spectrum yields three different components of

lifetime (τ_1, τ_2 and τ_3) along with their relative intensities (I_1, I_2 and I_3). The result is summarized in Table – 3.1. Here, we have obtained τ_1 = 188 ps and τ_2 = 375 ps and their relative intensities I_1 = 54.29, I_2 = 44.43 % respectively The presence of longest lifetime τ_3 = 3.09 ns is assigned to the annihilation of orthopositronium atoms (metastable spin triplet-state of the electron and positron), formed within the pores of the coral island [45]. Presently, 'τ_3' is noticed to be significantly less than theoretically predicted lifetime (140 ns) of orthopositronium atom. Such observation is explained on the basis of interaction of the orthopositronium with its surrounding electrons through pickoff process [46]. But, τ_3 for our synthesized sample is found to be very close to that of NiO nanoparticles, measured by S. Das *et al*. [47] indicating that the interaction of orthopositronium with its surroundings is same for NiO coral – like structure and nanoparticle. Pore size (R), calculated from the relation τ_3 = 1.88R – 5.07, is found to be 3.38Å [48]. Pore fraction (f_p), calculated from the relation $f_p = (4/3)\pi R^3 CI_3$, where C = 0.0018 [49], is found to be 37%. In general, 'τ_1' and 'τ_2' are assigned to the annihilation lifetime of positrons, trapped at the mono and di-vacancy defect sites respectively in bulk systems. Penetration depth (α^{-1}) of positron, calculated using the relation $\alpha = 16\frac{\rho}{E^{1.4}}$, where ρ and E represent the density of NiO (in gm/cm^3) and energy of the incident positron (in MeV) respectively [50, 51], is found to be 130 μm which very high than dimension of the nanorods, the constituent of coral – like microstructure sample. Thus, most of the positron would reach to the surface and their corresponding lifetimes are attributed to the trapping and annihilation of positron at the surfaces of the synthesized microstructure [52]. Among different defects states, two leading positron trapping centers are (i) broken and disordered bonds originating from cation vacancy (Ni^{2+} in present case) giving loss of periodicity at the surface and (ii) divacancy

defect cluster [53]. Presently, 'τ_1' is assigned to the annihilation of positron with surface electrons, trapped at Ni monovacancy defect sites residing at the surfaces of the nanostructure [47, 53], while 'τ_2' is ascribed to annihilation process at Ni divacancy defects. It is well known from previous studies that according to the independent particle model for annihilation, lifetime depends inversely on the density of the electrons [54, 55]. In addition, $\tau_2 > \tau_1$ implies that the density of accumulated electron at divacancy sites is less than monovacancy sites. $I_1 > I_2$ reveals that our synthesized sample possesses larger monovacancy defects than divacancy defects. Therefore from TEM, XPS and PALS studies, it may be stated that Ni^{2+} defects mostly reside at the edges of the nanorods and also cause formation of Ni^{3+} states.

Table 3.1 Positron annihilation lifetime parameters of S2.

τ_1 (ns)	τ_2 (ns)	τ_3 (ns)	I_1	I_2	I_3	$\chi 2$
0.1884 ±0.0050	0.3753 ±0.0061	3.0862 ±0.0318	54.2906 ±2.6780	44.4254 ±2.6562	1.2840 ±0.0408	1.04

3.3.5. Magnetic properties of NiO coral – like microstructure

Magnetic properties of the synthesized sample have been measured at various temperatures under DC magnetic field and corresponding susceptibilities ($\chi = M/H$) has been evaluated at zero field cooling (ZFC) and field cooling (FC) conditions in the presence of two different magnetic fields (40 and 100 Oe). During ZFC measurement, the sample was cooled from 300 K to 5 K in the absence of field after then the susceptibility data was recorded during heating cycle in the presence of 40 Oe magnetic fields (named as $\chi_{ZFC,40\ Oe}$, shown in Fig. 3.8 (a). Whereas during the FC measurement the sample was first cooled in

the presence of 40 Oe magnetic field and the susceptibility data was recorded during heating cycle in the presence of same magnetic field. For deep insight, a second set of ZFC – FC data was recorded in the presence of a different magnetic field ~ 100 Oe. Obtained susceptibilities at this field, named as $\chi_{ZFC,100\,Oe}$ and $\chi_{FC,100\,Oe}$ respectively, are also presented in Fig. 3.8 (a). We observed no overlap between ZFC and FC susceptibilities indicating irreversibility of non-equilibrium disordered magnetic state within the whole range of temperature [56] indicating that the irreversible temperature (T_{irr}), which is defined as divergence between ZFC and FC susceptibilities, is greater than 300 K [15, 57].

In contrast to T_{irr} of NiO flower-like microsphere (T_{irr} = 169 K) [14] and nanocube (T_{irr} = 230K) [58], our synthesized sample possesses much higher T_{irr}, similar to that of NiO nanorod [59]. Close inspections reveal that the difference between $\chi_{ZFC,100\,Oe}$ and $\chi_{FC,100\,Oe}$ at 300 K is more compare to the difference between $\chi_{ZFC,40\,Oe}$ and $\chi_{FC,40\,Oe}$ i.e. irreversibility of the magnetic properties of the synthesized significantly depends on applied magnetic field during FC and ZFC cycle. Thus according mean field theory, given by Almeida – Thouless [60-62], this observation may be ascribed to spin glass behaviour rather than superparamagnetic behaviour. Moreover, spin-glass-like behaviour is also supported from significantly different temperature dependence of $\chi_{FC,40\,Oe}$ and $\chi_{FC,100\,Oe}$ compare to $\chi_{ZFC,40\,Oe}$ and $\chi_{ZFC,100\,Oe}$.
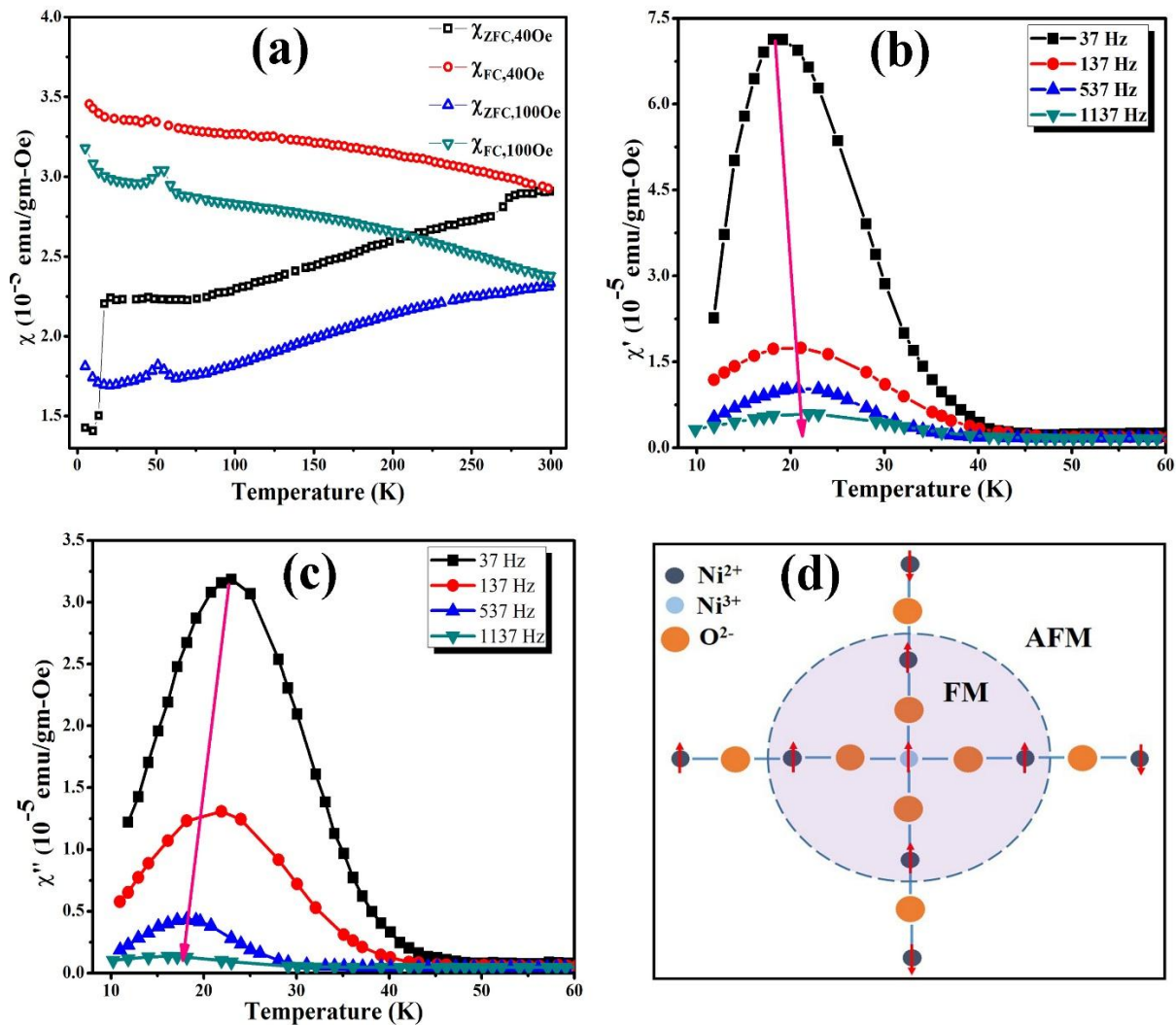
Fig. 3.8. (a) FC and ZFC curves of NiO measured at 40 & 100 Oe, (b) real part of the ac susceptibility, (c) imaginary part of the ac susceptibility of the sample S2, (d) Schematic diagram of the ferromagnetic domain within antiferromagnetic matrix.

Former two monotonically decrease with increasing temperature, whereas later two exhibit opposite trend. Moreover, peaks, appeared at 20 K in $\chi_{ZFC, 40\,Oe}$ and $\chi_{FC, 40\,Oe}$ curves, are attributed to the freezing of uncompensated surface spin [63] and can be explained as follows: in general magnetic property of NiO is described in terms of Stoner – Wohlforth's two sub-lattice model considering ferromagnetic exchange interaction between spins within

(111) plane followed by antiferromagnetic exchange interaction between adjacent (111) plane and each spins within (111) plane is directed along $< 11\overline{2} >$ direction which is easy axis of magnetization. Our previous PALS study (section 3.3.4) revealed that our synthesized sample contains mono- and divacancy Ni^{2+} defects; therefore we propose more than two metastable easy axis of magnetization, induced by these defects. In low temperature region, spins are oriented along these metastable axes, parameterized by different anisotropy energy [64]. During FC - ZFC measurement at 40 Oe, field is not sufficient to flip surface spins against energy barrier, they form local spin cluster. With increasing temperature, surface spin cluster gets randomized due to thermal energy, hence susceptibility gets decreased. During $\chi_{ZFC,100\ Oe}$ and $\chi_{FC,100\ Oe}$ measurements, the applied magnetic field orient local surface spins depending on temperature. Thermal energy causes spin-cluster flipping among metastable directions, hence magnetization gets enhanced. At temperature above 20 K, local spin-cluster gets randomized reducing magnetization. This particular temperature (20 K), defined as surface spin freezing temperature, has been observed at 18 K and 13 K in case NiO nanoflower [65] and nanoparticle [66] respectively. In order confirm spin − glass behaviour of surface spins, we have performed ac susceptibility measurements in between 10 and 60 K at different frequencies (37, 137, 537 and 1137 Hz). Fig. 3.8 (b) and (c) represent temperature dependence of ac susceptibility, including real part ($\chi'(T)$) and imaginary part ($\chi''(T)$) respectively. Peak around 20 K, observed in both $\chi'(T)$ and $\chi''(T)$ curves, confirms spin − glass behaviour that generally originate from non-uniformity of the magnetic domains within the synthesized samples. Here, we propose that non-uniformity is introduced by ferromagnetic $Ni^{3+} - O^{2-} - Ni^{2+}$ double exchange interaction, caused by Ni^{3+} (identified by XPS) while antiferromagnetic

Ni^{2+} – O^{2-} – Ni^{2+} superexchange interaction generally dominates in the defect free region within our synthesized samples. Thus, antiferromagnetic matrix of NiO coexists with some ferromagnetic domain around Ni^{3+} (shown in Fig. 3.8 (d)). Strong frequency dependence of the peak signifies that the ferromagnetic domain interacts strongly with antiferromagnetic matrix [67].

Field dependent magnetization, measured at room temperature, is shown in Fig. 3.9. Inset figure (down) illustrates expanded view of the loop. Importantly, the loop differs completely with respect to NiO nanoflower, nanorods [58, 65]. It is noticeable from figure that present loop gets shifted along the negative H-axis from H = 0 [68] giving ascending (H_c^+) as well as descending (H_c^-) coercive fields negative and signifying net magnetization in the absence of magnetic field. Such shift has also been observed in NiO nano-flower at 110K, not at room temperature [14]. Effective shift (ΔH_c), calculated using the equation $\Delta H_c = (H_c^+ + H_c^-)/2$, is found to be -0.825 kOe [69]. Symmetric hysteresis loop generally appears from inversion symmetry of the magnetocrystalline anisotropic energy barrier. We propose that the shift in hysteresis loop is caused by the absence of inversion symmetry, introduced by two competing magnetic exchange interactions in the presence of Ni^{3+} ions [70]. Briefly, it may be stated that ferromagnetic interaction around Ni^{3+} ions creates an exchange field that strongly interact with antiferromagnetic moments corresponding to Ni^{2+} ions, located near the surfaces of the nanoparticles. Notably, room temperature observation of this shift indicates strong interaction between ferromagnetic and antiferromagnetic moments.
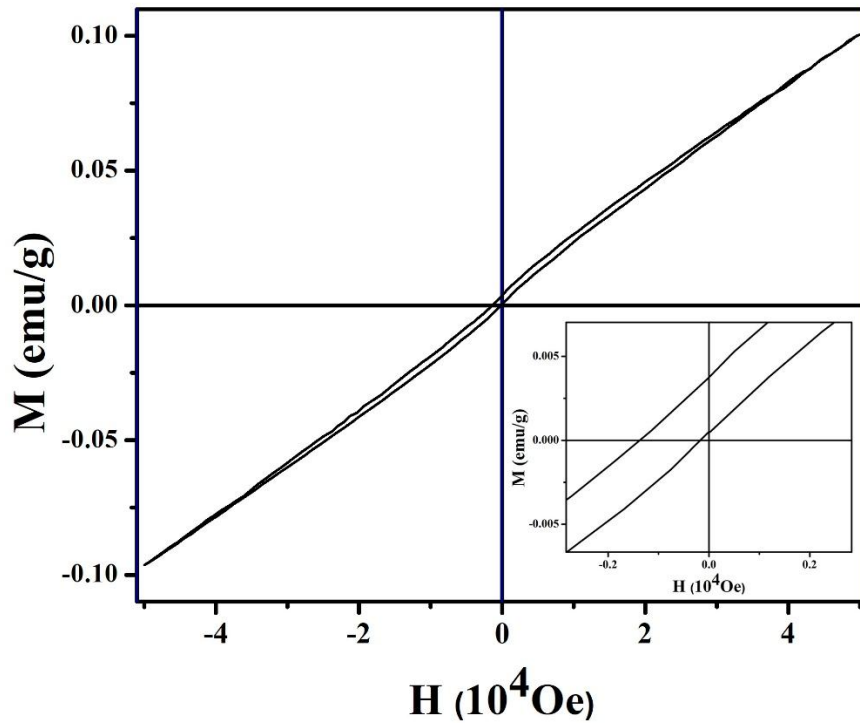
Fig. 3.9. M-H loop of S2, measured at room temperature (inset figure illustrates magnified image showing asymmetric hysteresis near H = 0).

Finite magnetization at H = 0 Oe indicates weak ferromagnetism within the sample. Following the 'law of approach', magnetization curve has been fitted with following equation [71, 72],

$$M = M_{sat}\left[1 - \frac{a}{H} - \frac{b}{H^2}\right] + cH \qquad 3.3$$

where, M_{sat} represents the saturation magnetization, 'a' (= 0.016) and 'b' (= 0.0028) are related to magnetocrystalline anisotropy. Constant 'c' (= 0.56 × 10^{-2} e.m.u./gm-Oe) in the last term corresponds to the linear paramagnetic contribution in the high field region. We have found M_{sat} = 0.002 emu/gm which is very less than M_{sat} of bulk NiO. Such low value of M_{sat} is attributed to magnetically inactive layer [73, 74], while high 'a' (= 160 Oe) and 'b' (= 28 × 10^4 Oe^2) correspond to the highly anisotropy magnetocrystalline anisotropy,

caused by interparticle interaction which in consequence influenced by vacancies. In this context, we have calculated anisotropy energy of the synthesized nanostructure using the following equation [75] and it is found to be 2.50×10^6 erg/cm^3.

$$\text{Anisotropy energy} = \mu_0 M_S \sqrt{\frac{105 \times b}{8}} \qquad 3.4$$

3.4. Conclusion

In summary, coral-like NiO microstructure, constituted by nanorods, has been prepared successfully using water-urea-PEG based hydrothermal methods followed by calcination. The effects of PEG concentration and hydrothermal treatment on the formation of NiO coral-like microstructure have been investigated and it is observed that the desired microstructure gets formed only at an optimized condition. The synthesized structure exhibits high porosity ~ 37% and Ni vacancies at the surfaces. The structure possesses spin-glass behaviour. Interestingly, the synthesized structure exhibits asymmetric hysteresis loop, appeared due to non-inversion nature of the anisotropic, induced by defects. In this context, it is to state that the interparticle interaction, inherent of this particular microstructure via surface defects, is strong enough to give asymmetric hysteresis at room temperature.

3.5. References

1. C. N. R. Rao, *Annual Review of Physical Chemistry*, 1989, **40**, 291-326.

2. H. Steinebach, S. Kannan, L. Rieth and F. Solzbacher, *Sensors and Actuators B: Chemical*, 2010, **151**, 162-168.

3. J. M. Tarascon and M. Armand, *Nature*, 2001, **414**, 359-367.

4. J. H. Pan, Q. Huang, Z. Y. Koh, D. Neo, X. Z. Wang and Q. Wang, *ACS Appl Mater Interfaces*, 2013, **5**, 6292-6299.

5. H. D. Lee, B. Magyari-Kope and Y. Nishi, *Physical Review B*, 2010, **81**, 193202.

6. X. Song and L. Gao, *The Journal of Physical Chemistry C*, 2008, **112**, 15299-15305.

7. Z. P. Wei, M. Arredondo, H. Y. Peng, Z. Zhang, D. L. Guo, G. Z. Xing, Y. F. Li, L. M. Wong, S. J. Wang, N. Valanoor and T. Wu, *ACS Nano*, 2010, **4**, 4785-4791.

8. W. Zhou, M. Yao, L. Guo, Y. Li, J. Li and S. Yang, *Journal of the American Chemical Society*, 2009, **131**, 2959-2964.

9. J. Hu, K. Zhu, L. Chen, H. Yang, Z. Li, A. Suchopar and R. Richards, *Advanced Materials*, 2008, **20**, 267-271.

10. R. Kodama, S. Makhlouf and A. Berkowitz, *Physical Review Letters*, 1997, **79**, 1393-1396.

11. E. Winkler, R. D. Zysler, M. Vasquez Mansilla, D. Fiorani, D. Rinaldi, M. Vasilakaki and K. N. Trohidou, *Nanotechnology*, 2008, **19**, 185702.

12. S. A. Makhlouf, F. T. Parker, F. E. Spada and A. E. Berkowitz, *Journal of Applied Physics*, 1997, **81**, 5561.

13. S. Tiwari and K. Rajeev, *Physical Review B*, 2005, **72**, 104433.

14. Y. Cui, C. Wang, S. Wu, G. Liu, F. Zhang and T. Wang, *CrystEngComm*, 2011, **13**, 4930-4934.

15. M. P. Proenca, C. T. Sousa, A. M. Pereira, P. B. Tavares, J. Ventura, M. Vazquez and J. P. Araujo, *Physical Chemistry Chemical Physics*, 2011, **13**, 9561-9567.

16. http://www.ing.unitn.it/~maud/).

17. H. M. Rietveld, *Acta Crystallographica*, 1967, **22**, 151-152.

18. H. M. Rietveld, *Journal of Applied Crystallography*, 1969, **2**, 65-71.

19. R. A. Young and D. B. Wiles, *Journal of Applied Crystallography*, 1982, **15**, 430-438.

20. L. Lutterotti and P. Scardi, *Journal of Applied Crystallography*, 1990, **23**, 246-252.

21. P. Kirkegaard and M. Eldrup, *Computer Physics Communications*, 1972, **3**, 240-255.

22. H. Wang, J. Gao, Z. Li, Y. Ge, K. Kan and K. Shi, *CrystEngComm*, 2012, **14**, 6843.

23. H. Li, J. Ma, D. G. Evans, T. Zhou, F. Li and X. Duan, *Chemistry of Materials*, 2006, **18**, 4405-4414.

24. X. Ge, C. D. Gu, X. L. Wang and J. P. Tu, *The Journal of Physical Chemistry C*, 2014, **118**, 911-923.

25. F. Yuan, Y. Ni, L. Zhang, S. Yuan and J. Wei, *Journal of Materials Chemistry A*, 2013, **1**, 8438.

26. M. Jobbágy, G. J. d. A. A. Soler-Illia, A. E. Regazzoni and M. A. Blesa, *Chemistry of Materials*, 1998, **10**, 1632-1637.

27. J. W. Lee, J. M. Ko and J.-D. Kim, *The Journal of Physical Chemistry C*, 2011, **115**, 19445-19454.

28. X. Tian, C. Cheng, L. Qian, B. Zheng, H. Yuan, S. Xie, D. Xiao and M. M. F. Choi, *Journal of Materials Chemistry*, 2012, **22**, 8029.

29. Z. Song, L. Chen, J. Hu and R. Richards, *Nanotechnology*, 2009, **20**, 275707.

30. Z. Gui, J. Liu, Z. Wang, L. Song, Y. Hu, W. Fan and D. Chen, *Journal of Physical Chemistry B*, 2005, **109**, 1113-1117.

31. S. K. Meher, P. Justin and G. R. Rao, *ACS Appl Mater Interfaces*, 2011, **3**, 2063-2073.

32. H. E. Kissinger, *Analytical Chemistry*, 1957, **29**, 1702-1706.

33. N. D. Phu, D. T. Ngo, L. H. Hoang, N. H. Luong, N. Chau and N. H. Hai, *Journal of Physics D: Applied Physics*, 2011, **44**, 345002.

34. N. Hoa and M. S. Mahmud, *Journal of the Korean Physical Society*, 2008, **52**.

35. M. Zhou, H. Chai, D. Jia and W. Zhou, *New Journal of Chemistry*, 2014, **38**, 2320-2326.

36. G. George and S. Anandhan, *RSC Advances*, 2014, **4**, 62009-62020.

37. X. Wang, L. Yu, P. Hu and F. Yuan, *Crystal Growth & Design*, 2007, **7**, 2415-2418.

38. C. Ghosh, S. Malkhandi, M. Mitra and K. Chattopadhyay, *Journal of Physics D: Applied Physics*, 2008, **41**, 245113.

39. S. Nandy, U. Maiti, C. Ghosh and K. Chattopadhyay, *Journal of Physics: Condensed Matter*, 2009, **21**, 115804.

40. W. Liu, C. Lu, X. Wang, K. Liang and B. K. Tay, *Journal of Materials Chemistry A*, 2015, **3**, 624-633.

41. G. Zhou, D.-W. Wang, L.-C. Yin, N. Li, F. Li and H.-M. Cheng, *ACS nano*, 2012, **6**, 3214-3223.

42. A. Roychowdhury, S. P. Pati, A. K. Mishra, S. Kumar and D. Das, *Journal of Physics and Chemistry of Solids*, 2013, **74**, 811-818.

43. R. Krause-Rehberg, H. Leipner, T. Abgarjan and A. Polity, *Applied Physics A: Materials Science & Processing*, 1998, **66**, 599-614.

44. T. Ghoshal, S. Biswas, S. Kar, S. Chaudhuri and P. M. Nambissan, *Journal of Chemical Physics*, 2008, **128**, 074702.

45. S. Kar, S. Biswas, S. Chaudhuri and P. M. G. Nambissan, *Nanotechnology*, 2007, **18**, 225606.

46. S. Chakraverty, S. Mitra, K. Mandal, P. Nambissan and S. Chattopadhyay, *Physical Review B*, 2005, **71**, 024115.

47. S. Das, T. Ghoshal and P. M. G. Nambissan, *physica status solidi (c)*, 2009, **6**, 2569-2571.

48. D. Dutta, B. N. Ganguly, D. Gangopadhyay, T. Mukherjee and B. Dutta-Roy, *Journal of Physics: Condensed Matter*, 2002, **14**, 7539.

49. H. Nakanishi, S. Wang and Y. Jean, eds., *Positron annihilation studies of fluids*, World Science, Singapore, 1988.

50. W. Brandt and R. Paulin, *Physical Review B*, 1977, **15**, 2511-2518.

51. R. Nieminen and M. Manninen, *Positrons in imperfect solids: theory*, Springer, 1979.

52. S. Kar, S. Biswas, S. Chaudhuri and P. Nambissan, *Physical Review B*, 2005, **72**, 075338.

53. A. K. Mishra and D. Das, *Materials Science and Engineering: B*, 2010, **171**, 5-10.

54. C. Rauch, I. Makkonen and F. Tuomisto, *Physical Review B*, 2011, **84**, 125201.

55. M. J. Puska, *Journal of Physics: Condensed Matter*, 1991, **3**, 3455-3469.

56. D. Peddis, C. Cannas, A. Musinu and G. Piccaluga, *The Journal of Physical Chemistry C*, 2008, **112**, 5141-5147.

57. A. H. Morrish, *The physical principles of magnetism*, 2001.

58. D.-P. Chen, X.-L. Wang, Y. Du, S. Ni, Z.-B. Chen and X. Liao, *Crystal Growth & Design*, 2012, **12**, 2842-2849.

59. S. Manna, A. K. Deb, J. Jagannath and S. K. De, *The Journal of Physical Chemistry C*, 2008, **112**, 10659-10662.

60. V. Tuboltsev, A. Savin, W. Sakamoto, A. Hieno, T. Yogo and J. Räisänen, *Journal of Materials Chemistry*, 2011, **21**, 781.

61. M. Singh, W. Prellier, M. Singh, R. Katiyar and J. Scott, *Physical Review B*, 2008, **77**, 144403.

62. S. Pati, A. Roychowdhury, S. Kumar and D. Das, *Journal of Applied Physics*, 2013, **113**, 17D708.

63. A. Roychowdhury, S. P. Pati, S. Kumar and D. Das, *Powder Technology*, 2014, **254**, 583-590.

64. W. Duan, S. Lu, Z. Wu and Y. Wang, *The Journal of Physical Chemistry C*, 2012, **116**, 26043-26051.

65. F. Cao, F. Zhang, R. Deng, W. Hu, D. Liu, S. Song and H. Zhang, *CrystEngComm*, 2011, **13**, 4903-4908.

66. S. Rakshit, S. Ghosh, S. Chall, S. S. Mati, S. P. Moulik and S. C. Bhattacharya, *RSC Advances*, 2013, **3**, 19348.

67. C. Zhang, T. Zhang, L. Ge, S. Wang, H. Yuan and S. Feng, *RSC Advances*, 2014, **4**, 50969-50974.

68. X. Sun, N. Frey Huls, A. Sigdel and S. Sun, *Nano Letters*, 2011, **12**, 246-251.

69. Y. Hou and S. Gao, *Journal of Materials Chemistry*, 2003, **13**, 1510.

70. X.-J. Yao, X.-M. He, X.-Y. Song, Q. Ding, Z.-W. Li, W. Zhong, C.-T. Au and Y.-W. Du, *Physical Chemistry Chemical Physics*, 2014, **16**, 6925-6930.

71. S. Mitra, K. Mandal and P. Anil Kumar, *Journal of Magnetism and Magnetic Materials*, 2006, **306**, 254-259.

72. V. Blanco-Gutierrez, J. Gallastegui, P. Bonville, M. a. J. Torralvo-Fernández and R. Saez-Puche, *The Journal of Physical Chemistry C*, 2012, **116**, 24331-24339.

73. R. Kodama, *Journal of Magnetism and Magnetic Materials*, 1999, **200**, 359-372.

74. K. Haneda and A. H. Morrish, *Journal of Applied Physics*, 1988, **63**, 4258.

75. L. Kumar and M. Kar, *Journal of Magnetism and Magnetic Materials*, 2011, **323**, 2042-2048.

Chapter 4

Fractional-dimension approach to tune non-adiabatic interfacial charge transfer and pseudocapacitive properties of NiO

Abstract

4.1. Introduction

4.2. Experimental

4.3. Results and discussion

4.4. Conclusion

4.5. References

Abstract:

In this study, NiO with different morphologies (coral – and flake – like) are successfully synthesized by facile hydrothermal method at 90^0C followed by calcination at 400^0C. Structural and morphological properties of the synthesized samples have been investigated by XRD, FESEM and HRTEM. BET measurement reveals that the synthesized coral – like nanostructure exhibits lower surface area (39.91 m^2/g) compared to flake – like nanostructure (91.38 m^2/g). It has been analyzed from Raman spectroscopy that coral – like nanostructure possesses higher electron – phonon interaction. The observation has been further confirmed from FWHM of the band edge emission spectra of the synthesized nanostructures. It is also analyzed that the electrons in the conduction band get relaxed by LO phonon mode, while electrons at defect sites are relaxed by 2LO phonon mode. Moreover, guided by superoxide generation assay, cyclic voltammetry and electrochemical impedance spectroscopy, we have drawn a conclusion that electron transport across the nanostructure interface is non-adiabatic in nature depending on electron – phonon interaction. We have observed that though coral – like nanostructure possesses less surface area, but it shows higher superoxide generation and better pseudocapative property (C_m ~ 343 and 163 at the scan rate of 2 mV/s for coral and flake – like nanostructure respectively). This phenomena is attributed to phonon assisted non-adiabatic electron transfer across the nanostructure interface and is well explained by Marcus theory of charge transfer. It is also found that the specific capacitance is determined by the lattice polarization effect, caused by electron – phonon interaction. While charging or discharging time, charge transfer resistance are analyzed to be dependent on activation energy for electron transfer across the interface. Fractional dimension of the synthesized nanostructures is found to tune the observed electron – phonon interaction, higher the fractional dimension higher the electron – phonon interaction. This new concept that we have

developed in the present chapter might be helpful to prepare efficient nanostructured photocatalyst and pseudocapacitive electrode materials for better performance.

4.1. Introduction

Due to rapid consumption of the natural energy resource, demand of advanced, cost – effective and environment friendly energy storage devices is growing rapidly to meet society's requirement in the field of various energy sectors like hybrid electric vehicles, space gadgets, memory back-up, mobile etc.[1-3] In this context, different energy storage devices like fuel cell, batteries, electrochemical capacitor have been developed by researchers having their own advantages and disadvantages. Amongst them electrochemical capacitors show potentiality of delivering high power, and depending on charge storing mechanism they are divided into two categories: electric double layer capacitor and pseudocapacitor. Electric double layer capacitors relies on charge storing capacity of carbonaceous electrode materials such as carbon nanotube, graphene, activated carbon etc. and storage ability originates from adsorption of ions at electrode surfaces, governed by diffusion of the ions.[4] Advantages of electric double layer capacitors are the high power density, long life cycle and stability, but they don't possess high value of specific capacitance (C_m).[5] In contrast, pseudocapacitor stores charge at electrode / electrolyte interface on the basis of reversible redox reaction utilizing variable oxidation states of the electrode materials.[6] It has been experimented that pseudocapacitors exhibit higher energy density and C_m compared to electric double layer capacitors. Generally, transitional metal oxides / hydroxides are used as electrode material for pseudocapacititive activity. It has been investigated that C_m of different pseudocapacitors depends on electrolyte and various electrolytes have been investigated in this regards owing to enhance

C_m. [7] Earlier, ruthenium oxide (RuO_2) was found to be a potential electrode material for pseudocapacitor due to its high C_m (~ 760 F/g) in aqueous electrolyte.[8] But, its usage is limited due to toxicity and high cost.[8] After RuO_2, different cost effective transitional metal oxides like MnO_2, NiO, V_2O_5, Co_3O_4 have been examined as replacements of RuO_2 for pseucapacititive electrode materials. Amongst them, NiO particularly has gain interest of researchers for potential electrode material due to its high theoretical value of C_m (2573 F/g within 0.5V,[9] low cost, bio-compatibility, thermal stability.[10] As charge storing capacity of NiO fundamentally includes reduction and oxidation of NiO at an applied potential which in consequence significantly depends on the morphology of NiO nanostructures.[11] As a result, during recent past, shape-controlled synthesis of NiO has emerged as an interesting topic of research owing to find out suitable morphology for industrial application of NiO based pseudocapacitive electrode and vast research has already been carried out in this field. For example, electrochemical studies on NiO hierarchical hollow nanofibers, nanotube arrays, chestnut-like, porous nanospheres like nanostructure revealed C_m ~ 700, 675, 982 and 1010 F g^{-1} respectively.[12-14] Different C_m are generally attributed to different redox reaction rate, surface area, diffusion path length of ions and significantly depends on morphology of the electrode material. It is generally accepted that electrode material with higher surface area exhibits higher C_m.[11] Electrical conductivity of the electrode material is also found to play a crucial role on C_m, since kinetic of the Faradic reaction determining redox reaction gets slowed down by poor conductivity of the electrode material.[15] Among various nanostructures, particularly 1D nanostructured NiO possesses high surface area and superior electrical conductivity those are beneficial for pseudocapacitive property of NiO.[16, 17] In this context, Pang *et al*.

have examined C_m of NiO nanowires of different length scales and have obtained that NiO nanowire with longest length exhibits highest C_m.[18] In order to enhance conductivity of the electrode material, researchers have adopted few strategies like combining NiO with conducting materials such as polyaniline, graphene etc.[19, 20] But in-situ growth of NiO on these materials suffers from incompatibility and stability. NiO nanostructures have also been grown on nickel foam, fluorine doped tin oxide (FTO) glass and they are found to exhibit better electrode material with higher C_m.[21] Though vast research has already been carried out on preudocapacitive activity of NiO, but C_m are found to be far below from theoretically calculated C_m. Thus technical challenges still remain open to researchers for commercial usage of NiO based electrochemical cell and vast researchs are still being carried out by scientists. It is generally accepted mechanism for pseudocapacititive activity that electrons travel towards electrode / electrolyte interface (in case of charging) or away from interface (in case of discharging) to drive Faradic redox reaction at electrode surface followed by electron transfer across the interface. Materials having weak electron – phonon coupling exhibits adiabatic electron transport and transfer across the interface solely depending on effective mass of the electron. But in nanostructured materials where electrons are strongly coupled with phonon, possesses non-adiabatic electron transport process where the electron – phonon interaction plays significant role in electron's conduction. In this context, it may be stated that several researchs have already been carried out on non-adiabatic processes in nanostructured materials in different optoelectronic applications. For example, phonon assisted excitonic transition has been identified in InAs/GaAs quantum dots.[22] The effect of electron – phonon interaction on optical absorption spectra of Si(111) 2×1 surface has been investigated by Ciccacci et al.[23]

Phonon assisted electron transport has been examined by Zhang et al. on n-type [110] silicon nanowire.[24] Very recently, it has been investigated by Ghosh *et al*. that electron – phonon interaction also effects on interfacial electron transfer across semiconductors heterojunction.[25] Non-adiabatic electron dynamics has been theoretically investigated by Hembree *et al*.[26] Though significant researches have already been carried out on pseudocapacitive activity of NiO, but the effect of electron – phonon interaction on this activity has not been carried out. In this chapter, we have investigated the effect of electron – phonon interaction on pseudocapacitive property of NiO nanostructured electrodes. Here, we have also emphasized the dependence of electron – phonon interaction on morphology of the synthesized nanostructures. In this context, we have found that fractional dimension of the nanostructures is crucial for electron – phonon interaction hence pseudocapacititive activity of NiO nanostructures could be tuned by this interaction.

In addition to capacititive property of NiO, researches have also been carried out in recent past on catalytic activity of NiO based heterojunctions. For example, Zahng et al has observed enhanced photocatalytic activity of nanofibers of *p*- type NiO / *n*- type NiO.[27] Photocatalytic activity has also been investigated for NiO / TiO_2 and NiO / Bi_2O_3 junction by Shifu et al.[28] and Hameed et al.[29] respectively. Enhancement in the photocatalytic has also been observed for NiO / Ag heterostructure by us.[30] So, in this context, we have also investigated the effect of electron – phonon interaction on the reactive oxygen species by photogeneration of electron and hole, responsible for photocatalytic activity. This study would also be helpful to understand the dynamics of electron in NiO nanostructured materials that could be useful to optimize morphology of nanostructure for enhanced pseudocapacitive activity and photocatalytic activity.

4.2. Experimental

4.2.1. Synthesis of NiO coral – like nanostructure

Synthesis method for NiO coral – like nanostructure was adopted as described by Pan *et al.*[31] In this typical synthesis procedure for NiO coral – like nanostructure, $Ni(NO_3)_2,6H_2O$ (Merck, India), urea (Merck, India) and polyethylene glycol – 600 (Merck, India) were used as the precursor materials. All the chemicals were of analytical grade and were used without further purification. In this typical synthesis process, 1.57 g of $Ni(NO_3)_2,6H_2O$ and 1.62 g of urea were dissolved into 90 ml of laboratory prepared triple distilled water. The solution was stirred until it turned into homogeneous green colour solution, followed by addition of 1.44 ml poly ethylene glycol – 600. The mixture was transferred into a 100 ml Schott bottle and was subjected to heating at 90^0C for 12 h. After cooling down the bottle at room temperature, the resultant fluffy greenish precipitate, formed during hydrothermal reaction, was collected after centrifugation, followed by repetitive washing with water and ethanol and drying at 60^0C for 10 h. Finally the dried sample was calcined at 400^0C (heating rate 5^0C min^{-1}) for 2 h in open atmosphere to obtain NiO coral – shaped nanostructure.

4.2.2. Synthesis of NiO flake – like nanostructure

In typical synthesis procedure for NiO flake – like nanostructure, 1.57 g of $Ni(NO_3)_2$, $6H_2O$ (Merck, India), 1.57 g of urea (Merck, India) and 0.79 g of hexamethylenetetraanine (Merck, India) were added into 90 ml of laboratory made triple distilled water. After continuous stirring at room temperature for 1 h, the mixture turned into greenish solution, and then it got transferred into 100 ml Schott Duran bottle and was kept in a hot air oven, maintained at 90^0C. After 6 h of reaction, dense light – green precipitate was obtained that

was filtered, followed by repeatative washing with water and ethanol. Precipitate was heated at 60^0C for 10 h for drying; finally the dried powder was heated at 400^0C (heating rate 5^0C min^{-1}) for 2 h in open atmosphere.

4.2.3.   Characterization

Morphological analysis of the as-prepared samples had been carried out by field emission scanning electron microscopy (FESEM) on S4800 microscope and transmission electron microscopy (TEM) on JEOL microscope. To confirm the proper phase formation and to identify purity of the synthesized samples, they were characterized by x-ray diffraction on Rigaku Ultima III, Japan powder diffractometer equipped with CuK_α radiation ($\lambda = 1.5404$ Å). Rietveld powder structure refinement analysis using the JAVA based software program MAUD was adopted to obtain the structural and microstructural refinement parameters through a least-square method.[32-36] The experimental profiles were fitted with the most suitable pseudo-Voigt[35] analytical function with asymmetry and the background of each pattern was fitted with fourth order polynomial function. Nitrogen adsorption−desorption experiments were carried out at 77K in conventional equipment (ASIQ MP, Quantachrome, USA). Surface area was evaluated from this experiment by adopting the well-known Brunauer−Emmet−Teller (BET) method within the relative pressure (P/P$_0$) range of 0.05−0.20. In addition, the pore size distribution was calculated from the volume of adsorbed nitrogen at the relative pressure (P/Po) of 0.99 using Barret−Joyner−Halenda (BJH) method. Raman spectra was recorded on alpha 300, Witec (laser excitation wavelength 530 nm, power 3 mW and spot size: 2 μm). Zeta analyser (Zetasizer NS Nano) was used to measure the surface potential of the synthesized nanocomposites. Optical properties of the synthesized samples was examined by JASCO

V650 spectrophotometer, whereas room temperature photoluminescence (PL) spectra of the synthesized nanostructures were taken by JASCO – S8200 spectrofluorometer.

4.2.4. Reactive oxygen species detection assay

Superoxide (O_2^-) as reactive oxygen species (ROS), generated by photoexcited electrons, was estimated by nitroblue tetrazolium dye (98%, Sigma-Aldrich) degradation method.[37] Nitroblue tetrazolium dye reacts with O_2^- to form purple coloured mono-formazone and di-formazone. Absorption maxima of nitroblue tetrazolium, measured at 259 nm, gets reduced in the presence of O_2^-, thus the absorption maxima was used to monitor the formation of O_2^-. Aqueous suspension of the synthesized nanostructures (120 mg L^{-1}) was incorporated into 1mM of nitroblue tetrazolium dye solution and the mixture was stirred by a magnetic stirrer for proper homogenization under UV irradiation (Phillips, 36W, wavelength ~ 285 nm) to monitor generation of O_2^-. 3ml aliquots, after centrifugation and filtration, were withdrawn at regular interval of time and the absorbance spectrum of the filtrate was recorded by UV-Vis spectrophotometer (JASCO 650) to monitor the degradation process.

Generation of hydroxyl radical ($^.OH$) as another ROS by the synthesized nanostructures was estimated by fluorescence spectroscopy using terepthalic acid ($C_8H_6O_4$, 98%, Sigma-Aldrich) as probe material.[38] In this typical assay, $^.OH$ reacts with TA terepthalic acid to form 2-hydroxy-terepthalic acid that exhibits characteristic fluorescence peak at 425 nm at an excitation wavelength of 312 nm and luminescence intensity carries a direct measurement of $^.OH$ generation.[37] Here, 2mM terepthalic acid was added dropwise into aqueous suspension of as prepared NiO nanostructures (120 mg L^{-1}) followed by stirring for proper homonization. Then 5mL aliquot, after centrifugation and filtration by membrane filter, was taken at regular interval of time and fluorescence spectrum was recorded by fluorescence spectrophotometer (Spectramax M5).

4.2.5.   Preparation of electrode and electrochemical measurement

Electrochemical performances of the NiO coral –like and flake – like nanostructures were evaluated using three electrode system at ambient condition. Briefly, working electrode gets constituted by mixing the as synthesized nanostructures as active materials, graphite powder as the conducting material and polyvinylidene fluoride as the binder with mass ratio of 85:10:5 and dissolved in N-methyl-2-pyrrolidone to form slurry. Working electrodes were prepared by the process of drop casting of the slurry onto the teflon coated graphite electrode, followed by drying in vacuum at 60^0C for 6 hours. Electrochemical studies were carried out with a CS313 multi-channel electrochemical workstation at room temperature using the traditional three-electrode system with graphite electrodes, coated with synthesized electroactive materials as working electrode, Ag/AgCl in 1M saturated KCl solution as reference electrode and Pt-sheet (1 cm × 1cm) as counter electrode. Weight of the electroactive materials loaded on the graphite electrode was maintained between 1.0 - 2.0 mg for better performance. Cyclic voltammetry (CV), electrochemical impedance spectroscopy (EIS) and galvanostatic charging – discharging (GCD) of the synthesized materials were evaluated in 3.0 M KCl solution as an electrolyte with different scan rates 2mV/s to75 mV/s in a potential window ranging from -0.2 to +1.1 V with respect to reference electrode. EIS measurements of the working electrodes were carried out in the frequency range between 100 KHz and 0.1 Hz with AC voltage of 10 mV.

4.3.   Results and discussion

4.3.1. Investigation of microstructural, structural and surface area of the synthesized samples by FESEM, TEM, XRD and BET

Structural characteristics of the synthesized nanostructures have been investigated by FESEM and TEM images. As illustrated in FESEM image, shown in Fig. 4.1(a),

morphology of the 3D coral – like nanostructure consists of large number of interconnected blooming nanorods. High magnification image (shown in Fig. 4.1(b)) shows that these nanorods are composed of nanoparticles. Distribution of the length of the nanorod and size of the nanoparticles as presented in Fig. 4.1 (c) illustrate length ~ 80 nm and size ~ 18 nm. It is noticed from FESEM images of flake – like morphology (shown in Fig. 4.1(d)) that the synthesized sample consists of several interconnected nanosheets having many open porous channels. Formation of pores within the nanosheets are ascribed to evaporation of water molecules, hexamethylenetetraanine and decomposition of chemically bonded groups within the synthesized nanostructure. It is noticed from FESEM images that edges of the nanosheets are common and are interconnected. High magnification image (shown in Fig. 4.2 (e)) shows that the nanosheets exhibit average thickness ~ 33 nm and its distribution is presented Fig. 4.2 (f).

Microstructure and complementary information of the synthesized nanostructures have been clarified further by TEM analysis. Fig. 4.2 (a) shows the typical TEM images of the as prepared coral – like NiO. Images manifest abundantly the formation of nanorods and reveal that the microstructures are indeed made up of distinguishable NiO nanorods having diameter and protrude out from the centre. The sharp contrast among the dark edges of the nanorods and their faded area illustrates the difference in the compactness of the nanorods in the central part rather than exterior region of the assembled structure. TEM images are found to be in well agreement with the FESEM images.
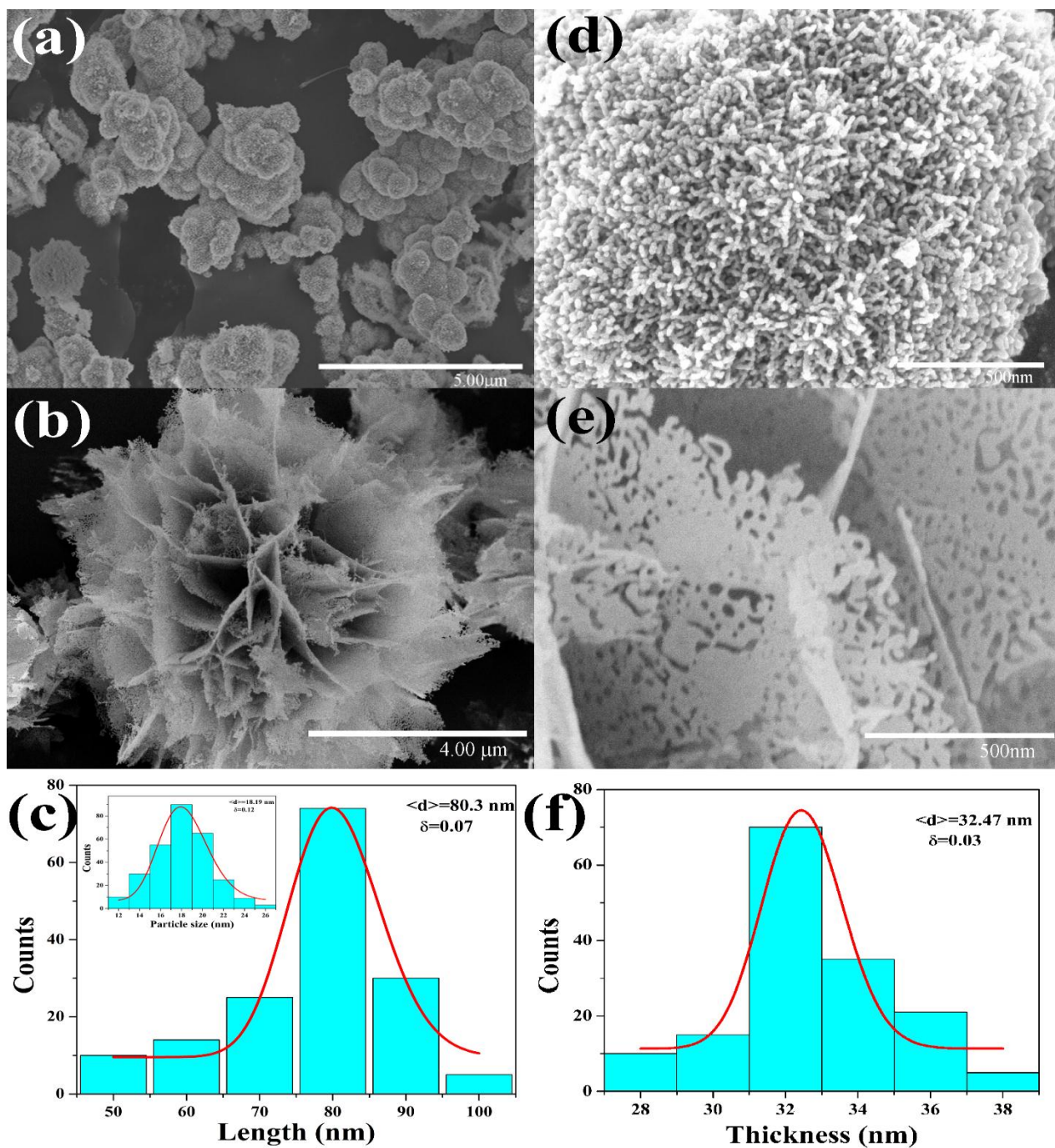
Fig. 4.1 (a , b): FESEM images of coral – like nanostructure, (c): distribution of the length of the nanorods, inset figure shows size distribution of nanoparticles, (d, e): FESEM images of flake – like nanostructure, (f): size distribution of width of the sheets in flake – like nanostructure.
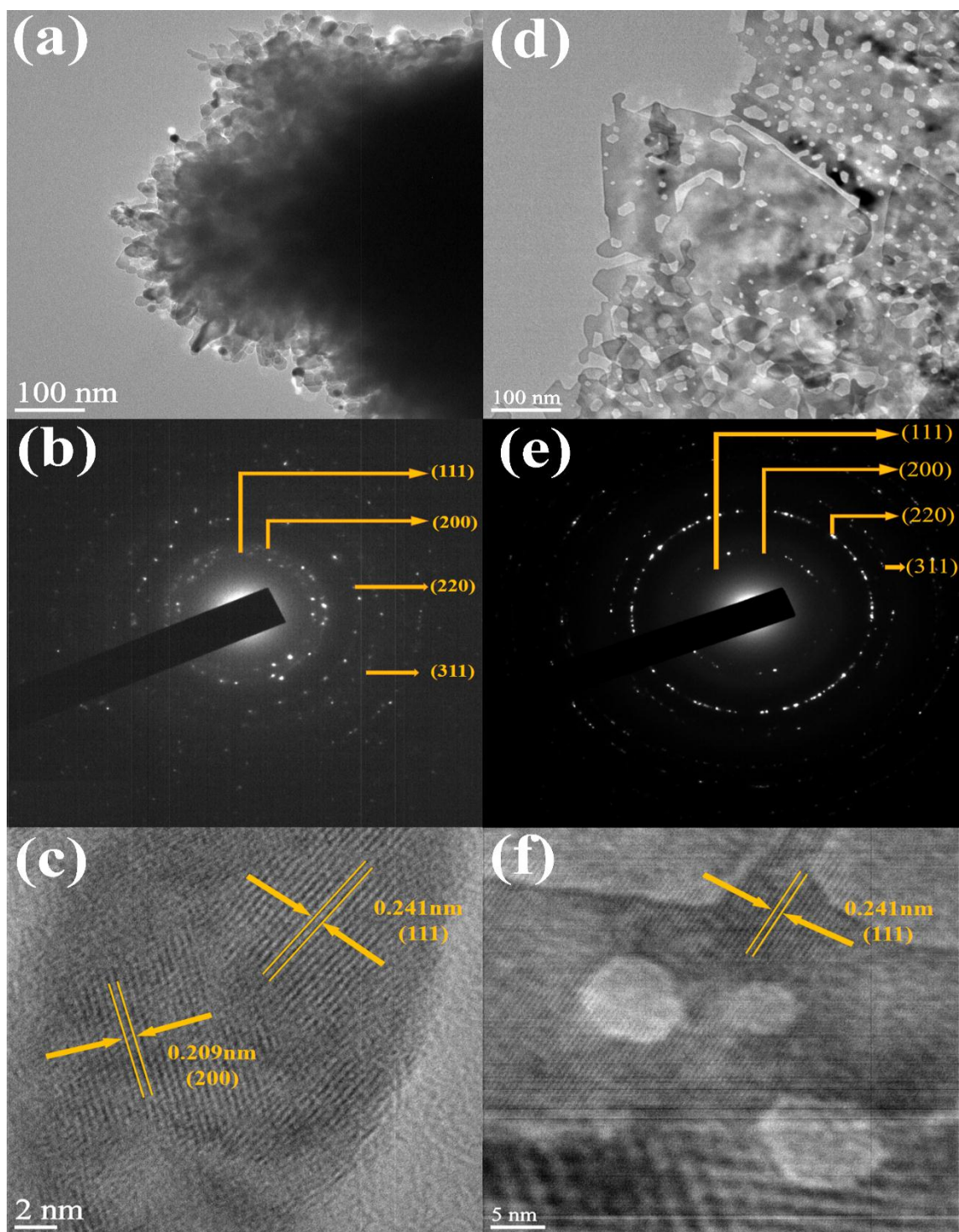
Fig. 4.2 (a): TEM image, (b): SAED pattern, (c): lattice fringe of the coral – like nanostructure, (d): TEM image, (e) SAED pattern and (f) lattice fringes of the flake – like nanostructure.

In order to investigate crystallinity of the as-prepared NiO nanorod assembly further, we have also taken selected area electron diffraction (SAED) pattern of the synthesized samples (illustrated in Fig. 4.2 (b)). The pattern can readily be indexed as the diffraction from (111), (200), (220) and (311) planes of cubic phase of NiO. To get more crystallographic information about the constituent nanorods, high resolution transmission electron microscopic (HRTEM) images were taken (shown in Fig. 4.2 (c)). The lattice fringe, measured to be 2.09 Å and 2.41 Å, correspond to the interplanar spacing between adjacent (200) and (111) crystallographic planes of NiO nanorods. It is evident from HRTEM images of the flake – like NiO nanostructure (shown in Fig. 4.2 (d)) that the as-prepared sample possesses irregular pores, generated by the evacuation of gaseous ingredients. SAED pattern, illustrated in Fig. 4.2 (e), confirms the polycrystalline nature of the synthesized nanosheets and corresponds to (111), (200), (220) and (311) planes of cubic phase of NiO. Lattice fringe, represented in the Fig. 4.2 (f), is found to be 2.41Å that corresponds to (111) plane.

To confirm phase purity, synthesized samples were characterized by x-ray diffractometer. Diffraction patterns of the samples, shown in Fig. 4.3 (a and b), consist of five diffraction peaks centered at 2θ = 37.14°, 43.18°, 62.79°, 75.33°, 79.34° and can readily be indexed as (111), (200), (220), (311) and (222) planes of face centered cubic phase of NiO (JCPDS card no. 47-1049). Interplanar spacings, measured from x-ray diffraction, are in well agreement with interplanar spacing, calculated from transmission electron microscope. In order to gain insight into any change in crystal structure of NiO, diffraction patterns were analysed by Rietveld refinement using space group of *Fm3m* considering basic structure of NiO from JCPDS for initial fitting parameters. Structure

refinement data converged to final R-factors $R_{wp} = 3.53\%$; $R_{exp} = 3.49\%$ for coral – like nanostructure and flake – like nanostructure they are found to be 4.84% and 4.49% respectively. Goodness of fit (GOF) = 1.01 and 1.07 for coral – and flake – like nanostructures respectively are calculated. Small value of GOF indicates reliability of the refinement process and confirms phase purity of the as prepared NiO. Broader diffraction pattern, observed in flake – like nanostructure, is an indicative of smaller crystallite size (~ 25.8 nm) compare to coral – like nanostructures (~ 43.7 nm). The value of lattice parameter, obtained for both samples, is found to be 4.18 Å, very close to the reported value for bulk NiO (4.176 Å) [39] while average O – Ni – O bond angle is found to be 90.0^0 for both of them. It is to be noted that average Ni – O bond length is higher for our synthesized samples compare to Ni – O bond length (2.09 Å), measured by Rinaldi-Montes et al (2.07 Å).[39]
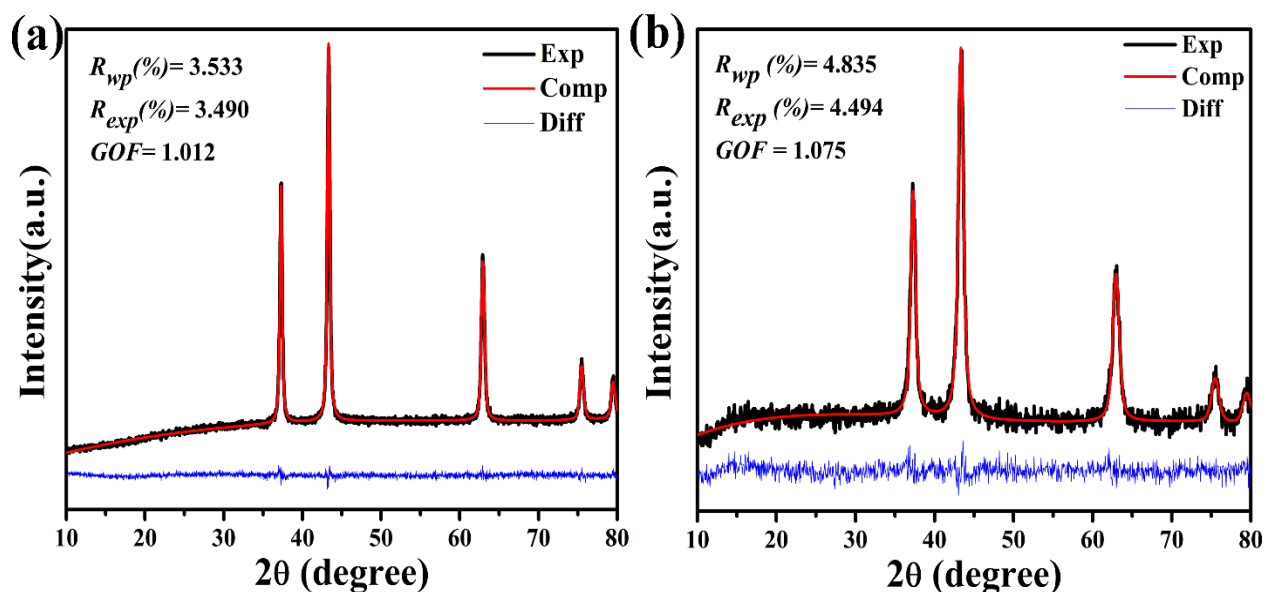
Fig. 4.3 X-ray diffraction pattern of (a) coral – like and (b) flake – like nanostructure.
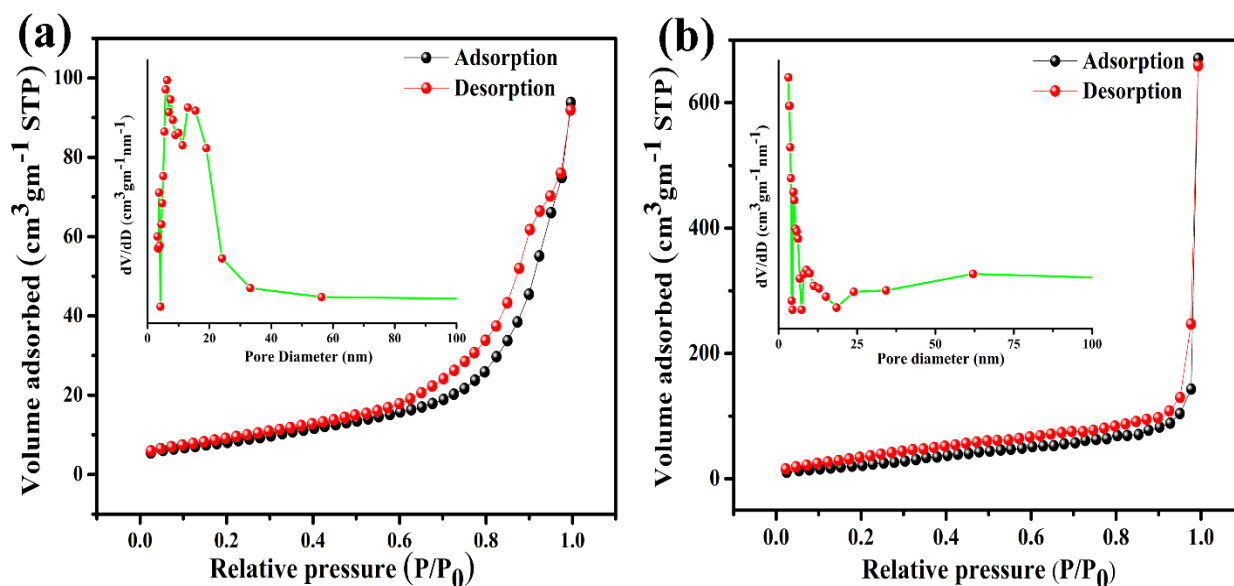
Fig. 4.4 Nitrogen adsorption – desorption isotherms (with BJH pore size distributions plots in the inset) measured at 77K for (a) coral – like and (b) flake – like NiO nanostructures.

Brunauer-Emmett-Teller (BET) and Barrett-Joyner-Halenda (BJH) methods have been employed to measure surface area and pore size distribution of the synthesized nanostructures from N_2 adsorption and desorption isotherms. As revealed in Fig. 4.4 (a and b), specific surface areas of coral – and flake – shaped nanostructure, obtained by fitting the isotherm with BET model, are found to be 39.9 and 91.4 m^2g^{-1} respectively. Higher surface is generally attributed to the two dimensional nature of the flake – like nanostructure. Adsorption – desorption curve possesses typical hysteresis nature of porous structure. Pore sizes, calculated from desorption - isotherm using BJH method, are found to be in the range 10 – 30 and 8 – 20 nm, whereas average pore diameters are ~ 6.23 and 3.11 nm for coral and flake – shaped nanostructure respectively (shown in the inset of Fig. 4.4 (a and b) respectively).

4.3.2. Investigation of electron – phonon interaction within the synthesized nanostructures by Raman spectroscopy and luminescence spectroscopy
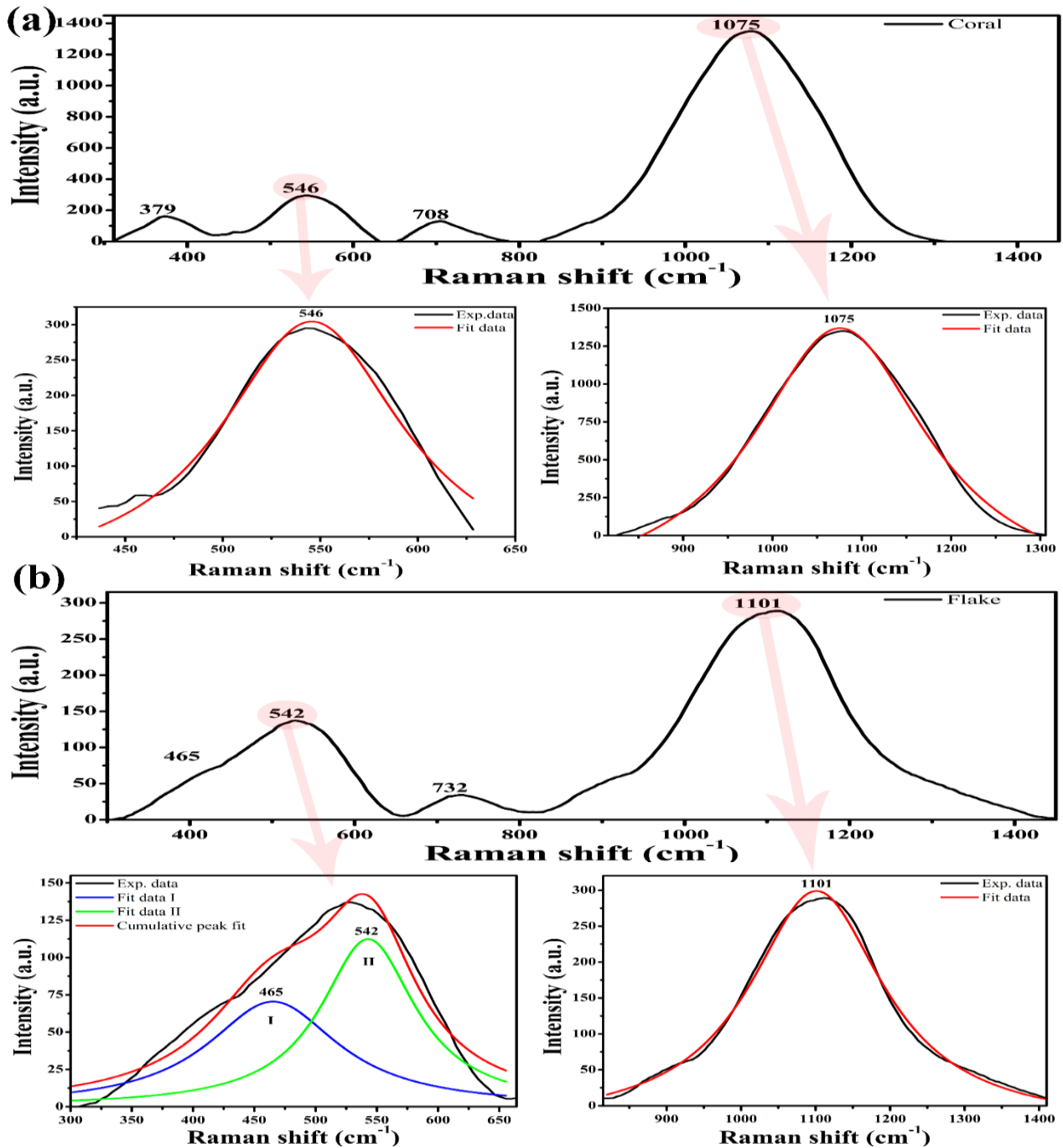
Fig. 4.5 Raman spectra of (a) coral – like and (b) flake – like NiO nanostructures.

Raman spectra of coral – shaped sample consists of four peaks (shown in Fig. 4.5 (a)), located at 379, 546, 708 and 1075 cm⁻¹, are assigned to transverse optical one-phonon (1TO), longitudinal optical one –phonon (1LO), transverse optical two-phonon (2TO) and longitudinal optical two-phonon (2LO) mode of vibration.[40-42] These peaks are noticed at 465, 542, 732 and 1101 cm⁻¹ respectively for flake – like nanostructure (shown in Fig. 4.5 (b)). It is well-known that phonon eigenstates of an ideal crystal possesses plane wave – like nature due to its infinite correlation length, thus k = 0 momentum selection rule needs to be satisfied for the first order Raman scattering as it gets transformed according to Γ_4^- in cubic phase.[43, 44] In the case of finite sized nanostructure, this rule gets relaxed due to parity – breaking imperfections originating from disorder, introduced by defects or scattering from extended region other than Brillouin zone center, ascribed to translational breaking symmetry within nanostructure[45] and it has been investigated that the first order phonon scattering occurs at wave vector $|k| = |k'| \pm 2\pi/L$, where k' and L represent the wave vector of the incident light and crystal size respectively. Thus the appearance of LO and TO mode is ascribed to the finite size of the system. Cross section (σ_n) of nth order Raman scattering is generally written as:[46]

$$\sigma_n(\omega) = \mu^4 \left| \sum_{i=0}^{\infty} \frac{\langle n|i\rangle\langle i|0\rangle}{E_0 + n\hbar\omega_{LO\ (TO)} - \hbar\omega + i\hbar\Gamma} \right|^2 \exp(-\frac{i\hbar\omega_{LO\ (TO)}}{k_B T}) \qquad 4.1$$

From this equation it could be stated that scattering cross section, hence intensity, decreases for higher order Raman scattering[46] as observed for TO scattering. But opposite trend is noticed for LO phonon scattering indicating either strong electron – LO phonon interaction in the synthesized samples or difference in deformation potential. In our present study, it is noticed that LO and 2LO modes exhibit much higher intensity in both samples compared to TO and 2TO modes indicating much higher scattering cross-section for TO and 2TO mode. And off course, no

difference has been found in crystal structure parameters as analyzed by Rietveld indicating no significant difference in deformation potential within the synthesized nanostructures. Therefore it may be stated that the electron – LO interaction, generated by long range macroscopic electric field, is prominent in the synthesized nanostructures rather than electron – lattice deformation interaction. In this context, we have measured zeta potential -14.7 mV and -13.2 mV for coral – and flake – like nanostructure respectively (shown in Fig. 4.6).
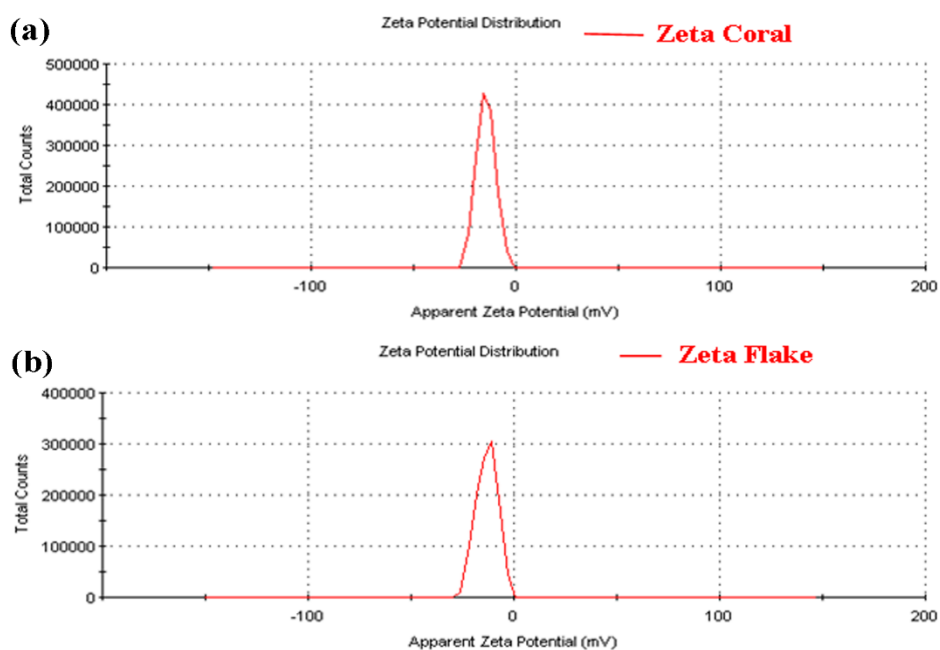
Fig. 4.6 Zeta potential for (a) coral-like and (b) flake-like nanostructure.

Thus higher intensity corresponding to LO and 2LO scattering is attributed to higher electron – LO phonon interaction due to electric field, generated by the localized electrons at the surfaces of synthesized nanostructures.[47-49] In this comparative study, we have kept all experimental parameters like laser wavelength, power, spot size etc. same for all Raman scattering experiment.[50] In this context, we have calculated intensity ratio of 2LO and LO scattering modes (I_{2LO}/I_{LO}) signifying electron – LO phonon interaction within Franck – Condon approximation.[51, 52] These ratios are found to be 9.2 and 4.3 for coral and flake – like nanostructure indicating

higher charge carrier – LO phonon interaction in coral – like nanostructure than flake – like nanostructure.

In order to quantify charge carrier – LO phonon interaction from optical property, we have examined luminescence property of synthesized nanostructures. In this context it may be stated that two bands (361 and 392 nm) in the UV region due to near band edge emission, two bands (436 and 467 nm) in visible region due to surface oxygen vacancy and green emission (560 nm) is assigned to cationic vacancy, interstitial oxygen trapping etc. as observed in NiO nanostructures previously by researchers including us.[30, 53] Qi *et al*. reveals that luminescence spectrum of NiO nanostructure is consisting of two peaks at 391 and 467 nm due to band edge and vacancy sites respectively.[54] Activation energy and lifetime corresponding to these transitions were examined by Guerra *et al*.[55] Interestingly in case of NiO nanowire, a strong orange peak at 660 nm and a relatively weak red peak at 680 nm have been identified by Lee et al., while no band edge emission has been found.[56]

In contrast to them, two emission peaks in the UV region, measured at ~ 336.1 and 358.6 nm for coral – and at ~ 333.5 and 355.2 nm for flake – like nanostructure, have been observed (shown in Fig. 4.7 (a and b)). Former emission is assigned to band edge emission spectrum, whereas later one is attributed to emission, related with surface localized electrons.[53] It has been investigated by many researchers including us that full width at half maxima (FWHM) of the emission spectrum primarily depends on charge carrier – phonon interaction, higher the interaction higher is the FWHM. Careful analysis of the spectrum reveals that band edge emission exhibits FWHM ~ 0.48 and 0.45 eV for band edge emission and 0.66 and 0.64 eV for surface defect related electronic transitions in case of coral – and flake – like nanostructures respectively. Therefore higher FWHM in case of coral – like nanostructure indicates higher charge carrier – phonon

interaction supporting Raman study. In this context, charge carrier – phonon interaction which is characterized by Huang – Rhys 'S – factor' relating FWHM of emission spectra with phonon frequency ($\hbar\omega_{LO}$) [30, 57] by the following relation has been calculated:

$$\text{FWHM} = 2\hbar\omega_{LO/2LO}\sqrt{2S} \qquad\qquad 4.2$$
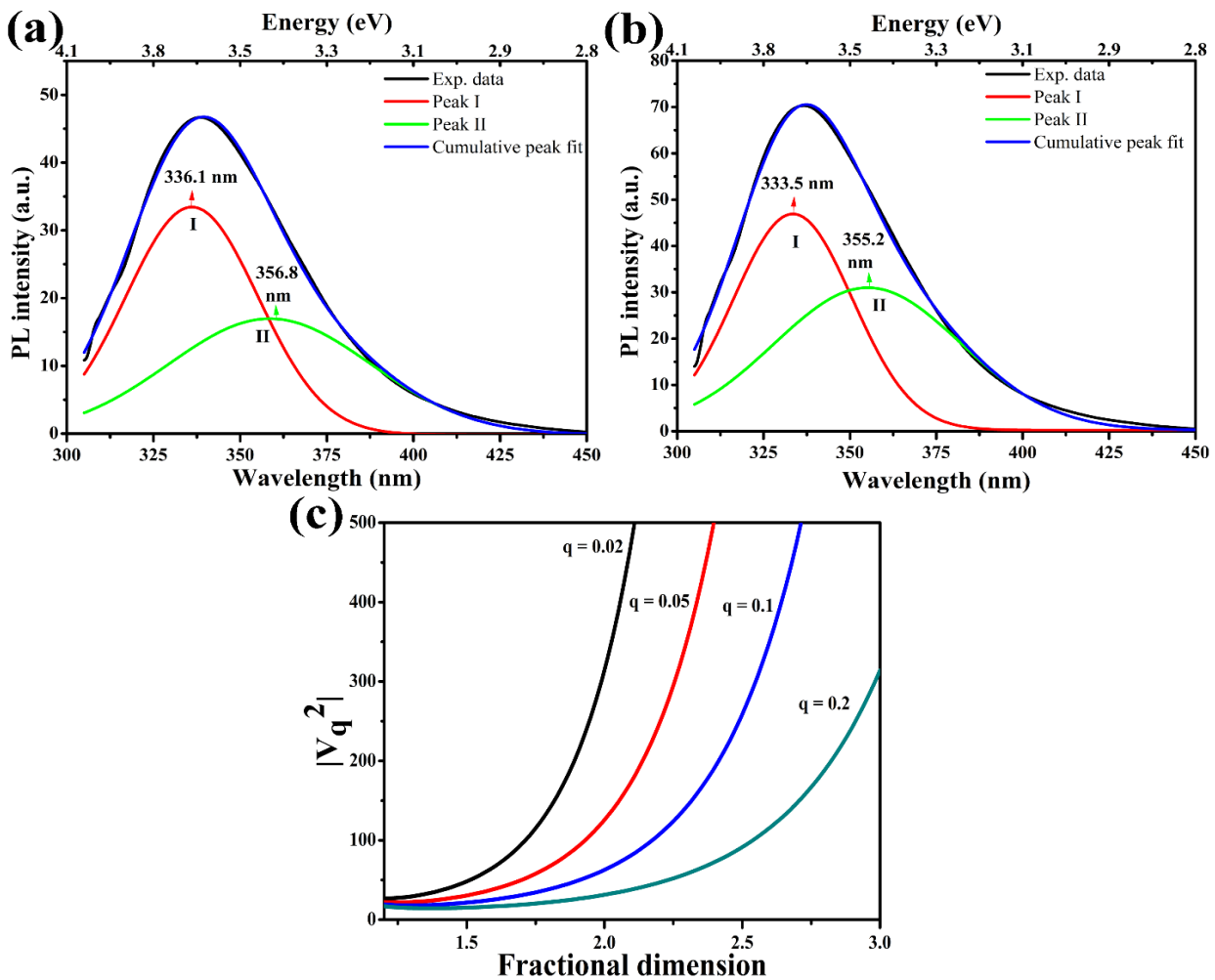
Fig. 4.7 Luminescence spectra of (a) coral – like and (b) flake – like NiO nanostructures (c) Variation of V_q^2 with fractional dimension.

In this expression, 'S-factor' (5.2 and 4.9 for coral-like and flake-like nanostructures respectively) has been calculated from the following expression:

$$S = \frac{\Delta}{2\hbar\omega_{LO/2LO}}$$ 4.3

where Δ (0.662 eV and 0.70 eV) for coral-like and flake-like nanostructure respectively) and $2\hbar\omega_{LO/2LO}$ represent Stoke shift and energy corresponding to LO and 2LO modes. 'Δ' has been calculated from the difference in peak positions between excitation and emission spectra. Excitation peaks have been found at 283.1 eV and 282.4 eV for coral-like and flake-like nanostructure respectively (represented in Fig. 4.8). In this context, it may be stated that the value of S-parameter, calculated for our synthesized systems, is noticed to exhibit higher magnitudes than S-factor, obtained for CdTe (0.71-1.24), [58] ZnO (0.9), [59] InGaN quantum dot (0.2).[60]
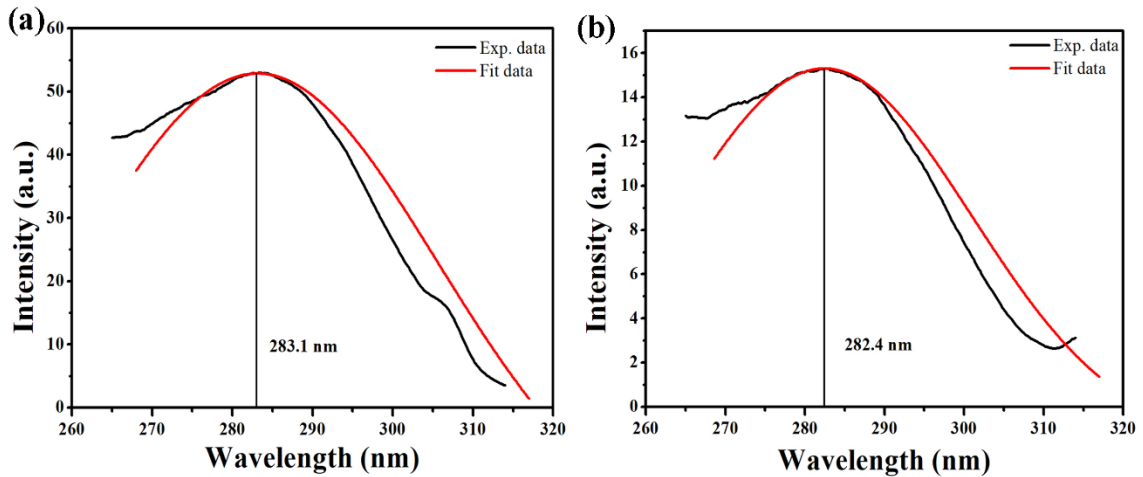
Fig. 4.8 Excitation peaks for (a) coral-like and (b) flake-like nanostructure respectively.

Using above equations, we have calculated FWHM of band edge emission to be 0.44 and 0.42 eV for coral and flake – shaped nanostructure respectively. In this context, it may be stated that the calculated FWHMs are found to very close to their experimentally measured values.

FWHMs get overestimated if we calculate it considering electron – 2LO interaction instead of electron – LO interaction, hence it could be concluded that electron – 2LO is not contributing to the relaxation of electrons corresponding to band edge transitions. In the case of surface localized electrons, similar calculation considering electron – 2LO interaction gives FWHM 0.68 and 0.67 eV for coral and flake – shaped nanostructure respectively i.e. calculated FWHMs are found to be very close to their experimentally measured values. Therefore in summary, it may be stated form Raman and emission analyses that the band to band transition and surface localized electronic relaxation are mediated by LO and 2LO phonon mode respectively and coral – like nanostructure exhibits higher electron – phonon interaction than flake – like nanostructure.

In order to understand the variation of S – factor and its correlation with charge – carrier phonon interaction for the synthesized nanostructures, we consider the following equation:

$$S = \sum_q \frac{|V_q^2|}{(\hbar\omega_{LO})^2} |\rho_q|^2 \qquad 4.4$$

where, V_q and ρ_q represents Fourier transformation of the strength of charge carrier – LO phonon interaction and charge density respectively. Our previous Rietveld refinement results no variation crystal structure within our synthesized nanostructures i.e. both nanostructure exhibits same ρ_q. In addition, $\hbar\omega_{LO}$ is found to have higher value for coral – like nanostructure i.e. higher magnitude of S – factor cann't be assigned to $\hbar\omega_{LO}$. Hence, observed variation in S – factor is purely ascribed to V_q and could be explained from dimensional effect of the synthesized nanostructures as follows: we consider V_q in fractional-dimensional space as discussed by Peeters *et al.*[61] In fractional dimension, V_q could be written in the following form:[62]

$$V_q = \sum_q [C(D)_q \widehat{b_q}(\exp(i\boldsymbol{q}.\boldsymbol{r})) + C(D)_q^* \widehat{b_q}^\dagger (\exp(-i\boldsymbol{q}.\boldsymbol{r}))] \qquad 4.5$$

where, $b_q{}^\dagger$ (b_q) and $C(D)_q$ represent creation (annihilation) operator for a phonon with wavevector **q** and electron – phonon coupling constant in fractional dimension. Considering basic Coulomb-like interaction in fractional-dimension, $C(D)_q$ gets simplified into the following form:

$$C(D)_q = -i\hbar\omega_{LO}\left(\frac{F_D(q)\alpha}{V_D}\right)^{\frac{1}{2}}\left(\frac{\hbar}{2m\omega_{LO}}\right)^{1/4} \qquad 4.6$$

where, $F_D(q) = (2\pi)^{D/2}\int_0^\infty dr\, r^{D-1}\, qr^{\left(1-\frac{D}{2}\right)}J_{\frac{D}{2}-1}(qr)\frac{1}{r}$ represents fractional dimensional Fourier transform of the Coulomb-like potential. In this expression, 'm', $'\alpha'$ and V_D represent electron effective mass, Fröhlich constant and fractional – dimensional volume of the crystal, defined in terms of Born – von Karman periodicity condition. After integration, $C(D)_q$, hence V_q^2 could be simplified into the form for free charge carriers, given below:

$$\left|V_q^2\right| = \frac{\Gamma\left(\frac{D-1}{2}\right)(4\pi)^{\frac{D-1}{2}}}{V_D}\alpha\frac{(\hbar\omega_{LO})^2}{q^{D-1}}\left(\frac{\hbar}{2m\omega_{LO}}\right)^{1/2} \qquad 4.7$$

In Fig. 4.7 (c), we have plotted $\left|V_q^2\right|$ versus 'D' in units of $\dfrac{\left(\frac{\hbar}{2m\omega_{LO}}\right)^{1/2}(\hbar\omega_{LO})^2}{V_D}\alpha$ considering q = 0.02, 0.05, 0.1 and 0.2. From figure it is clear that $\left|V_q^2\right|$ gets decreased with decreasing 'D' i.e. it may be stated that V_q gets decreased with decreasing fractional dimension of the system. In this context, we have calculated 'D' for our synthesized nanostructures using fractal box counting method utilizing ImageJ software[63] and FracLac plugin[64] and 'D' has been found to be 1.85 and 1.79 for coral – and flake – like nanostructures respectively

The methods have been developed on binarization of the FESEM images, application of masks to remove non-required details, and counting the number of boxes (N) at a given side length (ε), required to cover the required feature. (Shown in Fig. 4.9 (a and b) and (c and d) for coral-like and flake-like respectively) It has been found that N ∞ ε $^{-D}$. Slope of the log(N) versus log(ε)

represents D corresponding to synthesized nanostructures. Plots of log(N) versus log(ε) is shown in Fig. 4.9 (e and f) for coral – like and flake – like nanostructure respectively.
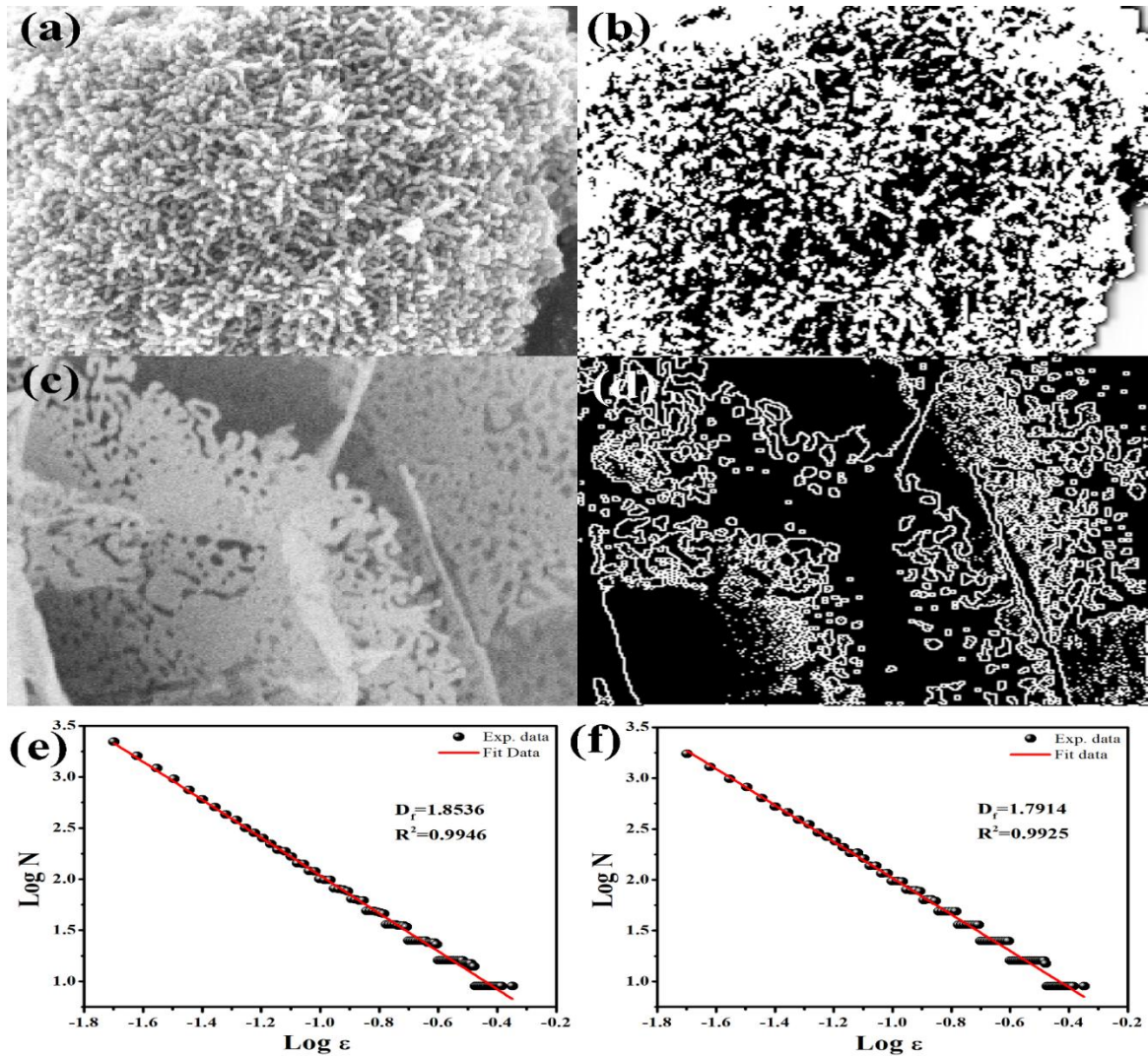
Fig. 4.9 (a, b) FESEM images showing coral-like and flake-like structures. (c, d): Binarized images where unwanted detail has been masked prior to fractal analysis. (e, f): Results obtained fractal dimension D_f =1.8536 and 1.7914 and correlation coefficient R^2=0.9946 and 0.9925 respectively.

Therefore, it may be concluded that the higher V_q of coral – like nanostructure is ascribed to higher magnitude of 'D'.

4.3.3. Effect of electron – phonon interaction on the generation of reactive oxygen species and electrochemical properties of the synthesized nanostructures
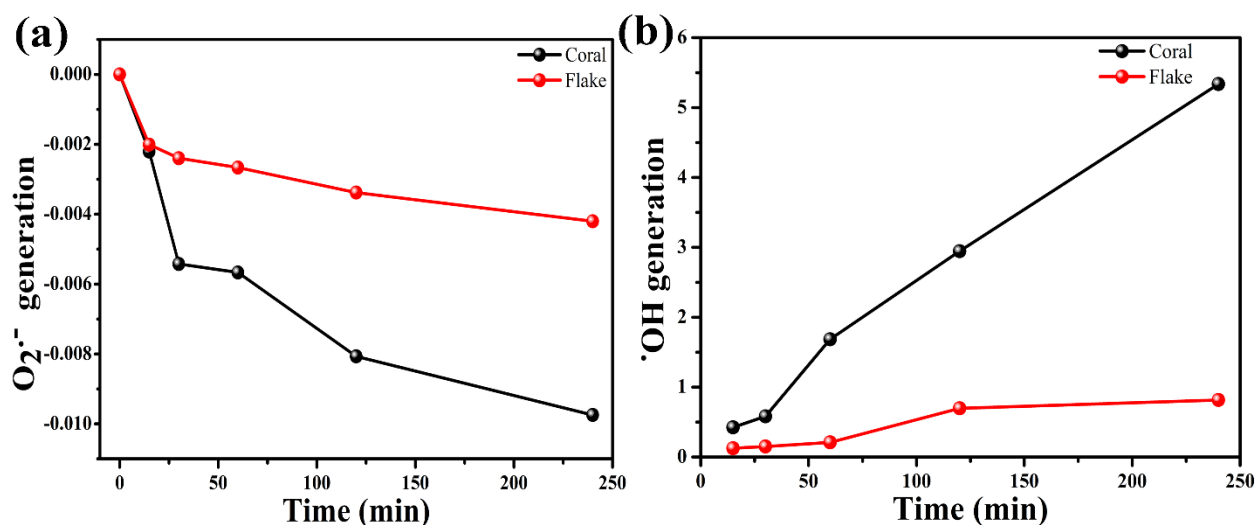
Fig 4.10 Generation of (a) superoxide and (b) hydroxyl ion per unit area of the sample at different time interval.

It has been well-investigated previously by many researchers that NiO has potential applications in the field of photocatalyst.[65] General mechanism for photocatalytic activity of NiO is that in the presence of radiation with energy greater than the band gap, electrons are getting excited into conduction band and react with ambient oxygen to produce superoxide ions (O_2^-). Owing to gain insight into the rate of O_2^- generation by the synthesized nanostructures, we have performed a series of experiment using nitroblue tetrazolium as probing dye to monitor the generation, calculated from using the relation $\frac{C_0 - C_t}{C_0}$, where C_0 and C_t represent initial absorption maxima and absorption maxima at time 't' respectively. O_2^-, generated per unit surface area of the synthesized sample is illustrated in Fig. 4.10 (a). It is evident from figure that the generation of O_2^- per unit surface area is higher for coral – like nanostructure than flake – like nanostructure. Generation of ·OH per unit area, investigated using terepthalic acid as probe dye, is also found to

higher for coral – like nanostructure (shown in Fig. 4.10 (b)). Thus, it can be stated that both component of ROS generation is higher for coral – like nanostructure compared to flake – like nanostructure. The observed phenomena can be explained as follows: it has been well explained previously by many researchers including us that the generation of O_2^- and $\cdot OH$ is dependent on conduction (E_{CB}) and valence band (E_{VB}) edge energies in neutral hydrogen electrode (NHE) scale with respect to redox potential of the O_2^- and $\cdot OH$ generation.[66] Feasibility of the redox reaction for O_2^- generation depends on E_{CB} and it should be higher than redox potential ($E_{redox,O/O_2^-}$) of O_2^- formation energy which is -0.33 eV on NHE scale. On the otherhand, contition of $\cdot OH$ generation is determined by E_{VB}. In this context, we have calculated E_{VB} from the empirical equation: $E_{VB} = \chi - E_c + 0.5 E_{g,[67]}$ where χ (2.31 eV for NiO) represents the absolute electronegativity of NiO which is the geometric mean of absolute electro-negativities of constituent atoms,[68-70] E_c (4.4 eV),[71] and E_g (3.68 and 3.72 eV for coral and flake – like nanostructure respectively, measured from band edge transition) are the energy of free electron on NHE scale and band gap respectively. From above equation, E_{VB} is calculated to be -0.25 and -0.23 eV, while E_{CB}, estimated form the equation $E_{CB} = E_{VB} - E_g$ [71] is found to be –3.93 and –3.95 eV for coral – and flake – like nanostructure respectively. Lower E_{CB} (in negative scale) for coral – like nanostructure is ascribed to higher electron – phonon interaction and can be explained as follows: under effective-mass approximation, Hamiltonian of an electron in conduction band in the presence of charge carrier – lattice interaction could be written in the following form:[58]

$$H = \frac{\hbar^2}{2m_{eff}} \nabla^2 - S\hbar\omega_{LO} \qquad 4.8$$

From this Hamiltonian, it can be stated that the conduction band edge energy gets lowered by charge – carrier electron interaction. Thermodynamic driving force for electron transfer,

defined by $\Delta G = E_{CB} - E_{redox,O/O_2^-}$, is found to be negative ($\Delta G < 0$) for both samples indicating feasibility of O_2^- generation by the synthesized NiO nanostructures. However, ΔG is found to be more negative for flake – like nanostructure compared to coral – like nanostructure indicating higher O_2^- generation by flake – like nanostructure.[72] But, in contrary, we have experimentally observed that coral – like nanostructure exhibits higher generation of O_2^-. The observed phenomena is assigned to phonon assisted non-adiabatic electron transfer in catalytic reaction (discussed later).

Redox potential for the generation of ˙OH from hole in valence band is +2.33 eV [73] which is very high compared to E_{VB} of NiO. Therefore it may be stated that the synthesized NiO nanostructures cannot produce ˙OH from the chemical reaction between h^+ of the valence band and ambient OH^- ions. Hence, the generation of ˙OH, in the present case, is attributed to the Haber – Weiss method, described by the following reaction steps:[74]

$$O_2^- + O_2^- + 2H^+ \rightarrow H_2O_2 + O_2 \qquad\qquad 4.9$$

$$H_2O_2 + O_2^- \rightarrow \cdot OH + OH^- + O_2 \qquad\qquad 4.10$$
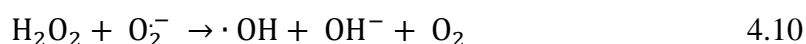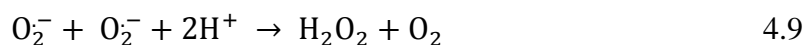
So, it can be stated that electron – phonon interaction within the synthesized samples doesn't have any direct effect on ˙OH generation.

NiO has been found to be a potential electrode material for electrochemical pseudocapacitor applications. In this context, it may be stated that the resistance of the electrode material, resistance corresponding to charge – transfer during redox reaction, ionic and diffusive resistance of the electrolyte effect the electrochemical activity and these parameters are found to be strongly depend on morphology of the nanostructures due to their characteristic distribution of surface charges, defects, pore size distribution etc.[75, 76] Our previous study revealed that the

interfacial charge transfer gets mediated by electron – phonon interaction, so in order gain insight into its effect on psudocapacitative activity of NiO, we have investigated electrochemical properties, CV, GCD and impedance spectroscopy of the synthesized nanostructures. Fig. 4.11 (a and b) shows the CV curves of the coral – and flake – like nanostructured NiO electrodes, measured at different scan rate ranging from 2 to75 mV/s within the potential windows from -0.2 V to +1.1 V (vs Ag/AgCl) using 3.0 M KCl solution as electrolyte. It is evident from figure that the flake – like nanostructure depictes two distinct peak at 0.44 and 0.80 V due to redox reaction at the electrode surface attributing oxidation of Ni^{+2} into Ni^{+3} and Ni^{+4} and indicates Faradic pseudocapacitive activity of the NiO electrodes.[77] Careful analysis of the curve reveals slightly positive shift for oxidation peak and slightly negative shift for reduction peak with increasing scan rate, which may be assigned to the resistance effect at the electrode - electrolyte interface and results kinetic reversibility of the redox reaction at the electrode surface.[78] Briefly, it can be stated that when electrolyte diffuses into pores of the electrodes during redox reaction, they imparts ohmic resistance and polarization causing irreversibility. It is also noted from figure that area under CV curve gets increased with increasing scan rate, retaining its shape indicating that nanostructures possesses pseudocapacitive activity.[79] Similar behaviour has also been observed by other researchers also.[80] In contrast to NiO flake – like nanostructure, no prominent peak corresponding to oxidation current has been observed in CV curve of coral – like nanostructure and it is attributed to poor conductivity.[78, 81, 82]

Specific capacitance (C_m, in F/g) of the synthesized NiO nanostructured electrodes has been calculated from CV curve according to the following equation:[83]

$$C_m = \frac{\int i \, dv}{2 \times m \times s \times \Delta V} \qquad 4.11$$

where, $\int i dv$ is the area under the CV curve, 'm', 's' and $\Delta V = (V_1 - V_2)$ represent working electrode material mass (in g), scan rate and applied potential window (V) respectively. C_m values are calculated to be 343 and 163 mF/cm^2 at the scan rate of 2 mV/s for coral and flake – like nanostructure respectively. In this context, it may be stated that though coral – like nanostructure doesn't possesses clear redox peak, but it exhibits higher C_m. Most important phenomena to be noticed here is that the coral – like nanostructure exhibits higher C_m though it has lower surface area as obtained from BET (discussed later). Dependence of C_m on scan rate is represented in Fig. 4.11 (c) that clearly illustrates gradual reduction of C_m with increasing scan rate.[84]

In order to investigate the charge storage ability of the synthesized electrodes at various current densities, constant current GCD measurements are carried out.[85] Fig. 4.11 (d and e) shows GCD plots of the NiO electrodes at various current density (0.3, 0.4, 0.5 and 0.7 mA/cm^2) within working potential windows from -0.2 V to +1.1 V, consistent with the potential range of CV testing. C_m for various current densities has also been calculated from the GCD curve using the following equation:

$$C_m = \frac{i \times t}{V \times m} \qquad\qquad 4.12$$

where 'i', 't', 'V' and 'm' represent discharge current (in A), discharge time (in sec), voltage range for full cycle (V) and mass of the electrode material (in g).
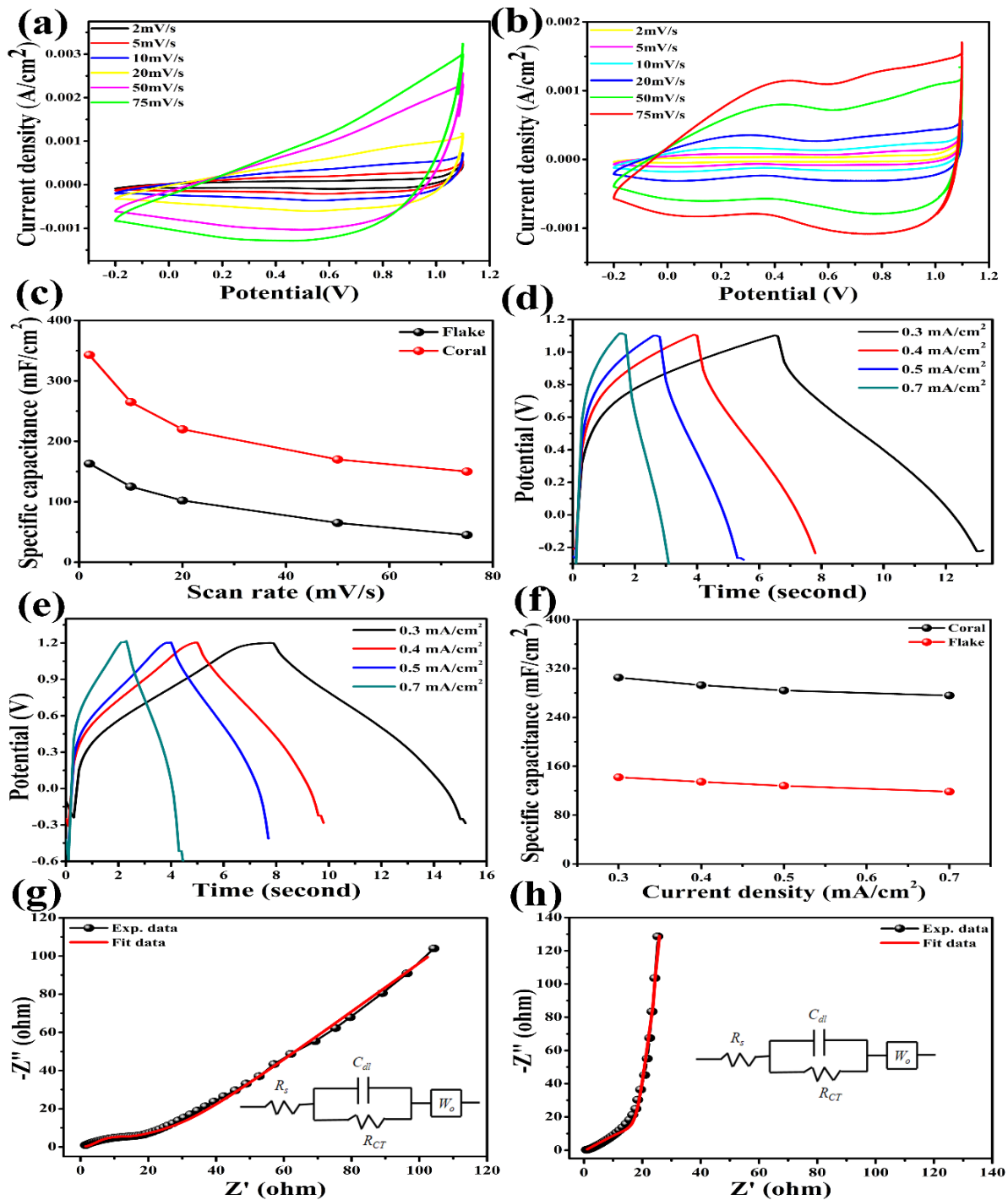
Fig. 4.11 (a, b): CV curves of coral and flake-like electrodes at various scan rates, (c): Effects of scan rate on specific capacitance for both samples, (d, e): GCD curves of coral and flake-like electrodes at various current densities, (f): Effects of current density on specific capacitance for both samples, (g, h): Nyquist plot of EIS for both coral and flake-like samples. The frequency is varied from 100 KHz to 0.1 Hz. Z′ is the real impedance and Z″ is the imaginary impedance. The inset shows the equivalent circuit

Maximum value of C_m of 305 and 142 mF/cm^2-has been obtained for both NiO-coral and NiO-flake at 0.3 mA/cm^2 current density, which is slightly less than C_m, calculated from CV plots. Fig. 4.11 (f) depicts variation of C_m with current density. It is noticed from figure that C_m gets decreased with increasing current density and this phenomena is assigned to the larger voltage drop across resistance of the electrode material which could be explain from electro chemical impedance spectroscopy (discussed later). Columbic efficiency (η) representing efficiency of electron transfer has been calculated for the synthesized nanostructures using the following equation:[86]

$$\eta = \frac{t_d}{t_c} \times 100 \qquad\qquad 4.13$$

where, t_d and t_c represent charging and discharging time respectively and it is found to be 93.6 and 99.6 for the synthesized coral and flake − like nanostructure respectively. Lower η of coral − like nanostructures is attributed to lower discharging time or higher charging time. Such phenomena is attributed to also corobortaes higher electron transfer efficiency across the electrode − electrolyte from electrolyte into electrode during discharging and reverse rate during charging (discussed later).

We have also measured electrochemical impedance property of the synthesized NiO electrodes. Fig. 4.11 (g and h) represent Nyquist plots of the coral − and flake − like nanostructured electrodes where the imaginary part of the impedance is plotted as a function of real counterpart in the frequency range between 0.1 Hz and 100 kHz with an excitation signal of 10mV. It is clear from Nyquist plots that coral − like nanostructure consists of a semi-circle in the high frequency region and a straight line in the low frequency region, while semi-circle is found to be invisible in flake − like nanostructured electrode. Such invisible semi-circle based Nyquist plot has also been

observed previously by other researchers.[87] In this context, it may be stated that the appearance of semi-circle in the high frequency region signifies the interfacial transfer of charge between electrode and electrolyte, whereas straight line nature of the plot in low frequency region represents capacititive activity due to ionic (Cl^- in the present case) diffusion in the electrolyte.[87] Slope of the straight line indicates gives an indication of ionic diffusion rate in the electrolyte. In this present study, higher slope for flake – like nanostructured electrode indicates faster ion diffusion. Since flake – like nanostructures exhibits less accumulation of electrons at the surfaces of nanostructures, so faster diffusion of Cl^- is attributed to the less repulsive interaction between Cl^- and surface accumulated electrons. It could also be interpreted as follows: Cl^- accumulation at the surface of nanostructure causes less lattice polarization due to less electron – phonon interaction giving easier diffusion path for Cl^-. In order to understand more insight into the electrode properties, Nyquist plots were fitted with equivalent Randles circuit parameters (presented in the inset of Fig. 4.11 (h).[88] R_s, known as series resistance, is a combination of the intrinsic resistance of the electrode material and ionic resistance.[89] Resistance, related with interfacial charge transfer, is denoted by R_{CT} and is being evaluated from the intercept of the semi-circle of Nyquist curve on real axis. Capacitance, connected in parallel with R_{CT}, is denoted by C_{dl} representing double layer capacitance. Inclined portion of the Nyquist curve from high frequency semi-circular region to low frequency region depends on frequency dependent ionic transport within the electrolyte and is termed as Warburg impedance (W). After careful analyses by Nyquist plots, it is observed that coral – and flake – like nanostructured electrodes possess $C_{dl} \sim 0.0004$ and 0.009 mF respectively. Lower C_{dl} for coral – like nanostructure is attributed less accumulation of Cl^-, caused by higher electron – phonon interaction. R_s is found to be 1.09 and 0.56 Ω for coral and flake – like nanostructured electrodes respectively. Higher R_s in coral – like nanostructure confirms higher

resistance due to higher electron – phonon interaction. R_{CT} is found to be 5 Ω for coral – nanostructured electrode, while for flake – nanostructured electrode, very insignificant contribution of R_{CT} (0.01 Ω) is noticed. In this context, it may be stated that Wu *et al.* found R_s and R_{CT} to be equal to 0.435 and 0.125 Ω for ultrathin NiO nanoflakes.[89] For NiO nanoparticle, these parameters are found to 6.2 and 6.4 Ω respectively.[90] So the obtained values corresponding to R_s and R_{CT} are consistent with other's results. Higher R_{CT} in coral – like nanostructure is attributed to higher activation energy for electron transfer across the interface (discussed later). Warburg impedances are found to be 60 and 50 Ω for coral and flake – like nanostructure respectively suggesting fast ionic diffusion in flake – like nanostructure though it has less surface area. Therefore from above study, it is revealed that though coral – like nanostructure exhibits less surface area, but it exhibits higher specific pseudocapacitance that is attributed higher electron transfer rate from electrode into electrolyte across the interface and phonon assisted electron transfer mechanism is assisted such activity. The observed phenomenon both in catalytic activity and pseudocapacitive activity could be explained as follows: Let G_i (G_i') be the Gibbs free energy of NiO system having an electron at valence (at conduction) band in case of pseudocapacitive activity (O_2^- generation) and G_f (G_f') be the Gibbs free energy of NiO when the gets transferred into electrolyte (to arial O_2). Then, $\Delta G = G_f - G_i$ ($= G_i' - G_f'$) represents the thermodynamic force responsible for transferring an electron from initial state into final state in the absence of electron – phonon interaction. Now in the presence of strong electron – phonon interaction, the electrode would suffer from local polarization due to transferred electron that gives rise reorganization of lattice, characterized by Huang – Rhys S – factor. Charge transfer process is schematically shown in Fig. 4.12. Briefly reorganizational energy (λ) is found to be proportion to 'S - factor' under linear approximation in reaction coordinate system. Then according to Marcus theory of non-

adiabatic electrons transfer rate ($k_{ET}(\Delta G)$) at temperature T for catalytic or pseudocapacitive activity can be witten in the following form:[91, 92]

$$k_{ET}(\Delta G) = k_{ET}^0 \exp\left(-\frac{(\lambda + \Delta G)^2}{4\lambda k_B T}\right) \qquad\qquad 4.14$$

Where, k_{ET}^0 represents constant representing electron transfer when $\Delta G \rightarrow 0$. Depending upon relative magnitude of ΔG and λ, we have two different consequences. When $\Delta G \gg \lambda$, then $k_{ET}(\Delta G)$ can be simplified as

$$k_{ET}(\Delta G) = k_{ET}^0 \exp\left(-\frac{\Delta G^2}{4\lambda k_B T}\right) \qquad\qquad 4.15$$

It can be stated from the equation that $k_{ET}(\Delta G)$ would be higher for higher λ. On the other hand when $\Delta G \ll \lambda$, $k_{ET}(\Delta G)$ is simplified into

$$k_{ET}(\Delta G) = k_{ET}^0 \exp\left(-\frac{\lambda}{4 k_B T}\right) \qquad\qquad 4.16$$

This equation states that $k_{ET}(\Delta G)$ gets decreased with increasing value of λ. For our synthesized samples, we have observed that the coral – like nanostructure having higher λ exhibits higher electron transfer rate across the interface compared to flake – like nanostructure for electron in conduction in case of photocatalytic process or electron in valence band in case of pseudocapacitive activity. Therefore it may be stated that electron transfer across the interface is guided by electron – phonon interaction. Briefly, the electron transfer across the junction is attributed to phonon assisted transfer mechanism. Absence of anodic or cathodic peak in CV curve in coral – like nanostructured electrode is generally attributed to fast charge transfer which originates from electron – phonon interaction or to the phonon assisted electron transfer mechanism. From the schematic diagram, it can be stated that the coral – like nanostructure exhibits higher activation energy due to higher electron – phonon interaction, hence higher

charging time of coral – like nanostructure is attributed to higher activation energy for an electron to cross the interface between NiO and electrolyte and reverse effect occurs during discharging process. Higher R_{CT} in coral – like nanostructured electrode is also assigned to higher activation energy (E_A) for the electron transfer process (Schematic diagram shown in Fig. 4.12).
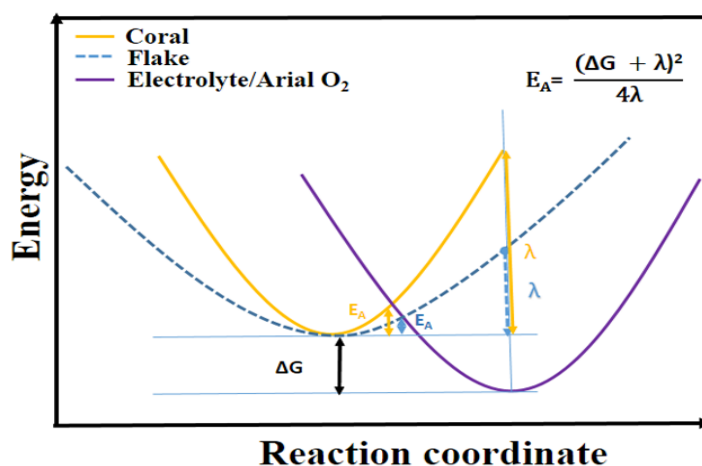
Fig. 4.12 Schematic diagram of electron transfer across the interface in reaction coordinate system.

4.4. Conclusion

In summary, we have successfully synthesized NiO coral – and flake – like nanostructure using facile hydrothermal method. XRD, SEM and TEM investigations confirmed the proper phase formation with well homogeneity in morphology. N_2 adsorption – desorption measurements gave higher surface area of flake – like ($91.38 \ m^2g^{-1}$) than coral – like ($39.91 \ m^2g^{-1}$) nanostructure. Raman spectrum analysis gives higher electron – phonon interaction in coral – like nanostructure compared to flake – like nanostructure and accumulated electrons at the surface of the nanostructures are athe source for higher electron – phonon interaction. This interaction got further supported by FWHM of the luminescence spectra, where electron – LO phonon interaction plays

the dominating role. Huang – Rhys 'S' – factor characterizing electron – phonon interaction has been quantified from excitation, emission of spectra corresponding to band edge emission. Higher fractional dimension of coral – like nanostructure is analyzed to be responsible for higher 'S' – factor. It has been demonstrated from ROS assay that coral – like nanostructure exhibits higher electron transfer rate per unit area compared to flake – like nanostructure. It had also been illustrated that coral – like NiO electrode exhibits higher electrochemical capacitance ($C_m = 343$ mF/cm^2) than flake – like nanostructure ($C_m = 163$ mF/cm^2) though former exhibits less surface area. Applying Marcus theory, it has been demonstrated that the charge transfer process in catalytic as well as in electrochemical process within the synthesized nanostructures are non-adiabatic in nature, guided by electron – phonon interaction. And finally, it is concluded that lattice polarization, caused by electron – phonon interaction, imparts the crucial role specific pseudocapacitance while charge transfer resistance and charging or discharging time are determined by activation energy of process where the same electron – phonon interaction also plays significant role.

4.5. Reference

1.   P. Pisu and G. Rizzoni, *Vehicle Power and Propulsion, 2005 IEEE Conference*, 2005, 8 pp.

2.   T. Smith, J. Mars and G. Turner, *Power Electronics Specialists Conference, 2002. pesc 02. 2002 IEEE 33rd Annual*, 2002, **1**, 124-128.

3.   M. Meinert, *Power Electronics and Applications, 2009. EPE'09. 13th European Conference on*, 2009, 1-10.

4.   U. Singh, A. Banerjee, D. Mhamane, A. Suryawanshi, K. K. Upadhyay and S. Ogale, *RSC Advances*, 2014, **4**, 39875-39883.

5.   X. Ren, C. Guo, L. Xu, T. Li, L. Hou and Y. Wei, *ACS applied materials & interfaces*, 2015, **7**, 19930-19940.

6.   H. Fan, Y. Zhong, L. Chang, S. Zhu, K. Wang, H. Shao, J. Wang, J. Zhang and C.-n. Cao, *RSC Advances*, 2016, **6**, 52957-52965.

7.   S. Sarangapani, B. Tilak and C. P. Chen, *Journal of the Electrochemical Society*, 1996, **143**, 3791-3799.

8.   P. Ragupathy, D. H. Park, G. Campet, H. Vasan, S.-J. Hwang, J.-H. Choy and N. Munichandraiah, *The Journal of Physical Chemistry C*, 2009, **113**, 6303-6309.

9.   H. Wang, H. Yi, X. Chen and X. Wang, *Journal of Materials Chemistry A*, 2014, **2**, 3223-3230.

10.   K. C. Liu and M. A. Anderson, *Journal of the Electrochemical Society*, 1996, **143**, 124-130.

11.   S. K. Meher, P. Justin and G. R. Rao, *Nanoscale*, 2011, **3**, 683-692.

12.   M. Zhang, Q. Li, D. Fang, I. A. Ayhan, Y. Zhou, L. Dong, C. Xiong and Q. Wang, *RSC Advances*, 2015, **5**, 96205-96212.

13.   F. Cao, G. Pan, X. Xia, P. Tang and H. Chen, *Journal of Power Sources*, 2014, **264**, 161-167.

14.   M. Liu, J. Chang, J. Sun and L. Gao, *Electrochimica Acta*, 2013, **107**, 9-15.

15. X. Ma, Y. Li, Z. Wen, F. Gao, C. Liang and R. Che, *ACS applied materials & interfaces*, 2014, **7**, 974-979.

16. R. S. Devan, R. A. Patil, J. H. Lin and Y. R. Ma, *Advanced Functional Materials*, 2012, **22**, 3326-3370.

17. J. Xu, Y. Xue, J. Cao, G. Wang, Y. Li, W. Wang and Z. Chen, *RSC Advances*, 2016, **6**, 5541-5546.

18. H. Pang, Q. Lu, Y. Zhang, Y. Li and F. Gao, *Nanoscale*, 2010, **2**, 920-922.

19. Z. Fan, J. Yan, T. Wei, L. Zhi, G. Ning, T. Li and F. Wei, *Advanced Functional Materials*, 2011, **21**, 2366-2375.

20. D. Ghosh, M. Mandal and C. K. Das, *Langmuir*, 2015, **31**, 7835-7843.

21. X. Xia, J. Tu, Y. Zhang, X. Wang, C. Gu, X.-b. Zhao and H. J. Fan, *ACS nano*, 2012, **6**, 5531-5538.

22. R. Heitz, I. Mukhametzhanov, O. Stier, A. Madhukar and D. Bimberg, *Physical review letters*, 1999, **83**, 4654.

23. F. Ciccacci, S. Selci, G. Chiarotti and P. Chiaradia, *Physical review letters*, 1986, **56**, 2411.

24. W. Zhang, C. Delerue, Y.-M. Niquet, G. Allan and E. Wang, *Physical Review B*, 2010, **82**, 115319.

25. S. Ghosh, M. Ghosh, P. Kumar, A. S. Sarkar and S. K. Pal, *The Journal of Physical Chemistry C*, 2016, **120**, 27717-27723.

26. R. H. Hembree and D. A. Micha, *The Journal of chemical physics*, 2013, **138**, 184708.

27. Z. Zhang, C. Shao, X. Li, C. Wang, M. Zhang and Y. Liu, *ACS applied materials & interfaces*, 2010, **2**, 2915-2923.

28. C. Shifu, Z. Sujuan, L. Wei and Z. Wei, *Journal of Hazardous Materials*, 2008, **155**, 320-326.

29. A. Hameed, V. Gombac, T. Montini, M. Graziani and P. Fornasiero, *Chemical Physics Letters*, 2009, **472**, 212-216.

30. S. Majumder, S. Bhattacharjee and C. K. Ghosh, *RSC Advances*, 2016, **6**, 56503-56510.

31. J. H. Pan, Q. Huang, Z. Y. Koh, D. Neo, X. Z. Wang and Q. Wang, *ACS applied materials & interfaces*, 2013, **5**, 6292-6299.

32. http://maud.radiographema.eu/, accssed 30 December, 2015.

33. H. Rietveld, *Acta Crystallographica*, 1967, **22**, 151-152.

34. H. Rietveld, *Journal of applied Crystallography*, 1969, **2**, 65-71.

35. R. Young and D. Wiles, *Journal of applied Crystallography*, 1982, **15**, 430-438.

36. L. Lutterotti and P. Scardi, *Journal of applied Crystallography*, 1990, **23**, 246-252.

37. V. Lakshmi Prasanna and R. Vijayaraghavan, *Langmuir*, 2015, **31**, 9155-9162.

38. K.-i. Ishibashi, A. Fujishima, T. Watanabe and K. Hashimoto, *Journal of photochemistry and photobiology A: chemistry*, 2000, **134**, 139-142.

39. N. Rinaldi-Montes, P. Gorria, D. Martínez-Blanco, A. Fuertes, L. F. Barquín, J. R. Fernández, I. de Pedro, M. Fdez-Gubieda, J. Alonso and L. Olivi, *Nanoscale*, 2014, **6**, 457-465.

40. J. Zhang, D. Zeng, S. Zhao, J. Wu, K. Xu, Q. Zhu, G. Zhang and C. Xie, *Physical Chemistry Chemical Physics*, 2015, **17**, 14903-14911.

41. X. Su, H. Chai, D. Jia, S. Bao, W. Zhou and M. Zhou, *New Journal of Chemistry*, 2013, **37**, 439-443.

42.   G. A. Babu, G. Ravi, T. Mahalingam, M. Kumaresavanji and Y. Hayakawa, *Dalton Transactions*, 2015, **44**, 4485-4497.

43.   W. Wang, Y. Liu, C. Xu, C. Zheng and G. Wang, *Chemical Physics Letters*, 2002, **362**, 119-122.

44.   R. Dietz, G. Parisot and A. Meixner, *Physical Review B*, 1971, **4**, 2302.

45.   W. Duan, S. Lu, Z. Wu and Y. Wang, *The Journal of Physical Chemistry C*, 2012, **116**, 26043-26051.

46.   H. Lange, M. Artemyev, U. Woggon, T. Niermann and C. Thomsen, *Physical Review B*, 2008, **77**, 193303.

47.   J. Ye, K. Teoh, X. Sun, G. Lo, D. Kwong, H. Zhao, S. Gu, R. Zhang, Y. Zheng and S. Oh, *Applied Physics Letters*, 2007, **91**, 091901.

48.   Z. Yang, D. Gao, K. Tao, J. Zhang, Z. Shi, Q. Xu, S. Shi and D. Xue, *RSC Advances*, 2014, **4**, 46133-46140.

49.   G. Zhang, L. Wang, Y. Liu, W. Li, F. Yu, W. Lu and H. Huang, *Journal of Materials Chemistry A*, 2016, **4**, 8211-8218.

50.   H.-M. Cheng, K.-F. Lin, H.-C. Hsu, C.-J. Lin, L.-J. Lin and W.-F. Hsieh, *The Journal of Physical Chemistry B*, 2005, **109**, 18385-18390.

51.   V. Dzhagan, M. Y. Valakh, A. Raevskaya, A. Stroyuk, S. Y. Kuchmiy and D. Zahn, *Nanotechnology*, 2008, **19**, 305707.

52.   S. S. Gaikwad, A. C. Gandhi, S. D. Pandit, J. Pant, T.-S. Chan, C.-L. Cheng, Y.-R. Ma and S. Y. Wu, *Journal of Materials Chemistry C*, 2014, **2**, 7264-7274.

53.   B. Karthikeyan, T. Pandiyarajan, S. Hariharan and M. S. Ollakkan, *CrystEngComm*, 2016, **18**, 601-607.

54.   Y. Qi, H. Qi, C. Lu, Y. Yang and Y. Zhao, *Journal of Materials Science: Materials in Electronics*, 2009, **20**, 479-483.

55.   C. Díaz- Guerra, A. Remon, J. Garcia and J. Piqueras, *physica status solidi (a)*, 1997, **163**, 497-503.

56.   S. Lee, S. Park, C.-W. Kim, D. Lee, C. Lee and C. Jin, *Thin Solid Films*, 2016, **598**, 33-38.

57.   S. Das, C. K. Ghosh, R. Dey and M. Pal, *RSC Advances*, 2016, **6**, 236-244.

58.   M. Soltani, M. Certier, R. Evrard and E. Kartheuser, *Journal of applied physics*, 1995, **78**, 5626-5632.

59.   D. Reynolds, D. C. Look and B. Jogai, *Journal of applied physics*, 2001, **89**, 6189-6191.

60.   S. Xu, G. Li, Y. Wang, Y. Zhao, G. H. Chen, D. Zhao, J. Zhu, H. Yang, D. Yu and J. Wang, *Applied Physics Letters*, 2006, **88**, 083123.

61.   F. Peeters, W. Xiaoguang and J. Devreese, *Physical Review B*, 1986, **33**, 3926.

62.   A. Matos-Abiague, *Semiconductor science and technology*, 2002, **17**, 150.

63.   J. Schindelin, I. Arganda-Carreras, E. Frise, V. Kaynig, M. Longair, T. Pietzsch, S. Preibisch, C. Rueden, S. Saalfeld and B. Schmid, *Nature methods*, 2012, **9**, 676-682.

64.   https://imagej.nih.gov/ij/plugins/fraclac/FLHelp/Introduction.htm, accssed April 15, 2017.

65.   X. Song and L. Gao, *The Journal of Physical Chemistry C*, 2008, **112**, 15299-15305.

66.   S. Podder, S. Halder, A. Roychowdhury, D. Das and C. K. Ghosh, *Journal of Nanoparticle Research*, 2016, **18**, 294.

67.   F. Dong, X. Xiao, G. Jiang, Y. Zhang, W. Cui and J. Ma, *Physical Chemistry Chemical Physics*, 2015, **17**, 16058-16066.

68.   L. Zhu, C. Li, Y. Li, C. Feng, F. Li, D. Zhang, Z. Chen, S. Wen and S. Ruan, *Journal of Materials Chemistry C*, 2015, **3**, 2231-2236.

69.   Z. Mei, S. Ouyang, D.-M. Tang, T. Kako, D. Golberg and J. Ye, *Dalton Transactions*, 2013, **42**, 2687-2690.

70.   R. G. Pearson, *Inorganic Chemistry*, 1988, **27**, 734-740.

71.   H. Cheng, B. Huang, X. Qin, X. Zhang and Y. Dai, *Chemical Communications*, 2012, **48**, 97-99.

72.   J. Jayabharathi, C. Karunakaran and V. Kalaiarasi, *New Journal of Chemistry*, 2015, **39**, 1800-1813.

73.   K. Krumova and G. Cosa, *Overview of Reactive Oxygen Species*, 2016.

74.   F. Haber and J. Weiss, *Proceedings of the Royal Society of London A: Mathematical, Physical and Engineering Sciences*, 1934, **147**, 332-351.

75.   S. Xiong, C. Yuan, X. Zhang and Y. Qian, *CrystEngComm*, 2011, **13**, 626-632.

76.   S. Vijayakumar, S. Nagamuthu and G. Muralidharan, *ACS Sustainable Chemistry & Engineering*, 2013, **1**, 1110-1118.

77.   A. K. Singh, D. Sarkar, G. G. Khan and K. Mandal, *ACS applied materials & interfaces*, 2014, **6**, 4684-4692.

78.   C. Wu, S. Deng, H. Wang, Y. Sun, J. Liu and H. Yan, *ACS applied materials & interfaces*, 2014, **6**, 1106-1112.

79.   V. Kannan, A. I. Inamdar, S. M. Pawar, H.-S. Kim, H.-C. Park, H. Kim, H. Im and Y. S. Chae, *ACS applied materials & interfaces*, 2016, **8**, 17220-17225.

80.   S.-I. Kim, J.-S. Lee, H.-J. Ahn, H.-K. Song and J.-H. Jang, *ACS applied materials & interfaces*, 2013, **5**, 1596-1603.

81.   M. Nakayama and H. Tagashira, *Langmuir*, 2006, **22**, 3864-3869.

82. T. Tao, A. M. Glushenkov, H. Liu, Z. Liu, X. J. Dai, H. Chen, S. P. Ringer and Y. Chen, *The Journal of Physical Chemistry C*, 2011, **115**, 17297-17302.

83. Y. Tang, Y. Liu, W. Guo, T. Chen, H. Wang, S. Yu and F. Gao, *The Journal of Physical Chemistry C*, 2014, **118**, 24866-24876.

84. U. Patil, K. Gurav, V. Fulari, C. Lokhande and O. S. Joo, *Journal of Power Sources*, 2009, **188**, 338-342.

85. M. Xu, L. Kong, W. Zhou and H. Li, *The Journal of Physical Chemistry C*, 2007, **111**, 19141-19147.

86. P. Xu, J. Liu, T. Liu, K. Ye, K. Cheng, J. Yin, D. Cao, G. Wang and Q. Li, *RSC Advances*, 2016, **6**, 28270-28278.

87. H. Li, Y. He, V. Pavlinek, Q. Cheng, P. Sáha and C. Li, *Journal of Materials Chemistry A*, 2015, **3**, 17165-17171.

88. K. M. Hercule, Q. Wei, A. M. Khan, Y. Zhao, X. Tian and L. Mai, *Nano letters*, 2013, **13**, 5685-5691.

89. S. Wu, K. Hui, K. Hui and K. H. Kim, *Journal of Materials Chemistry A*, 2016.

90. M. S. Kolathodi, M. Palei and T. S. Natarajan, *Journal of Materials Chemistry A*, 2015, **3**, 7513-7522.

91. O. Farver, P. Hosseinzadeh, N. M. Marshall, S. Wherland, Y. Lu and I. Pecht, *The journal of physical chemistry letters*, 2014, **6**, 100-105.

92. P. C. Sercel, *Physical Review B*, 1995, **51**, 14532.

Chapter 5

Electron – phonon interaction to tune metal – semiconductor junction characteristics: ultralow potential barrier and less non-thermionic emission

Abstract

We present a two-step facile method to prepare Ni_2O_3 coral–like and flower–like nanostructures first time followed by structural, optical characterizations by XRD, FESEM, HRTEM, Raman, luminescence spectroscopy etc. We also report rectifying *I–V* characteristics of Ni_2O_3 nanostructures / Al based metal–semiconductor junction with ultralow turn-on voltages (0.36 V), potential barrier (0.33 eV), very ideal thermionic current (η = 1.11). Photo-responsive character illustrates that the junction devices could be a promising material for light sensing application. Parameters like series resistance (111.4 Ω), electron mobility (16.73 $\times 10^{-10}$ $m^2V^1s^{-1}$), diffusion length (5.13 $\times 10^{-7}$ m), density of states (3.09 $\times 10^{40}$ eVm^{-3}) etc. have been evaluated and it is discussed that the defect (Ni^{3+} vacancy) induced electron–phonon interaction within the active semiconducting layer plays the crucial role to determine these parameters. Most importantly, it has been identified that the charge-transport across the junction follows non-adiabatic mechanism. Our results suggest a new insight into current transport mechanism that may be generalized to understand microstructural, defect dependence MS junctions.

5.1.   Introduction

Due to ability of converting light into electrical signal, metal–semiconductor (MS) junctions are ubiquitously used in the field of various optoelectronic devices such as solar energy, light-wave communication, photodetector etc. [1-3] With current research trends in the field of nanoscience and technology, focus has been shifted to develop low-dimensional nanoscale MS junctions those exhibit new optoelectronic characteristics, attributed to unique features of the nanomaterials. In this context, it may be stated that understanding of the optical and electrical properties of nano-junction is very important for the fabrication of reliable real field MS nano-optoelectronic devices. Several parameters like carrier lifetime, charge carrier-recombination rate, band gap, morphology etc. of the semiconductors are found to influence significantly on the

performance of these devices, therefore searching of efficient nano-junction for various nano-optoelectronic devices is the 'holy grail' research trend in this realm.[4, 5] ZnO, TiO_2, CdTe, CdSe, CdS, ZnS etc. are employed as potential semiconducting materials due to their easy tuneability of microstructure, chemical stability, easy availability, environmental compatibility etc.[6] There are evidential reports demonstrating that barrier inhomogeneity, attributed to grain boundary, defects, morphology etc., mostly influences the interfacial properties including potential ideality factor, reverse saturation current etc., while energy difference between Fermi energy of metal and conduction band of semiconductor determines the turn-on voltage. In this regard, Ren *et al.* have studied the effect of lattice mismatch on the barrier characteristics.[7] The effect of barrier fluctuation of barrier on current have been investigated by Tung[8] employing ballistic electron emission spectroscopy. Effect of lateral barrier inhomogeneity on ideality factor which is a measure of non-ideal *I–V* characteristic has been enumerated by Biber *et al.*[9] It has also been observed that MS junction characteristic gets also influenced by the dipole moment, formed at MS interface. For example, Endo *et al.* has revealed that the dipole moments perpendicular to either Zn-polar (0001) or O-polar $(000\bar{1})$ surfaces at Pt / ZnO MS junction lead different interfacial structure, barrier height, responsivity.[10] But on contrary, Chopra *et al.* didn't observe any polarity effect in Au / ZnO MS junction.[11] Recently, Yu et al. have observed temperature dependent polarity reversal in Au / $TlGaSe_2$ junction.[12] Therefore, it may be stated from above discussions that the MS nano-junction characteristics are very much complex and gets influenced by various properties of the nanostructured materials, thus more investigations are required. Moreover, our recent studies illustrate that the electronic processes is determined by the boundary conditions of the nanostructured materials, particularly in nanostructures where electron–phonon interaction is very strong.[13-17] To best of our knowledge, phonon-assisted tunneling in reversed biased MS junction have been studied by Pipinys et al.,[18] but no studies have been carried out to investigate the electron–phonon interaction on junction characteristics like barrier height,

ideality factors etc. under dark as well as in the presence of light upto now. Hence, in this present chapter, we have investigated the influence of electron–phonon interaction on MS nano-junction characteristic employing two different Ni_2O_3 nanostructures as prototype.

The choice of Ni_2O_3 is as follows: Ni being a transitional metal element possesses different oxidation states. Except NiO, other oxides are rarely been investigated. Recently few researchers including us have studied that Ni_2O_3 is a ferromagnetic n-type material and exhibit heavy metal removal ability and antibacterial activity, but there is no evidential studies on the optoelectronic properties of Ni_2O_3.[19, 20] It has been researched earlier that localized Ni 3d orbital mostly contribute to the conduction band of nickel oxide, thus strong electron–phonon coupling is expected for Ni_2O_3. To best of our knowledge, no such opto-electronic studies have ever been carried out on Ni_2O_3.

5.2. Experimental section

5.2.1. Synthesis of coral-like Ni_2O_3 nanostructure

In a typical synthesis of coral-like Ni_2O_3 nanostructure, 1.57 g $Ni(NO_3)_2.6H_2O$ (99.99%), 1.57 g of NH_2CONH_2 (99.99%) and 1.30 ml poly ethylene glycol-600 were taken in a beaker containing 60.00 ml de-ionized (DI) water and the whole mixture was stirred to form a clear greenish solution. The solution was then transferred into Schott Duran glass bottle and heated at 90 °C for 10 h. Thus formed greenish product of $Ni(OH)_2$, collected after centrifugation, was washed repeatedly with water and ethanol. After treating with 20 ml NaOCl solution which containing 4% active chlorine, the intermediate mixture was dried at 60 °C for 10 h to obtain the final product.

5.2.2. Synthesis of flower-like Ni_2O_3 nanostructure

To prepare Ni_2O_3 flower–like nanostructure, 0.48 g of $NiCl_2.6H_2O$ (99.99%), 1.20 g of NH_2CONH_2 (99.99%) and 0.10 g of sodium dodecyl sulphate were taken in a beaker and 10 ml

ethanol along with 10 ml DI water were added subsequently. After stirring the mixture for few minutes, the resultant solution was transferred into a 100 ml Schott Duran glass bottle, which was treated hydrothermally at 110 °C for 3 h. The resultant greenish product $Ni(OH)_2$, collected after centrifugation, was washed repeatedly with water and ethanol. Finally the intermediated product was treated with 20 ml NaOCl solution containing 4% active chlorine, followed by drying at 60 °C for 10 h to obtain final product.

5.2.3. Sample Characterizations

Crystallinity and phase purity of the synthesized samples were investigated by x-ray diffractometer (XRD, Ultima-III, Rigaku, Cu K$_\alpha$ radiation, $\lambda = 1.5404$ Å). Field emission scanning electron microscope (FESEM, S – 4800, Hitachi) and high resolution transmission electron microscope (HRTEM, JEM – 2100, JEOL) were employed to investigate the microstructure of the samples. Imperfections of the synthesized nanostructures were determined from positron annihilation lifetime spectroscopy (PALS). In this study, ^{22}Na positron source having strength ~8 μCi was used and the source got sandwiched between the radiation-exposed parts of the two pieces (diameter ~ 10 mm) of the material. Measurements were done at room temperature using fast-fast coincidence technique having a system resolution of 293 ps with ^{60}Co prompt spectrum at positron window settings, while the obtained data was analyzed by PATFIT program on the basis of positron trapping model after proper source and background corrections. Room temperature micro-Raman spectra were recorded on Raman spectrometer having laser excitation energy of 532 nm (alpha 300, WITEC, Germany). Fourier transform infrared spectrophotometer (Shimadzu IR Prestige, Japan) has been employed to obtain infrared spectrum in the wavenumber range 400 – 800 cm^{-1}. Steady state photoluminescence spectra of the synthesized samples were recorded at room temperature on RF5301 (Shimadzu, Japan). Lifetime of the electrons in excited state was measured by time-correlated single photon counting (TCSPC) at solid state condition. In this

typical experiment, all samples, kept in IBH fluorocube apparatus, were excited at 300 nm using NanoLED and full width at half maxima of the system was fixed at 90 ps. Decay profiles had been collected on a Hamamatsu MCP photomultiplier (R3809), while IBH DAS6 software was utilized to analyze the data.

5.2.4. Fabrication and measurement of the Ni_2O_3 nanostructure / Al Schottky device

To construct the MS junction devices, as-prepared Ni_2O_3 powders were dispersed in N, N-dimethylformamide and then spin-coated on the ITO substrate to develop thin film with the help of SCU-2007 spin coating unit. To evaporate the solvent, thin film was annealed under vacuum at 80 °C for 30 minutes. Thickness of the film was measured (~ 800 nm) with the help of surface profiler. 99.99% pure Al, chosen as the electrode materials, was deposited on Ni_2O_3 thin film to develop the MS interface by thermal evaporation technique using vacuum coating unit (12A4D HHV, Vacuum coating unit). $I - V$ characteristics of immediately fabricated ITO / Ni_2O_3 nanostructure / Al based devices were recorded by Keithley 2635B Source Meter, interfaced with computer under dark and AM 1.5G radiation. Dielectric constants of the synthesized samples were measured by E4980 LCR meter (Agilent).

5.3.   Results and discussion

5.3.1. Structural and micro-structural characterizations of the nanostructures by XRD, FESEM and HRTEM

X-ray diffraction patterns of the as-prepared samples are presented in Fig. 5.1 (a). Five diffraction peaks, identified at $2\theta = 27.34°$, $31.66°$, $45.41°$, $56.38°$ and $66.12°$, can readily be indexed as the reflection from (101), (002), (111), (202) and (004) planes of hexagonal Ni_2O_3 (JCPDS Card Number 14-0481, CAS Number 1314-06-3). Absence of any other peak validates phase purity of the synthesized material. Average crystallite sizes, calculated from well-known Scherer's relation ($0.9\lambda/\beta\cos\theta$, where β represents full width at half maxima (FWHM) of

diffraction peak), are found to be 39 nm and 40 nm for coral–like and flower–like nanostructures respectively indicating no significant difference in crystallite sizes.

FESEM image (Fig. 5.1 (b)) of the coral–like nanostructure depicts that it consists of large number of interconnected blooming nanorods, while high magnification image (Fig. 5.1 (c)) ensures that each nanorod is composed of nanoparticles. It is observed from FESEM images of flower–like sample (Fig. 5.1 (d) and (e)) that it is made of several interconnected 2D nanosheets.

Microstructures of the synthesized nanostructures have been further clarified by TEM analysis. TEM image of coral-like nanostructure (Fig. 5.2 (a)) manifests abundantly the formation of inter-connected nanoparticles corroborating FESEM studies. Three spots in the selected area electron diffraction (SAED) pattern (Fig. 5.2 (b)) are indexed as the electron diffraction from (002), (111) and (202) planes of hexagonal Ni_2O_3. HRTEM image (Fig. 5.2 (c)) depicts lattice fringes with spacing 2.82 Å and 3.23 Å corresponding to (002) and (101) planes. The Fig. 5.2 (d) shows typical TEM image of flower–like nanostructure illustrating its sheet–like constituent similar to FESEM images. SAED pattern (Fig. 5.2 (e)) is similar with that of coral–like nanostructures. Lattice fringes (Fig. 5.2 (f)) with spacing 2.82 Å and 1.99 Å correspond (002) and (111) planes. Distribution of particle sizes and thickness of the sheets in case of coral– and flower– like nanostructures respectively are presented in inset of Fig. 5.2 (a) and Fig. 5.2 (d) respectively. Possible growth mechanisms for both nanostructures are provided bellow.
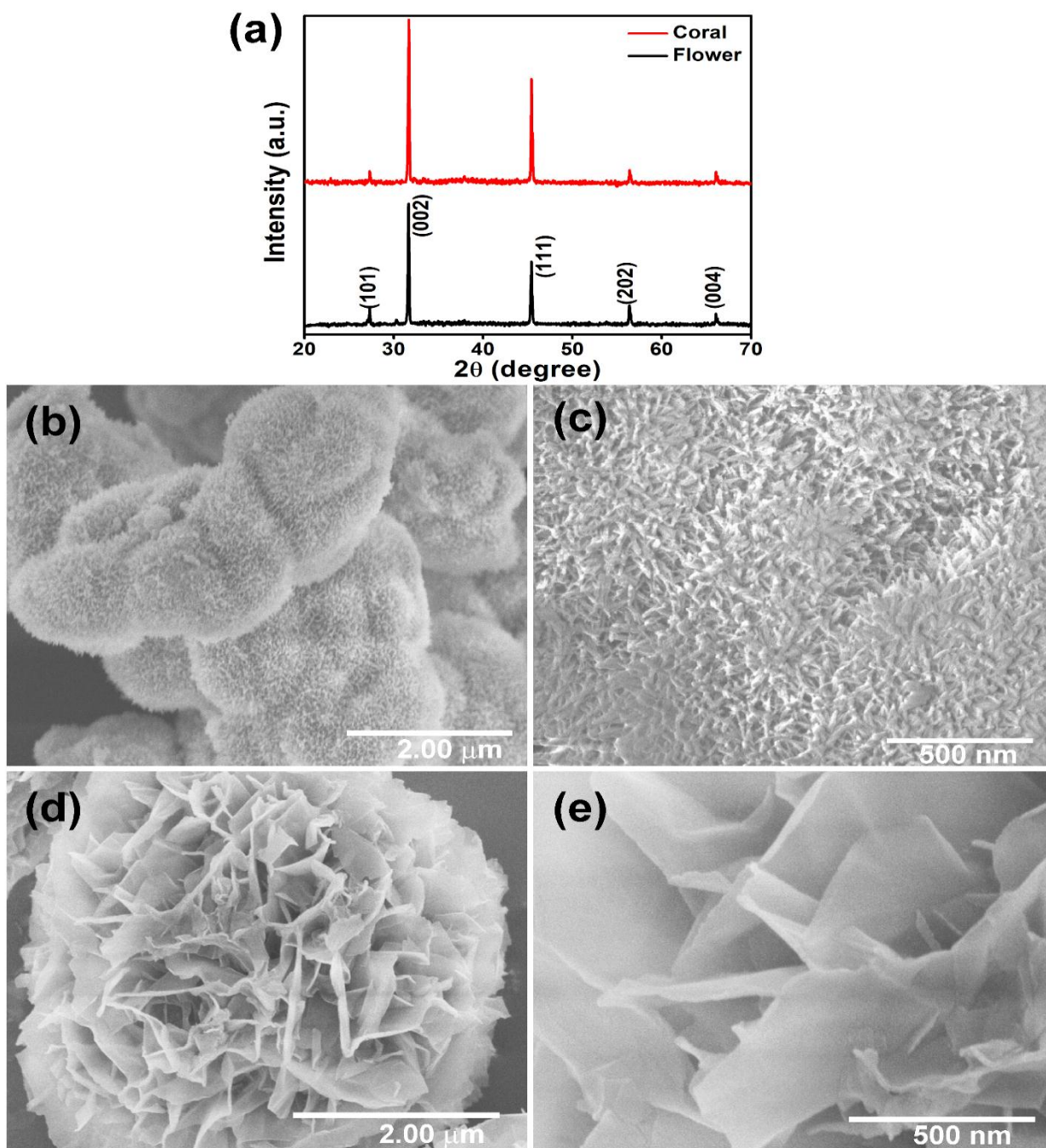
Fig. 5.1 Structural determination of prepared sample by (a). X-ray diffraction pattern of coral –
like and flower–like nanostructures. Top-view of field emission scanning electron microscopic
images of (b, c). coral–like and (d, e). flower–like nanostructures of Ni_2O_3.
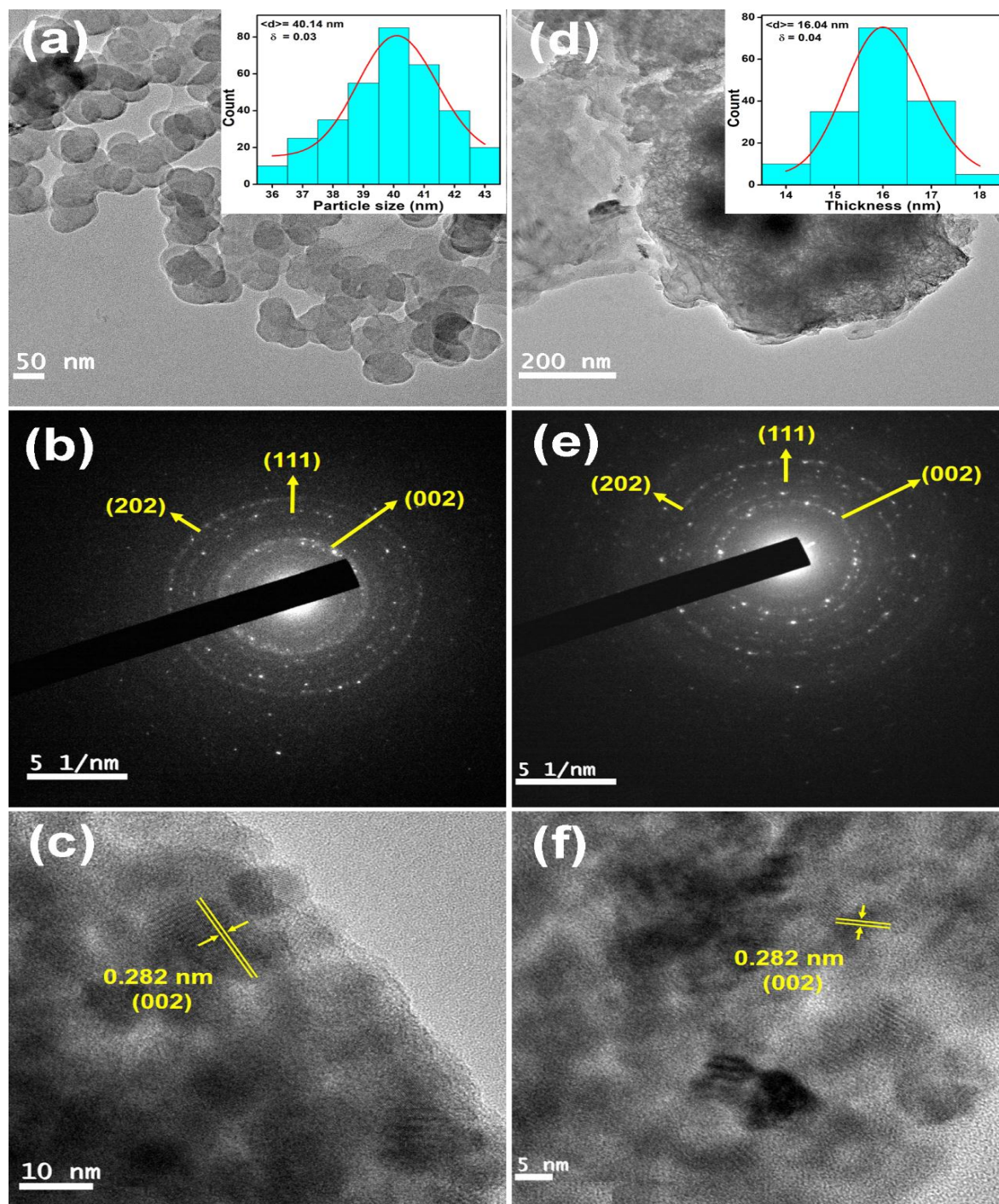
Fig. 5.2 TEM image of coral-like and flower-like Ni_2O_3 showing (a, d). Polycrystalline crystallites. (b, e). SAED pattern indicating the major diffraction planes and defect. (c, f). Lattice image showing strongest plane spacing. Inset Fig.5.2 (a, d). Distribution of the particle size of coral-like and thickness of flower-like of Ni_2O_3 nanostructures.

5.3.2. Growth mechanism

X-ray diffraction patterns of the intermediate product, formed after hydrothermal steps, are represented in Fig. 5.3 (a) (I-Coral and I-Flower represent as intermediate hydroxide of coral-like and flower-like nanostructure). In both cases, diffraction peaks, observed at 11.94˚, 24.01˚, 33.62˚, 37.36˚ and 60.26˚, correspond to the (003), (006), (101), (015) and (110) planes of the hexagonal phase of α-Ni(OH)$_2$ having lattice parameters of a = 3.08 and c = 22.2 Å.[21] This along with fact that no other peak was observed in any of the XRD patterns confirm the successful synthesis of phase pure α-Ni(OH)$_2$. Subsequently, FTIR spectroscopy analyses of these samples have been recorded (shown in Fig. 5.3 (b)). The spectra of both the samples reveal a band at around 3250 - 3550 cm^{-1} attributable to the O-H stretching vibrational mode of the H bonded water molecules (present in the interlamellar space of the turbostatic Ni(OH)$_2$).[22] Other bands that are common to both the samples have been observed at around 2230 cm^{-1},1630-1390 cm^{-1} and 680 cm^{-1} can be attributed to C≡N stretching vibration of OCN$^-$ ions (formed in the intermediate state owing to the use of urea), N-O stretching vibration mode of NO$_3^-$ (with C$_{2v}$ symmetry owing to grafting of ions to α-Ni(OH)$_2$ and D$_{3h}$ symmetry due to free movement of NO$_3^-$ within interlayer spacing of α-Ni(OH)$_2$) and Ni-OH bending vibration, respectively.[23] However, two distinct bands at around 830 cm^{-1} (for I-Coral) and 1135 cm^{-1} (for I-Flower) have been observed that can respectively be attributed to C-H bond bending vibration of PEG and S-O stretching in sodium dodecyl sulphate.
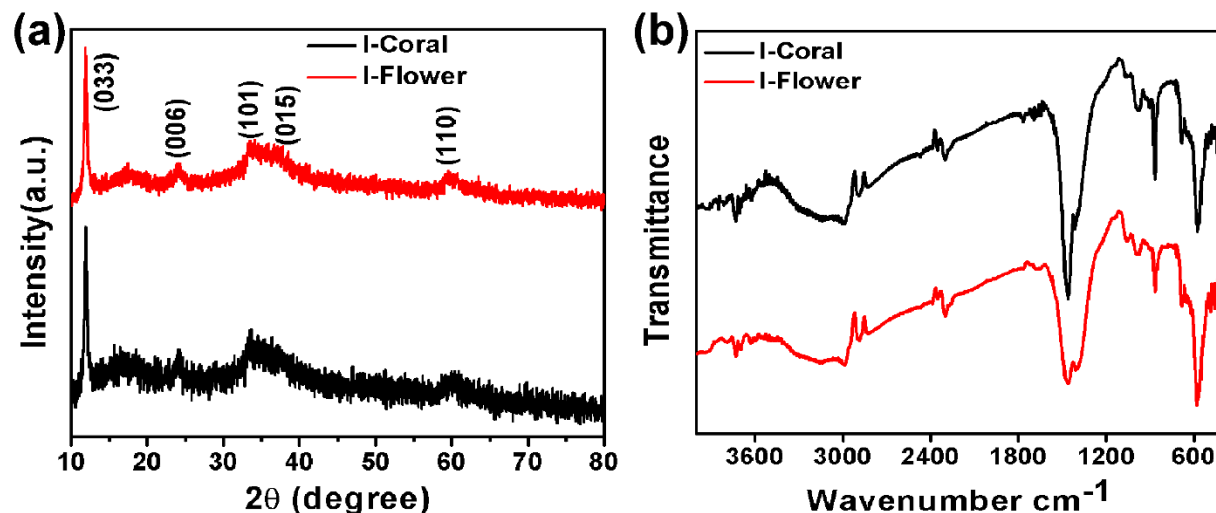
Fig. 5.3 (a). X-ray diffraction pattern of intermediate products for coral – and flower – like intermediate product; (b). Fourier transform infrared spectra of coral – and flower – like intermediate product.

Reaction mechanism of the synthesized nanostructures could be interpreted as follows: during hydrothermal step of coral–like nanostructure, aqueous solution of urea forms a closed cage-like structure through hydrogen bonding.[24] Urea starts acting as a host matrix for poly ethylene glycol (guest) as a filler of the gaps of this structure. The poly ethylene glycol's function, in this case, is to act as a binder for the Ni^{2+} ions. This binding takes place through the oxygen terminal of poly ethylene glycol. Subsequently on heating (during hydrothermal reaction), the urea decomposes to give CO_2 and NH_3. The resultant NH_3 then ionizes the water to form NH_4^+ and OH^-, a crucial step in the formation of the $Ni(OH)2$ nanostructures. The thus formed OH^- ions subsequently bind with the Ni^{2+} to form the resultant coral like structures, whose skeleton has been provided for by urea, as schematically shown below (Fig. 5.4).
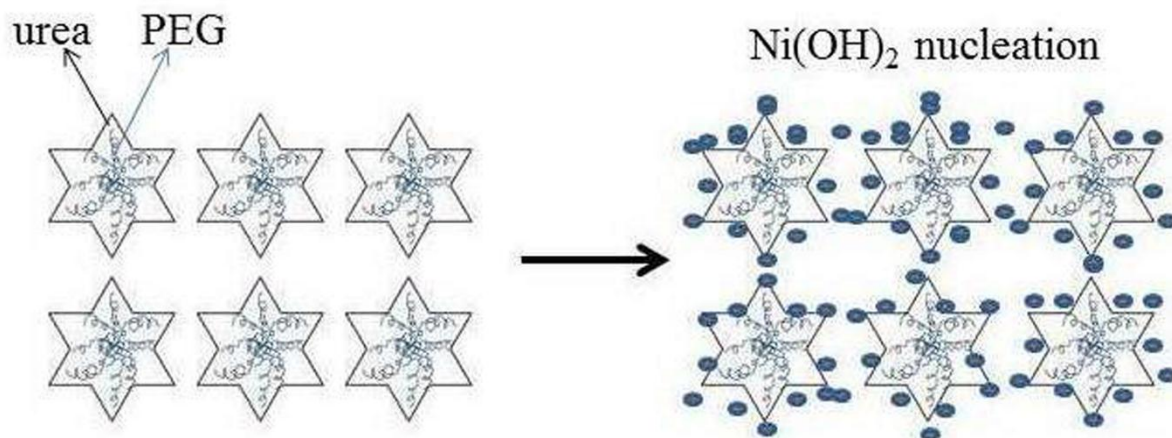
Fig. 5.4 Schematic diagram of formation of coral like morphology of Ni(OH)$_2$.

In case of synthesis of flower–like Ni$_2$O$_3$ nanostructure, the crucial part is the use of sodium dodecyl sulphate. Due to the presence of Na$^+$ ions in sodium dodecyl sulphate, cage like structure gets formed by decomposed urea [24] into small chain that binds to sodium dodecyl sulphate via hydrogen bonding. It is of utmost importance here that the fact that a urea molecule can form a maximum of our hydrogen bodings. Therefore, there is an abundance of sodium dodecyl sulphate molecule attachments to each of the hydrogen bonding sites. Sodium dodecyl sulphate also acts as binder to Ni^{2+} ions. Now as sodium dodecyl sulphate generally leads to the formation of sheet like structures, therefore considering each site of hydrogen bonding as a nucleation site, the resultant structure assumes a flower–like morphology (Fig. 5.5).

The overall reaction and the schematic of the mechanism can be illustrated as follows:
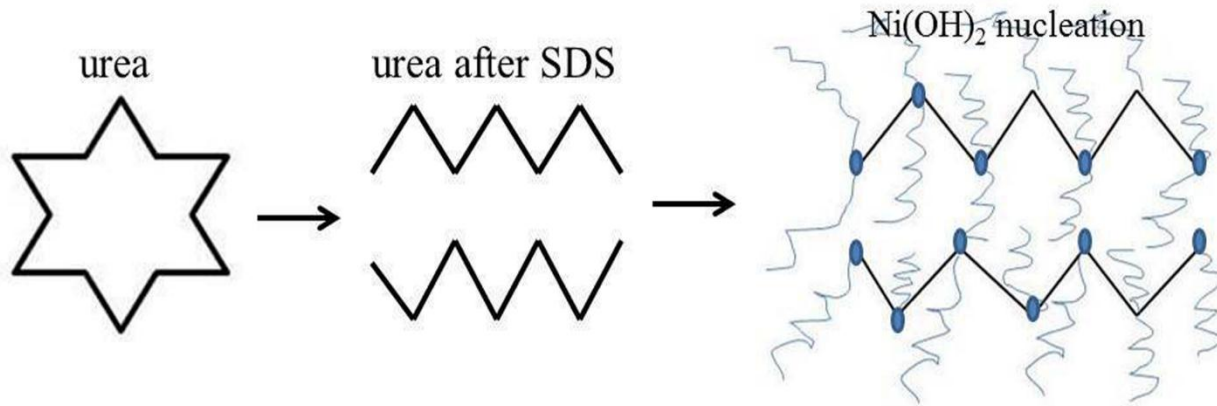
Fig. 5.5 Schematic diagram of formation of flower - like morphology of Ni(OH)$_2$.

The second step is the extended oxidation of the hydroxide nanostructure to form pure Ni$_2$O$_3$ nanostructure. Pure sodium hypochlorite, in presence of H$^+$ ions, forms unstable hypochlorus acid (HOCl) that decomposes into hydrochloric acid (HCl) and nascent oxygen ([O]). This nascent oxygen causes rapid oxidation of the hydroxide to eliminate the –OH from the hydroxide structure. This –OH, in turn, reacts with the Na$^+$ ions, present in the solution from the hypochlorite, to form NaOH. This NaOH then neutralizes the so formed HCl to form NaCl and H$_2$O. As the oxidation is very rapid and localized, the structure remains unaltered. The overall reaction ionic equation could be illustrated as follows:[20]

$$Ni(OH)_2 \xrightarrow{\text{In presence of polar solvent}} Ni^{2+} + 2OH^-$$

$$NaOCl \xrightarrow{\text{H}^+} Na^+ + OCl^-$$

$$H^+ + OCl^- \longrightarrow HOCl$$

$$HOCl \longrightarrow HCl + [O]$$

$$Ni^{2+}[O] \longrightarrow Ni^{3+} + 1e^-$$
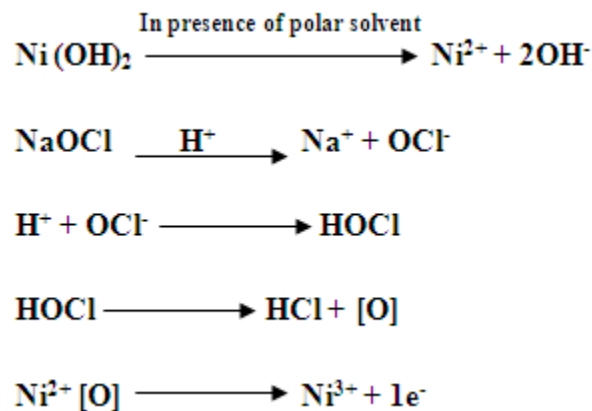
4.3.3. Determination of band gap

Optical properties of the synthesized nanostructures have been evaluated by employing UV-Vis absorption spectroscopy (Shimadzu 2401 PC). This study was carried out for the deposited thin films of our synthesized material by preparing well-dispersed solution in N,N-Dimethylformamide (DMF), in the range 300 – 700 nm. Direct bandgap (E_g) of the nanostructures were estimated using well-known Tauc equation:

$$\alpha = A\left(h\nu - E_g\right)^{1/2}/h\nu \qquad\qquad 5.1$$

where α, ν and 'A' represent the absorption coefficient, frequency of incident light and constant [25]. Using this equation, E_g has been calculated to be ~ 3.85 eV for both samples (shown in Fig. 5.6 (a, b).
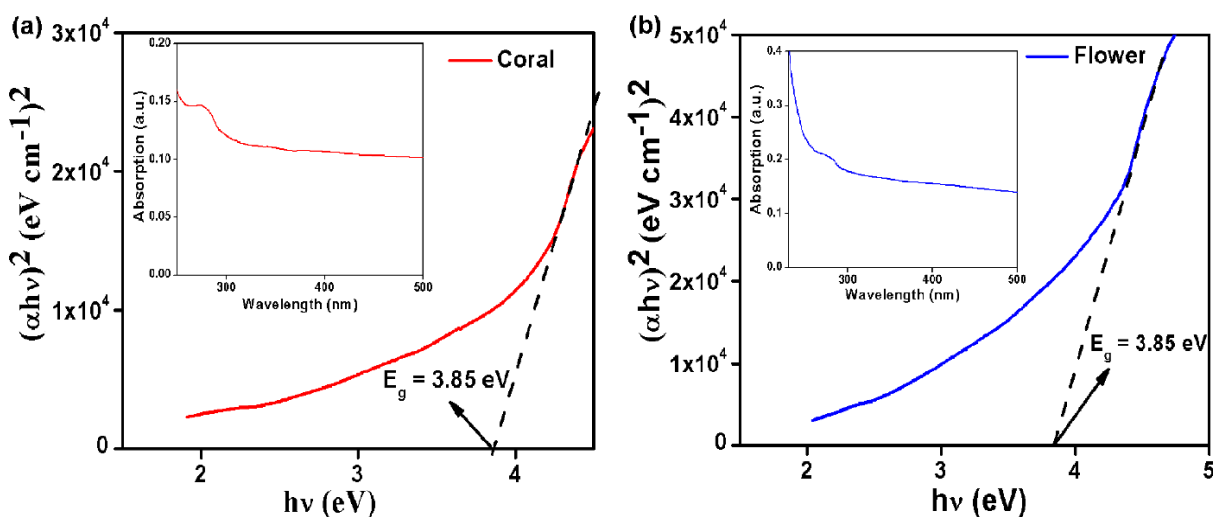
Fig. 5.6 (a, b) $(\alpha h\nu)^2$ vs. hν plots for the synthesized coral and flower-like nanostructures. (a, b Inset) figure shows their corresponding absorption spectra.

5.3.4. Investigation of the electron–phonon coupling by Raman and photoluminescence spectroscopy

Electron–phonon interaction which is crucial in the electronic processes in nanostructured materials as studied by many researchers including us [13, 16] has been evaluated by Raman spectroscopy. Raman spectra as shown in Fig. 5.7 (a) and (b) consists of two peaks, measured at 494 and 1072 cm^{-1} for coral–like nanostructure and 495 and 1067 cm^{-1} for flower–like nanostructure. Peaks are assigned to longitudinal optical one-phonon (1LO), longitudinal optical two-phonon (2LO) respectively.[26] Generally, phonons only at the center of the Brillouin zone contribute to the Raman spectra of an ideal bulk system, but non-zero wave vectors do contribute to Raman scattering when translational symmetry breaks down due to defects, impurities, finite size etc. Here, coral–like nanostructure exhibits higher Raman scattering intensity indicating higher defects in it. In this comparative study, we kept all experimental parameters like wavelength, power, spot-size of laser same for Raman scattering experiment.[27] Within Franck–Condon approximation, intensity ratio of 2LO and LO scattering modes (I_{2LO}/I_{LO}), known as Huang–Rhys S–factor, is a measure of electron–LO phonon interaction and it is calculated to be 0.40 and 0.22 for coral–like and flower–like nanostructures respectively.[28] Generally, S–factor is expressed by the following equation:

$$S = \sum_q \frac{|V_q^2|}{(\hbar\omega_{LO})^2} |\rho_q|^2 \qquad\qquad 5.2$$

where, V_q and ρ_q represent the strength of the electron–LO phonon interaction and Fourier transform of the charge density respectively. In order to examine contribution to 'S–factor' from either V_q or ρ_q, we have estimated ρ_q using PALS and the study illustrates less ρ_q for coral–like nanostructure which is attributed to higher defect concentration. Thus higher 'S–factor' in coral–

like nanostructure solely is attributed to higher V_q. Details of the PALS study have been discuss in section 5.3.5.
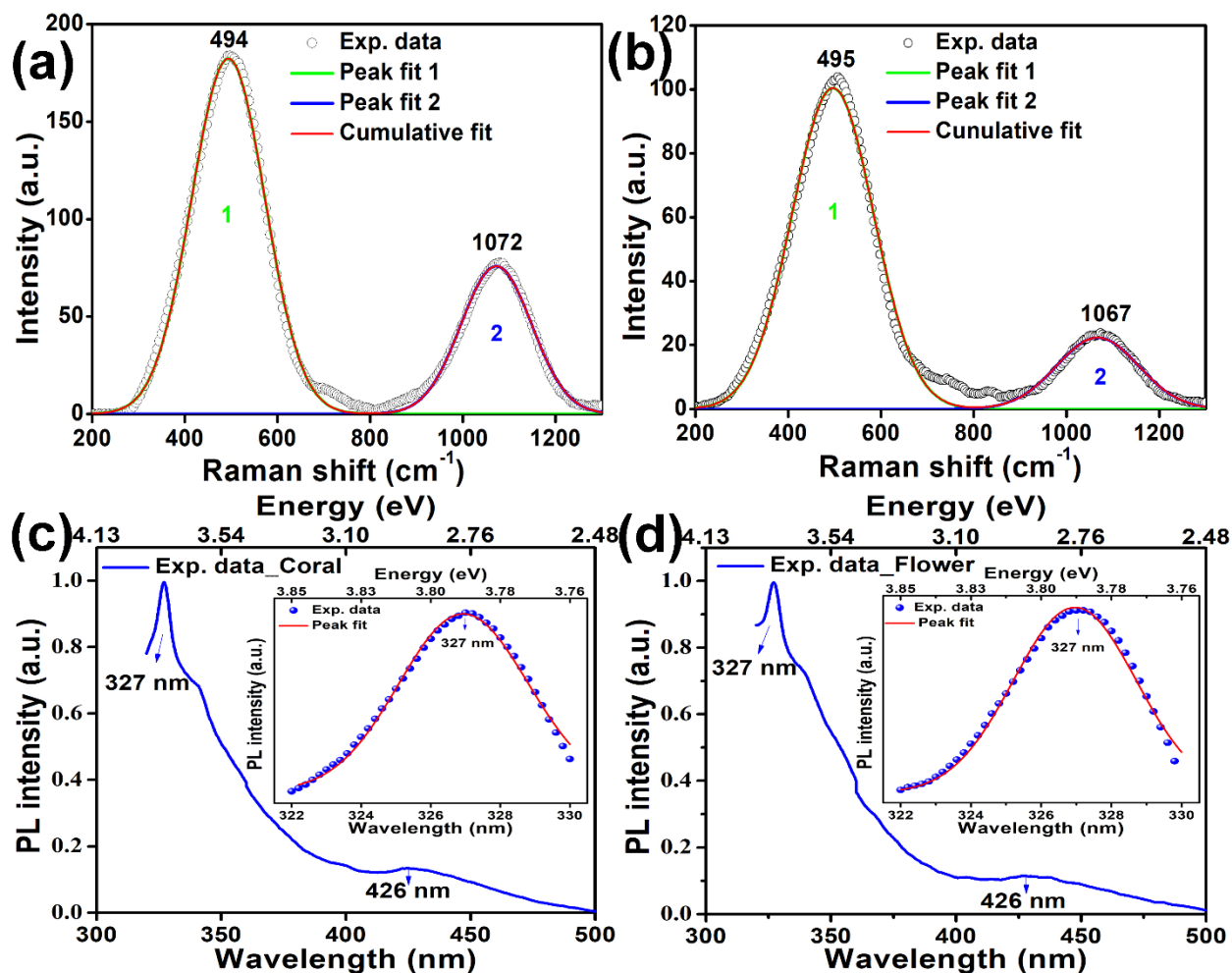
Fig. 5.7 (a, b). Raman spectra of the coral and flower – like nanostructures. (c, d). Experimentally measured and fitted (inset) normalized luminescence spectra of the synthesized coral and flower-like nanostructure.

Electron–LO phonon coupling has also been verified by spectroscopic studies. Normalized luminescence spectrum (Fig. 5.7 (c) and (d)) exhibits one prominent UV emission (327 nm) and one shoulder peak corresponding to visible emission (426 nm). UV peak is attributed to the near band edge emission, whereas visible peak denotes shallow impurity levels, formed due to Ni^{3+}

vacancies at the surface of the nanostructure. Higher intensity of visible peak in coral–like nanostructure also corroborates PALS and Raman studies. It has been examined previously by many researchers including us that FWHM of the emission band is linearly related to S–factor .[13] Presently, FWHM corresponding to band edge emission is measured 0.051 and 0.047 eV for coral–like and flower–like nanostructures respectively. Non-radiative decay being another a measure of electron–LO phonon coupling has also been studied by TCSPC which reveals higher electron–LO phonon interaction in coral–like nanostructure. Detail discussions on TCSPS measurement and analysis are provided in section 5.3.6. Therefore, above studies confirm that coral–like nanostructure possesses higher V_q compare to flower–like nanostructure.

5.3.5. Defect analysis by positron annihilation spectroscopy

Positron annihilation lifetime spectroscopy (PALS) has been employed to investigate defects as they acts as trapping center for positrons and utility of this technique in defect analyses has already been demonstrated by many researchers including us.[29-31] Annihilation parameters such as positron lifetimes, intensities detail the defect concentration, size of the defects within the synthesized nanostructures.[32] Analyzing the measured lifetime data with three lifetime component fit gives acceptable variance of fitting (0.94 – 0.97).[32] Experimentally measured spectra are represented in Fig. 5.8. Obtained three lifetime components, designed as shortest (τ_1), intermediate (τ_2) and largest (τ_3) lifetime and their respective I_1, I_2 and I_3 giving their contributions along with their uncertainties are presented in Table 5.1. τ_3 is generally attributed to the formation of orthopositronium atoms in the free space separating the nanostructure. Orthopositronium is assigned to the temporary bound states, formed within free space of the nanostructures like in between nanorods of the coral–like nanostructure and in between nanosheets

of the flower–like nanostructures. It is noticed from table that though τ_3 has largest value (> 2 ns), but its contribution is very small ($< 1\%$). Thus, first two components (τ_1 and τ_2) are selected for all practical purpose.[32] τ_1 is generally attributed to positron annihilation in defect – free bulk system, but nanostructures rarely grow with defect-free when prepared. Therefore, in nanostructures, τ_1 is generally assigned to smaller vacancies such as mono- or divacancies or shallow positron trapping centers.[30, 33]
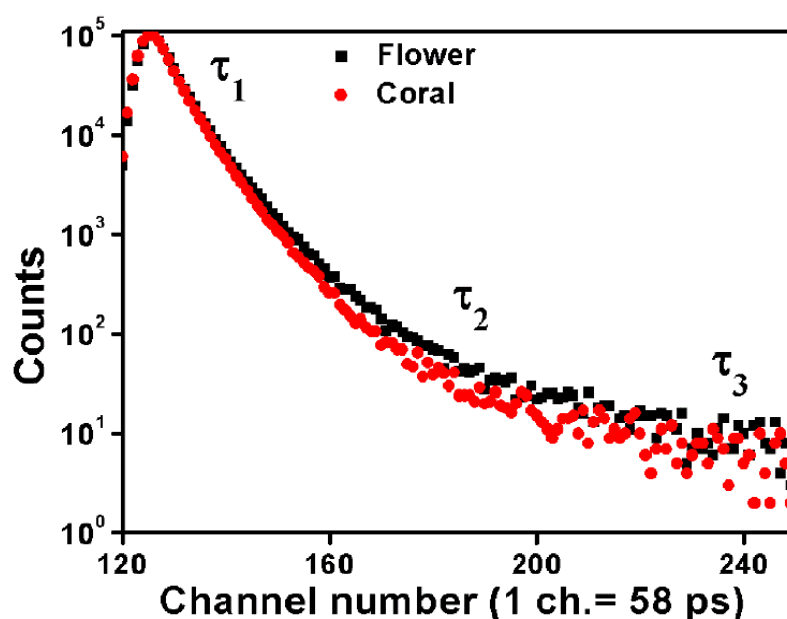
Fig. 5.8 PALS spectra for the synthesized nanostructures.

In this context, it may be stated that O^{2-} vacancy reduces average electron density leading to an enhancement of annihilation time, while Ni^{3+} vacancy exhibits reverse effect. Here, it has been observed that τ_1 is much higher than positron annihilation time in bulk system ($\tau_b = 0.002$ ns, calculated from the relation:[34] $\frac{1}{\tau_b} = \frac{I_1}{\tau_1} + \frac{I_2}{\tau_2}$, hence the positron trapping centers are referred to O^{2-} vacancies. It is observed from table that τ_1 as well as I_1 correspond higher magnitude in coral–like nanostructure compare to flower–like nanostructure i.e. it may be stated

that not only size of the anionic vacancies get decreased in flower–like nanostructure, but also concentration of such vacancies is getting decreased in flower–like nanostructures compared to coral–like nanostructure. τ_2 (> 300 ps) is generally referred to positron annihilation at vacancy clusters, formed due to agglomeration of smaller vacancies.[35] Average electron density in larger-sized vacancies is lower than that in mono- or divacancies, hence annihilation rate gets decreased here increasing annihilation lifetime.[36] Since, thermal diffusion length of positron in most of metallic oxide systems is ~ 50 - 100 nm which is much higher than size of our synthesized nanostructures, so τ_2 is assigned to annihilation of positron at vacancy clusters at surfaces of nanostructures.[37] Such surface vacancy cluster may be ascribed to the unsaturated bonds due to either O^{2-} vacancy or Ni^{3+} vacancy. But $\tau_2 > \tau_1$ indicates that vacancy clusters at the surface or intergrain region or free spaces between triple junctions of the synthesized nanostructures originates from O^{2-} vacancy.[38] Similar type of result was obtained by Fang et al.[39] It is observed from table that the magnitude of τ_2 also gets decreased from coral–like nanostructure compared to flower–like morphologies; hence average size of the O^{2-} vacancy clusters gets reduced in flower–like nanostructure compared to coral–like nanostructure. In contrast to I_1, it is noticed that I_2 increases from coral–like nanostructures to flower–like nanostructure i.e. vacancy cluster at the surface of the nanostructure is found to higher in case of flower–like nanostructure. In this context, it may be stated that good and statistically accurate parameter is the average lifetime τ_{av} indicating average vacancy in nanostructured materials has been calculated using the equation $\tau_{av} = \frac{\tau_1 I_1 + \tau_2 I_2}{I_1 + I_2}$ and are represented in Table 5.1. From table, it can be stated that the coral–like nanostructure possesses higher value of τ_{av} (higher overall defects) indicating less average electron density in coral–like nanostructure and is assigned to higher defects.

Table 5.1 Positron annihilation lifetime parameters of the synthesized coral-like and flower–like nanostructures.

Sample name	τ_1 (ns)	τ_2 (ns)	τ_3 (ns)	I_1	I_2	I_3	τ_{av}(ns)	χ^2
Coral–like nanostructure	0.1619 ±0.0044	0.3231 ±0.0053	2.4370 ±0.1418	44.0747 ±2.7130	55.5632 ±2.6997	0.3621 ±0.0295	251.79	0.97
Flower–like nanostructure	0.1479 ±0.0037	0.3116 ±0.0061	2.9218 ±0.1355	37.5124 ±2.2992	62.0845 ±2.2903	0.4030 ±0.0228	249.94	0.94

5.3.6. Determination of radiative and non-radiative lifetime of Ni_2O_3 nanostructures

Time correlated single photon counting (TCSPC) spectroscopy is employed in an effort to examine the effect electron – phonon interaction in the excited state of the electron. Careful analysis of the emission spectra reveals that all the spectra could be satisfactorily fitted by double-exponential decay function: $B_{NR}exp(-t/\tau_{NR}) + B_R exp(-t/\tau_R)$, where τ_i and B_i (i = R, NR) represent the time-constant and percentage of contribution respectively.[40]
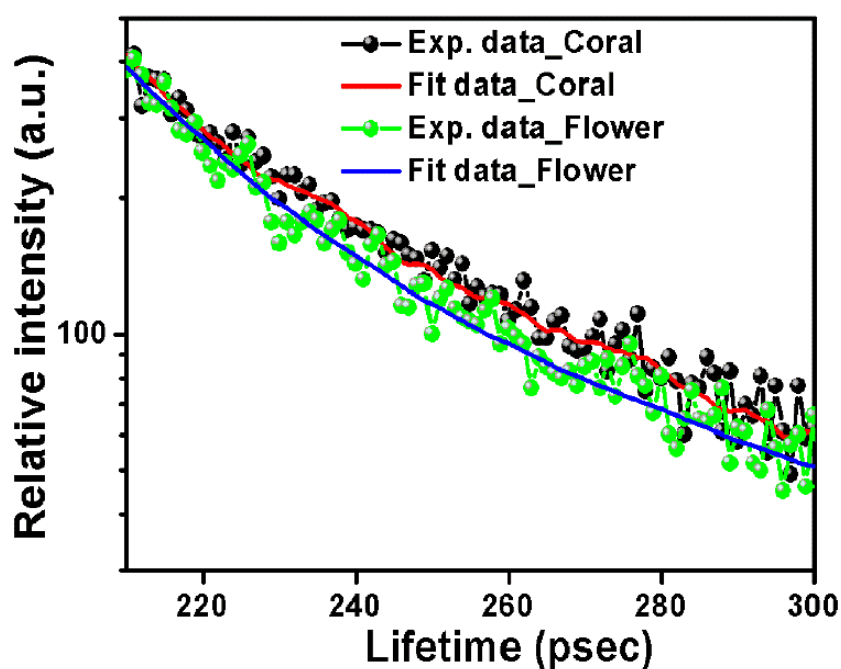
Fig. 5.9 Experimentally measured time-resolved PL spectra, fitted with exponential decay curve.

After fitting (shown in Fig. 5.9), τ_i and B_i (i = R, NR) are obtained and are listed in Table 5.2. B_{NR}, referred as non-radiative contribution, dominates over B_R, defined as radiative contribution, for both the samples signifying major contribution of former to the relaxation of excited electrons. τ_{NR}, attributed to non-radiative recombination lifetime of photoexcited electrons, is less for coral–like nanostructure compared to other indicating higher non-radiative transition probability in it, attributed to higher electron – phonon interaction. τ_R possesses opposite trend that can be described briefly according to the following way: radiative recombination rate, $W_R = \left(\dfrac{1}{\tau_R}\right)$, is described by the following equation :[41]

$$W_R \propto |\int \psi_f P \psi_i dv|^2 \qquad 5.3$$

where, P represents the momentum operator. In the case when they are not tightly bound to the crystal, the radiative recombination rate can be expressed as [42]

$$W_R(r) = W_R e^{-2r/a_B} \qquad 5.4$$

where r and a_B represent the delocalization of the electron-hole pair and Bohr radius respectively. Thus, higher τ_R in coral–like nanostructure is attributed to the higher localization of charge carriers due to electron – phonon interaction. Lower quantum yield (4.7% and 13.6% for coral–like and flower–like nanostructure respectively) is attributed to the higher nonradiative, assigned to higher electron – LO phonon interaction in coral – like nanostructure. As shown in Table 5.3, our synthesized nanostructures possess quantum yield similar to other photosensitive materials.

Table 5.2 Radiative, nonradiative, luminescence lifetime and their contribution and quantum yield.

Sample name	τ_{NR}(ns)	τ_R(ns)	B_{NR} (%)	B_R (%)	τ_{PL} (ns)	Quantum yield (%)
Coral–like nanostructure	0.140	2.80	92.6	7.4	0.133	4.7
Flower–like nanostructure	0.432	2.75	77.7	22.3	0.373	13.6

Table 5.3 Quantum yield of few photovoltaic materials

Material	Quantum yield (in %)	References
$CuInSe_2$	3.4	Wu *et al*.[43]
TOPO functionalized CdSe	13.2	Liu *et al*.[44]
Mn doped ZnSe	3.5	Gopi *et al*.[45]

5.3.7. Understanding of the electron – phonon interaction for different nanostructures

Defects which inherently depends on the synthesis process of the nanostructured material significantly effect in many electronic processes such as exciton, absorption, refractive index, polaronic effect etc. [46] Generally, fractional-dimensional space approach is employed to understand the defect induced electronic processes within the nanostructured materials. In this method, defect induced anisotropic electronic interaction is considered as an isotropic interaction in an effective-order fractional-dimensional space where fractional-dimension provides the measure of anisotropy of the actual physical system. Importantly, such space, named as dynamic space, differs from actual geometric space, in that its dimensionality is determined by physical interactions. As coral–like nanostructure contains higher defect compare to flower–like nanostructure, thus it may be stated that coral–like nanostructure exhibits higher fractional–

dimension. Within fractional-dimensional space approach, variation of V_q on morphology can be explained as follows: considering the approach by Peeters *et al.* [47], V_q can be written in the form: [48]

$$V_q = \Sigma_q[C(\mathcal{D})_q \widehat{b_q}(\exp(iq.r)) + C(\mathcal{D})_q^* \widehat{b_q}^\dagger(\exp(-iq.r))] \qquad 5.5$$

where, $b_q^\dagger$ (b_q) and $C(\mathcal{D})_q$ represent creation (annihilation) operator for a phonon with wavevector q and V_q in 'D-dimension.' Assuming Coulomb-like interaction between electron and phonon in 'D-dimension,' $C(\mathcal{D})_q$ gets simplified into the following form:

$$C(\mathcal{D})_q = -i\hbar\omega_{LO}\left(\frac{F_\mathcal{D}(q)\alpha}{V_\mathcal{D}}\right)^{\frac{1}{2}} \left(\frac{\hbar}{2m\omega_{LO}}\right)^{1/4} \qquad 5.6$$

where, $F_\mathcal{D}(q) = (2\pi)^{\mathcal{D}/2}\int_0^\infty dr\, r^{\mathcal{D}-1} qr^{\left(1-\frac{\mathcal{D}}{2}\right)} J_{\frac{\mathcal{D}}{2}-1}(qr)\frac{1}{r}$ represents fractional dimensional Fourier transform of the Coulomb-like potential. In this expression, 'm', $'\alpha'$ and $V_\mathcal{D}$ represent electron effective mass, Fröhlich constant and volume of the crystal in 'D-dimension' according to Born–von Karman condition. After integrating $C(\mathcal{D})_q$ and substituting its expression, the following form of V_q^2 can be obtained:

$$\left|V_q^2\right| = \frac{\Gamma\left(\frac{D-1}{2}\right)(4\pi)^{\frac{D-1}{2}}}{V_\mathcal{D}}\alpha\frac{(\hbar\omega_{LO})^2}{q^{\mathcal{D}-1}}\left(\frac{\hbar}{2m\omega_{LO}}\right)^{1/2} \qquad 5.7$$

Fig. 5.10 depicts the variation of $\left|V_q^2\right|$ with 'D' in units of $\frac{\left(\frac{\hbar}{2m\omega_{LO}}\right)^{1/2}(\hbar\omega_{LO})^2}{V_\mathcal{D}}\alpha$ (q = 0.02, 0.05, 0.1 and 0.2). It is noted from figure that V_q gets decreased with decreasing 'D' illustrating higher V_q in coral–like nanostructure due to higher fractional–dimension, induced by defects.
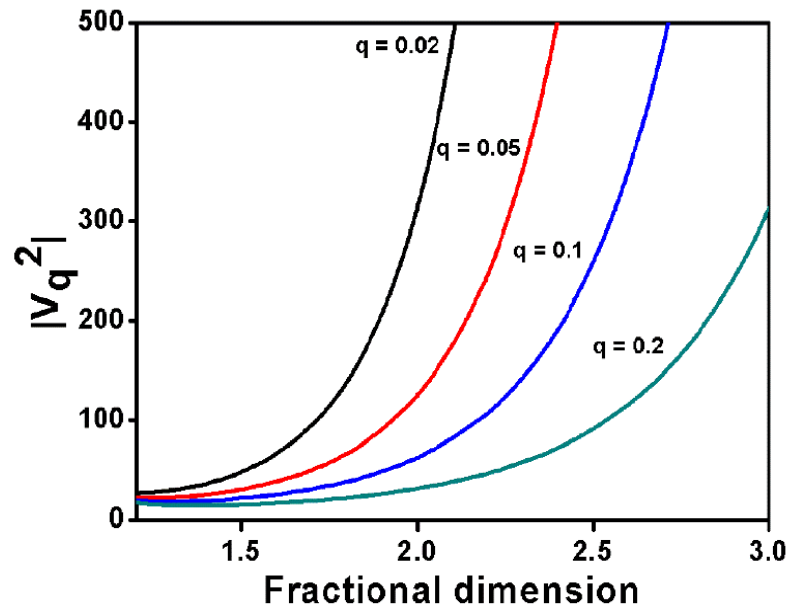
Fig. 5.10 Variation of electron–phonon coupling with fractional dimension of the system.

5.3.8. Ni_2O_3 nanostructure / Al metal – semiconductor junction: space charge limited current mechanism of the device, non-adiabatic charge transport

As has been calculated from well–known empirical equation [49] ($\delta = \chi - 4.5 - 0.5E_g$, χ and E_g represent electronegativity and band gap respectively), electron affinity (δ) of Ni_2O_3 is 3.71 eV which considerably differs from work function (φ) of Al (4.08 eV). As such, upward band bending is expected at the interface that gives non-Ohmic contact.[50] In order to gain insight into the electronic transport processes across the junction, owing to their potential in optoelectronic devices particularly as photo-responsive material, traditional current–voltage (*I–V)* testing was employed on the fabricated Al / Ni_2O_3 nanostructure / ITO heterojunction device (schematic diagram Fig. 5.11 (a)).
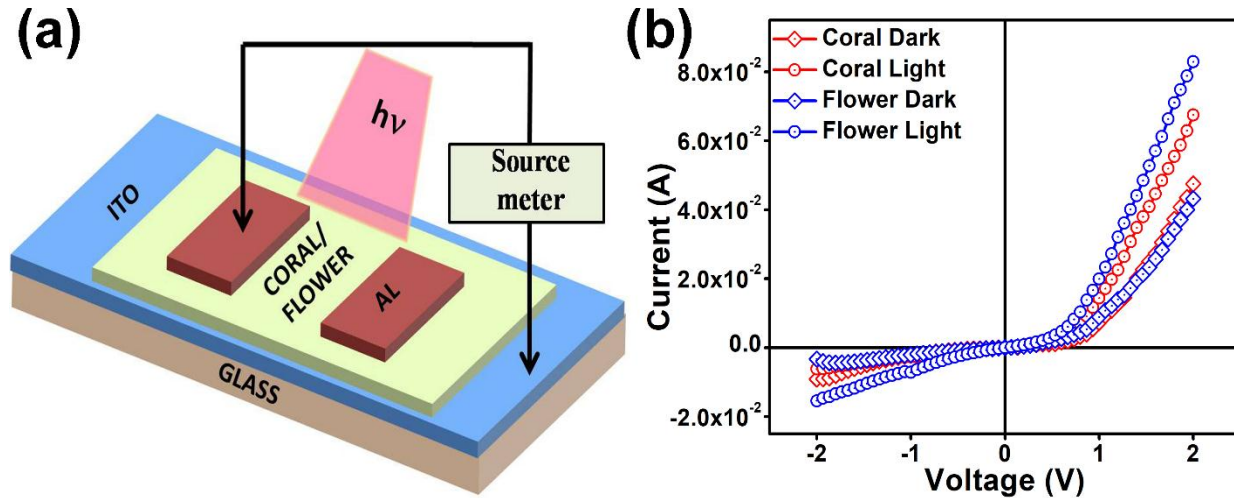
Fig. 5.11 (a). Al/Ni$_2$O$_3$ nanostructure / ITO sandwich heterojunction device at light irradiance for both coral and flower-like nanostructure; (b). I – V characteristic of Al/Ni$_2$O$_3$ nanostructure Schottky junction under dark and irradiance of light.

Here, all the measurements were carried out at room temperature at an applied bias voltage of ± 2V under dark as well as under photo-irradiation. *I–V* characteristic (Fig. 5.11 (b)) shows typical diode rectifying nature with rectification ratio (I$_{forward}$ / I$_{reverse}$) ~ 21.4 and 31.2 for coral–like Ni$_2$O$_3$ and 26.3 and 37.5 for flower–like nanostructures at ± 2V under dark and photo-irradiance respectively. Rectifying character of diode is attributed to MS junction, formed at the interface between Ni$_2$O$_3$ and Al.[51] Fairly low turn-on voltage ~0.53 and 0.36 V are deduced from *I–V* curve under forward biased condition for coral–like and flower–like nanostructure based devices respectively. Generally, forward *I–V* characteristic of these Schottky typed MS devices obeys thermionic emission, described by equation 5.8: [6, 52-55]

$$I = I_0 \left[\exp\left(\frac{q(V-IR_s)}{\eta kT} \right) - 1 \right] \qquad 5.8$$

$$\text{with, } I_0 = A|A^*|^2 T^2 \exp\left(\frac{-q\emptyset_B}{kT} \right) \qquad 5.9$$

where, I, I_0 and V represent the forward current, reverse saturation current and applied bias voltage respectively. q, K, η, R_S and T are the electronic charge, Boltzmann constant, ideality factor, diode series resistance and absolute temperature respectively.[52] A is the active surface area of the diode, A^* the Richardson's constant and $\emptyset_B$ the Schottky barrier height. In this context, it is to mention that η, R_S, $\emptyset_B$ are the parameters, used to characterize MS devices. Presently, η and R_S are estimated from intercept and slope of the dV/dln(I) versus I curve (Fig. 5.12 (a) and (b)) obeying equation 5.10 which has been derived from equation 5.8 [56]:

$$\frac{dV}{dln(I)} = \left(\frac{\eta kT}{q}\right) + IR_S \qquad 5.10$$

Here, A is equal to 7.065×10^{-2} cm^2, determined by shadow mask for all the samples, while A^* is 32 AK^{-2} cm^{-2}. [2] Table 5.4 represents the calculated values of η and R_S for the fabricated devices. In general, η = 1 solely attributes thermionic current across the junction, while η > 1 affords non-thermionic current transports due to electron-hole recombination in the depletion region, tunneling etc. Briefly, 1 < η < 2 corresponds to combination of recombination and diffusion currents, while η > 2 reflects the dominance of recombination current in this devices.[57] Presently, we have noticed 1 < η < 2 for our devices indicating non-thermionic charge transport, ascribed to diffusive current.[58] Presently, we have observed that η value gets decreased in the presence of light irradiation indicating dominance of thermionic current. Compare to coral–like, flower–like nanostructure based device exhibits η lies close to unity signifying less diffusive current.
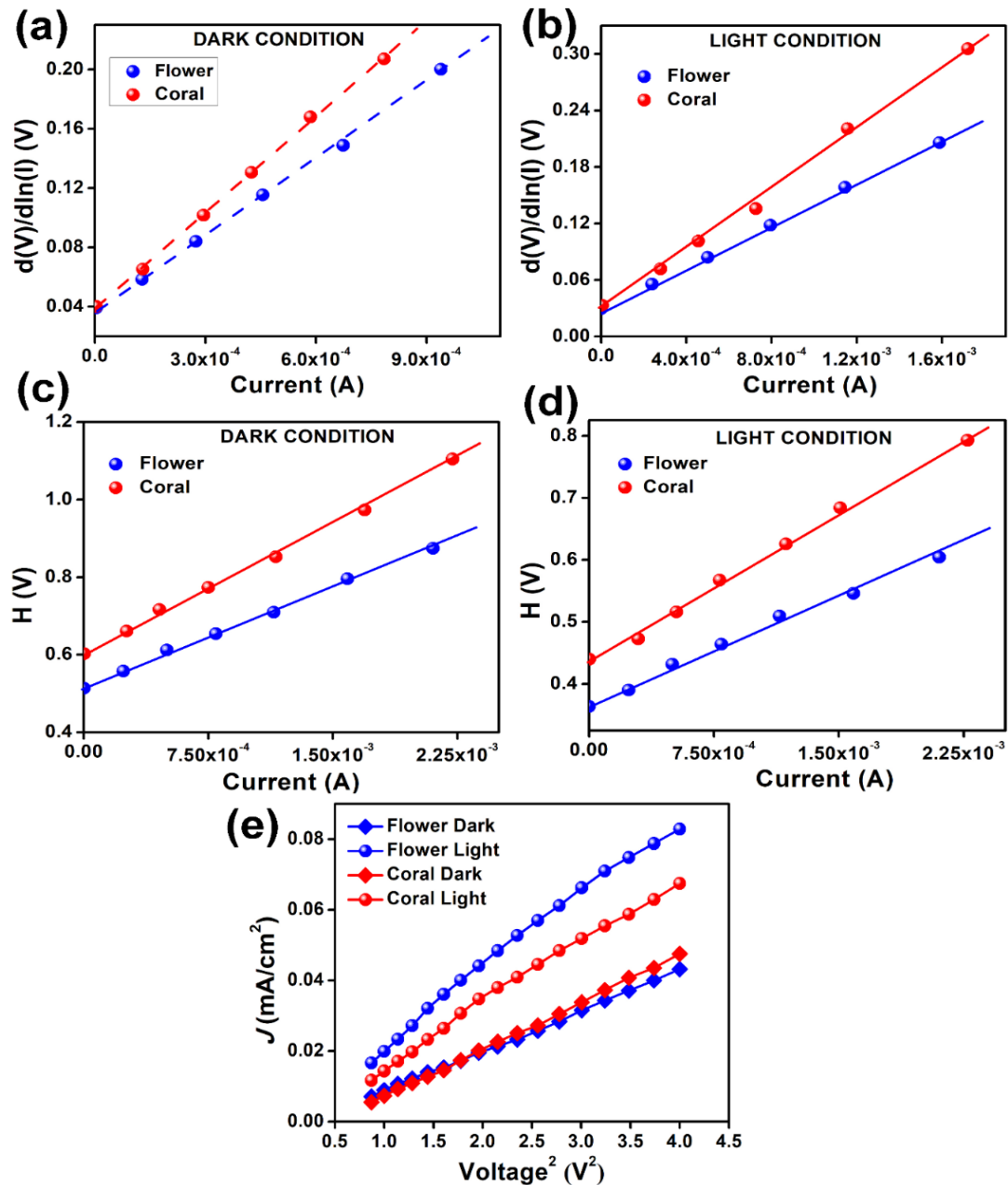
Fig. 5.12 Al/Ni$_2$O$_3$ nanostructure Schottky junction characteristic at under dark and light irradiance for both coral and flower-like nanostructure. (a, b). dV/dln(I) versus I curves under dark and light irradiance; (c, d). H versus I curves under dark and irradiance of light; (e). J versus V^2 plot under dark and irradiance of light.

In addition, $\eta > 1.25$ (under dark) along with higher R_S of coral–like nanostructure based devices indicates that this particular device doesn't exhibit an intimate MS contact such as flower–

like based device, but instead possesses metal–interface–semiconductor configuration. Such variation is assigned to the enhanced interfacial inhomogeneity due to Ni^{3+} vacancies of coral–like nanostructure. $\emptyset_B$ which primarily depends on the interface and determines turn-on voltage has been calculated using well-known Cheung function H(I), given by equation 5.11. [31]

$$H(I) = IR_S + \eta\emptyset_B \qquad\qquad 5.11$$

Main advantage of the present method is that the device parameters can be calculated from single forward *I–V* characteristics, unlike Norde's and Sato–Yasumura's approach.[59] Table 5.4 represents $\emptyset_B$, measured under dark and light irradiation from intercept on y-axis corresponding to H(I) vs. I curve (Fig. 5.12 (c) and (d)). Importantly, $\emptyset_B$, measured under dark, is higher than $\emptyset_B$, obtained in the presence of light irradiation. Such variation is attributed to Fermi level pinning effect. Though, $\emptyset_B$ primarily depends on the difference between 'δ' of Ni_2O_3 and 'φ' of Al,[60, 61] but presently, we have observed different $\emptyset_B$ for two different nanostructure based devices (discussed later). Carrier mobility (μ_{eff}), lifetime (τ), density of states at Fermi energy ($\rho(E_F)$), diffusion length (L_D) etc. are parameters, required to characterize MS device. In this context, μ_{eff} illustrating whether or not generated charge carrier can be extracted before recombination has been evaluated here according to Mott-Gurney theory. Main advantage of the present method is that unlike field effect transistor or Hall measurement giving in-plane mobility, it probes out-of-plane mobility, required for photosensitive device and also helps to understand charge transport through the interface.[62] According to this method, current density–voltage (*J–V*) characteristic is described by space charge limited current (SCLC). At low bias voltages, thermally generated charge carriers dominate conduction mechanism giving linear *J–V* characteristic. With increasing bias voltage, injected charge carriers exceed thermally generated charge carriers and fill the trap states giving SCLC. In this applied voltage regions, carrier injection into the device increases

exponentially that builds up a self-limiting space charge region, then the device follows Mott–Gurney SCLC, described by equation 5.12:[63]

$$J = \frac{9\mu_{eff}\varepsilon_0\varepsilon_r}{8}\left(\frac{V^2}{d^3}\right) \qquad\qquad 5.12$$

where, ε_0, ε_r and 'd' are permittivity of free space, dielectric constant and thickness of the device respectively. Straight line nature of J–V^2 (Fig. 5.12 (e)) confirms Mott-Gurney characteristics of our fabricated MS device.[64] Employing ε_r (4.21 and 1.32 for coral– and flower–like nanostructure respectively, measured by LCR meter) into equation 5.12, μ_{eff} has been calculated (Table 5.4). We propose electron–phonon interaction originating from defects of the nanostructures causes such variation in μ_{eff} (discussed later). $\rho(E_F)$, L_D, τ etc. of the devices have been evaluated using equations 5.13 – 5.15 under dark as well as light irradiation (presented in Table 5.4):[31]

$$\rho(E_F) = \frac{2\varepsilon_r\varepsilon_0\Delta V}{qd^2\Delta E_F}, \qquad\qquad 5.13$$

where

$$\Delta E_F = kT\ln\left(\frac{I_2V_1}{I_1V_2}\right)$$

$$\tau = \frac{9\varepsilon_0\varepsilon_r}{8d}\left(\frac{V}{J}\right) \qquad\qquad 5.14$$

and

$$L_D = \sqrt{2D\tau} \qquad\qquad 5.15$$

here, V_1, V_2, I_1, I_2 and D represent different voltages and currents applied to the diode in the space charge region and diffusion coefficient respectively. In this context, it may be stated that L_D also follows the trend of μ_{eff}. We have compared our device parameters with few other MS devices (represented in Table 5.5). It would be important to mention that our Ni_2O_3 / Al based MS devices exhibit (i) less non-thermionic current, (ii) low R_S and (iii) low $\emptyset_B$ suitable for low turn-on voltage.

In addition, the junction characteristic is found to be dependent on the defect of the nanostructures and is very sensitive to light irradiation. Therefore, the junction, fabricated with Ni_2O_3 as an active semiconducting material, is predicted be an attractive for photo-responsive optoelectronic devices.

Table 5.4 MS heterojunction parameter for Coral-like and Flower-like Ni_2O_3.

Sample name	Condition	η	R_s (Ω)	$\emptyset_B$(eV)	μ_{eff} (m²V^{1}s^{-1}) x 10^{-10}	τ (Sec) x 10^{-3}	L_D (m) x 10^{-7}	$\rho(E_F)$ (eVm^{-3}) x 10^{40}
Coral – like	DARK	1.59	216.1	0.39	5.31	4.64	3.56	7.13
	LIGHT	1.25	155.8	0.35	8.65	4.89	4.87	6.56
Flower – like	DARK	1.47	178.3	0.36	9.43	3.80	4.12	4.94
	LIGHT	1.11	111.4	0.33	16.73	3.05	5.13	3.09

Table 5.5 Comparison of MS heterojunction parameters with few other MS heterojunctions.

Hetero structure	Condition	η	R_s (Ω)	$\emptyset_B$(eV)	μ_{eff} (m²V^{1}s^{-1}) x 10^{-10}	τ (Sec) x 10^{-3}	L_D (m) x 10^{-7}	$\rho(E_F)$ (eVm^{-3}) x 10^{40}	Reference
Cd(II)-MOF	DARK	5.52	805.3	0.367	0.01091	0.0102	0.738	0.0416	[65]
	LIGHT	3.54	404.4	0.337	0.01099	0.0053	0.741	0.0459	
ZnO	DARK	0.38		0.57	7300000	0.00000309	0.00117	7.41 x 10^{-14}	[31]

Heterostructure	η	R_s (Ω)	$\emptyset_B$(eV)	References
CH3NH3PbBr₃/Pt	1.7 (dark)	169.2 x 10³ (dark)		[25]
	3.3 (light)	212.2 (light)		
SnTe/Si	1.89 (dark)			[66]
Coral-like Ni₂O₃/Al	1.59 (dark)	216.1 (dark)	0.39 (dark)	Present work
	1.25 (light)	155.8 (light)	0.35 (light)	
Flower-like Ni₂O₃/Al	1.47 (dark)	178.3 (dark)	0.36 (dark)	Present work
	1.11 (light)	111.4 (light)	0.33 (light)	
CoSi2/Ti	1.52 (dark)		>0.60	[67]
Pt/ZnO	3.69 (dark)			[68]
Ag/n-GaAs	1.11 (dark)		0.81 (dark)	[69]
n-GaN(0001)/Pt	1.7(dark)		1.11 (dark)	[70]
nGaN(0001)/Au	1.46 (dark)		0.91 (dark)	[70]
n type β-Ga2O3 / Au (100)	1.09 (dark)		1.07 (dark)	[71]
ploymethylmethacrylate – graphene – silicon	1.7 (dark)			[72]
graphene oxide / silicon	3.98-2.03 (dark)			[73]
Pt/CdSe	9.9 (dark)			[3]
Al – Si	1.8 (dark)			[74]
Pt/CH₃NH₃PbBr₃	1.7 (dark)	169.2 (dark)		[25]
		212.2 (light)		
Graphene / n-type Si			0.41	[75]

5.3.9. Understanding of the MS junction parameters on defect of the nanostructures

In order to understand the effect of V_q on MS device parameters, we consider thermionic–emission–diffusion theory, described by Crowell and Sze.[76] According to this theory, electron transport through MS junction devices is governed by two current–limiting processes, namely

diffusion and drift of carriers within the semiconductor region of the contact and thermionic emission across the metal–semiconductor interface. It has been examined previously that the current through MS junction is determined either by the process causing larger impediment to the charge carrier or by their combined effect if they are comparable. This theory assumes that current density, J(V), at an applied voltage 'V' is described by equation 5.16 and 5.17: [77]

$$J(x; V) = |e|\mu(x)\, n(x; V)\, \mathcal{E}(x; V) + |e|D(x; V)\frac{dn\,(x;\,V)}{dx} \qquad 5.16$$

$$\frac{\partial E(x)}{\partial x} = \frac{|e|}{\epsilon}(N_D - n\,(x)) \qquad 5.17$$

where, $n(x; V)$, $D(x; V)$, $\mathcal{E}(x; V)$ are the electron density, diffusion coefficient of electrons and electric field $(= -\frac{dV(x)}{dx})$ respectively. $|e|$, ϵ and N_D represent the magnitude of the electronic charge, dielectric permittivity and donor density in the semiconducting region. Other current-limiting process, thermionic emission, across the junction depends on the boundary condition at the top of the potential barrier and is described in terms of the effective recombination velocity (v_r) of the charge carriers, expressed by equation 5.18:

$$J(x; V) = |e|[n_0(x) - n_0^{eq}(x)]v_r \qquad 5.18$$

where, $n_0(x)$, $n_0^{eq}(x)$ and v_r are the electron density, quasi-electron density at thermal equilibrium and recombination electron velocity respectively. Briefly, $n_0(x)v_r$ and $n_0^{eq}(x)v_r$ represent electron flux from semiconductor to metal and flux in reverse direction respectively. $n_0^{eq}(x)$ and v_r are generally related with density of states (N_c) of semiconductor by the expressions $n_0^{eq} = N_c e^{-\frac{q\phi_B}{kT}}$ and $v_r = A^*T^2/|e|N_c$ respectively. Here, β, defined by $\beta = \mu_{eff}kT/|e|L_Dv_r = k\mu_{eff}N_c/L_DA^*T$, is used to measure diffusion and thermionic contributions to current. Generally,

$\beta \gg 1$ indicates thermionic emission contribution, while $\beta \ll 1$ signifies diffusion contribution. Thus, material with either lower μ_{eff} or lower N_c or higher L_D would exhibit lower thermionic contribution to junction current giving higher value of η. Presently, we have noted lower N_c and higher L_D for our coral–like nanostructured device, thus these two parameters can't be attributed to higher diffusion contribution to the current. Therefore, higher η in coral–like nanostructured devices is solely attributed to lower μ_{eff}, assigned to higher V_q as shown in the flow chart (Fig. 5.13 (a)) Similarly, lower L_D and higher N_c in coral–like nanostructure are also be ascribed to defect.

The variation of $\emptyset_B$ can be explained in the following way: in case of adiabatic charge transfer processes, $\emptyset_B$ is defined by the difference between 'δ' and 'φ'. Introduction of V_q generally enhance δ, thus coral–like nanostructure would exhibit less $\emptyset_B$ in comparison to flower–like nanostructure. However, opposite trend has been observed here indicating that the charge transport mechanism can't be explained using adiabatic process; rather it can be explained on the basis of non-adiabatic mechanism. According to this approximation, when an electron migrates from semiconductor, it causes rearrangement of the lattice that is characterized by reorganization energy (λ). Assuming non-adiabatic electron transfer process across the MS interface, electron transfer rate (k_e) from conduction band of Ni_2O_3 into Fermi energy of Al is given by equation 5.19, according to Marcus theory:[78]

$$k_e \propto \exp\left(- \frac{(\lambda + \emptyset_B)^2}{4\lambda k_B T}\right) \qquad 5.19$$

Therefore, from equation (6) and (14), effective potential barrier ($\emptyset_{B,eff}$) can be written as $\emptyset_{B,eff} \propto \frac{(\emptyset_B + \lambda)^2}{4\lambda}$. Thus, it may be inferred that depending on relative magnitude of $\emptyset_B$ and λ either

$\emptyset_{B,eff} \propto \frac{\emptyset_B{}^2}{4\lambda}$ (when $\emptyset_B \gg \lambda$) or $\emptyset_{B,eff} \propto \frac{\lambda}{4}$ when $\emptyset_B \ll \lambda$. Presently, we have observed higher $\emptyset_B$ for materials with higher λ indicating that barrier height is determined by V_q i.e. junction current is determined by electron – phonon interaction within the active semiconducting material (Shown in Fig. 5.13 (b)).
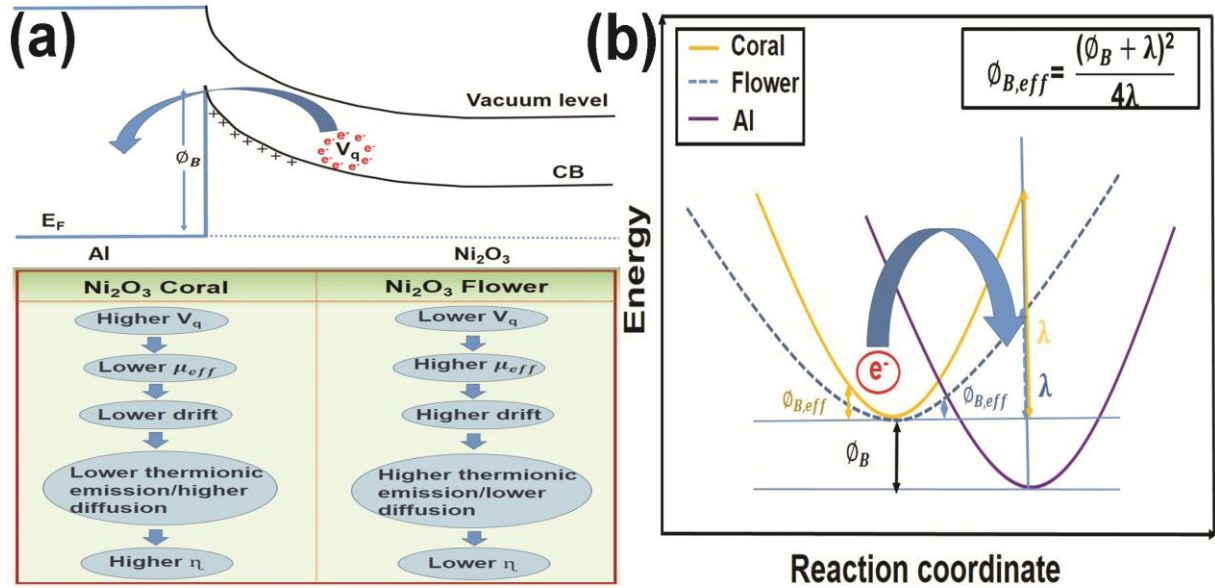
Fig. 5.13 (a). Energy band diagram of metal – semiconductor contact at thermal equilibrium and the flow chart represents variation of ideality factor with electron – phonon interaction; (b). Schematic diagram illustrating phonon-assisted electron transfer process from conduction of Ni_2O_3 into Fermi level of Al.

5.4.   Conclusion

In conclusion, it has been demonstrated that Ni_2O_3 coral–like and flower–like nanostructures could be synthesized by hydrothermal method. PALS and optical studies illustrate that coral–like nanostructure exhibits higher electron – phonon interaction in comparison to flower–like nanostructure due to defects (Ni^{+3} vacancies). Fractional dimension space approach has been taken

account to explain defect dependence of electron – phonon interaction. We have successfully fabricated rectifying metal – semiconductor junction having fairly low turn – on voltages (0.36 and 0.53 V for flower and coral-like nanostructures respectively) using Ni_2O_3 as an active semiconducting materials. A number of electrical parameters like electron mobility, carrier lifetime, diffusion length, nature of current transport etc., associated with MS junction, have been evaluated. These parameters significantly depend on defect concentrations of the nanostructures. Notably, this has been first time examined that the charge transport across the junction follows non-adiabatic process rather than adiabatic character. Importantly, our synthesized nanostructures reveal dominating thermionic current though exhibit low potential barrier i.e. the synthesized MS nano-junction is very much suitable for opto-electronic applications. A comparison reveals that the junction characteristics are very much suitable for optoelectronic applications due to low series resistance, ideality factor close to one despite ultralow barrier height.

5.5.   References

1.   J. Tian, Z. Zhao, A. Kumar, R. I. Boughton and H. Liu, *Chemical Society Reviews*, 2014, **43**, 6920-6937.

2.   D. Wu, Y. Jiang, Y. Zhang, Y. Yu, Z. Zhu, X. Lan, F. Li, C. Wu, L. Wang and L. Luo, *Journal of Materials Chemistry*, 2012, **22**, 23272-23276.

3.   S. Kwon, S. J. Lee, S. M. Kim, Y. Lee, H. Song and J. Y. Park, *Nanoscale*, 2015, **7**, 12297-12301.

4.   J. Osvald, *Journal of Applied Physics*, 1999, **85**, 1935-1942.

5.   L. Mi, H. Wang, Y. Zhang, X. Yao, Y. Chang, G. Li, G. Li and Y. Jiang, *Nanotechnology*, 2016, **28**, 055202.

6.   M. Das, J. Datta, A. Dey, R. Jana, A. Layek, S. Middya and P. P. Ray, *RSC Advances*, 2015, **5**, 101582-101592.

7.   J. Ren, D. Yan, G. Yang, F. Wang, S. Xiao and X. Gu, *Journal of Applied Physics*, 2015, **117**, 154503.

8.   R. Tung, *Physical Review B*, 1992, **45**, 13509.

9.   M. Biber, Ö. Güllü, S. Forment, R. Van Meirhaeghe and A. Türüt, *Semiconductor science and technology*, 2005, **21**, 1.

10.   H. Endo, M. Sugibuchi, K. Takahashi, S. Goto, S. Sugimura, K. Hane and Y. Kashiwaba, *Applied Physics Letters*, 2007, **90**, 121906.

11.   B. Coppa, C. Fulton, S. Kiesel, R. Davis, C. Pandarinath, J. Burnette, R. Nemanich and D. Smith, *Journal of Applied Physics*, 2005, **97**, 103517.

12.   M. Y. Seyidov, R. A. Suleymanov and Y. Bakış, *Journal of Applied Physics*, 2009, **105**, 043710.

13.   S. Majumder, S. Bhattacharjee and C. K. Ghosh, *RSC Advances*, 2016, **6**, 56503-56510.

14.   S. Das, C. K. Ghosh, R. Dey and M. Pal, *RSC Advances*, 2016, **6**, 236-244.

15.   S. Das, U. K. Ghorai, R. Dey, C. K. Ghosh and M. Pal, *Physical Chemistry Chemical Physics*, 2017, **19**, 22995-23006.

16.   S. Banerjee, P. Bhattacharyya and C. K. Ghosh, *Applied Physics A*, 2017, **123**, 640.

17.   H. J. Ha, B. H. Kang, S.-W. Yeom, J. Park, Y.-H. Lee and B.-K. Ju, *Nanotechnology*, 2015, **26**, 485501.

18. P. Pipinys, A. Pipiniene and A. Rimeika, *Journal of Applied Physics*, 1999, **86**, 6875-6878.

19. S. Dey, S. Bhattacharjee, R. S. Bose and C. K. Ghosh, *Applied Physics A*, 2015, **119**, 1343-1354.

20. S. Dey, S. Bhattacharjee, M. G. Chaudhuri, R. S. Bose, S. Halder and C. K. Ghosh, *RSC Advances*, 2015, **5**, 54717-54726.

21. P. Jeevanandam, Y. Koltypin and A. Gedanken, *Nano letters*, 2001, **1**, 263-266.

22. G. J. d. A. Soler-Illia, M. Jobbágy, A. E. Regazzoni and M. A. Blesa, *Chemistry of materials*, 1999, **11**, 3140-3146.

23. L. Xu, Y.-S. Ding, C.-H. Chen, L. Zhao, C. Rimkus, R. Joesten and S. L. Suib, *Chemistry of materials*, 2007, **20**, 308-316.

24. D. Kenneth, *Chemical Society Reviews*, 1997, **26**, 279-289.

25. P. A. Shaikh, D. Shi, J. R. D. Retamal, A. D. Sheikh, M. A. Haque, C.-F. Kang, J.-H. He, O. M. Bakr and T. Wu, *Journal of Materials Chemistry C*, 2016, **4**, 8304-8312.

26. G. A. Babu, G. Ravi, T. Mahalingam, M. Kumaresavanji and Y. Hayakawa, *Dalton Transactions*, 2015, **44**, 4485-4497.

27. H.-M. Cheng, K.-F. Lin, H.-C. Hsu, C.-J. Lin, L.-J. Lin and W.-F. Hsieh, *The Journal of Physical Chemistry B*, 2005, **109**, 18385-18390.

28. S. S. Gaikwad, A. C. Gandhi, S. D. Pandit, J. Pant, T.-S. Chan, C.-L. Cheng, Y.-R. Ma and S. Y. Wu, *Journal of Materials Chemistry C*, 2014, **2**, 7264-7274.

29. T. S. Mondal, S. Bhattacharjee, A. Roychowdhury, S. Majumder, D. Das, M. K. Mitra and C. K. Ghosh, *Materials Research Express*, 2015, **2**, 046102.

30.   X. Liu, K. Zhou, L. Wang, B. Wang and Y. Li, *Journal of the American Chemical Society*, 2009, **131**, 3140-3141.

31.   A. Dey, A. Layek, A. Roychowdhury, M. Das, J. Datta, S. Middya, D. Das and P. P. Ray, *RSC Advances*, 2015, **5**, 36560-36567.

32.   A. V. Thorat, T. Ghoshal, J. D. Holmes, P. Nambissan and M. A. Morris, *Nanoscale*, 2014, **6**, 608-615.

33.   X. Jiang, Y. Zhang, J. Jiang, Y. Rong, Y. Wang, Y. Wu and C. Pan, *The Journal of Physical Chemistry C*, 2012, **116**, 22619-22624.

34.   S. K. Gupta, K. Sudarshan, P. Ghosh, A. Srivastava, S. Bevara, P. Pujari and R. Kadam, *Journal of Materials Chemistry C*, 2016, **4**, 4988-5000.

35.   J. Yan, G. Wu, N. Guan, L. Li, Z. Li and X. Cao, *Physical Chemistry Chemical Physics*, 2013, **15**, 10978-10988.

36.   D. Sanyal, D. Banerjee and U. De, *Physical Review B*, 1998, **58**, 15226.

37.   M. Kong, Y. Li, X. Chen, T. Tian, P. Fang, F. Zheng and X. Zhao, *Journal of the American Chemical Society*, 2011, **133**, 16414-16417.

38.   W. Shi, Y. Li, J. Hou, H. Lv, X. Zhao, P. Fang, F. Zheng and S. Wang, *Journal of Materials Chemistry A*, 2013, **1**, 728-734.

39.   W. Sun, Y. Li, W. Shi, X. Zhao and P. Fang, *Journal of Materials Chemistry*, 2011, **21**, 9263-9270.

40.   D. Pant and H. H. Girault, *Physical Chemistry Chemical Physics*, 2005, **7**, 3457-3463.

41.   R. Dingle, *Physical Review*, 1969, **184**, 788.

42.   K. Colbow, *Physical Review*, 1966, **141**, 742.

43. B.-L. Wu, H.-J. Chao, C.-P. Chen, C.-H. Yang and J.-Y. Chang, *RSC Advances*, 2015, **5**, 36605-36613.

44. I.-S. Liu, H.-H. Lo, C.-T. Chien, Y.-Y. Lin, C.-W. Chen, Y.-F. Chen, W.-F. Su and S.-C. Liou, *Journal of Materials Chemistry*, 2008, **18**, 675-682.

45. C. V. Gopi, M. Venkata-Haritha, S.-K. Kim and H.-J. Kim, *Nanoscale*, 2015, **7**, 12552-12563.

46. A. A. Middleton, *Physical Review B*, 2000, **61**, 14787.

47. F. Peeters, W. Xiaoguang and J. Devreese, *Physical Review B*, 1986, **33**, 3926.

48. J. Kundrotas, A. Čerškus, S. Ašmontas, G. Valušis, M. P. Halsall, E. Johannessen and P. Harrison, *Semiconductor science and technology*, 2007, **22**, 1070.

49. J. Shang, W. Hao, X. Lv, T. Wang, X. Wang, Y. Du, S. Dou, T. Xie, D. Wang and J. Wang, *ACS Catalysis*, 2014, **4**, 954-961.

50. F. Wan, L. Kong, C. Wang, Y. Li, Y. Liu and X. Zhang, *Dalton Transactions*, 2017, **46**, 1487-1494.

51. S. Lu, J. Qi, Y. Gu, S. Liu, Q. Xu, Z. Wang, Q. Liang and Y. Zhang, *Nanoscale*, 2015, **7**, 4461-4467.

52. S. M. Sze and K. K. Ng, *Physics of semiconductor devices*, John wiley & sons, 2006.

53. S. K. TC and G. Gupta, *RSC Advances*, 2014, **4**, 27308-27314.

54. S. Mahato and J. Puigdollers, *Physica B: Condensed Matter*, 2018, **530**, 327-335.

55. S. K. Gupta, B. Shankar, W. R. Taube, J. Singh and J. Akhtar, *Physica B: Condensed Matter*, 2014, **434**, 44-50.

56. S. Cheung and N. Cheung, *Applied Physics Letters*, 1986, **49**, 85-87.

57. F. Yakuphanoglu, *The Journal of Physical Chemistry C*, 2007, **111**, 1505-1507.

58. F. Léonard and A. A. Talin, *Nature nanotechnology*, 2011, **6**, 773-783.

59. S. Dhar, T. Majumder and S. P. Mondal, *ACS applied materials & interfaces*, 2016, **8**, 31822-31831.

60. A. De Vrieze, K. Strubbe, W. Gomes, S. Forment and R. Van Meirhaeghe, *Physical Chemistry Chemical Physics*, 2001, **3**, 5297-5303.

61. O. Pakma, Ş. Çavdar, H. Koralay, N. Tuğluoğlu and Ö. F. Yüksel, *Physica B: Condensed Matter*, 2017, **527**, 1-6.

62. M. J. Speirs, D. N. Dirin, M. Abdu-Aguye, D. M. Balazs, M. V. Kovalenko and M. A. Loi, *Energy & Environmental Science*, 2016, **9**, 2916-2924.

63. A. Dey, S. Middya, R. Jana, M. Das, J. Datta, A. Layek and P. P. Ray, *Journal of Materials Science: Materials in Electronics*, 2016, **27**, 6325-6335.

64. J. Kwan Kim, J. Hoon Song, H. Choi, S. Jae Baik and S. Jeong, *Journal of Applied Physics*, 2014, **115**, 054302.

65. S. Halder, A. Dey, A. Bhattacharjee, J. Ortega-Castro, A. Frontera, P. P. Ray and P. Roy, *Dalton Transactions*, 2017, **46**, 11239-11249.

66. S. Gu, K. Ding, J. Pan, Z. Shao, J. Mao, X. Zhang and J. Jie, *Journal of Materials Chemistry A*, 2017, **5**, 11171-11178.

67. S. Zhu, R. Van Meirhaeghe, C. Detavernier, F. Cardon, G.-P. Ru, X.-P. Qu and B.-Z. Li, *Solid-State Electronics*, 2000, **44**, 663-671.

68. W. Guo, Y. Yang, J. Liu and Y. Zhang, *Physical Chemistry Chemical Physics*, 2010, **12**, 14868-14872.

69.   T. Kampen, S. Park and D. Zahn, *Applied surface science*, 2002, **190**, 461-466.

70.   K. Tracy, P. Hartlieb, S. Einfeldt, R. Davis, E. Hurt and R. Nemanich, *Journal of Applied Physics*, 2003, **94**, 3939-3948.

71.   M. Mohamed, K. Irmscher, C. Janowitz, Z. Galazka, R. Manzke and R. Fornari, *Applied Physics Letters*, 2012, **101**, 132106.

72.   T. Jiao, D. Wei, J. Liu, W. Sun, S. Jia, W. Zhang, Y. Feng, H. Shi and C. Du, *RSC Advances*, 2015, **5**, 73202-73206.

73.   M. Zhu, X. Li, Y. Guo, X. Li, P. Sun, X. Zang, K. Wang, M. Zhong, D. Wu and H. Zhu, *Nanoscale*, 2014, **6**, 4909-4914.

74.   P. V. More, S. Jeong, J.-Y. Lee, Y.-H. Seo, B.-H. Ryu and Y. Choi, *Journal of Materials Chemistry*, 2012, **22**, 23553-23560.

75.   X. Li, H. Zhu, K. Wang, A. Cao, J. Wei, C. Li, Y. Jia, Z. Li, X. Li and D. Wu, *Advanced Materials*, 2010, **22**, 2743-2748.

76.   C. Crowell and S. Sze, *Solid-State Electronics*, 1966, **9**, 1035-1048.

77.   A. Iqbal, M. S. Hossain and K. H. Bevan, *Physical Chemistry Chemical Physics*, 2016, **18**, 29466-29477.

78.   S. Ghosh, M. Ghosh, P. Kumar, A. S. Sarkar and S. K. Pal, *The Journal of Physical Chemistry C*, 2016, **120**, 27717-27723.

Chapter 6

The effect of particle size on the dielectric behavior of nanocrystalline nickel (III) oxide

Abstract

Nanocrystalline nickel (III) oxide (Ni_2O_3) with various particle sizes have been prepared through a low temperature chemical route. Structural and morphological information have been obtained by X-ray diffraction, field emission scanning electron microscope, Fourier Transform infrared spectroscopy and Raman Spectroscopy analysis. The frequency dependent (40 Hz-10^8 Hz) dielectric properties have been studied extensively at room temperature. The effect of particle size and frequency on the dielectric behavior of nanocrystalline Ni_2O_3 is discussed on the basis of point defects. In this work a qualitative interpretation on dielectric constant and loss are presented. The grain and grain boundary play and important role for ac conductivity. This material has been studied for the first time to evaluate the dielectric properties and ac conductivity. It is observed that this material has high values of ε' of the order of 10^5 and low loss, which is highly desired for power systems and advance electronics.

6.1. Introduction

The nanosize materials have received widespread attention among the scientific community due to its unusual electrical properties different from single crystals, polycrystals (bulk), thin films and glasses even though they are identical in chemical composition [1-5]. Besides, nanosize materials have shown great potential to device applications including sensors, electrodes, switching devices, microelectronic devices and solar cells [6-9]. Furthermore, the electrical properties of nanosize materials are different from their bulk because of the high surface to volume ratio of the grains, high defect density, quantum confinement of charge carriers and disordered grain boundary [10-12]. Disordered grain boundary in nanosize materials without short or long order arrangement have been shown by many researchers [4]. In nanosize materials, the nature of the defect, grain and grain boundaries play a very significant role for the electrical

properties. In this context, nanosize oxide materials have drawn attention of researchers. Among different oxide materials, developed so far, nickel oxide has shown potential for the above applications. Apart from these advantages, the fact that nickel exhibits variable valence states has ignited further interest. Till recently, variable valence of nickel oxide in forms of Ni_2O_3, Ni_3O_4, NiO_2 etc., are believed to be unstable at room temperature [13, 14]. However, Cairns and Ott et al successfully prepared $Ni_2O_3.2H_2O$ and identify the structure and composition using X-ray diffraction technique [15]. It has also been observed that many oxides or polymer combined with Ni_2O_3 improve their properties [16, 17]. Furthermore, Richardson successfully prepared Ni_2O_3. H_2O and found that it behaves like n-type semiconducting material with ferromagnetic coupling between the nickel atoms [18]. Recently, we have reported the synthesis of different Ni_2O_3 hydrates and pure Ni_2O_3 with different particle sizes and their effect on heavy metal removal and biological application [19, 20]. However, to the best of our knowledge, no further report still exists in the field of electrical properties of pure Ni_2O_3.

In this chapter, we have prepared different particle size of Ni_2O_3 using low temperature chemical precipitation method with varying temperature and investigated the electrical properties. The impedance spectroscopic analysis and ac conductivity of different Ni_2O_3 nanoparticles have been measured at room temperature. In nanocrystalline Ni_2O_3 impedance spectroscopy and conductivity are expected to separate out the grain and grain boundary contributions to the overall electrical response of the samples.

6.2. Experimental

6.2.1. Synthesis of Ni$_2$O$_3$ nanoparticles

Nickel (III) oxide (Ni$_2$O$_3$) nanoparticles were prepared by chemical oxidation method. All the chemicals were used of analytical grade (MERCK India Pvt. Ltd.) and subsequently used without any further purification. Nickel nitrate hexahydrate [Ni(NO$_3$)$_2$.6H$_2$O] was used as source of Ni^{2+} ion. The reaction process for synthesis of Ni$_2$O$_3$ nanoparticles was adopted from our previous work [20]. The reaction process contained two different solutions, 1.00 g of Ni(NO$_3$)$_2$.6H$_2$O in 20 ml de-ionize (DI) water and 1.60 g sodium hydroxide (NaOH) in 15 ml of sodium hypochlorite (NaOCl). Both solution were continuously stirred until its get clear solution. The NaOCl solution was added drop wise into the nickel source solution under constant stirring, following which almost immediate flocculation and subsequent formation of black hydrated. After settle down, the precipitate was collected and dried to get grayish black sample. 20 ml NaOCl was added into the dried sample and left until effervescence stops. Then the precipitate is filtered, washed and dried to get dark black powder. Thus, the entire synthesis procedure was carried out at different temperature (0°C, 30°C and 50°C) to investigate the effect on defect and particle size. In the present article, these particular samples have been denoted as P1, P2 and P3 for synthesized temperature 0°C, 30°C and 50°C respectively.

6.2.2. Characterizations

The identification and phase purity of the synthesized samples were investigated by Ultima-III, Rigaku X-ray diffractometer (XRD) (Cu K$_\alpha$ radiation, λ = 1.5404 Å). In the diffraction data, continuous scanning mode was selected in 2θ ranging from 20° to 70° with an interval of 0.02^o and the scanning rate is 5°/min. The morphologies and sizes of the nanomaterial were

measured using a Hitachi S4800 the field emission scanning electron microscopic (FESEM).

Fourier transform infrared (FTIR) spectra were recorded by IR – Prestige (Shimadzu, Japan).

Raman spectra were obtained by alpha 300, Witec (excitation wavelength 530 nm, power 3 mW

and spot size: 2 μm). For the electrical measurements, pellets of 12 mm diameter and 2.3 mm

thickness were pressed under a uniaxial pressure of 11×10^4 kN/m^2 for 2 min followed by drying

at 40 ^{o}C for 6 h. The electrical measurements were carried out in the frequency range 40 Hz to 10^8

Hz using an LCR HI-Tester (Hioki 3522-50) after incorporation of Ag electrodes with Ag paste

on both sides of the pellets to ensure Ohmic contact.

6.3. Results and discussion

6.3.1. Microstructural study

XRD patterns of Ni_2O_3 nanoparticles for synthesized at different temperatures are shown

in Fig. 6.1 (a). It is evident from figure all the samples are polycrystalline Five diffraction peaks

corresponding to all the synthesized samples, identified at 2θ = 27.34^o, 31.66^o, 45.41^o, 56.38^{o}and

66.12^o, are readily indexed as the reflection from (101), (002), (111), (202) and (004) planes of

hexagonal Ni_2O_3 (JCPDS Card Number 14-0481, CAS Number 1314-06-3). Absence of any other

peak validates phase purity of the synthesized material. Crystallite sizes, calculated using Scherer's

formula:

$$D = \frac{0.9\lambda}{\beta cos\theta} \qquad\qquad 6.1$$

where, λ is the wavelength of the X-ray, β is the full width at half maximum (FWHM) and

θ is the diffraction angle. The calculated particle sizes are found to be ~26nm, ~36nm and ~43 nm

for P1, P2 and P3 samples respectively. The morphology of samples P1, P2 and P3 are shown in

Fig. 6.1 (b, c & d) respectively. In reality it is found from the FESEM images that the particles are highly agglomerated. The agglomerated grains appear to be in the micro meter range.

Subsequently, the analysis of the FTIR and Raman spectra reveal that the functional groups and structure of the as prepared Ni_2O_3 nanoparticles. It has been observed from FTIR spectrum (Fig. 6.2 (a)) that bands at around 430 cm^{-1}, 570 cm^{-1} and 870 cm^{-1} are common to all the three samples marked by dotted lines in the figure. First two can readily be assigned to Ni-O stretching vibration, while the latter one point towards the successful synthesis of Ni_2O_3 by forming Ni–O–Ni bonds. The peaks between 1000 cm^{-1} and 1500 cm^{-1} are represent the – OH group bending vibrations and rest of the peak above 1500 cm^{-1} attribute to the –OH stretching vibrations due to the water molecule [21, 22].
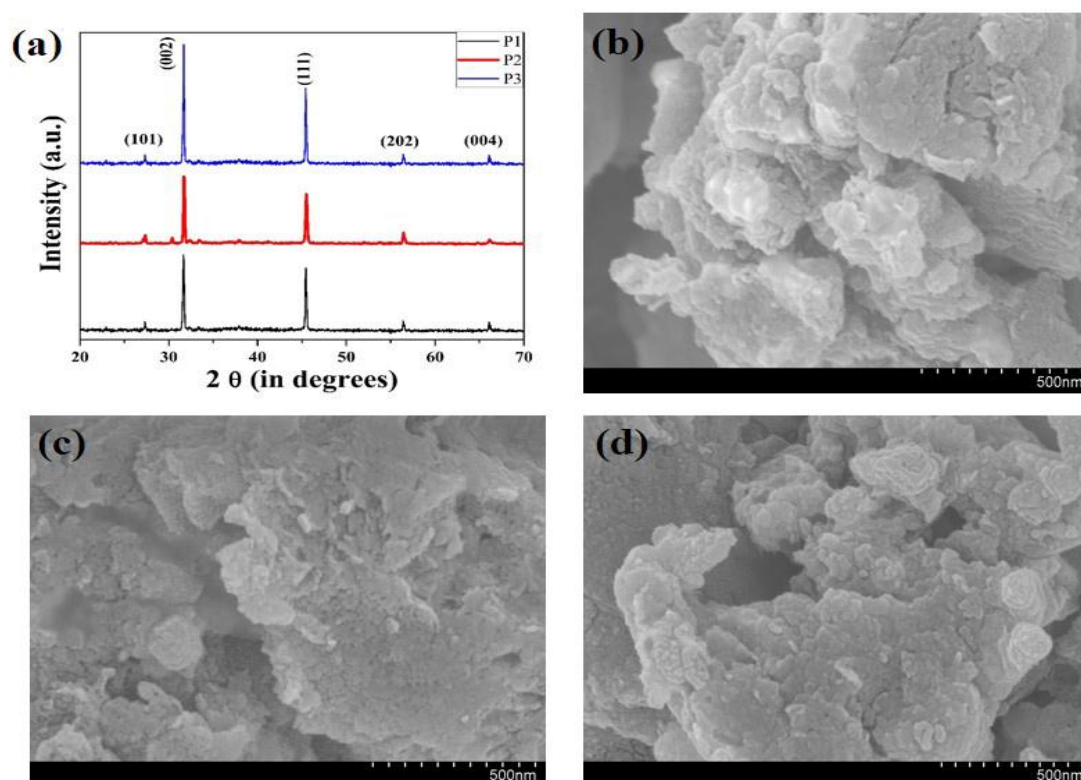
Fig. 6.1 (a) X-ray diffraction patterns, (b, c, d) FESEM images of the samples P1, P2 and P3.

Hence, in order to investigate the bond mode, we have employed Raman spectroscopy. Raman spectra of these synthesized Ni_2O_3 nanoparticles consist of two peaks marked by dotted lines (measured at 494 cm^{-1} and 1072 cm^{-1} shown in Fig. 6.2 (b) are assigned to longitudinal optical one-phonon (1LO), longitudinal optical two-phonon (2LO) respectively [23, 24]. Corresponding to the coupling interaction of Ni–O oscillations.
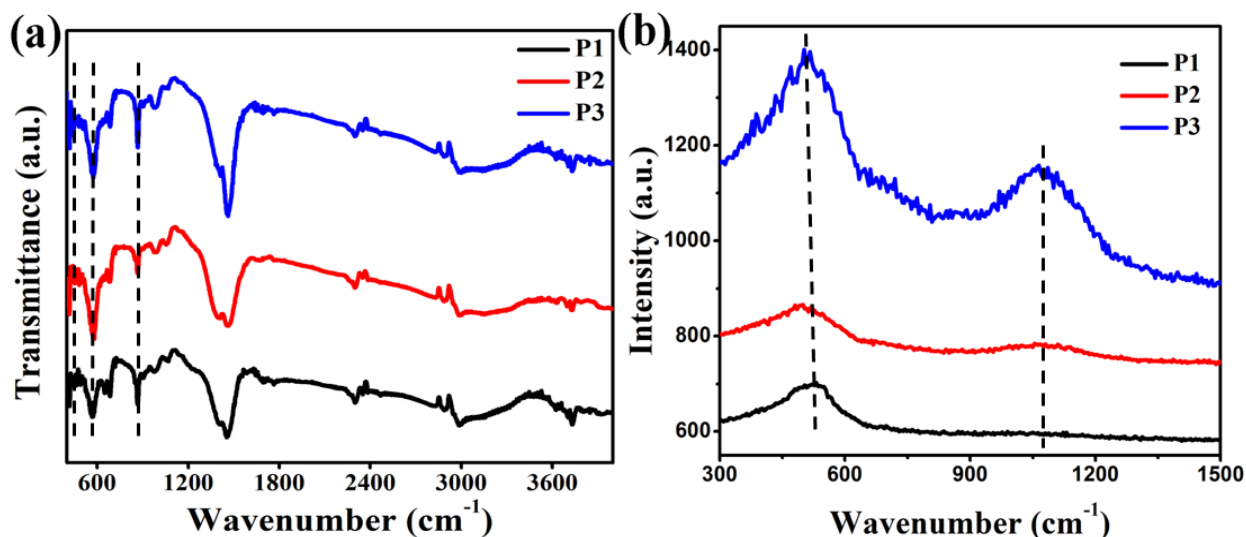
Fig. 6.2 Spectroscopic investigation of Ni_2O_3 particles (a) FTIR spectrum and (b) Raman spectrum.

6.3.2. Dielectric Properties

The process of energy transfer into a dielectric material is too much complicated and involves several contributions to the electric polarization of molecules. The energy is transferred from the electric field into the dielectric material due to the rotation of polarized atoms or molecules in response to an applied electric field. In solid materials, the complex dielectric properties can be explained as a function of frequency, crystal structure and other important parameters. The frequency and temperature dependent dielectric response in a solid material can be expressed as a complex quantity made up of a real and imaginary component Eq. 6.1, i.e.,

$$\varepsilon^*(\omega) = \varepsilon'(\omega) + j\varepsilon''(\omega) \qquad\qquad 6.1$$

where ε′(ω) and ε″(ω) are the frequency dependent real and imaginary part of dielectric constant (ε*). The ε′(ω) measures the amount of energy stored in the material due to the applied electric field and ε″(ω) is a measure of an amount of energy dissipated in the material due to an applied electric field. Another most important electrical parameter is $tan\delta$ or also known as loss tangent, which is defined as the ratio of amount of energy dissipated (ε″(ω)) to the amount of energy stored (ε′(ω)) within a material due to applied electric field in Eq. 6.2

$$tan\delta = \frac{\varepsilon''(\omega)}{\varepsilon'(\omega)} \qquad\qquad 6.2$$

In order to understand the effect of compositions and microstructure on the electrical properties of a dielectric material, the frequency dependent real part of complex dielectric constant is calculated using Eq. 6.3

$$\varepsilon'(\omega) = \frac{C \times d}{\varepsilon_0 A} \qquad\qquad 6.3$$

where C, d, A and ε_0 are the capacitance of the material, thickness, area of the sample pellet and dielectric permittivity of vacuum (8.854×10^{-12} F/m), respectively. The frequency dependent real part of dielectric constant ε′(ω) (Fig. 6.3 (a)) of as prepared Ni_2O_3 nanomaterial shows that the dielectric constant decreases as the particle size increases from P1 to P3. It is also observed that ε′(ω) decreases rapidly with slight increase of frequency in the low frequency region for all samples but at higher frequency region it become almost constant independent of particle size. The decrease of ε′(ω) with increase of particle size for Ni_2O_3 samples at low frequency region may be due to the decrease of space charge polarization. Generally, at low frequency region the presence of all four types of polarizations like space charge, orientation, electronic and ionic polarization contributes

significantly to the increase of dielectric constant. At low frequency, electrons are able to reach to the grain boundary position and accumulated to developed significant polarization. But, with increases in frequency the previously gathered charge carriers have been started to move reverse direction which oppose further accumulation of electron at grain boundary and results in a sharp decreases of $\varepsilon'(\omega)$. The $\varepsilon'(\omega)$ values at low frequency for all samples varies over the range of the order of 10^5 which is greater than those reported earlier on NiO [25, 26]. This could be explained as follows: Firstly the nanocrystalline materials possess enormous number of interfaces and secondly large number of defects are likely to be present at these interfaces. Since grain boundary in these nanostructured materials is comparatively open, rearrangement of +Ve and −Ve charges with applied alternating field are easier and therefore giving rise to space charge polarization. Inherently, the relaxation of space charge polarization is a slow process [27]. Hence it will contributes to dielectric constant at lower frequency only and thus the dielectric constant of these samples P1, P2 and P3 could be high at lower frequencies. This is observed experimentally shown in Fig. 6.3 (a). Another major contribution for high dielectric constant is orientation polarization. Since, both Ni^{3+} and Ni^{2+} are present in the Ni_2O_3 system. The formation of Ni^{2+} form Ni^{3+}, can be represented using KrÖger- Vink notation by the following defect equation Eq. 6.4 as follows:

$$Ni_{Ni} + O_O \rightarrow Ni'_{Ni} + V_O^\circ + \frac{1}{2}O_2 \uparrow \qquad\qquad 6.4$$
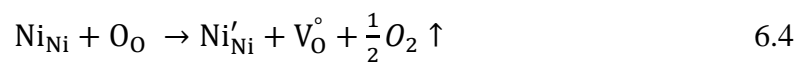
For charge balance, positively charge oxygen vacancy is created in the lattice. Thus in the lattice negatively charged Ni'_{Ni} is separated from positively charged V_O° and thus this forms a permanent electric dipole. Polarization arising out of this permanent dipole in the presence of alternating field is called orientation polarization. Relaxation of this orientation polarization is faster compared to space charge polarization. At the beginning, at lower frequency, contribution to dielectric constant $\varepsilon'(\omega)$ comes both from space charge as well as from orientation polarization. Now with increasing

frequency first contribution from space charge polarization decreases leading to decreases in $\varepsilon'(\omega)$. At high frequency contribution would come from orientation polarization alone, which would also decreases at high frequency. This explains the decreases in $\varepsilon'(\omega)$ with frequency [28, 29]. Among, P1, P2 and P3, particle size increases from P1 to P3. Thus at P1 particle size being smallest would have higher grain boundary volume fraction and secondly more number of defects would be there. Thus at P1 space charge polarization in the grain boundary region would be more. So also the concentration of Permanent dipole from defects would also increases. Therefore the polarization would be maximum at P1 and as the particle size increases from P2 to P3 net polarization would decreases and hence $\varepsilon'(\omega)$ will decreases from P2 to P3. Thus the dielectric constant from P1 to P3 decreases for given frequency which actually observed (Fig. 6.3 (a)).
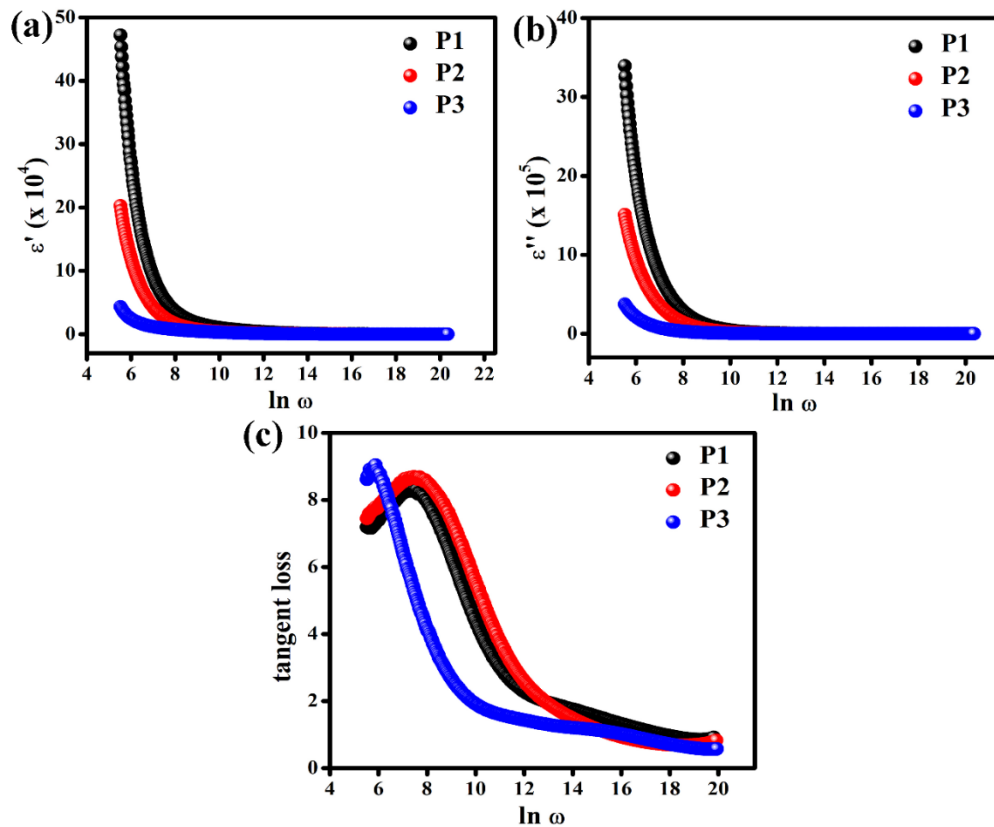
Fig. 6.3 Variation of (a) real part of dielectric constant ε^*, (b) imaginary part of dielectric constant ε^* and (c) tangent loss (tan δ) with frequency.

The variation of imaginary part of dielectric constant $\varepsilon''(\omega)$ with frequency (Fig. 6.3(b)) at 300 K shows that it follow the similar nature as $\varepsilon'(\omega)$ i.e. it decreases sharply in low frequency region and also with increase of particle size decreases. In high frequency region it becomes almost independent of frequency and particles size. Fig. 6.3 (c) also shows the variation of dielectric loss ($tan\delta$) with frequency at room temperature. It is usually considered to be produced by domain wall resonance. According to the Eq. 6.2 tangent loss is found to proportional to the $\varepsilon''(\omega)$. The variation of tangent loss (Fig. 6.3 (c)) clearly shows that it decreases with the increase in frequency for all prepared samples and exhibit dispersion nature. The plot of tangent loss displays small relaxation peaks at lower frequencies for all samples. This relaxation peaks suggested that the hopping frequency of localized charge carriers becomes almost equal to the applied field frequency at that point. It is also observed that the relaxation peak shifted towards lower frequency with increasing particle size. The peak value of tangent loss for P1 and P2 appeared at approximately 500 KHz. From the above discussion it is clear that for P3 having the largest size major contribution to loss comes from interparticle grain boundary space charge polarization which occurs at lower frequency. Compared to P3, for P2 and P1 having smaller size, larger contribution to polarization comes from defect induced permanent dipoles as explained earlier. Orientation polarization does not much contribute to lower frequency but on the other hand it contribute to loss at high frequency. Therefore for P3, since major contribution comes from space charge polarization which is sluggish to follow the alternating field. Tangent loss would be more at lower frequency which is observed. On the other hand for P1 and P2 since major contribution comes from orientation polarization which can easily fallow the alternating field at lower frequency thereby contributing less to the dielectric loss compared to P3. As frequency increases its starts lagging fallowing the field and so contributes more to the dielectric loss. Therefore maximum loss

for P1 and P2 would shift to higher frequency compared to P3. With further increase in frequency it starts not to follow the high frequency, alternating field and contributes less to loss factor. Thus for P2 and P1 the loss factor passes through a maximum which is observed experimentally shown in Fig. 6.3 (c).

6.3.3. Impedance analysis

In order to analyse electrical behavior of Ni_2O_3, in more details, impedance spectroscopic study has been carried out. This choice is made because of the large range of frequencies allowed by impedance spectroscopy, under which different electric or dielectric phenomena can be assessed. The resistive and capacitive behaviors can be separately detected and analyzed [31]. Fig. 6.4 (a) and Fig. 6.4 (b) shows the variation of the real part of impedance ($Z'(\omega)$) and imaginary part of impedance ($Z''(\omega)$) with frequency, respectively. At high frequency regime, $Z'(\omega)$ didn't change with frequency and non-dispersive nature clearly reveals the presence of space charge. This also indicates that ac conductivity will be enhanced at high frequency due to release of space charge and modified barrier properties. It is observed that the magnitude of $Z'(\omega)$, increases with increase of particle size of the Ni_2O_3 nanoparticles which indicates an increase of resistivity with increasing particle sizes. In complex impedance plot, a broad peak has appeared which confirm about relaxation process. The broad peak also suggested that the distribution of relaxation time over a range i.e. non-Debye type relaxation. The peak maxima has appeared at mean relaxation frequency and the relaxation frequency shifts to higher value with decreasing particle sizes indicating that relaxation mechanism depends on particle size.
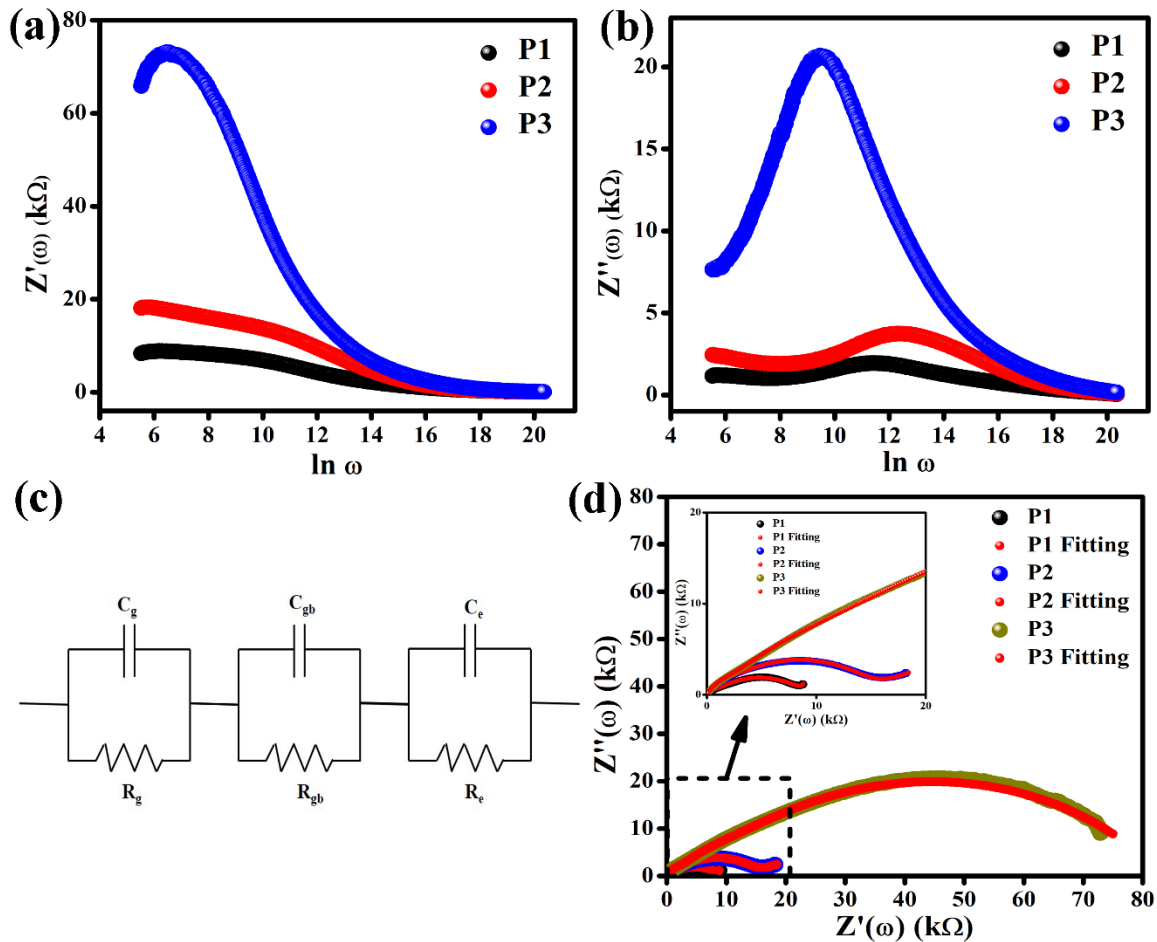
Fig. 6.4 Variation of (a) real part of impedance Z′(ω), (b) imaginary part of impedance Z″(ω) with frequency and (c) Equivalent circuit of the nyquist plot, (d) Nyquist plot of Ni_2O_3 nanoparticles.

In P1 and P2 samples the relaxation is observed at around 10^4 to 10^5 Hz. For P3, the relaxation is seen at lower frequencies, 10^3 Hz, which is typical for more insulating than other two materials. Due to formation of Ni^{2+} from Ni^{3+} due to the electro-neutrality condition, the charged oxygen vacancy is generated. This defect generation can be explain from Eq. 6.4. $Ni'_{Ni} - V_O^{\circ}$ forms this permanent dipole moment. For P3 sample this dipole polarization is responsible for this dielectric loss around 500 kHz and for P1 and P2 samples dipolar relaxation occurs at around 100 kHz due to the formation of dipole as mention above. It is expected that this permanent dipole would give

rise to orientation polarization around 100 kHz frequency region for this smaller particles. This is true for smaller particle, because small size would help in this defect generation. However as opposed to this for larger particles the formation of these defect would be reduced and as a result generation of permanent dipole seems to the insignificant. Then for large particles this low frequency relaxation arises mainly due to this space charge polarization of ionic solid Ni_2O_3.

Complex impedance analyses enable one to resolve the contribution of various processes, for instance, bulk effects and interfaces of grain boundaries [30]. The grain and grain boundary have great influence on the electrical properties. Conventionally, the grain and grain boundary contributions to the overall impedance can be resolved by exploiting differences in its responses to the applied field. The impedance data is based on modeled by an equivalent electrical circuit. The single semicircle can be modeled as an equivalent circuit of a grain resistance (R_g) and a grain capacitance (C_g) in parallel. In general, the electrical properties of the polycrystalline material have contributions from both the grain and the interface. Each contribution may be represented by a semicircle in an impedance spectrum plot if the relaxation process occurs at the grain and/or the interface. In some cases presence of two semicircles is observed where the high frequency semicircle can be attributed to the bulk (grain) property of the material arising due to the parallel combination of bulk resistance and bulk capacitance of the material where as low frequency semicircle is due to the grain boundary effect consists of parallel combination of grain boundary resistance (R_{gb}) and grain boundary capacitance (C_{gb}). The two semicircular arcs due to grain interior and grain boundary are consistent with the brick layer model for polycrystalline materials [31] and it can be expressed as an equivalent circuit consisting of parallel combination of two resistances and capacitances connected in series with the contributions of the electrodes. The electrode- electrolyte interface circuit consists of parallel combination of resistance (R_e) and

capacitance (C_e). The modeled equivalent circuit comprises of a series and parallel resistor-capacitor (R-C) elements, as shown in Fig. 6.4 (c). In order to explore the grain and grain boundary effects, we discussed our results in the basis of grain and grain boundary. The circuit consists of a series array of three sub-circuits, first two represents grain effects and the grain boundaries and third one represents electrode- electrolyte interface effect (Fig. 6.4 (c)). Each sub-circuit is composed of a resistor and capacitor joined in parallel. Let (R_g, R_{gb}, R_e) and (C_g, C_{gb}, C_e) be the resistances and capacitances of grains, grain boundaries and interface, respectively, then the impedance real (Z') and imaginary (Z') parts of the total impedance of the equivalent circuit in this system is given below, (Eq. 6.5 and Eq. 6.6).

$$Z' = \frac{R_g}{1+(\omega R_g C_g)^2} + \frac{R_{gb}}{1+(\omega R_{gb} C_{gb})^2} + \frac{R_e}{1+(\omega R_e C_e)^2} \qquad 6.5$$

$$Z'' = R_g\left[\frac{\omega R_g C_g}{1+(\omega R_g C_g)^2}\right] + R_{gb}\left[\frac{\omega R_{gb} C_{gb}}{1+(\omega R_{gb} C_{gb})^2}\right] + R_e\left[\frac{\omega R_e C_e}{1+(\omega R_e C_e)^2}\right] \qquad 6.6$$

The best fitting of equivalent circuit for different particle size of Ni_2O_3 are shown in Fig. 6.4 (d). Fig. 6.4 (d) shows the Nyquist plots (complex impedance spectrum) for the Ni_2O_3 particles and fitting curve of each samples with equivalent circuit. The grain and grain boundary contributions to the impedance can be determined by fitting equivalent circuit. Impedance spectra are analyzed through an equivalent circuit which is discused above. The semicircular arcs are clearly observed for all studied samples. From the Fig. 6.4 (d), its clearly observed that the higher the particle size higher the resistance value. The theoretical values of grain resistance and grain boundary resistance have been obtained from the fitting and are listed in Table 6.1.

Table 6.1 Resistance and capacitances obtained from frequency dependent impedance spectroscopy data for Ni_2O_3.

Sample name	Particle Size (nm)	R_g (k Ω)	C_g (nF)	R_{gb} (k Ω)	C_{gb} (nF)	R_e (k Ω)	C_e (nF)	GOF (χ^2)
P1	26	6.2	11	9.5	0.04	0.5	0.001	0.9835
P2	36	23.5	16	10.1	0.53	1.5	0.005	0.9627
P3	43	56.2	23	12.5	1.38	3.5	0.007	0.9852

The experimental data of capacitance indicates that the low frequency semicircle can be attributed to the electrical processes through the grain and the high frequency has been assigned to the grain boundary conduction. The value R_g and R_{gb} have been obtained from the fitting data [28]. It is noted in table that R_{gb} decreases with decreases particle size. The value of R_{gb} at different samples was estimated from the complex impedance spectrum. This plot indicates the changes in grain boundary resistance of different samples representing the role of grain boundaries in electrical conduction process of material. The conduction mechanism for grains and grain boundaries are different. A hopping mechanism through various defect sites contributes to the intra-grain conduction whereas the interface barrier potential plays the major role for inter-grain boundary condition. The existence of two semicircular arcs suggests that Ni_2O_3 exhibits electrically heterogeneous structure. Comparing the Nyquist plot of all samples at room temperature, the impedance value of larger particle is larger than that of small particle and spectra show that the grain boundary resistance of smaller particle is lower than the grain boundary resistance of larger particle. For small particle size grain boundaries are higher therefore the electrons are able to reach

to the grain boundary position and accumulated to developed significant polarization. This can be attributed to the high dielectric constant of smaller particles.

6.3.4. Modulus analysis
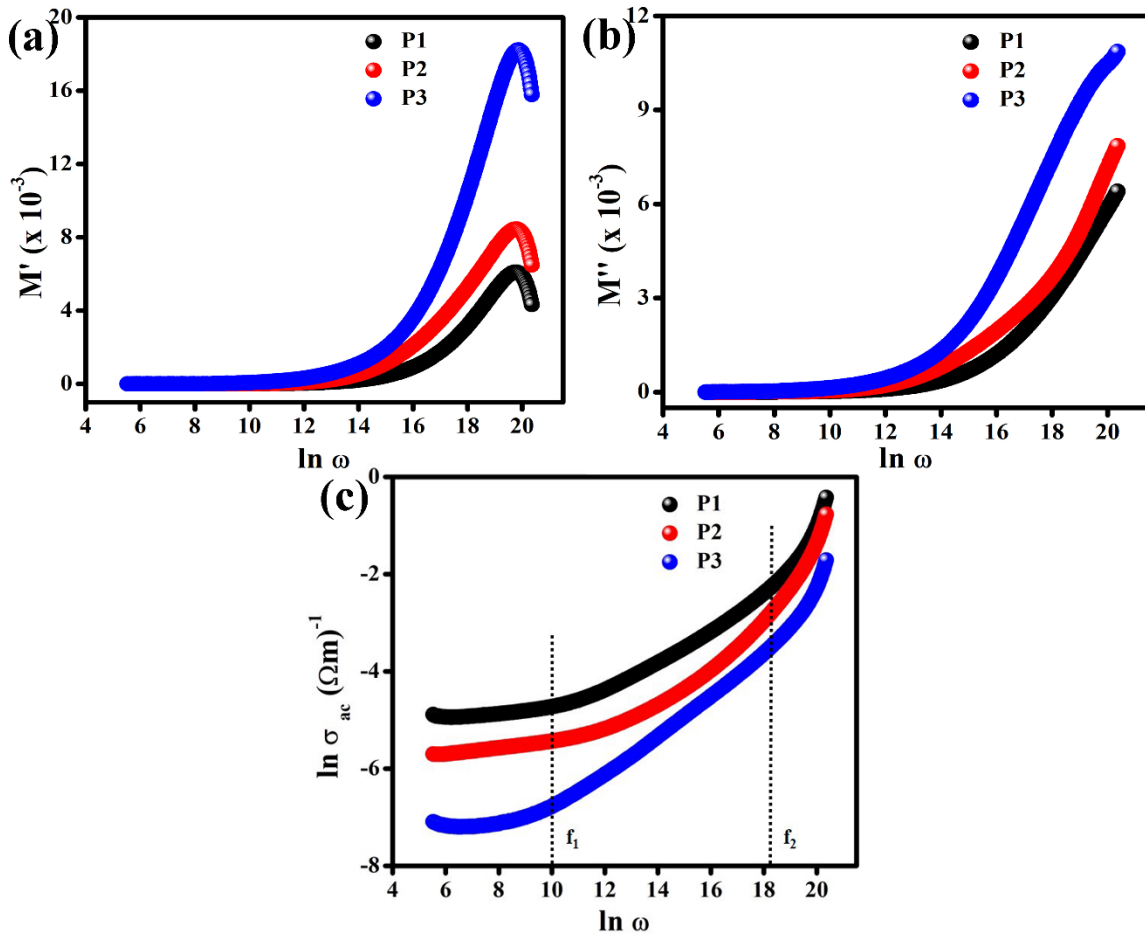
Fig. 6.5 Variation of (a) real part of electric modulus (M′), (b) imaginary part of electric modulus (M″) and (c) ac conductivity plot with frequency of Ni_2O_3 nanoparticles.

The complex electric modulus formalism is a useful tool to understand the bulk response of dielectric materials. The complex electric modulus (M*) can be represented as the inverse of complex dielectric constant (ε^*) i.e.

$$M^* = (\varepsilon^*)^{-1} \qquad\qquad 6.7$$

$$M^* = M^{'} + jM^{"} = \frac{\varepsilon'}{\varepsilon'^2 + \varepsilon''^2} + j\frac{\varepsilon''}{\varepsilon'^2 + \varepsilon''^2} \qquad\qquad 6.8$$

where M′ , M″ are the real and imaginary parts of electric modulus and ε ′ , ε ″ are the real and imaginary parts of the dielectric constant respectively. In our investigation, Fig. 6.5 (a) shows the frequency dependence of the real part of the electric modulus (M′) for three different particle size. It is evident from the figure that at low frequencies, M′ approaches zero for the all sample, this can be assigned by absence of sufficient electrode polarization. In high frequency region, M′ increases continuously showing a dispersive nature indicating the lack of movable charge carrier due to restoring force produce by applied field. The frequency dependence imaginary part of the electric modulus (M″) which signifies the total energy loss under electric field has shown in Fig. 6.5 (b). In every curve, a relaxation peak has appeared which confirms the presence of relaxation process. The peak broadness suggests the distribution of relaxation time and a deviation from ideal Debye relaxation. This relaxation peak tends to shift towards higher frequencies with particle size clearly reveals that relaxation mechanism depends on the size of particle. The frequency regime to the left of this relaxation peak (i.e. below f_{max}) is associated with the hopping conduction due to mobile charge carriers over long distances. The region to the right of this peak (i.e. above f_{max}) corresponds to the short range or localized motion of charge carriers as they are spatially confined to the potential wells. The frequency range where the relaxation peak occurs is suggestive of the transition from long range to short range mobility of charge carriers.

6.3.5. AC conductivity analysis

AC conductivity of the samples can be evaluated using the relation [32]:

$$\sigma_{ac} = \varepsilon_0\varepsilon_r\omega tan\delta \qquad\qquad 6.9$$

where ω is the angular frequency of the applied field. Fig. 5(c) shows the variation of ac conductivity with frequency for P1, P2 and P3 nanoparticles (log-log scale). It can be seen that conductivities increased greatly to give a maximum with particle size reduction to 26 nm (P1). To understand the reason of the maximum conductivity, we have to consider the factors that are responsible for the conductivity. First, the conductivity of Ni_2O_3 nanoparticles might be primarily contributed by the holes and protons because: (1) Ni_2O_3 is a semiconductor and (2) Ni_2O_3 nanoparticles may show proton conduction for their hydrated surfaces as shown in FTIR [15, 18]. With regards to the protonic contribution, particle size reduction would give the enlarged surface area and enhanced surface hydration which are expected to produce a increased conductivity. Therefore, it is most likely that the observation of maximum conductivity could be a consequence of the balance between the concentration of charge carriers, holes and protons. Fig.6.5 (c) shows that all samples exhibit same pattern of conductivity, i.e. it is observed three regions which is separated by two threshold frequencies, f_1 and f_2. At low frequency ($>f_1$), conductivity is independent to the frequencies which denotes σ_{dc}. For the region $>f_1$ and $<f_2$, conductivity increase with frequencies which is called moderate frequencies region. At high frequencies region conductivity increases linearly with increases frequencies can reveals that the localized hopping [33-35]. However, as the frequency increases, electrons gain energy from the applied electric field and conductivity begins to rise at the higher frequency side. It also shows from table 1 that the grain resistance of large particle is approximately ten times that of small particles. [36]. At lower frequency, conductivity mainly due to mobilization of charge carriers over long range. Whereas, at high frequency regime the localization of charge carriers contributed to the ac conductivity.

6.4.   Conclusion

A low temperature chemical route has been adapted to synthesize nickel (III) oxide (Ni_2O_3) nanoparticles whose particle size can be varied by tuning the reaction temperature. XRD data confirmed the single phase hexagonal phase of the synthesized nanoparticles whose particulate nature can be further affirmed by FESEM analysis. The presence of signature bonds have been seen in FTIR analysis. The longitudinal optical one-phonon (1LO), longitudinal optical two-phonon (2LO) modes corresponding to the coupling interaction of Ni–O oscillations also been observed by Raman studies. The dielectric studies in the frequency range from 10 Hz-10^6 Hz at room temperature shows the samples has high dielectric constant and low loss. Further the impedance measurements reveal the effects of particle size and frequency on the dielectric behavior of nanocrystalline Ni_2O_3 and moreover effect of grain and grain boundary has been identified. The grain boundary effect is understood by fitting the RC equivalent circuit in the Nyquist plot derived from impedance spectroscopy. This samples holding high values for dielectric constant and low loss can be a possible candidate for dielectric amplification and wireless application. The ac conductivity of these materials shows three prominent region which can give the nature of conductivity change with frequencies and also shows that P1 has high conductivity compared to other two. The dielectric properties and ac conductivities of these material has been measured for the first time. The high dielectric permittivity and low loss of this material could be used for power systems and advance electronics.

6.5. References

1.   N. Sivakumar, A. Narayanasamy, N. Ponpandian and G. Govindaraj, *Journal of applied physics*, 2007, **101**, 084116.

2.   S. A. Makhlouf, M. A. Kassem and M. Abdel-Rahim, *Journal of materials science*, 2009, **44**, 3438.

3.   P. Marquardt, G. Nimtz and B. Mühlschlegel, *Solid state communications*, 1988, **65**, 539-542.

4.   H. Gleiter, *Advanced Materials*, 1992, **4**, 474-481.

5.   V. Biju and M. A. Khadar, *Materials Science and Engineering: A*, 2001, **304**, 814-817.

6.   H. Steinebach, S. Kannan, L. Rieth and F. Solzbacher, *Sensors and Actuators B: Chemical*, 2010, **151**, 162-168.

7.   S. Shrestha, C. Yeung, C. Nunnerley and S. Tsang, *Sensors and Actuators A: Physical*, 2007, **136**, 191-198.

8.   J. H. Pan, Q. Huang, Z. Y. Koh, D. Neo, X. Z. Wang and Q. Wang, *ACS applied materials & interfaces*, 2013, **5**, 6292-6299.

9.   X. Wang, G. Sun, N. Li and P. Chen, *Chemical Society Reviews*, 2016, **45**, 2239-2262.

10.   R. Birringer, *Materials Science and Engineering: A*, 1989, **117**, 33-43.

11.   M. Abdulkhadar and B. Thomas, *Nanostructured materials*, 1998, **10**, 593-600.

12.   C.-W. Nan, A. Tschöpe, S. Holten, H. Kliem and R. Birringer, *Journal of applied physics*, 1999, **85**, 7735-7740.

13.   L. Wohler and O. Balz, *Z. Elektrochem*, 1921, **27**, 406-419.

14.   S. Han, H.-Y. Chen, C.-C. Chen, T.-N. Yuan and H. C. Shih, *Materials Letters*, 2007, **61**, 1105-1108.

15.   R. Cairns and E. Ott, *Journal of the American Chemical Society*, 1933, **55**, 527-533.

16.   X. Wen, J. Gong, H. Yu, Z. Liu, D. Wan, J. Liu, Z. Jiang and T. Tang, *Journal of Materials Chemistry*, 2012, **22**, 19974-19980.

17.   J. Gong, K. Yao, J. Liu, X. Wen, X. Chen, Z. Jiang, E. Mijowska and T. Tang, *Chemical engineering journal*, 2013, **215**, 339-347.

18.   J. T. Richardson, *The Journal of Physical Chemistry*, 1963, **67**, 1377-1378.

19.   S. Dey, S. Bhattacharjee, R. S. Bose and C. K. Ghosh, *Applied Physics A*, 2015, **119**, 1343-1354.

20.   S. Dey, S. Bhattacharjee, M. G. Chaudhuri, R. S. Bose, S. Halder and C. K. Ghosh, *RSC Advances*, 2015, **5**, 54717-54726.

21.   Y. Qian, C. Zuo, J. Tan and J. He, *Energy*, 2007, **32**, 196-202.

22.   A. Citra, G. V. Chertihin, L. Andrews and M. Neurock, *The Journal of Physical Chemistry A*, 1997, **101**, 3109-3118.

23.   X. Su, H. Chai, D. Jia, S. Bao, W. Zhou and M. Zhou, *New Journal of Chemistry*, 2013, **37**, 439-443.

24.   G. A. Babu, G. Ravi, T. Mahalingam, M. Kumaresavanji and Y. Hayakawa, *Dalton Transactions*, 2015, **44**, 4485-4497.

25.   K. Rao and A. Smakula, *Journal of applied physics*, 1965, **36**, 2031-2038.

26.   V. Biju and M. A. Khadar, *Journal of materials science*, 2003, **38**, 4055-4063.

27.   W. D. Kingery, 1960.

28.   A. Ray, A. Roy, S. Bhattacharjee, S. Jana, C. K. Ghosh, C. Sinha and S. Das, *Electrochimica Acta*, 2018, **266**, 404-413.

29.   C. Ghosh, S. Malkhandi, M. Mitra and K. Chattopadhyay, *Journal of Physics D: Applied Physics*, 2008, **41**, 245113.

30.   E. Barsoukov and J. R. Macdonald, *Impedance spectroscopy: theory, experiment, and applications*, John Wiley & Sons, 2005.

31.   O. Raymond, R. Font, N. Suárez-Almodovar, J. Portelles and J. Siqueiros, *Journal of applied physics*, 2005, **97**, 084107.

32.   A. Ray, A. Roy, S. De, S. Chatterjee and S. Das, *Journal of applied physics*, 2018, **123**, 104102.

33.   A. Oueslati, F. Hlel, K. Guidara and M. Gargouri, *Journal of Alloys and Compounds*, 2010, **492**, 508-514.

34.   P. Muralidharan, M. Venkateswarlu and N. Satyanarayana, *Materials chemistry and physics*, 2004, **88**, 138-144.

35.   S. Mahboob, G. Prasad and G. Kumar, *Bulletin of Materials Science*, 2006, **29**, 347-355.

36.   C. F. Windisch Jr, K. F. Ferris and G. J. Exarhos, *Journal of Vacuum Science & Technology A: Vacuum, Surfaces, and Films*, 2001, **19**, 1647-1651.

Chapter 7

Non-stoichiometric Ni_2O_3 nanoparticles as a fast and efficient photocatalyst for dye degradation in industrial waste water

Abstract

Industrialization has led to an exponential escalation of water contamination particularly by organic dyes in South East Asia where textile industries are at bloom. In this study, non-stoichiometric Ni_2O_3 synthesized by an environmentally friendly low temperature (0° to 50^oC) solution phase synthesis approach was demonstrated as a novel photocatalyst for fast and highly efficient degradation of Congo Red (CR) and Methylene Blue (MB) dyes under solar irradiation. The degradation efficiency was pH dependent and was obtained as 99.2% and 97.4% for CR and MB respectively with 1 hour of exposure time. The pH dependency study showed highest degradation at 4.3 and 5.6 pH respectively for CR and MB which are close to the characteristic pH of the dyes in solution. Hence, no pH modulation is required for efficient degradation. The mechanism showed enhanced formation of $^{\bullet}OH$ and $^{\bullet}O_2H$ free radicals responsible for the degradation/oxidation of the dye due to the use of defective (non-stoichiometric) Ni_2O_3 as catalyst. The catalyst was also found to be highly stable and re-usable (tested consecutively for six times) with an average deviation of 0.79% and 0.67% respectively for CR and MB. This catalyst was hence potent enough to efficiently degrade CR and MB at a fast rate to their non-toxic forms and hence can challenge the existence of the conventional photocatalysts used in the industry.

7.1. Introduction

With modernization, the growth rate of industries has exponentially increased in all sectors viz. chemical, textile, steel and power in order to meet the daily requirements and comfortable lifestyle of people. This directly or indirectly enhances the pollution in and around the industrial area [1]. Though pollution and industrialization are linearly dependent due to several industrial waste disposal strategies, pollution abatement is not yet very effective. One such waste disposal strategy is industrial discharge in running water which is known to cause serious damage to the

aquatic and in turn, human biota. The available physical, chemical and biological techniques have several drawbacks, are not cost efficient and hence are not commercially viable. Among the toxic constituents of industrial discharge in water, certain azo-dyes and there degraded by-products e.g. aromatic amines, have been reported to be a mutagen [2] as well as an enhancer of the carcinogenesis, chromosomal fractures and respiratory toxicity [3].

Conventional separation techniques viz. degradation, adsorption, coagulation, electrophoresis and extraction, though useful in certain scenarios, involve high energy consumption, low efficiency, large footprint and inadequate selectivity [4]. Apart from these, several other technologically advanced methods such as flocculation, biological treatment and electrolysis have been introduced to remove dye from waste water [5]. Among all these methods, photo catalytic degradation of dyes is relatively simple and cost efficient though the low photochemical activities for most visible light and ultra violet light active semiconducting photo catalysts and quantum yields are low. This bars the catalysts from practical use [6]. Adsorption based dye removal technique via mesoporous adsorbents are often considered due to its simple operation. However, synthesis of mesoporous adsorbents involve complex chemical synthesis strategy and when used in acidic environments (especially metal oxides) are unstable [7]. South East Asia has a flourishing bloom of textile industries where congo red (CR), a benzidine-based anionic diazo dye and methylene blue (MB), a phenothiazine derivative cationic dye are among the commonly used dyes that are found mostly as industrial discharge in water. Both CR and MB have vast range of side effects starting from cardiovascular to haematologic [8].

Focussing on photo catalytic degradation of toxic dyes into their non-toxic oxidized products involves light activated catalysis of a series of free radical reactions. Most metal oxides e.g. ZnO [9], TiO_2 [10], NiO [11], CuO [12] and their composites [13-16] catalyze effectively in presence of the UV spectrum due to their wide bandgap. However, UV irradiation is not

industrially viable mainly due to its oncogenic nature to human beings. Hence, there is an urgent need of a material that can catalyze in the visible range. Several metal oxides can catalyze organic dye oxidation under sunlight either in combination with other metal oxides or after undergoing defect engineering. However, synthesis of such materials is quite complex, time consuming, high temperature and power requirement and hence not environmentally friendly and requires skilled manpower and hence costly [17, 18].

Among different transition metal oxides (TMOs) used as photo catalysts, porous nickel oxide nanostructures and their composites having non-stoichiometric defects have shown excellent photo degradation properties over the entire solar spectrum [19-23]. However, the synthesis methods of these materials involve rigorous steps, high temperature operation, sophisticated instrumentation and specific reagents which are not very user and environmentally friendly. Thus, an environmentally friendly synthesis technique involving lesser complex reagents and lower synthesis temperature can be suggested for preparing non-stoichiometric nickel oxide which can serve as excellent photocatalyst by creating a chemically oxidizing environment at room temperature or even below. As a proof of concept, the authors have already prepared nickel (III) oxide (Ni_2O_3) nanostructures within 0^oC to 70^oC for excellent adsorption mediated Cr(VI) ion removal/monitoring in their previous works [24-27]. In this paper, the authors present non-stoichiometric Ni_2O_3 nanoparticles synthesized by a mild environmentally friendly room temperature oxidative co-precipitation approach as an excellent wide band photocatalyst capable of degrading CR and MB under solar irradiation. The degradation efficiency, reusability and stability of the catalyst have been studied under different reaction conditions (exposure time and pH). A dye degradation mechanism was proposed considering the effect of induced surface defects and non-stoichiometric band tailoring on the photo catalytic activity of Ni_2O_3 catalysts.

7.2. Experimental

All chemicals were of analytical grade, procured from Merck India Pvt. Ltd. and were used without further purification.

7.2.1. Synthesis of non-stoichiometric Ni₂O₃

In a typical process, 1.57 g of $Ni(NO_3)_2.6H_2O$ was dissolved in 20 mL de-ionized (DI) water to obtain a greenish transparent solution. To this, 15 mL of alkaline NaOCl solution prepared by dissolving 0.1 M NaOH in 15 mL NaOCl was added slowly at the rate of 1 mL/min under constant stirring at 500 rpm. The stirring was continued till 15 mins and then the greyish black precipitate was washed with DI water thrice, filtered and dried at 50°C in a hot air oven. The dried powder was further subjected to sustained oxidation in 15 mL NaOCl solution and kept till the effervescence ceased. This was done to oxidize any un-reacted Ni^{2+} ion and remove pseudo-hydrate phase (if any). The final product was washed with DI water, filtered and dried at 50°C. The particle size and crystalinity was varied by varying the synthesis temperature from 0°C to 50°C to study the effect of synthesis temperature on catalytic property of the material.

7.2.2. Characterizations

The phase and crystal structure analysis of the non-stoichiometric Ni₂O₃ nanoparticles were performed by X-ray diffraction (Rigaku, Cu $\lambda_{K\alpha}$ = 1.5404 Å). The morphological analysis of the sample was done by FESEM (S-4800, Hitachi) and TEM (JEOL) with EDAX facility. Dye (CR & MB) degradation studies were carried out under solar irradiation and subsequent characterization were done by UV-visible spectrophotometer (JASCO V-650).

7.2.3. Photocatalytic activity measurements

The photo degradation activity was carried out in triplets under solar irradiation in 100 mL glass beakers. All solutions were prepared using volumetric flask to minimize measurement errors.

The photocatalysis test setup was custom made chamber with a programmable stirrer to control the stirring speed accurately. The chamber was designed so as to minimize dispersive and radiative losses of the incident wavelengths. 0.01 g of catalyst was dispersed in a 50 mL stock solution (CR & MB) with an initial concentration of 1mg/L. The whole setup was then exposed to solar radiation under a constant stirring of 500 rpm. The degraded dye solution, after certain time, was centrifuged (20,000 rpm for 10 minutes) to remove the catalyst which was collected separately. The absorbance spectra of the centrifuged dye solutions were recorded using a UV-Vis spectrometer to estimate the concentration of CR and MB. The batch experiment was carried out for each of the three different particle sizes (based on synthesis temperature). In order to study the dependence of the reaction on physical parameters, the experiment was repeated by varying the reaction physical conditions like pH, amount of adsorbate, amount of adsorbent etc. Both dyes were tested with the photocatalyst in dark condition to confirm absence of any catalytic reaction in the absence of white light.

7.2.4. Reusability of catalyst

The catalyst after separation from the dye solution was washed with 0.1 M NaOH solution thrice followed by 15 mL NaOCl solution once to remove any adsorbed dye molecule and regenerate any Ni_2O_3 (if it has at all reduced).

7.3. Results and discussion

7.3.1. XRD and morphology analysis

The XRD patterns of the synthesized samples have been shown in Fig. 7.1 (a). The observed patterns were in conformity with the standard reference patterns (JCPDS Card Number 14-0481, CAS Number 1314-06-3). The peaks corresponding to pure hexagonal Ni_2O_3 appearing at 27.34º, 31.66°, 45.41º, 56.38º and 66.12º can be indexed to (101), (002), (111), (202) and (004)

planes. The absence of any other peak in the spectrum confirms the formation of pure hexagonal Ni_2O_3. The particle size was calculated using the Scherrer's formula [28] as tabulated in Table 6.1. From the spectrum, it was also observed that growth alone the (002) plane increased with increase in synthesis temperature thereby signifying directional growth dependency on the synthesis temperature.

Table 7.1 Variation of particle size with synthesis temperature.

Temperature of Synthesis	Particle Size (in nm)
0°C	25.8
RT (25°C)	34.2
50°C	42.6

The morphology analysis was performed from SEM and TEM micrographs (shown in Fig. 7.1 (b), (c) and (d)). The formation of nanoparticles with average size of ~ 20 nm was observed and was found to be in good agreement to the calculated dimension from the XRD spectrum. Fig. 7.1 (e) demonstrated the lattice image of non-stoichiometric Ni_2O_3 and was measured to be ~ 2.8 Å which is corresponding to the (002) plane of hexagonal Ni_2O_3. The EDAX profile taken at 10 nm scale for Ni_2O_3 showed the presence of Ni and O in a non-stoichiometric ratio thus confirming the formation of the Ni_2O_3 nanoparticles. All characterizations were performed for the sample prepared at 0°C. Other samples were also expected to show similar observations.
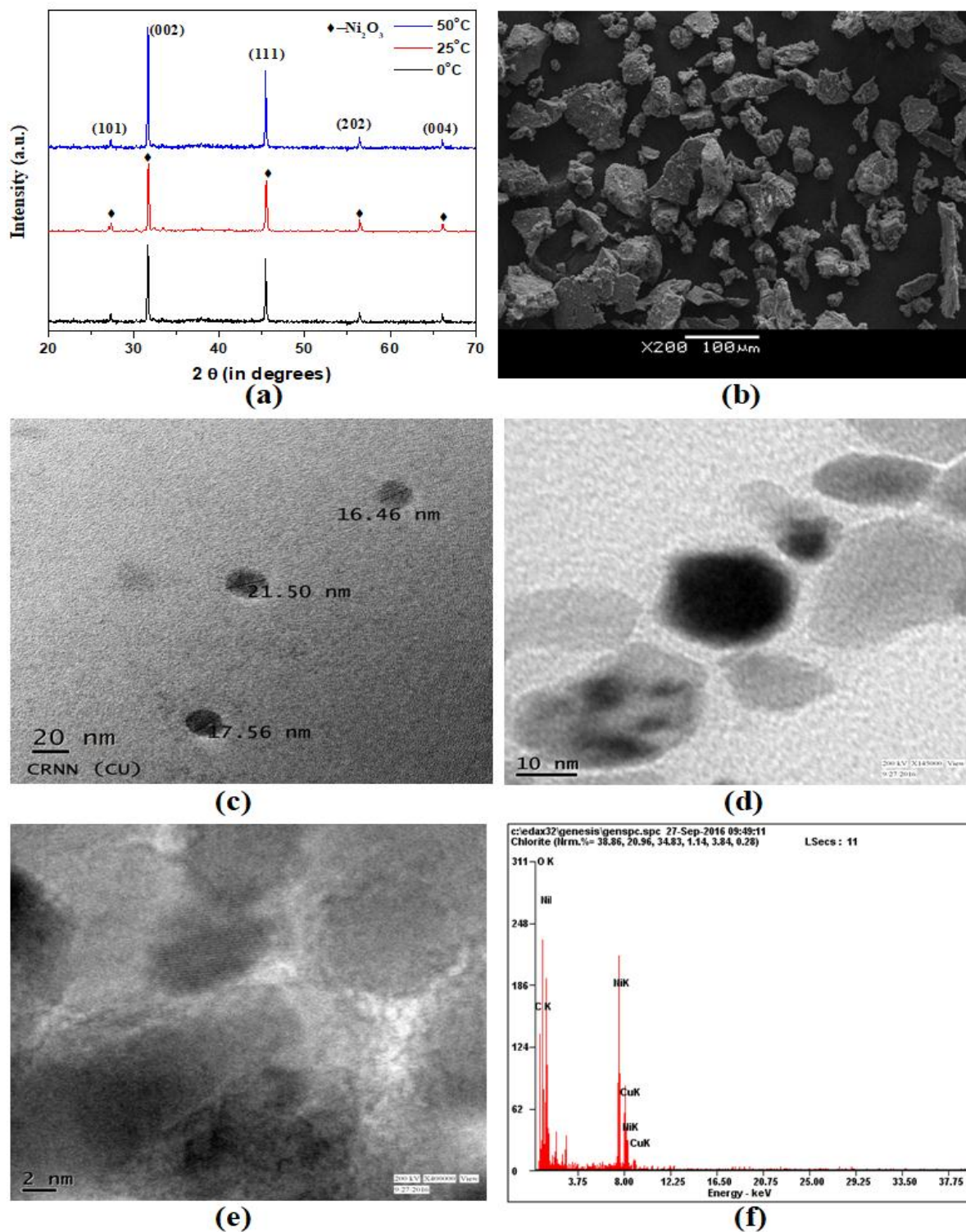
Fig. 7.1 (a) X-ray diffractogram (b) FESEM image (c) TEM image (in 20 nm scale) (d) TEM image of a single nanoparticle (in 10 nm scale) (e) Lattice image (f) EDAX report showing the elemental composition of pure non-stoichiometric Ni_2O_3 nanoparticles.

7.3.2. Photocatalytic degradation of CR and MB

7.3.2.1. Effect of exposure time

Fig. 7.2 (a) and (b) shows the photocatalytic degradation of CR and MB dyes respectively with non-stoichiometric Ni_2O_3 as photocatalyst with varying exposure time (7.5 - 60 mins). It was observed that the photocatalytic activity degraded with increase in particle size with a maximum degradation rate of ~ 99.2% of CR and ~ 97.4% of MB for particles synthesised at 0^oC exposed for 1 hour. The initial degradation rate for CR was however reversed in terms of particle size. Negligible amount of dye was degraded in absence of light in comparison to that of light and so it was neglected.
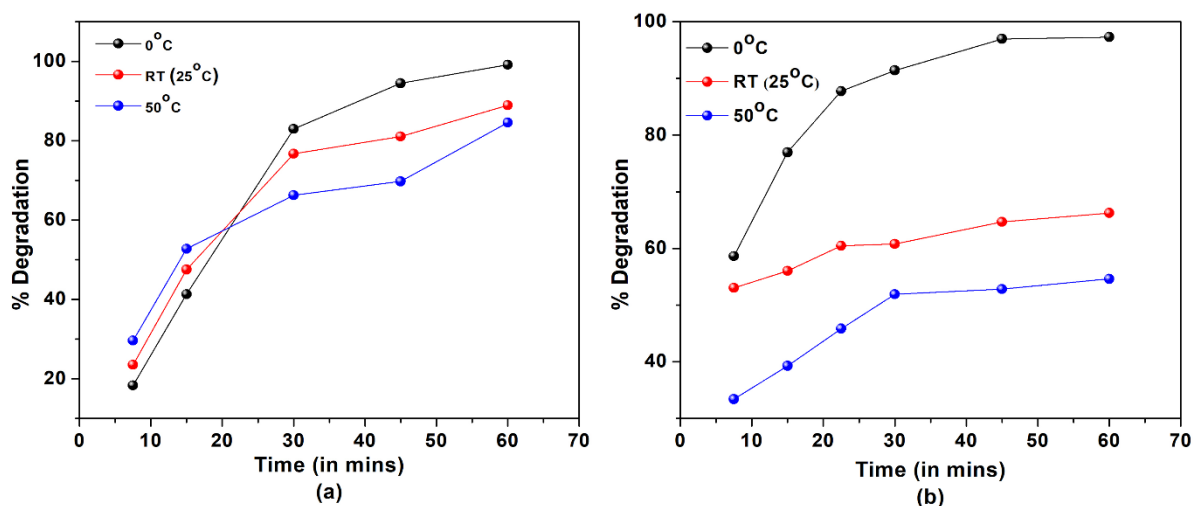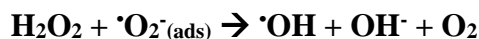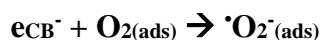

Fig. 7.2 Variation of (a) CR (b) MB dye degradation with exposure time in presence of non-stoichiometric Ni_2O_3 as photocatalyst.

7.3.2.2. Effect of pH

pH is an integral parameter that controls the efficiency of a chemical reaction. In the present photo degradation experiment, degradation efficiency was studied by varying the pH of the solution (pH 3 – pH 12). It was observed that highest degradation was obtained in the acidic pH (~4.3 for CR and ~5.6 for MB) while the degradation progressively decreased with an increase in [OH^-]

(illustrated in Fig. 7.3 (a) and (b)). It is well known that acidic pH enhances the degradation of dyes due to the formation of OH$^\bullet$ free radicals as follows [29]:

$$e_{CB}^- + O_{2(ads)} \rightarrow {}^\bullet O_2{}^-_{(ads)}$$

$${}^\bullet O_2{}^-_{(ads)} + H^+ \rightarrow {}^\bullet HO_2$$

$$2{}^\bullet HO_2 \rightarrow O_2 + H_2O_2$$

$$H_2O_2 + {}^\bullet O_2{}^-_{(ads)} \rightarrow {}^\bullet OH + OH^- + O_2$$

Interestingly, both the dyes have negative sulphur centres that are more prone towards degradation at lower pH. Also, at lower pH, the apparent surface of the Ni_2O_3 nanoparticles are pseudo positively charged due to the H^+ ions shielding aiding to more efficient catalysis (by adsorption). However, as the concentration of OH^- ions increase, the negative centres of the bulky dye molecules face competitive attraction towards the catalyst resulting in lower reaction mediated by adsorption. Hence the effective degradation decreases with increase in pH of the medium.
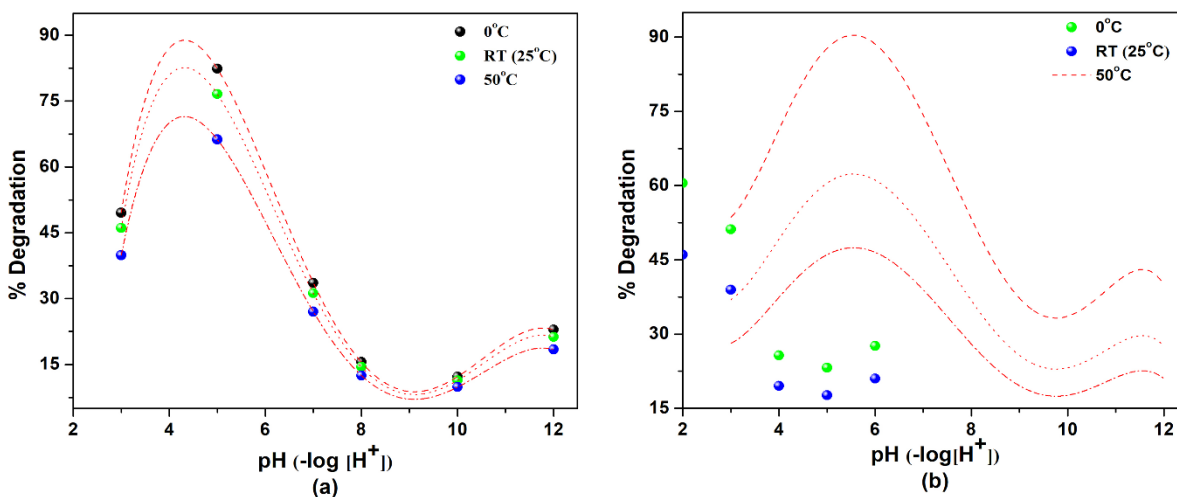

Fig. 7.3 Variation of (a) CR (b) MB dye degradation with pH in presence of non-stoichiometric Ni_2O_3 as photocatalyst (exposure time: 30 mins)**.**

7.3.3. Regeneration, reusability and stability of catalyst

In photo degradation studies, regeneration and stability of the catalyst is an important aspect in terms of long term use of the same. The non-stoichiometric Ni_2O_3 was collected and washed thrice for removal of any adsorbed dye and converted $Ni(OH)_2$. The XRD spectrums recorded before and after experiments were found to be almost identical in terms of peak positions and peak intensity thereby confirming the catalyst to be stable and regenerable.

For reusability study, the catalyst was re-used repeatedly for six times each with exposure of 30 minutes for both the dyes. It was observed that the catalyst showed a good reusability with an average adsorption rate of (80.61 ± 0.79) % for CR and (89.55 ± 0.67) % for MB. The deviation errors calculated as standard error of mean could be considered within the error range and hence ignored. The reusability results for CR and MB are illustrated in Fig. 7.4 (a) and (b) below.
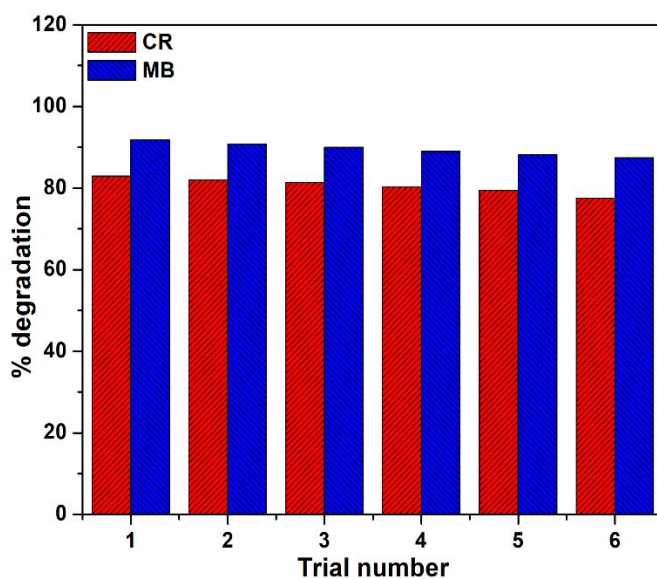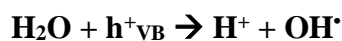

Fig. 7.4 Reusability of non-stoichiometric Ni_2O_3 catalyst for photo degradation of CR (red) and MB (blue) (exposure time ~30 minutes).

7.3.4. Mechanism of photocatalysis of CR and MB by non-stoichiometric Ni₂O₃ nanoparticles

In order to understand the photocatalytic degradation of CR and MB in presence of Ni_2O_3 nanoparticles as catalyst, the band structure of Ni_2O_3 must be taken into account. Ni_2O_3 is a p-type semiconductor with an intrinsic bandgap of ~ 3.67 eV [30]. Due to its non-stoichiometric composition and induced defects, several impurity defect levels are expected to be formed which would result in several electronic transition. As a result, the material was found to be active under solar irradiation instead of UV irradiation only. When photon is incident on the catalyst surface, the conduction band gets populated with electrons (e^-_{CB}) from pre-existing electron-hole pairs leaving a hole back in the valance band (h^+_{VB}). This proton breaks down water molecule to release an $OH^•$ and H^+ thereby making the solution acidic. Also, OH^- ions in solution take up one proton to convert to $OH^•$. This $OH^•$ is responsible for degradation of the dye. On the other hand, electron in the conduction band converts molecular O_2 to $^•O^{2-}$ which initiates the Fenton reaction in acidic pH. Now, decolourization of the dye can take place by three ways: (i) degradation of the dye by $OH^•$ (ii) oxidation of the dye by proton resulting in the formation of non-toxic degraded/oxidised products and (iii) progress of the Fenton reaction (formation of $O_2H^•$ radical with $^•O^{2-}$) in acidic pH (i.e. in presence of H^+ ions in solution) that once again helps in effective oxidation of the dye (already explained earlier). The overall reactions can be summarized in the following free radical equations:

$$Ni_2O_3 + h\nu \rightarrow Ni_2O_3 \; (e^-_{CB} + h^+_{VB})$$
$$O_2 + e^-_{CB} \rightarrow {}^•O^{2-} \text{ (initiation of Fenton reaction)}$$
$$H_2O + h^+_{VB} \rightarrow H^+ + OH^•$$
$$OH^- + h^+_{VB} \rightarrow OH^•$$
$$Dye + OH^• \rightarrow \text{Degraded dye}$$
$$Dye + h^+_{VB} \rightarrow dye^{•+} \text{ (oxidized dye)}$$

The whole mechanism is illustrated in the Fig. 7.5 shown below:
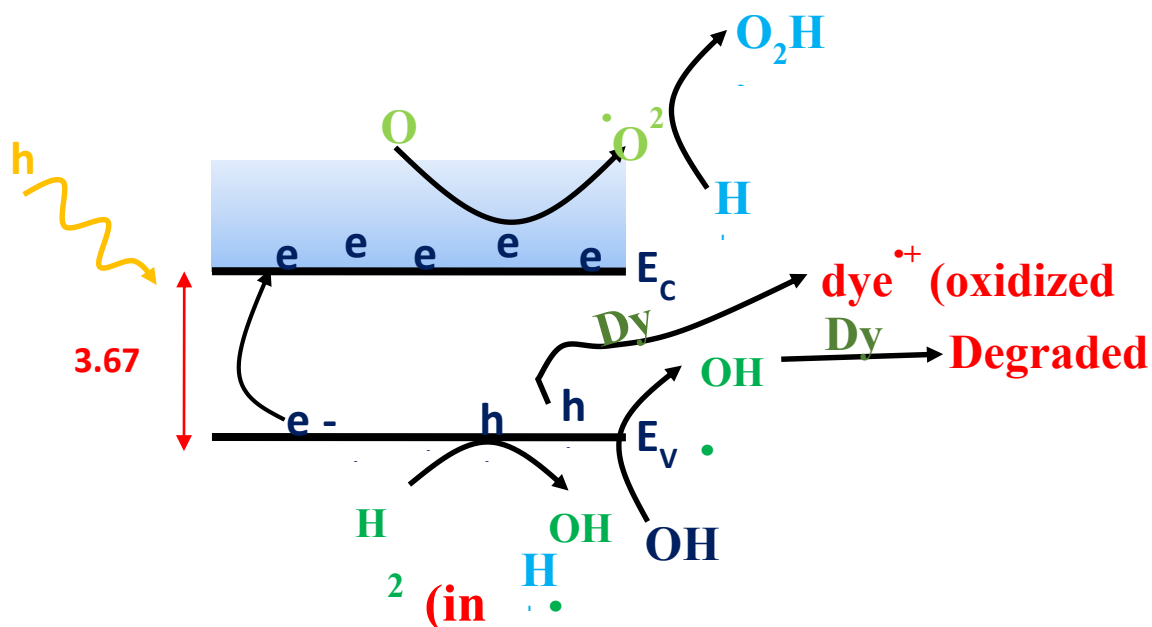
Fig. 7.5 Mechanism of photo degradation of MB and CR by non-stoichiometric Ni_2O_3 nanoparticles.

The ease of degradation depends on the negative centre present in the dye (sulphur in case of both CR and MB). The peroxide radical based degradation is most effective on sulphur centres resulting in excellent and fast degradation of both CR and MB by similar mechanism.

7.4. Conclusion

Thus, the study demonstrated non-stoichiometric Ni_2O_3 as a potential photocatalyst which can degrade CR (99.2%) and MB (97.1%) dyes at 1 hour under solar irradiation. The synthesis strategy poses a novel environmentally friendly room temperature technique which would be industrially viable in terms of power and time requirement. The catalyst was found to be re-usable after six consecutive cycles with an average deviation error of 0.79% and 0.67% for CR and MB respectively. The catalyst was most active in slight acidic pH which is the characteristic pH of both

CR and MB and hence no pH modulation was required. The proposed mechanism demonstrates enhanced $^{\bullet}OH$ and $^{\bullet}O_2H$ formation by the utilization of the full solar spectrum resulting in fast degradation of the dye in comparison to other potent photocatalyst. This catalyst offers a simple, fast and solar irradiation assisted proto degradation of CR and MB and hence can be very well used commercially in competition to its conventional industrial counterparts.

7.5. References

1.   G. Kale, S. Arbuj, U. Kawade, S. Rane, J. Ambekar and B. Kale, *Materials Chemistry Frontiers*, 2018, **2**, 163-170.

2.   B. Cheng, Y. Le, W. Cai and J. Yu, *Journal of Hazardous Materials*, 2011, **185**, 889-897.

3.   E. N. Zare, A. Motahari and M. Sillanpää, *Environmental Research*, 2018, **162**, 173-195.

4.   C. Liu, L. Cheng, Y. Zhao and L. Zhu, *Journal of Hazardous Materials*, 2017, **337**, 217-225.

5.   C. Su, *Journal of Hazardous Materials*, 2017, **322**, 48-84.

6.   H. Yang, F. Teng, W. Gu, Z. Liu, Y. Zhao, A. Zhang, Z. Liu and Y. Teng, *Journal of Hazardous Materials*, 2017, **333**, 250-258.

7.   Y. Shao, B. Ren, H. Jiang, B. Zhou, L. Lv, J. Ren, L. Dong, J. Li and Z. Liu, *Journal of Hazardous Materials*, 2017, **333**, 222-231.

8.   E. Brillas and C. A. Martínez-Huitle, *Applied Catalysis B: Environmental*, 2015, **166**, 603-643.

9.   M. Pirhashemi and A. Habibi-Yangjeh, *Journal of colloid and interface science*, 2017, **491**, 216-229.

10. K. Alamelu, V. Raja, L. Shiamala and B. M. J. Ali, *Applied Surface Science*, 2018, **430**, 145-154.

11. S. V. Sancheti, C. Saini, R. Ambati and P. R. Gogate, *Catalysis Today*, 2018, **300**, 50-57.

12. S. Mosleh, M. R. Rahimi, M. Ghaedi, K. Dashtian and S. Hajati, *Ultrasonics Sonochemistry*, 2018, **40**, 601-610.

13. E. Abroshan, S. Farhadi and A. Zabardasti, *Solar Energy Materials and Solar Cells*, 2018, **178**, 154-163.

14. T. A. Kurniawan, L. Yanyan, T. Ouyang, A. B. Albadarin and G. Walker, *Materials Science in Semiconductor Processing*, 2018, **73**, 42-50.

15. M. Nasirian, C. F. Bustillo-Lecompte and M. Mehrvar, *Journal of environmental management*, 2017, **196**, 487-498.

16. F. Siadatnasab, S. Farhadi and A. Khataee, *Ultrasonics Sonochemistry*, 2018, **44**, 359-367.

17. E. Abroushan, S. Farhadi and A. Zabardasti, *RSC Advances*, 2017, **7**, 18293-18304.

18. R. P. Barkul, M. K. Patil, S. M. Patil, V. B. Shevale and S. D. Delekar, *Journal of Photochemistry and Photobiology A: Chemistry*, 2017, **349**, 138-147.

19. M. A. Ahmed, *Journal of Photochemistry and Photobiology A: Chemistry*, 2012, **238**, 63-70.

20. H. Derikvandi and A. Nezamzadeh-Ejhieh, *Journal of Hazardous Materials*, 2017, **321**, 629-638.

21. F. Hashemzadeh, A. Gaffarinejad and R. Rahimi, *Journal of Hazardous Materials*, 2015, **286**, 64-74.

22. A. Pourtaheri and A. Nezamzadeh-Ejhieh, *Chemical Engineering Research and Design*, 2015, **104**, 835-843.

23. F. Torki and H. Faghihian, *RSC Advances*, 2017, **7**, 54651-54661.

24. S. Dey, S. Bhattacharjee, R. S. Bose and C. K. Ghosh, *Applied Physics A*, 2015, **119**, 1343-1354.

25. S. Dey, S. Bhattacharjee, M. G. Chaudhuri, R. S. Bose, S. Halder and C. K. Ghosh, *RSC Advances*, 2015, **5**, 54717-54726.

26. S. Dey, S. Podder, A. Roychowdhury, D. Das and C. K. Ghosh, *Journal of environmental management*, 2018, **211**, 356-366.

27. S. Dey, S. Santra, A. Midya, P. K. Guha and S. K. Ray, *Environmental Science: Nano*, 2017, **4**, 191-202.

28. A. L. Patterson, *Physical Review*, 1939, **56**, 978-982.

29. N. Daneshvar, D. Salari and A. R. Khataee, *Journal of Photochemistry and Photobiology A: Chemistry*, 2003, **157**, 111-116.

30. M. Shaban, M. R. Abukhadra and A. Hamd, *Clean Technologies and Environmental Policy*, 2018, **20**, 13-28.

Chapter 8

Grand conclusion and future scope

8.1. Conclusion of the thesis

8.2. Future scope

8.1. Conclusion of the thesis

A comprehensive summary of the work done in the present thesis is drawn in this chapter.

- Coral-like NiO microstructure, constituted by nanorods, has been prepared successfully using water-urea-PEG based hydrothermal methods followed by calcination. The effects of PEG concentration and hydrothermal treatment on the formation of NiO coral-like microstructure have been investigated and it is observed that the desired microstructure gets formed only at an optimized condition. Structure and morphology of the synthesized samples have been examined by XRD, FESEM and HRTEM. The synthesized structure exhibits high porosity ~ 37% and Ni vacancies at the surfaces, which is investigated by Positron annihilation spectroscopy. Magnetic study illustrates spin-glass like behaviour. Interestingly, the synthesized structure exhibits asymmetric hysteresis loop at room temperature. Later one is attributed to non-inversion symmetry of the anisotropic energy barrier, introduced by defect induced ferromagnetic domain within antiferromagnetic matrix of NiO. Numerical values of the anisotropy parameters have also been evaluated using law of approach method. The present study evidences that the microstructure could be helpful for developing magnetization based memory devices due to its high barrier height ~ 2.50×10^6 erg/cm^3. In this context, it is to state that the interparticle interaction, inherent of this particular microstructure via surface defects, is strong enough to give asymmetric hysteresis at room temperature.

- In this study, NiO with different morphologies (coral–like and flake–like) are successfully synthesized by facile hydrothermal method at 90^{0}C followed by calcination at 450^{0}C. Structural and morphological properties of the synthesized samples have been investigated by XRD, FESEM and HRTEM. BET measurement reveals that the synthesized coral –

like nanostructure exhibits lower surface area (39.91 m^2/g) compared to flake – like nanostructure (91.38 m^2/g). Raman spectrum analysis gives higher electron – phonon interaction in coral – like nanostructure compared to flake – like nanostructure and accumulated electrons at the surface of the nanostructures are the source for higher electron – phonon interaction. This interaction got further supported by FWHM of the luminescence spectra, where electron – LO phonon interaction plays the dominating role. Huang – Rhys 'S' – factor characterizing electron – phonon interaction has been quantified from excitation, emission of spectra corresponding to band edge emission. Higher fractional dimension of coral – like nanostructure is analyzed to be responsible for higher 'S' – factor. It has been demonstrated from ROS assay that coral – like nanostructure exhibits higher electron transfer rate per unit area compared to flake – like nanostructure. It had also been illustrated that coral – like NiO electrode exhibits higher electrochemical capacitance ($C_m = 343$ mF/cm^2) than flake – like nanostructure ($C_m = 163$ mF/cm^2) though former exhibits less surface area. Applying Marcus theory, it has been demonstrated that the charge transfer process in catalytic as well as in electrochemical process within the synthesized nanostructures are non-adiabatic in nature, guided by electron – phonon interaction. And finally, it is concluded that lattice polarization, caused by electron – phonon interaction, imparts the crucial role specific pseudocapacitance while charge transfer resistance and charging or discharging time are determined by activation energy of process where the same electron – phonon interaction also plays significant role.

- We present a two-step facile method to prepare Ni$_2$O$_3$ coral–like and flower–like nanostructures first time followed by structural, optical characterizations by XRD, FESEM, HRTEM, Raman, luminescence spectroscopy etc. PALS and optical studies

illustrate that coral–like nanostructure exhibits higher electron – phonon interaction in comparison to flower–like nanostructure due to defects (Ni^{+3} vacancies). Fractional dimension space approach has been taken into account to explain defect dependence of electron – phonon interaction. We have successfully fabricated rectifying metal – semiconductor junction having fairly low turn – on voltages (0.36 and 0.53 V for flower and coral-like nanostructures respectively) using Ni_2O_3 as an active semiconducting materials. A number of electrical parameters like electron mobility, carrier lifetime, diffusion length, nature of current transport etc., associated with MS junction, have been evaluated. These parameters significantly depend on defect concentrations of the nanostructures. Notably, this has been first time examined that the charge transport across the junction follows non-adiabatic process rather than adiabatic character. Importantly, our synthesized nanostructures reveal dominating thermionic current though exhibit low potential barrier i.e. the synthesized MS nano-junction is very much suitable for opto-electronic applications. A comparison reveals that the junction characteristics are very much suitable for optoelectronic applications due to low series resistance, ideality factor close to one despite ultralow barrier height.

- A low temperature chemical route has been adapted to synthesize nickel (III) oxide (Ni_2O_3) nanoparticles whose particle size can be varied by tuning the reaction temperature. XRD data confirmed the single phase hexagonal phase of the synthesized nanoparticles whose particulate nature can be further affirmed by FESEM analysis. The presence of signature bonds have been seen in FTIR analysis. The longitudinal optical one-phonon (1LO), longitudinal optical two-phonon (2LO) modes corresponding to the coupling interaction of Ni–O oscillations have also been observed by Raman studies. The dielectric

studies in the frequency range from 10 Hz-10^6 Hz at room temperature show that the sample has high dielectric constant and low loss. Further the impedance measurements reveal the effects of particle size and frequency on the dielectric behavior of nanocrystalline Ni_2O_3 and moreover effect of grain and grain boundary have been identified. The grain boundary effect is understood by fitting the RC equivalent circuit in the Nyquist plot derived from impedance spectroscopy. This sample holding high values for dielectric constant and low loss can be a possible candidate for dielectric amplification and wireless application. The ac conductivity of these materials shows three prominent region which can give the nature of conductivity change with frequencies and also shows that smaller size nanomaterial has high conductivity compared to other two higher size nanomaterials. The dielectric properties and ac conductivities of these material have been measured for the first time. The high dielectric permittivity and low loss of this material could be used for power systems and advance electronics.

- In this study, non-stoichiometric Ni_2O_3 synthesized by an environmentally friendly low temperature (0° to 50^oC) solution phase synthesis approach was demonstrated as a novel photocatalyst for fast and highly efficient degradation of Congo Red (CR) and Methylene Blue (MB) dyes under solar irradiation. The degradation efficiency was pH dependent and was obtained as 99.2% and 97.4% for CR and MB respectively with 1 hour of exposure time. The synthesis strategy poses a novel environmentally friendly room temperature technique which would be industrially viable in terms of power and time requirement. The catalyst was found to be re-usable after six consecutive cycles with an average deviation error of 0.79% and 0.67% for CR and MB respectively. The catalyst was most active in slight acidic pH which is the characteristic pH of both CR and MB and hence no pH

modulation was required. The proposed mechanism demonstrates enhanced $^{\bullet}OH$ and $^{\bullet}O_2H$ formation by the utilization of the full solar spectrum resulting in fast degradation of the dye in comparison to other potent photocatalyst. This catalyst offers a simple, fast and solar irradiation assisted proto degradation of CR and MB and hence can be very well used commercially in competition to its conventional industrial counterparts.

8.2. Future scope

- To investigate the effect of other morphology of NiO on magnetic properties including pattern hysteresis loop and its asymmetry.

- To study the effect of interparticle interaction on magnetic properties of NiO including phase transition, structure etc.

- To study the effect of morphology and size on magnetic properties of Ni_2O_3.

- To study the effect of morphology of Ni_2O_3 on dielectric and electrical properties.

Contents lists available at ScienceDirect

Physica B: Condensed Matter
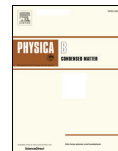
Electron – Phonon interaction to tune metal – Semiconductor junction characteristics: Ultralow potential barrier and less non-thermionic emission

Swarupananda Bhattacharjee[a], Arka Dey[b], Sayan Dey[a,1], Anirban Roychowdhury[c,2], Partha P. Ray[b,**], Dipankar Das[c], Gopes C. Das[d], Chandan K. Ghosh[a,*]

[a] *School of Materials Science and Nanotechnology, Jadavpur University, Kolkata, 700032, India*
[b] *Department of Physics, Jadavpur University, Kolkata, 700032, India*
[c] *UGC-DAE Consortium for Scientific Research, Kolkata Centre, III/LB-8, Bidhannagar, Kolkata, 700098, India*
[d] *Department of Metallurgical and Materials Engineering, Jadavpur University, Kolkata, 700032, India*

ARTICLE INFO

ABSTRACT

We present a two-step facile method to prepare Ni_2O_3 coral–like and flower–like nanostructures first time followed by structural, optical characterizations by XRD, FESEM, HRTEM, Raman, luminescence spectroscopy etc. We also report rectifying *I–V* characteristics of Ni_2O_3 nanostructures/Al based metal–semiconductor junction with ultralow turn-on voltages (0.36 V), potential barrier (0.33 eV), very ideal thermionic current ($\eta = 1.11$). Photo-responsive character illustrates that the junction devices could be a promising material for light sensing application. Parameters like series resistance (111.4 Ω), electron mobility (16.73×10^{-10} $m^2V^1s^{-1}$), diffusion length (5.13×10^{-7} m), density of states (3.09×10^{40} eVm^{-3}) etc. have been evaluated and it is discussed that the defect (Ni^{3+} vacancy) induced electron–phonon interaction within the active semiconducting layer plays the crucial role to determine these parameters. Most importantly, it has been identified that the charge-transport across the junction follows non-adiabatic mechanism. Our results suggest a new insight into current transport mechanism that may be generalized to understand microstructural, defect dependence MS junctions.

1. Introduction

Due to ability of converting light into electrical signal, metal–semiconductor (MS) junctions are ubiquitously used in the field of various optoelectronic devices such as solar energy, light-wave communication, photodetector etc. [1–3] With current research trends in the field of nanoscience and technology, focus has been shifted to develop low-dimensional nanoscale MS junctions those exhibit new optoelectronic characteristics, attributed to unique features of the nanomaterials. In this context, it may be stated that understanding of the optical and electrical properties of nano-junction is very important for the fabrication of reliable real field MS nano-optoelectronic devices. Several parameters like carrier lifetime, charge carrier-recombination rate, band gap, morphology etc. of the semiconductors are found to influence significantly on the performance of these devices, therefore searching of efficient nano-junction for various nano-optoelectronic devices is the 'holy grail' research trend in this realm [4,5]. ZnO, TiO_2, CdTe, CdSe,

CdS, ZnS etc. are employed as potential semiconducting materials due to their easy tuneability of microstructure, chemical stability, easy availability, environmental compatibility etc. [6] There are evidential reports demonstrating that barrier inhomogeneity, attributed to grain boundary, defects, morphology etc., mostly influences the interfacial properties including potential ideality factor, reverse saturation current etc., while energy difference between Fermi energy of metal and conduction band of semiconductor determines the turn-on voltage. In this regard, Ren et al. have studied the effect of lattice mismatch on the barrier characteristics [7]. The effect of barrier fluctuation of barrier on current have been investigated by Tung [8] employing ballistic electron emission spectroscopy. Effect of lateral barrier inhomogeneity on ideality factor which is a measure of non-ideal *I–V* characteristic has been enumerated by Biber et al. [9] It has also been observed that MS junction characteristic gets also influenced by the dipole moment, formed at MS interface. For example, Endo et al. has revealed that the dipole moments perpendicular to either Zn-polar (0001) or O-polar

Full Length Article

Non-inversion anisotropy energy in NiO coral structure: Asymmetric hysteresis loop at room temperature

Swarupananda Bhattacharjee [a], Gopes Chandra Das [a], Anirban Roychowdhury [b],
Dipankar Das [c], Chandan Kumar Ghosh [d,*], Dipten Bhattacharya [e], Pintu Sen [f]

[a] Department of Metallurgical and Material Engineering, Jadavpur University, Kolkata, 700032, India
[b] Department of Physics, Krishnath College, Berhampore, 742101, India
[c] UGC-DAE Consortium for Scientific Research, Kolkata Centre, Kolkata, 700098, India
[d] School of Materials Science and Nanotechnology, Jadavpur University, Kolkata, 700032, India
[e] Central Glass and Ceramic Research Institute, Kolkata, 700032, India
[f] Variable Energy Cyclotron Centre, Kolkata, 700064, India

ARTICLE INFO

ABSTRACT

Coral-like microstructure of NiO has been synthesized via a facile template free hydrothermal technique followed by calcination. Structure and morphology of the synthesized samples have been examined by x-ray diffractometer, field emission scanning electron microscope and transmission electron microscope. Positron annihilation spectroscopy reveals high porosity (37%) and cationic vacancies within the microstructures. Magnetic study illustrates spin-glass like behaviour and asymmetric hysteresis loop at room temperature. Later one is attributed to non-inversion symmetry of the anisotropic energy barrier, introduces by defect induced ferromagnetic domain within antiferromagnetic matrix of NiO. Numerical values of the anisotropy parameters have also been evaluated using law of approach method. The present study evidences that the microstructure could be helpful for developing magnetization based memory devices due to its high barrier height $\sim 2.50 \times 10^6$ erg/cm^3.

© 2018 Published by Elsevier B.V.

1. Introduction

Over the last decade, extensive research work has been carried out on transition metal oxide nanostructures due to their importance in fundamental researches as well as in applications in many fields [1]. Among different transitional metal oxide based nanostructure, investigated so far, NiO nanostructures have particularly drawn attention due to their potentiality in different applicational fields e.g. battery cathodes, catalysis, smart windows, sensing, p-type transparent conducting oxide films, electrochromic films, active optical fibers, photovoltaics, supercapacitors etc. [2–4]. NiO nanostructures have proven its candidature as an upcoming material for next generation resistive switching memory devices, spin valves, tunnel junction etc [5]. Till date, various hierarchical nanostructures of NiO such as hollow spheres [6], nanorods nanowires [7], polyhedrons [8], plates [9], has been synthesized and it has been observed that they often exhibit exotic properties completely different from bulk, thus applicational opportunity in additional fields gets opened up. Comparatively less attention

has been given to investigate magnetic properties of different NiO hierarchical structures. But, few studies that have already been carried out demonstrates that they often exhibit unique magnetic properties that has not been observed in bulk NiO [10]. For example, in contrast to antiferromagnetic bulk NiO, hierarchical structures show weak ferromagnetism, enhanced coercivity, enhanced hysteresis loop, well-described by Kodama et al. on the basis of multi-sublattice spin configuration [10], while earlier two-sublattice model, proposed by L. Neel in the year 1961, was not able to explain these newly observed magnetic properties [10]. Recently, spin glass response due to freezing of the surface spins has been observed in NiO structure by Winkler et al. [11]. In general, uncompensated surface spins and their interaction with local environment that significantly depends on morphology determine their magnetic properties where interparticle interaction plays crucial role [11–13]. In this context, magnetic properties of lotus-root and flower-like micro-spherical NiO were investigated by Cui et al. [14]. Proenca et al. examined the effect of size on the magnetic behaviour of nanocrystalline spherical NiO [15]. Here, it is to state that for better understanding the dependence of magnetic properties of hierarchical structure of NiO upon morphology and underlined magnetic interaction, intense research has to be carried out on various hierarchical structure of NiO. In this manuscript, magnetic

* Corresponding author.
E-mail address: chandan.kghosh@jadavpuruniversity.in (C.K. Ghosh).